TECHNISCHE UNIVERSITÄT MÜNCHEN

Lehrstuhl für Biotechnologie

Structural and Functional Principles of the Small Heat Shock Protein α-Crystallin

Jirka Peschek

Vollständiger Abdruck der von der Fakultät für Chemie der Technischen Universität München zur Erlangung des akademischen Grades eines Doktors der Naturwissenschaften (Dr. rer. nat.) genehmigten Dissertation.

Vorsitzender:	Univ.-Prof. Dr. B. Reif
Prüfer der Dissertation:	1. Univ.-Prof. Dr. J. Buchner
	2. Univ.-Prof. Dr. S. Weinkauf
	3. Univ.-Prof. Dr. M. Rief

Die Dissertation wurde am 28.6.2012 bei der Technischen Universität München eingereicht und durch die Fakultät für Chemie am 10.9.2012 angenommen.

TECHNISCHE UNIVERSITÄT MÜNCHEN

Lehrstuhl für Biotechnologie

Structural and Functional Principles of the Small Heat Shock Protein α-Crystallin

Jirka Peschek

Contents

1 Summary

The α-crystallins are molecular chaperones which belong to the small heat shock protein (sHsp) family. sHsps contribute to the maintenance of the cellular protein homeostasis by binding to partially unfolded substrate proteins preventing deleterious protein aggregation. There are two α-crystallin genes. However, while the expression of αA-crystallin is essentially restricted to the eye lens, αB-crystallin is ubiquitously expressed and thus associated to several human diseases. A remarkable structural feature of α-crystallins is the formation of dynamic oligomers with variable number of subunits. In this work, the molecular architecture of these complexes was elucidated using an integrated approach combining different biochemical and biophysical methods. A pseudoatomic model of 24-meric αB-crystallin was generated based on cryo-EM data. Furthermore, the functional principles of the chaperone activity of α-crystallins were studied. The reduction-induced aggregation of the model substrate lysozyme was used to probe the holdase function of αB-crystallin in more detail. A FRET-based assay was established to monitor substrate binding and release directly. Thus, αB-crystallin was shown to bind lysozyme early during the unfolding process. In heat-stressed HeLa cell lysates, αB-crystallin bound promiscuously to miscellaneous client proteins indicating a function as “generalist” in the proteostasis network. Although sHsps are considered to bind substrates in an ATP-independent manner, their chaperone activity is regulated. αB-crystallin is phosphorylated *in vivo* at three distinct serine residues in response to various kinds of stress. Phosphorylation leads to a reduced mean oligomer size and an increased chaperone activity. Mimicking of phosphorylation by glutamate mutants was used as tool to study the structure-function relationship of αB-crystallin. These results show that the N-terminal domain (NTD) provides a phosphorylation-controlled switch for oligomerization and activation of substrate binding. The introduction of proximal negative charges by phosphorylation causes a partial dissociation, which concomitantly alters the surface properties. The activated small oligomers bind preferentially to partially folded polypeptides. Taken together, these results imply a model in which the interaction of αB-crystallin with substrate proteins can be precisely modulated by differential phosphorylation of sites within the N-terminal domain. In addition, the release and refolding of denatured substrates by the interplay between alpha-crystallins and the Hsp70 system was revealed.

2 Introduction

Proteins are ubiquitous in the animate world. Structure, function and metabolism of life depend on them. Proteins are essential constituents of all organisms and they participate in every biological process. Accompanied by their functional diversity, a vast structural complexity of proteins has emerged in the course of evolution. To fulfill its specific function in the cell, every protein has to adopt a unique three-dimensional structure. This process, which leads from a synthesized polypeptide chain to a native structure, is termed protein folding (Dobson and Karplus, 1999).

The work of Christian Anfinsen on ribonuclease A in the early 60s showed that protein folding is a reversible process and that proteins are able to adopt their native conformations spontaneously. He concluded that the three-dimensional structure of a protein is determined by its primary structure, encoded in the DNA (Anfinsen, 1973; Anfinsen et al., 1961). This conclusion is applicable to *in vitro* folding in most instances as isolated proteins in dilute buffer solutions usually fold into their native, biologically active structure spontaneously and without assistance (Jaenicke, 1987). However, the huge number of possible conformations a polypeptide chain can adopt renders protein folding a highly complex process, which depends on the correct and coordinated formation of many weak and non-covalent interactions. The energetic component of this process can be depicted by funnel-shaped energy landscapes (Figure 1). From the unfolded state, represented by high-entropy states at the top of the funnel, proteins fold along multiple, parallel downhill routes to the native structure, which corresponds to the most thermodynamically stable structure (Dinner et al., 2000; Udgaonkar, 2008).

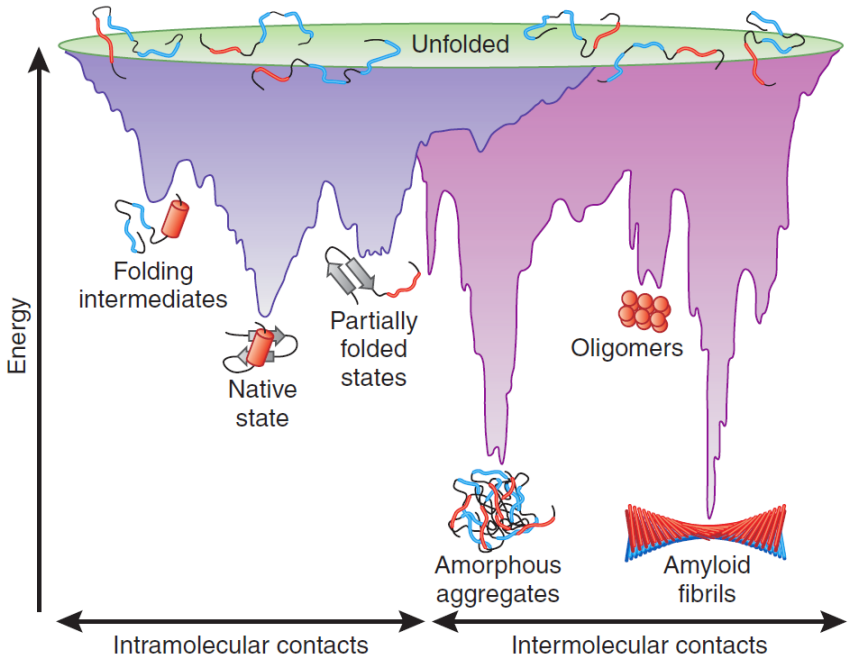

Figure 1 | Energy landscape scheme of protein folding and aggregation. Scheme of the funnel-shaped free-energy surface that proteins explore during folding. The unfolded state, represented by high-entropy states at the top of the funnel, folds along multiple, parallel downhill routes to the native structure. The free-energy surface is often rugged and contains local energy minima that could trap the protein in intermediate or even misfolded and aggregated states.
Reprinted by permission from Macmillan Publishers Ltd: Nature Structural and Molecular Biology (Hartl and Hayer-Hartl, 2009), © 2009

The difference in free energy between native and unfolded states merely accounts for 4-60 kJ/mol (Fersht and Daggett, 2002). The native state is considered not to be simply a snapshot of one single structure but rather an ensemble of conformers. This concept is emphasized by the vast number of flexible and dynamic proteins and finds its extreme realization by the presence of intrinsically unfolded domains or proteins within the proteome (Dyson, 2011). As mentioned, many parallel paths down the funnel exist but the free-energy surface is often rugged and contains local energy minima that could trap the protein in intermediate or even misfolded and aggregated states (Udgaonkar, 2008). The latter can exhibit deleterious effects on many cellular functions and are thus associated with aging as well as aggregation diseases such as neurodegenerative diseases, myopathies and even cancer (Balch et al., 2008). In addition, not only newly synthesized proteins are at risk of aberrant folding within the cellular environment, but also native proteins can undergo unfolding and aggregation under certain conditions like stress (Dobson, 2003; Jahn and Radford, 2005). To counteract that, cells possess a complex protein quality control network comprising various signaling pathways and components dedicated to the maintenance of proteostasis (protein homeostasis) (Balch et al., 2008; Powers et al., 2009).

2.1 Protein Folding in the Cell

Regarding protein folding, the situation in the cell differs considerably from that *in vitro*. The cytosol is a highly viscous and crowded environment. High protein concentrations of 300-400 g/l (Zimmerman and Trach, 1991) and the presence of a large number of other macromolecules cause the so called “excluded volume effect”. Under these conditions, intermolecular interactions become strongly favored (Ellis, 2001; Ellis and Minton, 2006). For an unfolded protein, the formation of aggregates, which is mainly mediated by exposed hydrophobic patches, competes with protein folding (Kiefhaber et al., 1991). The mechanism by which proteins are synthesized at the ribosome requires certain measures to assist and ensure correct folding of newly synthesized polypeptides to the native state (Frydman, 2001). In addition, various kinds of stresses can lead to protein misfolding or aggregation, posing a threat to all organisms (Richter et al., 2010; Tyedmers et al., 2010).
Cells of all kingdoms of life have developed a sophisticated protein quality control system to maintain proteome integrity and homeostasis. Proteostasis is achieved by several hundred proteins integrated in a complex network, including proteins, which act either to assist folding or refolding of proteins, the so-called molecular chaperones, or to remove misfolded or aggregated proteins by proteolytic degradation. The removal is mainly mediated by two paths: the ubiquitin-proteasome system (UPS) and autophagy (Balch et al., 2008; Hartl et al., 2011)
Selected aspects of the cellular proteostasis system will be introduced in the following sections, with a special emphasis on molecular chaperones, in particular the small heat shock protein family and their most prominent members, the α-crystallins, which are the subject of this thesis.

2.1.1 Molecular Chaperones in Protein Folding and Proteostasis

Molecular chaperones have been defined as a functional class of proteins that interact with non-native polypeptides to prevent their unspecific aggregation and to assist in their folding, transport and assembly without being part of the final structure (Ellis, 1987; Ellis et al., 1989). Many molecular chaperones were first identified as part of the heat shock response as their expression is strongly upregulated upon heat stress, leading to the term heat-shock proteins (Hsp) (Ellis, 1987; Georgopoulos and Welch, 1993). This implies that, besides the co- and posttranslational folding assistance, chaperones are also essential for providing tolerance towards various stress conditions.

Molecular chaperones are divided into several families according to their molecular weights. The main families are usually classified into Hsp100, Hsp90, Hsp70, Hsp60 (also termed chaperonins), Hsp40 and small heat-shock proteins (sHsps) (Buchner, 1996). The mechanisms of the major molecular chaperone families are illustrated in Figure 2. Proteins from the same class often show a large amount of sequence homology and are structurally and functionally related. However, no homology exists between representatives of the different chaperone families (Walter and Buchner, 2002). Other heat-inducible proteins like the redox-regulated Hsp33 from *E. coli* (Jakob et al., 1999) or Hsp12 from *S. cerevisiae*, which is intrinsically disordered and modulates membrane function (Welker et al., 2010), are attributed to none of the chaperone families mentioned above, demonstrating that the heat shock proteins also encompass many functionally different and even uncharacterized proteins (Narberhaus, 2002).

Molecular chaperones are involved in a plethora of proteome-maintenance functions including *de novo* folding, refolding of stress-induced non-native states, protein assembly, protein trafficking and even degradation. Thus, most chaperones bind rather promiscuously to unfolded proteins, leading to a broad range of clients (Tyedmers et al., 2010).

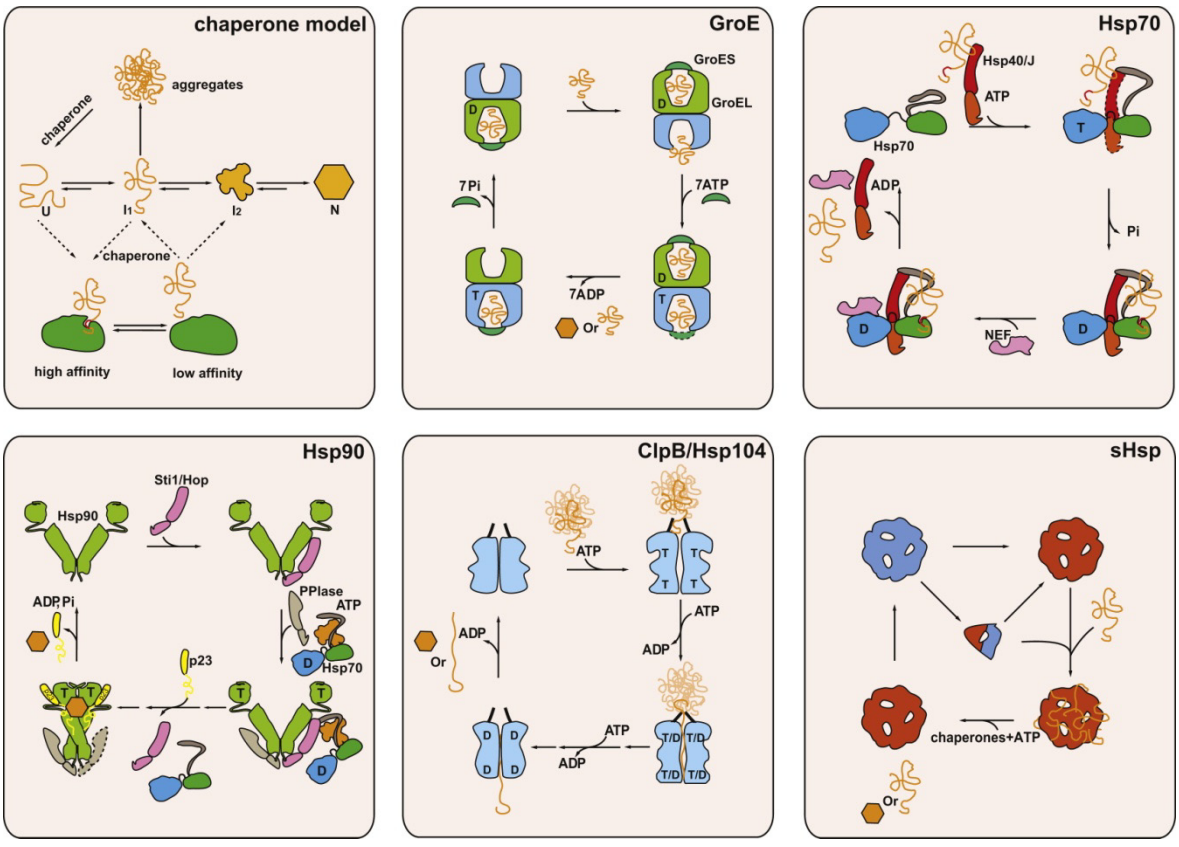

Figure 2 | Molecular chaperone mechanisms. Chaperone model: In general, proteins fold via increasingly structured intermediates (I1, I2) from the unfolded state (U) to the folded state (N). Under stress conditions, this process can be

reversed. Molecular chaperones bind proteins in nonnative conformations. The shift from the high-affinity binding state to the low-affinity release state is often triggered by ATP binding and hydrolysis.
GroE: The GroE machinery in bacteria, mitochondria, and chloroplasts consists of two identical rings that enclose a central cavity each. Nonnative protein is bound by the apical domains of the rings, and upon binding of ATP and the cochaperone GroES, the protein is encapsulated and released into the cavity. ATP hydrolysis in one ring results in the release of GroES and substrate protein from the opposite ring. During encapsulation the protein may fold partially or completely, depending on the characteristics of the respective substrate protein.
Hsp70: The Hsp70 system comprises two cochaperones, an activating protein (Hsp40/J-protein) and a nucleotide exchange factor (NEF). The activating protein can bind the nonnative protein and deliver it to Hsp70. It forms a complex with Hsp70 and stimulates its ATPase. Hsp70 binds a stretch of seven amino acids in the substrate protein. The NEF will induce the exchange of nucleotide. This further accelerates the ATPase cycle. The substrate protein is released presumably in a nonnative form.
Hsp90: In this chaperone system a large number of proteins work together. First, for a number of substrate proteins, Hsp70 delivers the substrates to Hsp90. It is not clear whether this is true for all substrates. More than a dozen cochaperones of Hsp90 exist in eukaryotes, which seem to modulate the system. One of them, Sti1/Hop, binds both Hsp70 and Hsp90 and at the same time inhibits Hsp90s ATPase (in yeast). In this complex, which also contains an additional PPIase cochaperone, the substrate protein is transferred from Hsp70 to Hsp90. Sti1/Hop is released once Hsp90 binds nucleotide and a further cochaperone (p23).
ClpB/Hsp104: In bacteria and yeast, this chaperone is able to dissolve aggregates by actively pulling proteins through a central channel of the hexameric structure. Each protomer contains two ATPase sites, which have quite distinct characteristics concerning turnover and function. During passage through the chaperone complex, the substrate protein is unfolded. Refolding can occur upon release, and, to some extent, it can also occur in cooperation with other chaperones.
sHsps: sHps are oligomeric complexes that are often activated, e.g., by heat or modifications. Many are believed to dissociate into smaller oligomers to become active. sHsps can bind many nonnative proteins per complex. Release requires cooperation with other ATP-dependent chaperones such as Hsp70.
Figure taken from Richter et al. (2010). Reprinted by permission from the authors.

According to their main function, chaperones can be divided into two classes: “foldases” and “holdases”. Foldases including the Hsp70/40 system, Hsp90 and the chaperonins depend on ATP-hydrolysis. They are multicomponent molecular machines that switch between states of different affinity towards unfolded substrates through ATP- and cofactor-regulated binding and release cycles (Hartl et al., 2011). Holdases bind aggregation-prone clients and thus protect proteins from aggregation, often under distinct stress conditions, and include chaperones like sHsps or the redox-regulated Hsp33 (Basha et al., 2012; Haslbeck et al., 2005a; Jakob et al., 1999).

It is a well-established concept that different classes of molecular chaperones cooperate in the cell to form multi-chaperone networks. The interaction between the Hsp90 system and the Hsp70 system via the mediator Hop (Hsp70-Hsp90 organizing protein) or between Hsp70 and GroE are examples for such networks in protein folding (Buchberger et al., 1996; Langer et al., 1992). Protein disaggregation can be mediated by a bi-chaperone system comprised of the cooperative action of the Hsp70 system with members of the Hsp100 family (Tyedmers et al., 2010). Furthermore, ATP-independent holdases, e.g. sHsps, bind to unfolding proteins during stress. When non-stress conditions resume, bound client proteins are released for refolding assisted by foldases (Haslbeck et al., 2005a; Hoffmann et al., 2004). Many examples of such chaperone networks have been described and studied during the last decades. Nevertheless, the regulation of such proteostasis

networks and the precise mechanisms of cooperation and substrate transfer are not understood comprehensively.

2.1.2 From Ribosome to Folded Protein

The protein synthesis on the ribosome is a vectorial process, starting from the N terminus of the polypeptide chain, which leads to important implications in the folding process. The rate of synthesis (4-20 amino acids/s) is comparable to the folding rate of many proteins ($t_{1/2} < 1$ s). Thus, folding starts when the N terminus exits the ribosome, whereas the C-terminal part is not yet synthesized (Hartl et al., 2011).

A considerable number of nascent polypeptides are prone to aggregation when emerging from the ribosome. The exposure of hydrophobic surfaces by a nascent polypeptide chain renders them prone to aggregation (Hartl and Hayer-Hartl, 2002; Young et al., 2004). Folding assistance by chaperones can occur both co- and posttranslationally (Langer et al., 1992). A first group of chaperones binds in proximity to the ribosomal exit site and includes trigger factor (TF) in bacteria and distinct Hsp70 complexes (e.g. ribosome-associated complex, Rac) and nascent-chain-associated complex (NAC) in eukaryotes (Frydman, 2001). Other chaperones, including non-ribosome-bound members of the Hsp70 family, chaperonins (Frydman et al., 1994) and Hsp90 (Wandinger et al., 2008), work further downstream in the process.

2.1.3 Cellular Strategies for Proteome Maintenance and Control of Aggregation

As the energy barrier between native and non-native states is usually small, not only newly synthesized proteins during co- and posttranslational folding but also native proteins are at permanent risk of unfolding, especially under various stress conditions (Figure 3). Among these conditions are mutations that result in protein misfolding and aggregation, defects in protein biogenesis, environmental stress and aging (Tyedmers et al., 2010).

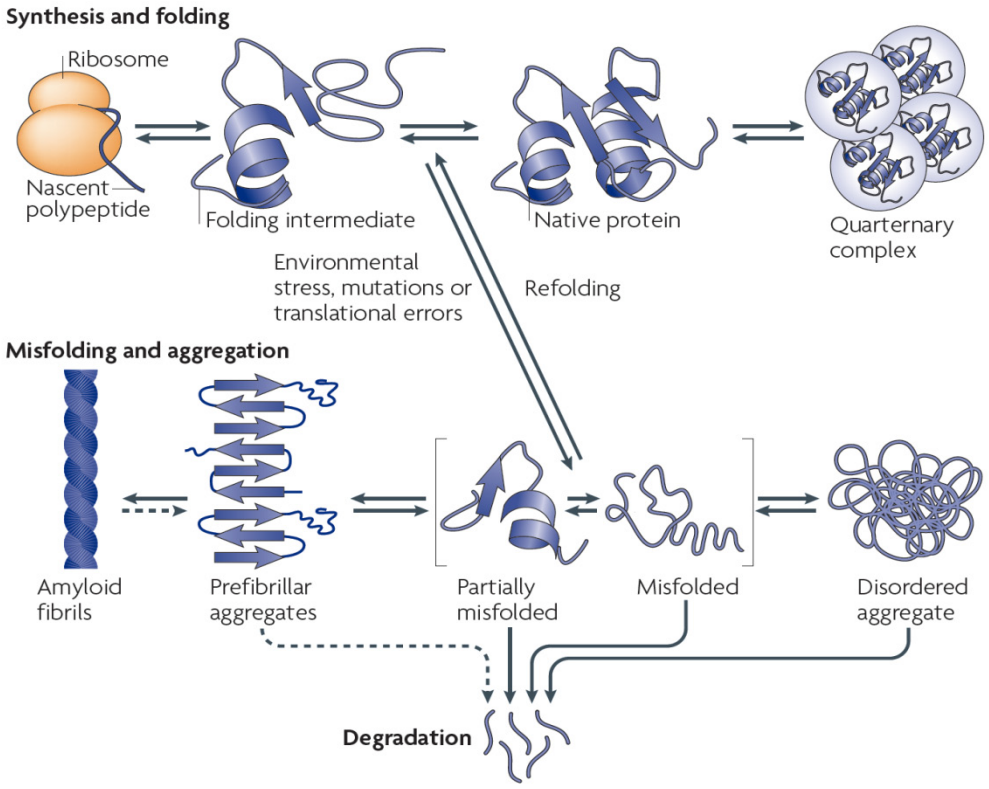

Figure 3 | Overview of cellular protein aggregation. A protein during and after its synthesis at the ribosome folds through different intermediates to its native, three-dimensional structure. Different kinds of stress, mutations in the synthesized protein or translational errors can cause protein misfolding. Misfolded intermediates can be refolded to the native state or be degraded by different cellular proteolysis systems that prevent the accumulation of misfolded proteins. Aggregates can form during persisting stress conditions, increased amounts of aberrant proteins or in aged cells. Their formation can be guided by molecular chaperones. The morphology of aggregates is variable and ranges from mostly unstructured, disordered aggregates to prefibrillar species and highly ordered β-sheet-rich amyloid fibrils. Arrows indicate a process that can include several single steps; dashed arrows indicate a process of minor significance.
Reprinted by permission from Macmillan Publishers Ltd: Nature Reviews Molecular Cell Biology (Tyedmers et al., 2010), © 2010

Partially or globally unfolded proteins are prone to aggregation because of an increased exposure of hydrophobic residues that are normally buried in the native structure. Protein aggregation is a higher-order reaction and thus concentration-dependent (Kiefhaber et al., 1991). Different aggregating protein species can also influence each other or even cause proteins to co-aggregate. A proteomics study in human cells showed that metastable proteins are at risk to be targeted by such interactions, resulting in their co-aggregation (Olzscha et al., 2011). The presence of protein aggregates is being discussed to be associated with cell toxicity and several aberrant medical conditions. Trapping other proteins in aggregates was suggested to cause toxicity associated with polyglutamine aggregation in neurodegenerative diseases (Chai et al., 2002; Nucifora et al., 2001). Another manifestation of such a toxicity mechanism is a recent study that has shown the

oncogenic potential of mutant p53 to sequester wild-type p53 into co-aggregates (Xu et al., 2011).

Cells have evolved strategies to control protein aggregation: They can prevent the accumulation of aggregation-prone misfolded proteins by chaperone-mediated refolding or by removal of such species through proteolytic degradation or autophagy. In addition, there are several measures that help to cope with formed aggregates by disaggregation activities or pathways for the cellular sequestration of protein aggregates (Tyedmers et al., 2010).

The function of the various families of molecular chaperones in protein folding and refolding (Figure 2) is the first and most effective way to control protein aggregation by preventing the accumulation of aggregation-prone states. However, aggregates are not necessarily dead-end products *in vivo*. The Hsp70 system together with Hsp100 family members forms a bi-chaperone system that exhibits a combined disaggregase and refolding function (Goloubinoff et al., 1999; Mogk et al., 1999; Parsell et al., 1994). The specific role of sHsps in preventing protein aggregation and their interplay with other chaperone systems is discussed in the next chapter in more detail. An alternative path for the removal of protein aggregates is the degradation by cellular proteases. In bacteria, AAA+ chaperones (e.g. ClpA in *E. coli*) act together with peptidases (e.g. ClpP) in disaggregation and removal of aggregates (Dougan et al., 2002). In higher eukaryotes, the ubiquitin proteasome system (UPS) is important for the removal of misfolded proteins (Goldberg, 2003). However, the degradation of pre-existing aggregates by the UPS was shown to be not possible *in vitro* (Venkatraman et al., 2004; Verhoef et al., 2002) and is questioned by *in vivo* studies as well (Bence et al., 2001; Holmberg et al., 2004). However, selective microautophagy has been described as alternative pathway for the clearance of misfolded and aggregated proteins in mammalian cells (Kirkin et al., 2009; Rubinsztein, 2006).

When the described quality-control systems fail to prevent aggregation, protein aggregates are usually deposited at specific cellular sites. This sequestration can be regarded as a "second cellular path to control protein aggregation" (Tyedmers et al., 2010). Directing aggregates to specific deposition sites can potentially protect the cell from such toxic oligomeric protein species. For amyloidogenic proteins, there is growing evidence that rather soluble oligomers than amyloids exhibit cytotoxic effects. Spatial sequestration of aggregates might also facilitate their removal (Kaganovich et al., 2008; Taylor et al., 2003; Wigley et al., 1999). In bacteria, the heterologous expression of proteins can cause the formation of inclusion bodies, which usually localize at the old cell pole for yet not fully understood reasons (Kopito, 2000; Ventura and Villaverde, 2006; Winkler et al., 2010).

This asymmetric distribution of aggregated proteins might function as a strategy for rejuvenating the progeny (Lindner et al., 2008). In mammalian cells, a certain form of inclusion bodies, termed aggresomes, forms in response to stresses, which generate large amounts of misfolded protein (Johnston et al., 1998; Kopito, 2000). Protein aggregation has been intensely studied in *S. cerevisiae*. In yeast cells, it was shown for some substrates that they partition between two distinct quality control compartments: A compartment in proximity to the nuclear membrane, termed the juxtanuclear quality-control compartment (JUNQ), and a second compartment adjacent to the vacuole, termed the insoluble protein deposit (IPOD) (Kaganovich et al., 2008). Recently, an involvement in aggregate sorting of Hsp42, one of two sHsps in yeast, was described (Specht et al., 2011). Taken together, protein aggregation in cells seems to be a rather organized process due to the evolution of several quality-control systems.

2.2 The Small Heat Shock Proteins

The small heat shock proteins (sHsps or HspB) represent an almost ubiquitous, moderately conserved family of proteins. Despite their broad diversity, the members of the sHsps possess nevertheless several common characteristics, which distinguish them as a protein family. Although sHsps share only a little overall sequence homology, they all have a common conserved sequence motif: the α-crystallin domain. As the designation “small Hsps” indicates, sHsps are low-molecular-mass proteins. Their monomer molecular weight varies from 12 to 43 kDa, whereas the predominant number of representatives is in the range of about 20 kDa (Haslbeck et al., 2005a; Narberhaus, 2002). However, most sHsps are large, dynamic oligomers.

sHsps were first discovered in *Drosophila melanogaster* as proteins of small molecular monomer mass induced after heat shock (Tissieres et al., 1974). In fact, the cellular concentration of many sHsps is strongly increased in response to a variety of stresses, but they can also function constitutively in many organisms and tissues (Basha et al., 2012; Haslbeck et al., 2005a; Narberhaus, 2002). The sHsps studied were shown to act as ATP-independent molecular chaperones. They function as holdases by binding to partially folded proteins and efficiently preventing their aggregation (Horwitz, 1992; Jakob et al., 1993).

sHsps are often described as dispensable chaperones. Under optimal conditions most bacteria produce either no or negligible amounts of sHsps. Under stress conditions, the

increase at mRNA and protein level can be dramatic (Narberhaus, 2002). Microarray-based expression profiling in *E. coli* showed that transcription of *ibpA* and *ibpB* was heat-induced by a factor of 300 (Richmond et al., 1999). However, a temperature-sensitive growth defect of *E. coli ibpAB* mutants is hardly detectable (Kitagawa et al., 2000; Thomas and Baneyx, 1998). The importance of sHsps was demonstrated by knock-out mice lacking the gene for the human homologue of αA-crystallin, which develop cataract in early life ages (Brady et al., 1997). Deletion strains of *Synechocystis* sp. lacking the Hsp16.6 gene become sensitive to severe heat shock (Lee et al., 1998). Dysfunctions of αB-crystallin and Hsp27 were found to be involved in the development of neurodegenerative diseases, e.g. Alzheimer's or Alexander disease (Iwaki et al., 1993; Iwaki et al., 1989).

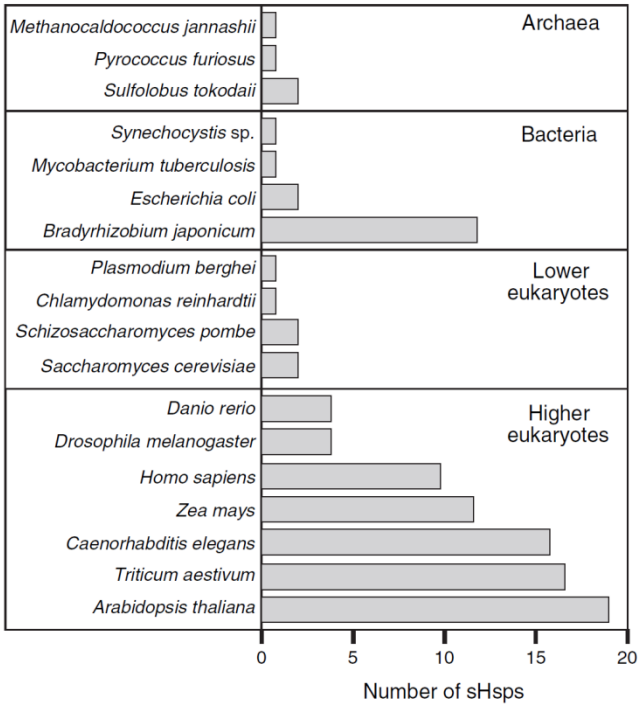

Figure 4 | Schematic overview of the number of representatives of the sHsp family in different organisms.
Figure taken from Haslbeck et al. (2005a). Reprinted by permission from the authors.

Small heat-shock proteins are widely distributed among all taxonomic kingdoms and their presence has been reported in almost all organism except for some, mainly pathogenic, bacteria (Haslbeck et al., 2005a; Narberhaus, 2002). The growing number of completely sequenced genomes allows an exact statement about the existence and quantity of sHsps in a diverse array of organisms (Kriehuber et al., 2010). The individual number of small heat-shock proteins in different organisms varies significantly from only one or two – as it is true for many archaea and bacteria – up to 19 in some plants (Figure 4). The universal

occurrence of sHsps might be indicative of an early phylogenetic origin of this protein family (Basha et al., 2012; Haslbeck et al., 2005a).

Based on the results of the Human Genome Project, ten different small heat-shock proteins were specified in humans (Kappe et al., 2003; Seal et al., 2011) (Table 1). For some of these human sHsps only little is known about their cellular function and regulation, whereas the most prominent representatives αA- and αB-crystallin, as well as Hsp27 are comparatively well characterized. In general, the human small heat shock proteins can be divided into two groups: On the one hand ubiquitous sHsps and on the other hand those, whose expression and localization are restricted to distinct tissues.

Table 1 | Overview of human small heat shock proteins. Currently accepted nomenclature from the HUGO Human Genome Nomenclature Database (http://www.gene.ucl.ac.uk/cgi-bin/nomenclature/searchgenes.pl) (Seal et al., 2011). The ten different human sHsp members are depicted along with their synonyms, specifications of localization and associated diseases.

HUGO	Synonyms	Mass (kDa)	Localization	Diseases
CRYAA	αA-Crystallin, HSPB5	19.9	Eye lens	Cataract
CRYAB	αB-Crystallin, HSPB4	20.2	Ubiquitous	Neuropathy, Myopathy, Cancer, Cataract, Ischemia
HSPB1	Hsp27	22.3	Ubiquitous	Neuropathy, Cancer, Ischemia
HSPB2	MKBP	20.2	Heart and muscle	Myopathy, Ischemia
HSPB3	HSPL27	17.0	Heart and muscle	
HSPB6	Hsp20, p20	17.1	Ubiquitous	Neuropathy, Ischemia
HSPB7	cvHsp	18.6	Heart and muscle	Cardiomypathy
HSPB8	Hsp22, H 11 Kinase	21.6	Ubiquitous	Neuropathy, Ischemia, Cancer
HSPB9	–	17.5	Testes	Cancer
ODF1	HSPB10	28.4	Testes	

2.2.1 sHsp Primary Structure

Small heat-shock proteins share a common structural organization: The conserved α-crystallin domain is flanked by a variable N-terminal domain and a moderately conserved C-terminal domain (Caspers et al., 1995; de Jong et al., 1998; Kriehuber et al., 2010). Despite their structural organization, sHsps exhibit little sequence homology. Multiple sequence alignments revealed only a few conserved amino acid residues (de Jong et al., 1998). Three are part of the sequence motif A-x-x-x-n-G-v-L at the end of the α-crystallin domain. This motif is the most significant indicator for this domain. In addition, two further consensus motifs can be found: F-x-R-x-x-x-L, also located within in the α-crystallin domain, as well as I-x-I in the C-terminal region (Figure 5). However, not a single amino acid was found to be invariant in all members of the sHsp family. A

bioinformatics study of more than 8,700 sHsp sequences revealed an average length of 161 amino acids, corresponding to about 18 kDa (Kriehuber et al., 2010).

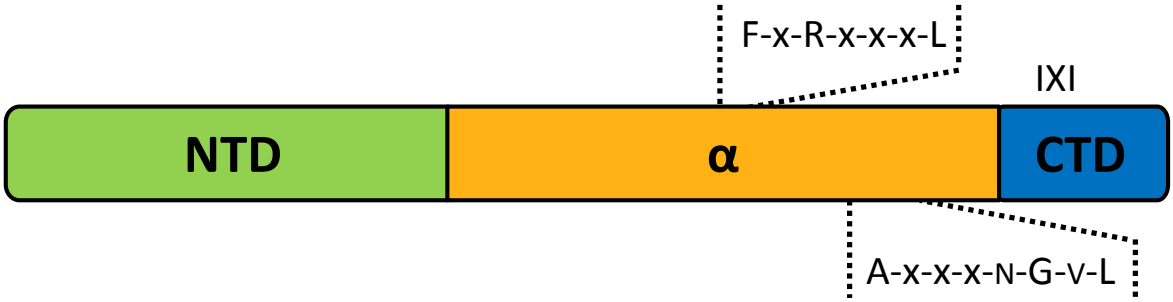

Figure 5 | Domain organization of sHsps. The central α-crystallin domain (α) is shown in orange. The flanking N-terminal domain (NTD) and C-terminal domain (CTD) are depicted in green and blue, respectively, The approximate locations of consensus sequences are indicated by dotted lines.

The central α-crystallin domain (ACD; PFAM accession number PF00011, PROSITE profile PS01031) is a conserved sequence of about 90 amino acids. The existence of the ACD is arguably the most important criterion for the integration of proteins in the sHsp family (Kappe et al., 2010). The sequence homology varies depending on the phylogenetic relationship between 20% and 60%. Genomic data revealed a high occurrence of charged amino acids and an underrepresentation of aromatic residues in the ACD when compared to the occurrence in the complete genome (Kriehuber et al., 2010).

The N-terminal domain (NTD) is very diverse in sequence and thus largely responsible for the sequence variation of different sHsps within one organism. The NTD is essentially omnipresent and has an average length of 56 residues. However, the length ranges from 25 residues in Hsp12 proteins from *C. elegans* up to 247 in yeast Hsp42 (Haslbeck et al., 2005a). In yeast Hsp26, a part of the NTD that is adjacent to the ACD was defined as extra domain ("middle domain") based on limited proteolysis (Haslbeck et al., 2004b). The aromatic amino acids Trp and especially Phe as well as Pro residues are overrepresented in the NTD (Kriehuber et al., 2010). Most sites of posttranslational modifications also seem to be located within this region (MacCoss et al., 2002).

Like the NTD, the length and sequence of the C-terminal domain (CTD; also referred to as C-terminal extension) vary considerably. The CTD has an average length of 10 residues and does typically not exceed 20 amino acids. In some sHsp family members, e.g. human Hsp20, it is missing completely. The CTD contains the highly conserved IXI motif, which was found to be important for inter-dimer contacts (Basha et al., 2012; Haslbeck et al., 2005a; Hilton et al., 2012). Charged and polar amino acids are overrepresented in the

C-terminal extension, while aliphatic and aromatic residues are underrepresented (Kriehuber et al., 2010).

2.2.2 The α-Crystallin Domain Dimer

Obtaining high-resolution structural data for full-length sHsps has been very challenging and so far not possible for any oligomeric form of a metazoan sHsp. However, the growing number of available structures of isolated ACDs allows drawing a rather detailed picture of the structural organization of the domain. Recombinantly produced truncated ACDs of various sHsps form stable dimers (Bagneris et al., 2009). Hence, the isolated ACD is not sufficient for oligomer formation. Its function is rather to form a dimeric substructure, which is the basic building block of all sHsps (Basha et al., 2012; Hilton et al., 2012). The ACD has a conserved primary sequence, but the homology is even greater on the structural level. All ACDs fold into an immunoglobulin-like β-sheet sandwich of up to nine antiparallel β-strands, but two dissimilar dimer interfaces are possible: Dimerization in plant, archaeal and bacterial sHsps occurs via reciprocal strand swapping of the β6 strands into the β-sandwich of the neighboring monomer (Figure 6) (Kim et al., 1998; van Montfort et al., 2001). In contrast, a different dimer structure is present in metazoan sHsps. The β6 strand has fused with β7 into an elongated strand (β6+7), which forms the dimer interface with the β6+7 strand of the other monomer in antiparallel orientation (Figure 9) (Bagneris et al., 2009; Jehle et al., 2009; Laganowsky et al., 2010).

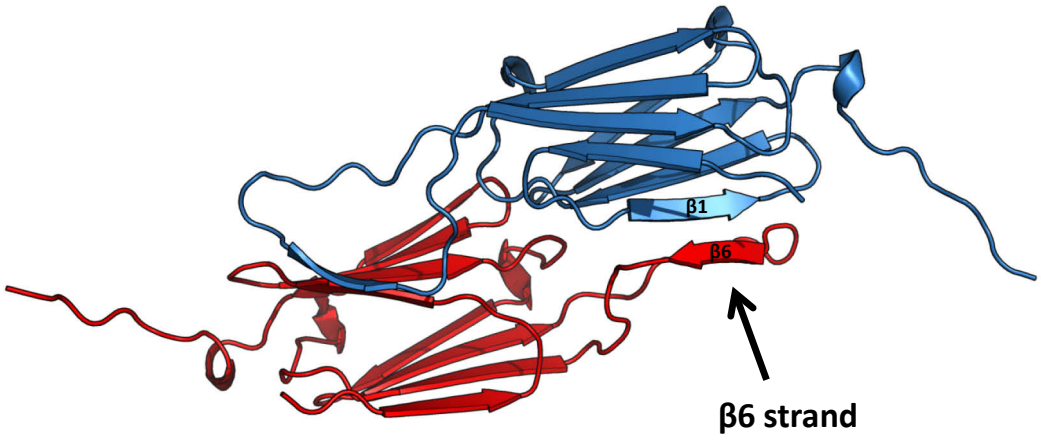

Figure 6 | The sHsp dimer. Dimer structure of Hsp16.5 from *Methanocaldococcus jannaschii.* (PDB 1SHS). Individual monomers are colored red and blue.

2.2.3 The Molecular Architecture and Dynamic Oligomer Equilibrium of sHsps

A key feature of most sHsps is their ability to assemble into large oligomers. Many sHsps form oligomers consisting of 12 or 24 identical subunits (Haslbeck et al., 2005a). However, smaller as well as larger complexes have been reported. The oligomer size ranges from dimers, like Hsp20 from rats, to 50mers, as described for α-crystallins (Groenen et al., 1994; van de Klundert et al., 1998). Detailed structure determination of a broad variety of sHsps remains challenging due to the high dynamics of the oligomers. So far, only two high resolution crystal structures of oligomeric small heat shock proteins were resolved, Hsp16.5 from the archaeon *Methanocaldococcus jannaschii* and Hsp16.9 from *Triticum aestivum* (wheat). Hsp16.5 forms spherical complexes of 24 subunits with octahedral symmetry containing eight triangular and six square openings (Kim et al., 1998) (Figure 7A&B). Hsp16.9 possesses a distinctly different quaternary structure consisting of two hexameric double-discs (van Montfort et al., 2001) (Figure 7C&D).

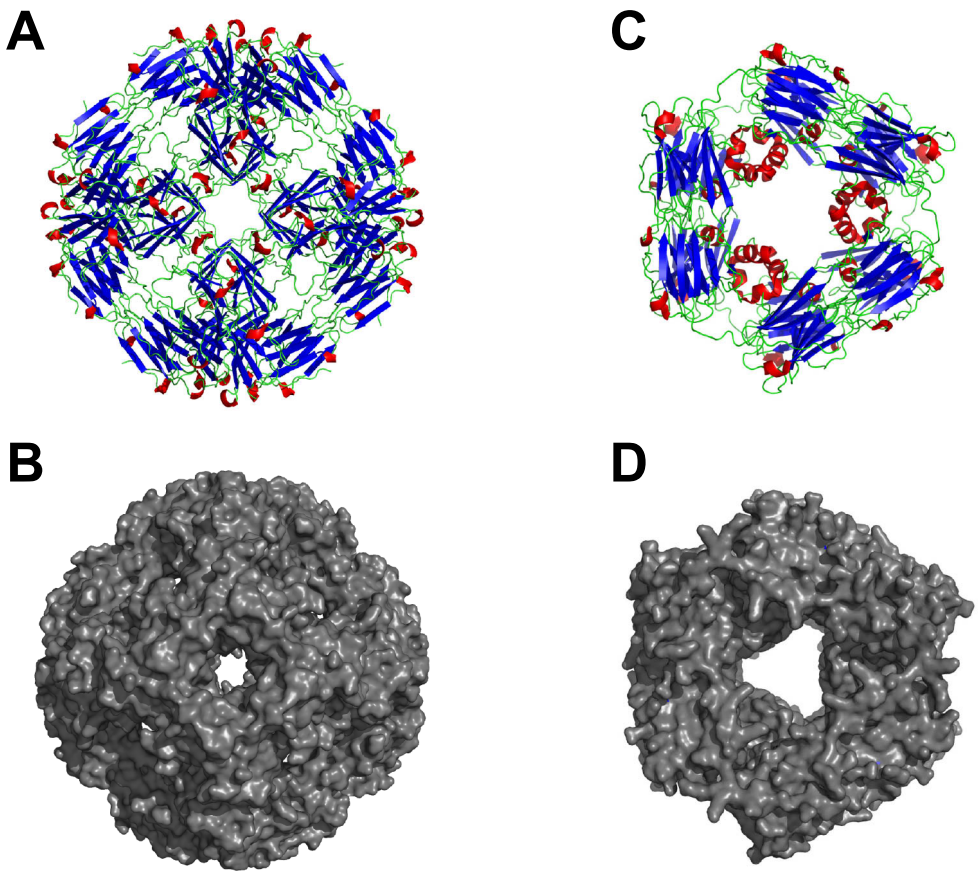

Figure 7 | Structures of sHsp oligomers. (A) Secondary structure and (B) surface representation based on the crystal structure (PDB 1SHS) of the Hsp16.5 24-mer from *Methanocaldococcus jannaschii (Kim et al., 1998)*. (C) Secondary structure and (D) surface representation based on the crystal structure (PDB 1GME) of the Hsp16.9 12-mer from *Triticum aestivum* (wheat) (van Montfort et al., 2001). The secondary structure elements are depicted in the same color code with α-helices in red, β-strands in blue and loop regions in green.

Although the overall quaternary structures of Hsp16.5 and Hsp16.9 are different, comparison of the two sHsp X-ray structures allowed defining common structural features across the sHsp family. In the two crystal structures the CTDs are involved in stabilizing the oligomer structure (Kim et al., 1998; Van Montfort et al., 2001; van Montfort et al., 2001). The C-terminal IXI motif, which is present in over 90% sHsp sequences, patches a hydrophobic segment formed by β4 and β8 in the α-crystallin domain of a neighboring subunit. Truncation of the CTD in Hsp16.5 fully abrogates the assembly into oligomers. Mutational studies show that the IXI motif also participates in inter-subunit interactions of metazoan sHsps (Pasta et al., 2004). However, the precise role of the CTD in sHsps from higher eukaryotes remains elusive.

C-terminal contacts are usually not sufficient to form native oligomeric assemblies. Most sHsps fail to maintain the native oligomer structure after partial or complete deletion of the NTD. Hsp16.2 from *C. elegans* served as a model to investigate the relevance of the NTD for oligomerization and chaperone function. Deletion mutants lacking the first 15, 32 or 44 amino acids failed to form native-like oligomers, but rather exhibited trimeric and tetrameric species (Leroux et al., 1997). Neither of the truncated versions showed chaperone-like activity. Similar studies with other sHsp family members confirmed the critical role of the NTD of small heat-shock proteins for the assembly of native oligomers (Bova et al., 2000; Narberhaus, 2002). The isolated ACD of yeast Hsp26 is even a stably folded monomer, which requires the "middle domain" or the C-terminal extension including the IXI motif for dimerization (Chen et al., 2010). However, the role of the NTD in oligomer assembly remains for the most part enigmatic. Even in the two available crystal structures, the NTDs are either not (Hsp16.5) or only partially (Hsp16.9) resolved. This might imply a rather high degree of flexibility or an unstructured region (Haslbeck et al., 2005a).

sHsp oligomers are dynamic structures. *In vitro*, the dynamic behavior of sHsps can be followed by monitoring the exchange of subunits. To this end, oligomers can be covalently modified with fluorescence dyes, suitable for fluorescence resonance energy transfer (FRET) and the exchange of subunits can be followed using fluorescence spectroscopy (Bova et al., 1997; Bova et al., 2000). More recently, mass spectrometry (MS) was applied to study the oligomer dynamics (Painter et al., 2008; Stengel et al., 2010). Besides these so-called homo-oligomers, some sHsps can form mixed complexes. IbpA and IbpB, two representative sHsps from the prokaryote *E. coli*, were found to form hetero-oligomers (Matuszewska et al., 2005). In mammalian cells, hetero-oligomerization was described for

the closely related αA and αB subunits of α-crystallins and for αB-crystallin with Hsp27 (Bova et al., 1997; Bova et al., 2000). In addition, the small heat-shock proteins HspB2 and HspB3 form well-defined hetero-oligomers, consisting of 4, 8, 12, 16, 20 and 24 subunits, in a unique 3 to 1 subunit ratio (den Engelsman et al., 2009).

2.2.4 The Molecular Chaperone Function of sHsps

The cellular function of small heat-shock proteins remained elusive for a long time after their discovery. In the early 1990s, *in vitro* studies showed that sHsps function as molecular chaperones that bind non-native proteins thereby preventing their aggregation. Bovine α-crystallin and murine Hsp25 were the first sHsp family members with a reported chaperone function (Horwitz, 1992; Jakob et al., 1993). Since then, many sHsps from various species were shown to possess such a holdase function. sHsps are now generally regarded as ATP-independent molecular chaperones involved in proteostasis (Basha et al., 2012; Haslbeck et al., 2005a).

Several *in vitro* methods have been established to monitor the aggregation suppression by sHsps. Most commonly applied are aggregation assays, in which a (model) substrate protein is denatured by heat or reduction and the effect of sHsps on the resulting aggregation is followed by light scattering. A more detailed summary of methods to study the chaperone function of sHsps is given elsewhere (Basha et al., 2012; Buchner et al., 1998). sHsps suppress the aggregation already in equimolar ratios in relation to the monomer concentration. Thus, they are able to bind multiple substrate proteins per oligomer. Their substrate binding capacity is severalfold higher than for all other molecular chaperone families (Haslbeck et al., 2005a; Narberhaus, 2002). This intriguing ability to bind comparably high amounts of non-native substrate proteins led to the term "molecular sponges" (Eyles and Gierasch, 2010). Yet, it is not clear, how sHsps recognize unfolded substrates. There is evidence that substrates are bound early during the unfolding process and kept in a native-like and refolding-competent state (Cheng et al., 2008; McHaourab et al., 2009). The interaction of sHsps with substrates is presumably mediated by exposure of hydrophobic patches, but so far no common recognition pattern within unfolded polypeptides was found. The same is true for the identification of the substrate binding site of sHsps. Several studies describe the attempt to determine the sites within sHsps that mediate direct physical contact with substrate proteins. Interaction sites have been probed using deletion mutants and cross-linking methods (Ahrman et al., 2007; Ghosh et al., 2007; Jaya et al., 2009). It appears that there is no single, specific substrate interaction surface

and that multiple sites located at all domains of sHsps contribute to binding. However, a study with pea Hsp18.1 revealed the highest cross-linking efficiency to the NTD (Jaya et al., 2009). This finding is consistent with other studies that proposed a major contribution of N-terminal regions to substrate binding (Basha et al., 2006; McHaourab et al., 2009).

The complexes that form between sHsps and substrates are usually stable enough to study their size and morphology by different methods *in vitro*. sHsp-substrate complexes are large and heterogeneous depending on the ratio of sHsp to substrate and the conditions during their formation (Basha et al., 2012; Hilton et al., 2012). Substrate complexes between pea Hsp18.1 and luciferase were quantified by a tandem-MS approach. Hundreds of different stoichiometries were identified, variable in the number of both components (Stengel et al., 2010).

At current, the picture emerges that the ability to bind unfolded proteins and to prevent their aggregation is not limited to a certain number of subunits. Some sHsps, such as HspB6, only form dimers and show chaperone activity (Bukach et al., 2004). However, it was shown for different sHsps that mutants with impaired ability to form oligomers have reduced chaperone-like function (Leroux et al., 1997; van de Klundert et al., 1998). Regarding oligomer dynamics and subunit exchange, contradictory results were published (Aquilina et al., 2005; Franzmann et al., 2005; Haslbeck et al., 1999; Shashidharamurthy et al., 2005). The biological importance of subunit exchange remains elusive and the phenomenon requires further comprehensive analysis.

Since sHsps do not possess an ATPase activity, they do not progress through a regulatory cycle controlled by nucleotide hydrolysis like members of the Hsp60, Hsp70 or Hsp90 chaperone families. Yet, the activity of sHsps is regulated by different means. The expression of several sHsps is increased under conditions that promote the accumulation of unfolded proteins such as heat-stress (Klemenz et al., 1991; Narberhaus, 2002; Richmond et al., 1999). In addition, sHsps can switch between an inactive or less active state (commonly referred to as "storage form") and a state of high affinity towards unfolded substrate proteins. These states are often associated with different oligomeric assemblies of the sHsp (Stengel et al., 2010). Changes in temperature or pH as well as posttranslational modifications are described as triggers that promote this shift, thus reflecting an additional level of regulation (Franzmann et al., 2008; Hayes et al., 2009; Koretz et al., 1998).

The naturally occurring substrates of small heat shock proteins are largely unknown. Given the immense diversity of model substrates, sHsps seem to suppress the unproductive aggregation of diverse client proteins within the cellular context. Proteomic studies in

S. cerevisiae and *Synechocystis* sp. have shown that about one third of the cytosolic proteins is kept soluble by sHsps under stress conditions (Basha et al., 2004; Haslbeck et al., 2004a). The question of substrate specificity is of special interest in organisms with multiple different sHsps in their genome. The presence of more than one sHsp in the same cell or cellular compartment implies distinct functions and substrate interactions. Especially for mammalian sHsps, some more specific interactions are reported. For instance, HspB8 was found in complexes with the Hsp70 cochaperone Bag3 (Carra et al., 2008). Other studies revealed binding of Hsp27 and αB-crystallin to caspase-3 in its procaspase state (Pandey et al., 2000). Furthermore, an important role for the assembly and stabilization of different cytoskeletal components was suggested (Launay et al., 2006), although quantitative data are lacking to describe these interactions in more detail. In general, there is still not much known about the substrate specificity of sHsps and many questions remain to be answered.

2.2.5 Role of sHsps in the Cellular Proteostasis Network

The chaperone-like function of small heat shock proteins was shown to be independent of ATP-hydrolysis. Apparently, sHsps lack refolding activity and rather function as a molecular buffering system for unfolding proteins disposed in the cell to prevent the formation of insoluble protein aggregates. sHsps bind denaturing substrate proteins via formation of stable substrate complexes whereby they are maintained in a refolding-competent state (Ehrnsperger et al., 1997). Subsequently, the bound proteins can be refolded by the interaction with ATP-dependent molecular chaperones, involving the Hsp70 chaperone family (Ehrnsperger et al., 1997; Lee et al., 1997) and also the Hsp100 proteins (Cashikar et al., 2005; Haslbeck et al., 2005b; Mogk et al., 2003). The position of sHsps in the context of a dynamic and synergistic multi-chaperone network is depicted in Figure 8. Recent studies also suggest an involvement of sHsps in protein degradation (Vos et al., 2011).

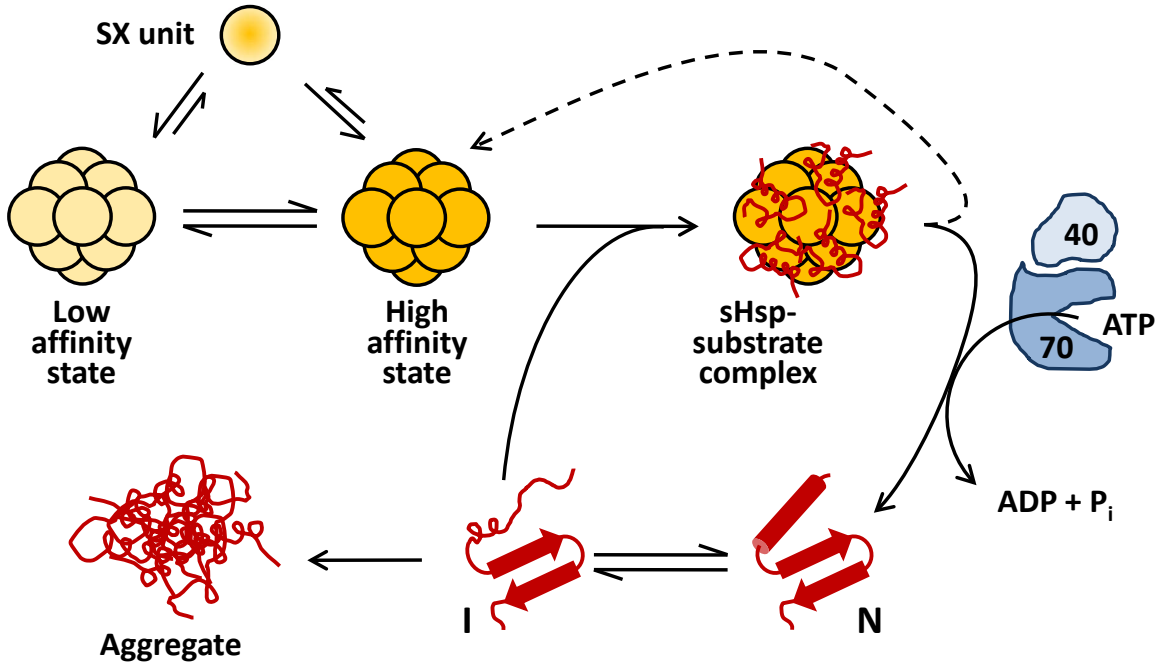

Figure 8 | Function of sHsps in the multi-chaperone network. Most sHsps form large dynamic oligomers which exchange subunits in a temperature-dependent manner. sHsps can switch between a low affinity state ("storage form") and a high affinity state, which binds unfolding intermediates (I) by forming large sHsp-substrate complexes. Thus, the aggregation of non-native proteins is inhibited. Bound substrates are maintained in a refolding-competent state. The subsequent release and refolding to the native state (N) is mediated by ATP-dependent chaperones like the Hsp70 system.

2.3 The α-Crystallins

2.3.1 The Crystallin Family of Eye Lens Proteins

In 1830, the Swedish chemist Jöns Jakob Berzelius described a protein fraction from vertebrate eye lenses that he called "Krystallin" (Berzelius, 1830). Nowadays, the term is still used to describe the family of soluble proteins that are the major constituents of the vertebrate eye lens. At the end of the 19th century, Carl Th. Mörner isolated and characterized different proteins of the eye lens, whereby he obtained two highly abundant water-soluble proteins, which he termed α- and β-crystallin, and a third protein isolated in too small amounts for analysis (Mörner, 1894). Since that time, our knowledge of crystallins, including their genomic organization, evolution, expression profiles, structure and function, has grown tremendously but their historically established nomenclature is still valid. The α- and β-crystallins are present in all animals but they are usually complemented by other crystallins in different species. Often, these proteins exhibit an enzymatic activity and are thus associated with a completely different function in other tissues.

2.3.2 Genomic Organization and Expression Profiles of α-Crystallins

There are two α-crystallin genes, *Cryaa* and *Cryab*, which are located on different chromosomes, encoding proteins that share around 60% sequence identity. In humans, the *Cryaa* gene is found on chromosome 21 and encodes for a 173 amino acid residue protein with a molecular mass of 19,909 Da, while the *Cryab* gene is found on chromosome 11 encoding for a 175 residue protein of 20,159 Da (Seal et al., 2011). The tissue with the highest α-crystallin concentration is by far the vertebrate eye lens with up to 40% of the total protein amount (Bloemendal et al., 2004; Clark et al., 2012). The expression of αA-crystallin is essentially limited to the lens, only traces are found in some other tissues, it is thus the lens-specific isoform (Horwitz et al., 1999). αB-crystallin is considered to be a ubiquitous protein and is, besides the lens, particularly abundant in brain, heart and muscle (Bloemendal et al., 2004; Horwitz, 2003).

2.3.3 Structure and Dynamic Molecular Architecture of α-Crystallins

As members of the sHsp family, α-crystallins exhibit the typical domain structure consisting of an NTD, the eponymous ACD and a C-terminal extension (Figure 5). They also assemble into large oligomers with varying numbers of subunits, which constantly exchange subunits in a dynamic oligomer equilibrium. The observed heterogeneity (often referred to as polydispersity) and the dynamic behavior have hampered high-resolution structural studies. In 2009, Bagnéris et al. published the first ACD high-resolution structure of truncated human αB-crystallin (Figure 9). Since then, several studies using X-ray crystallography or NMR yielded atomic structures of isolated ACDs from αA- and αB-crystallin as well as the disease-causing mutant αB-R120G (Bagneris et al., 2009; Clark et al., 2011; Laganowsky et al., 2010). All these studies confirm that the ACD without flanking regions forms stable dimers and that dimerization occurs via elongated β6+7 strands (Figure 9). Solid-state NMR spectroscopy has determined the atomic structure of a highly curved αB dimer in the context of the complete assembly (Jehle et al., 2010). This study showed that the C-terminal IXI motifs fill B4/B8 pockets of adjacent dimers. The least amount of structural information is available on the NTD.

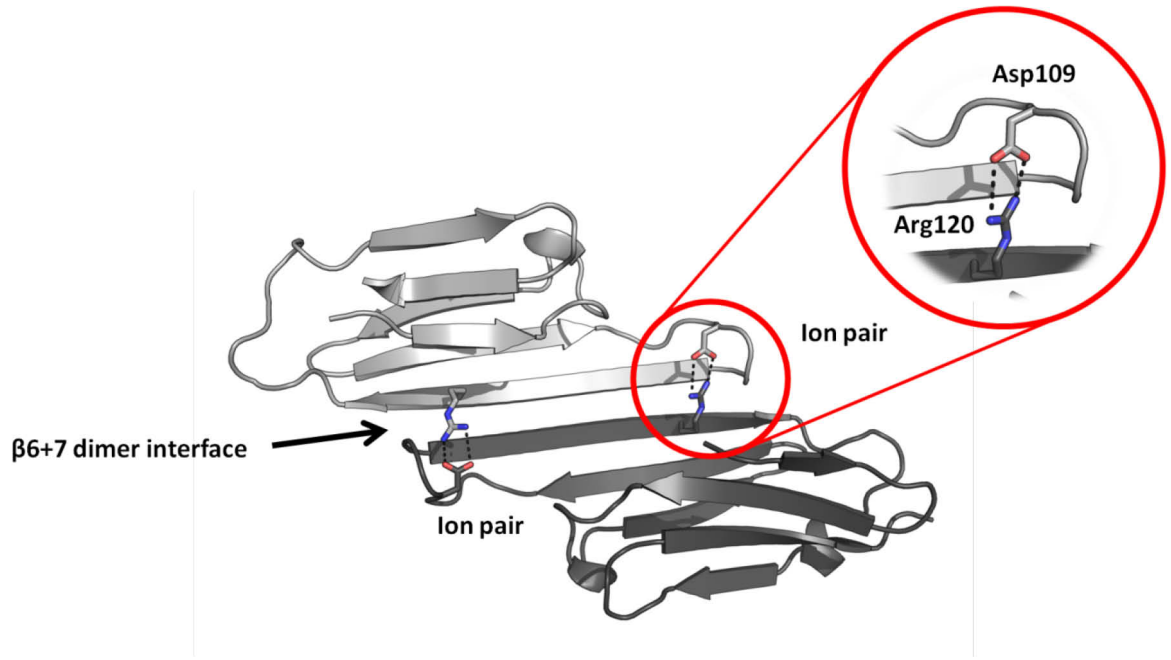

Figure 9 | Structure of the αB-crystallin ACD. Structural features of the ACD dimer of human αB-crystallin are illustrated. The β6+7 dimer interface is indicated by a black arrow. The conserved R120 ("disease arginine") of each domain forms a bidentate ion pair across the interface with Asp109. The figure is based on the PDB coordinates 2WJ7 (Bagneris et al., 2009).

Obtaining structural data for oligomeric sHsps has been an extremely difficult task and remains challenging. However, models for human αB-crystallin have been obtained by single particle electron microscopy (EM). A cryo-EM study presented an asymmetric model with a large central cavity of a 32-meric assembly at low resolution (Figure 10) (Haley et al., 2000; Haley et al., 1998). In addition, an MS study described the population of oligomers in αB-crystallin to range from 24 to 32 subunits.

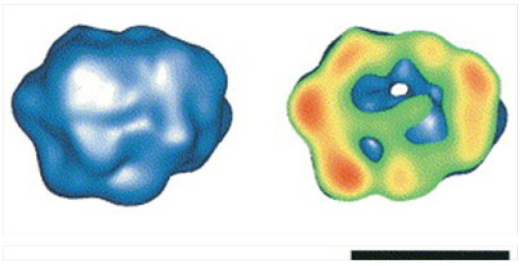

Figure 10 | Single particle reconstruction of αB-crystallin. The cryo-EM reconstruction is based on ~1000 particle images, which were processed without imposed symmetry. The depicted model, corresponding to a 32-meric assembly, is asymmetric and shows a central cavity. The scale bar represents 100 Å.
The figure is adapted and reprinted from Haley et al. (2000), © 2000, with permission from Elsevier.

Within the scope of this thesis, the structure of α-crystallins was studied. In collaboration with the group of Prof. Weinkauf at Technische Universität München, the EM structure of negatively stained αB was determined. It showed an oligomer with tetrahedral symmetry

representing an 24-meric assembly (Peschek et al., 2009). For a detailed summary of this study and further data on the structural principles of α-crystallins see the *Results* of this thesis. Very recent efforts to study the structure of αB-crystallin using "hybrid" approaches that combine information from multiple structural and biophysical methods, led to a better understanding of this dynamic oligomer equilibrium (Baldwin et al., 2011a) and the underlying molecular architecture (Baldwin et al., 2011a; Jehle et al., 2011).

2.3.4 The Chaperone Function of α-Crystallins and Its Regulation

α-crystallin was demonstrated by Horwitz in 1992 to possess chaperone-like activity *in vitro* (Horwitz, 1992). On the basis of these results, Horwitz proposed that α-crystallin would bind aggregating β- or γ-crystallins, thus preventing precipitation and lens opacity.
The role of α-crystallins in the eye lens is particular as they are presumed to function both as chaperones and structural proteins (Figure 11). The latter function includes the contribution to the refractive index of the eye lens (Bloemendal et al., 2004). Lens cells lose their nuclei and mitochondria during development and do then not exhibit any protein turnover. That is why the set of proteins has to maintain lens transparency over the whole life time (Horwitz, 2003).

Figure 11 | Bovine eye lens. The depicted eye lens was prepared from a cow eye during the process of αL-crystallin purification. The picture illustrates the transparency and optical magnification.

The chaperone-like activity of α-crystallins has been the subject of numerous studies and on their basis different functional models have been proposed. Although binding of nucleotides was reported (Biswas and Das, 2004; Ghosh et al., 2006; Mendoza et al., 2012), the chaperone function is generally considered to be independent of ATP-hydrolysis (Clark et al., 2012; Horwitz et al., 1999; Van Montfort et al., 2001). A thermodynamic analysis based on electron spin resonance showed that αA-crystallin was able to

distinguish between a range of model T4 lysozyme mutants according to their stability. This study suggested a mechanism with two modes of interaction, involving binding of substrates with distinct conformational states, one more native-like and one closer to the unfolded state (McHaourab et al., 2002).

Several sites have been postulated to be involved in substrate interaction. Since the exposure of hydrophobic regions is characteristic of unfolding proteins, the proposed binding sites are mainly hydrophobic. In some studies binding is restricted to the NTD (Smulders and de Jong, 1997), while others report an involvement of the ACD (Basha et al., 2012). Even a synthetic peptide (residues 71 to 88 of αA-crystallin) was found to prevent thermally-induced aggregation of ADH, albeit with lower efficiency (Sharma et al., 2000). The relevance of this region is stressed by the fact that one residue, Phe71, was shown to be essential for chaperone function in αA-crystallin (Santhoshkumar and Sharma, 2001). It is an established concept that parts of the N-terminal region are important for the chaperone-like function, but the exact binding site has not been identified yet and an involvement of other regions cannot be excluded.

α-crystallins exhibit chaperone-like function *in vitro* over a range of temperatures. As it functions in mammals at body temperature, a temperature-dependent activation mechanism is rather improbable and has not been reported yet. Other mechanisms for the activation of αB-crystallin were suggested. The control of its chaperone-activity as response to various types of cellular stress is reported to occur on the transcriptional level (Ito et al., 1996; Klemenz et al., 1991). Changes in pH as well as posttranslational modifications are described as triggers that promote this shift. Based on solid-state NMR structural data, rearrangements within αB-crystallin oligomers at acidic pH and a concomitant activation of its chaperone function was described (Jehle et al., 2010). Furthermore, αB-crystallin is known to be phosphorylated at several serine residues *in vivo* (Ito et al., 1997; MacCoss et al., 2002). Experiments with cultured cells identified three major sites, Ser19, 45 and 59, being phosphorylated in response to various kinds of stress with different site-specificities, kinase activities and regulatory pathways being involved (Hoover et al., 2000; Kato et al., 1998). The effect of phosphorylation on αB-crystallin was studied both *in vivo* and *in vitro* by mimicking phosphoserines with aspartate or glutamate mutants. Mimicking phosphorylation by introduction of glutamates at the phosphorylation sites caused a reduction in oligomer size and an altered substrate binding ability (Aquilina et al., 2004; Ito et al., 2001). Most studies describe an increased binding property but also contrary results have been published (Ahmad et al., 2008).

2.3.5 α-Crystallins in Stress and Disease

The essential role of the α-crystallins within the context of the eye lens has been the subject of investigation for many years (Bloemendal et al., 2004; Clark et al., 2012). Their importance was unequivocally demonstrated by knock-out mice. The αA-crystallin null mouse develops cataract early in life, due to the formation of inclusion bodies containing αB- and γ-crystallin (Brady et al., 1997). The αB-crystallin null mouse has no lens phenotype indicating that αA may play a greater role in maintaining the transparency of the lens then αB (Brady et al., 2001). However, the latter is also required for proper lens development as the lens of the αA/αB-crystallin double knock-out mouse is significantly smaller than single knockouts and displays additional morphological aberrations (Figure 12). In the single α-crystallin knockout mice, the remaining α-crystallin may fully or partially compensate for some of the functions of the missing protein (Boyle et al., 2003).

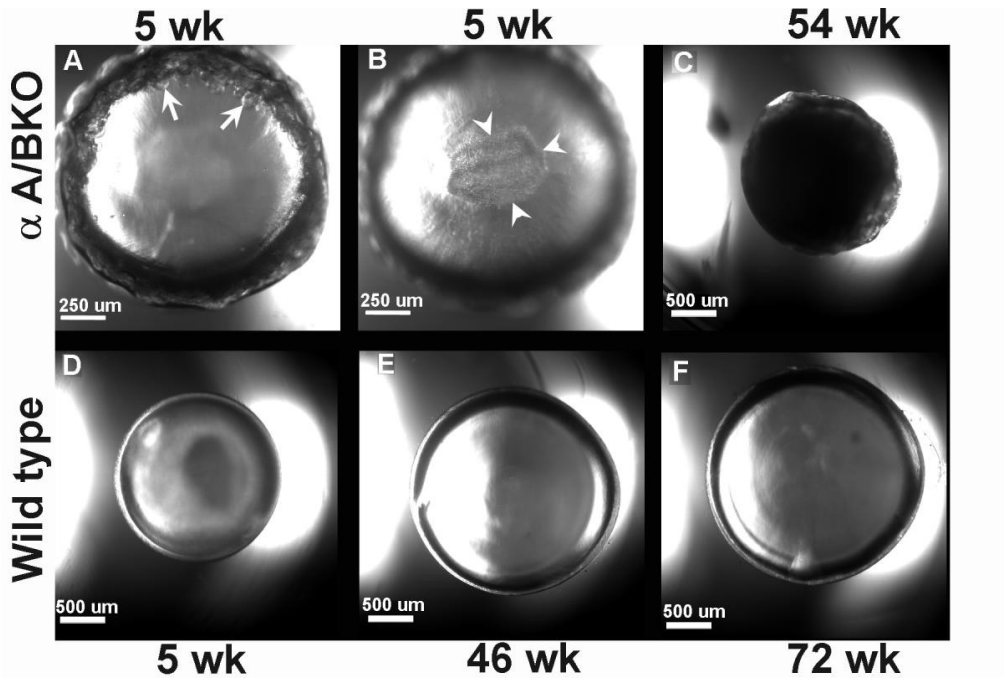

Figure 12 | Light micrographs of lenses from eyes of αA/B double KO (A-C) and wild-type (D-F) mice. Representative micrographs of lenses from 5 wk alphaA/BKO mice, showing changes in the equatorial (A) and posterior sub capsular (B) regions. (C) The micrograph of 54 wk alphaA/BKO mouse lens showing dense whole lens cataract. (D-F) Representative clear lenses from 5 wk (D), 46 wk (E), and wk 72 (F) wild-type mice. Figure taken from Boyle et al. (2003); © 2003 Boyle et al; licensee BioMed Central Ltd. (http://www.biomedcentral.com/1471-2415/3/3).

Since αB-crystallin was found to be expressed in almost all tissues with particularly high amounts in brain, heart and muscle, its functional importance is not restricted to the eye lens (Iwaki et al., 1990). Although αB knock-out mice do not develop cataract, these

animals show selective muscle degeneration accompanied by severe postural anomalies, and shorter life spans compared to wild-type controls (Boyle et al., 2003).

αB-crystallin interacts with different filamentous proteins and thereby affects their assembly dynamics. In striated tissues, αB-crystallin prevents the aggregation of client proteins such as desmin, a cytoskeletal intermediate filament protein, thus maintaining muscle integrity and stress tolerance (Rajasekaran et al., 2007; Xiao and Benjamin, 1999). Some aggregation-related skeletal myopathies and cardiomyopathies are caused by mutations in αB-crystallin (Clark et al., 2012; Vicart et al., 1998). In the brain, overexpression of αB-crystallin is associated with a number of neuropathological diseases including Alzheimer's, Alexander's, Parkinson's and Creutzfeldt-Jakob disease (Iwaki et al., 1993; Iwaki et al., 1989; Renkawek et al., 1992; Renkawek et al., 1994). αB-crystallin is the most abundant gene transcript present in early active multiple sclerosis lesions in the brain, whereas such transcripts are absent in normal brain tissue (Chabas et al., 2001). It has anti-apoptotic (Andley et al., 2001; Bai et al., 2003) and neuroprotective (Masilamoni et al., 2006; Masilamoni et al., 2005) functions *in vivo*. In a recent study, Ousman and co-workers described how autoimmunity to αB-crystallin can contribute to inflammatory injury of the central nervous system (Ousman et al., 2007). They showed that autoimmune attack on αB-crystallin does not directly cause tissue damage, but rather it worsens the severity of damage. Furthermore, they injected the protein into mice with an autoimmune model of multiple sclerosis and showed that it reduced disease (Ousman et al., 2007). Its versatile influence on many cellular functions is underlined by the involvement of αB-crystallin in cell cycle control and apoptosis, associating it also with cancer (Launay et al., 2010; Lin et al., 2006; Stegh et al., 2008). Collectively, these findings have shown that αB-crystallin may have a variety of biological functions.

3 Materials and Methods

3.1 Materials

3.1.1 Devices

Autoclave Varioclav EP-Z	H+P
Cell Disruption Apparatus Basic Z	Constant Systems
Centrifuges	
Avanti J25 and J26 XP	Beckman Coulter
Optima XL-A (equipped with FDS)	Beckman Coulter (Aviv)
Optima XL-I	Beckman Coulter
Rotina 46R	Hettich
Universal 32R	Hettich
Tabletop centrifuge 5415 C	Eppendorf
Chromatography systems	
ÄKTA FPLC	GE Healthcare
ÄKTA Prime	GE Healthcare
Frac-900/950 fraction collectors	GE Healthcare
Superloops (various volumes)	GE Healthcare
Circular dichroism spectropolarimeters	
J710 (with PTC 343 Peltier device)	Jasco
J715 (with PTC 343 Peltier device)	Jasco
Electron microscope JEOL 100 CX	JEOL
Eppendorf-Thermomixer	Eppendorf
Fluorescence spectrophotometers	
FluoroMax-2	Spex
FluoroMax-3	Spex
FluoroMax-4	Spex
Gel documentation system Biodoc II	Biometra
Gel electrophoresis and blotting devices	Hoefer
Homogeniser Ultra Turrax DIAX900	Heidolph
HPLC systems	GE Healthcare
Ice maker	Zieger
Incubator	New Brunswick Scientific
Magnetic stirrer Heidolph MR2000	Heidolph
Mass spectrometers	
LTQ Orbitrap XL	Thermo Scientific
Ultraflex II MALDI ToF/ToF	Bruker Daltonics

pH meter	WTW
Power amplifiers EPS 3500, 3501 and 1001	GE Healthcare
Scales	
BP 121 S	Sartorius
BL 310	Sartorius
Thermal cycler Primus 25	MWG
Thermoblock TB 1	Biometra
Typhoon 9400	GE Healthcare
Ultra filtration cell 8050	Amicon
UV-Vis spectrophotometers	
Varian Cary 50 Bio	Agilent
Varian Cary 100 Bio	Agilent
Lambda 5	PerkinElmer
Nanodrop	Peqlab
Novaspec II	GE Healthcare
Vortex MS2	IKA
Water bath F6-K	Haake
X-ray film processor Optimax TR	MS Laborgeräte

3.1.2 Chemicals

2-Mercaptoethanol	Sigma
5,5'-Dithiobis(2-nitrobenzoic acid) (DTNB)	Sigma
8-Anilino-1-naphthalenesulfonic acid (ANS)	Sigma
Acetic acid	Roth
Acrylamid/Bis solution 38:2 (40% w:v)	Serva
Adenosin-5'-triphosphate (ATP) disodium salt	Roche
Agar Agar	Serva
Agarose	Serva
Ammonium persulfate (APS)	Roth
Ampicilin sodium salt	Roth
Bacto-pepton	BD Biosciences
Bacto-trypton	BD Biosciences
Coomassie Brilliant Blue R-250	Serva
Deoxynucleoside triphosphates (dNTPs)	Roche
Dimethyl sulfoxide (DMSO)	Sigma
Dithiothreitol (DTT)	Roth
EDTA	Merck

Ethidium bromide	Sigma
Galactose	Merck
Glucose	Merck
Glutathione, oxidized (GSSG)	Sigma
Glutathione, reduced (GSH)	Sigma
Glycerol	Roth
Guanidinium chloride (GdnCl)	Sigma
HEPES	Roth
Imidazole	Sigma
Isopropyl β-D-1-thiogalaktopyranoside (IPTG)	Serva
Kanamycin sulfate	Roth
LB medium	Serva
Milk powder	Roth
NADH	Roche
Oxaloacetic acid	Sigma
Phenylmethanesulfonyl fluoride (PMSF)	Sigma
Phosphoenolpyruvate (PEP)	Sigma
Protease inhibitor Mix FY, G, HP, M	Serva
Sodium dodecylsulfate (SDS)	Serva
Stain G	Sigma
TCEP	Pierce
TEMED	Roth
Tris	Roth
Tween-20	Merck
Urea	Merck

3.1.3 Consumables

Amicon Ultra-15 Centrifugal Filter Units	Millipore
Amicon Ultra-4 Centrifugal Filter Units	Millipore
Blotting paper	Whatman
Cuvettes, plastic, 1 mL	Brand
Cuvettes, plastic, half-micro	Brand
Dialysis membranes Spectra/Por (various MWCOs)	Spectrum Laboratories
Immobilon-P membrane (PVDF)	Roth
Membrane discs	Sartorius

PCR tubes	BioRad Laboratories
PE tubes, 15 and 50 mL	Greiner & Söhne
Petri dishes, PS, 94 mm	Greiner & Söhne
pH indicator	Merck
Reaction tubes, various volumes	Sarstedt
UV cuvettes, plastic, micro	Brand
X-ray film X-OMAT AR	Kodak

3.1.4 Enzymes, Standards and Kits for Molecular Biology

1 kb DNA ladder	Peqlab
Pfu DNA polymerase	Promega
Pwo DNA polymerase	Roche
QuikChange II Mutagenesis Kit	Stratagene
Restriction enzymes	NEB
T4 ligase	Promega
Taq DNA polymerase	Promega
Wizard Miniprep kit	Promega
Wizard PCR product purification and gel extraction kit	Promega

3.1.5 Oligonucleotides

Name	**Sequence (5' to 3')**
aB-A172C (JP02)	GATCGCGGCCGCCTATTTCTTGGGGCATGC
aB-A4C	GATCCCATGGACATCTGCATCCACCACCC
aB-A4C/H6C (JP07)	GATCCCATGGACATCTGCATCTGCCACCC
aB-S115C (JP03)	GGTTTCATCTGCAGGGAGTTCC
aB-S115Crev (JP04)	GGAACTCCCTGCAGATGAAACC
aB-S135C	CCTCTCACCATTACTTGCTCCCTG
aB-S135Crev	CAGGGAGCAAGTAATGGTGAGAGG
aBS19E	CTTCTTTCCTTTCCACGAGCCCAGCCGCCTCTTTG
aBS19Erev	CAAAGAGGCGGCTGGGCTCGTGGAAAGGAAAGAAG
aBS45C	GACGTCTACTTCCCTGTGTCCCTTCTACCTTCG
aBS45Crev	CGAAGGTAGAAGGGACACAGGGAAGTC
aBS45E	GACGTCTACTTCCCTGGAGCCCTTCTACCTTCG
aBS45Erev	CGAAGGTAGAAGGGCTCCAGGGAAGTAGACGTC

aB-S59C (JP05)	GCACCCTGCTGGTTTGACACTGG
aB-S59Crev (JP06)	CCAGTGTCAAACCAGCAGGGTGC
aBS59E	CTTCCTGCGGGCACCCGAGTGGTTTGACACTGG
aBS59Erev	CCAGTGTCAAACCACTCGGGTGCCCGCAGGAAG
aBV145C	GTCCTCACTGTGAATGGACCAAGG
aBV145C	GTCCTCACTTGCAATGGACCAAGG
aBV145Crev	CCTTGGTCCATTCACAGTGAGGAC
aBV145Crev	CCTTGGTCCATTGCAAGTGAGGAC
aBwt (JP01)	GATCCCATGGACATCGCCATCCACCACC
aBwtrev	GATCGCGGCCGCCTATTTCTTGGGGGCTGC
S135C	CCTCTCACCATTACTTGCTCCCTG
S135Crev	CAGGGAGCAAGTAATGGTGAGAGG
S153C	GCACCCTGCTGGTTTGACACTGG
S153Crev	GCACCCTGCTGGTTTGACACTGG
S19A	CTTCTTTCCTTTCCACGCTCCCAGCCGCCTCTTTG
S19Arev	CAAAGAGGCGGCTGGGAGCGTGGAAAGGAAAGAAG
S19C	GCACCCTGCTGGTTTGACACTGG
S19Crev	GCACCCTGCTGGTTTGACACTGG
S35C	GCACCCTGCTGGTTTGACACTGG
S35Crev	GCACCCTGCTGGTTTGACACTGG
S45A	GACGTCTACTTCCCTGGCTCCCTTCTACCTTCG
S45Arev	CGAAGGTAGAAGGGAGCCAGGGAAGTAGACGTC
S59A	CTTCCTGCGGGCACCCGCGTGGTTTGACACTGG
S59Arev	CCAGTGTCAAACCACGCGGGTGCCCGCAGGAG
T7 prom	TAATACGACTCACTATAGGG
T7 term	GCTAGTTATTGCTCAGCGG

3.1.6 Bacterial Strains and Plasmids

E. coli Strains

Strain	Genotype	Origin
BL21 (DE3) codon plus	F– *ompT hsdS*(rB– mB–) *dcm*+ Tetr *gal endA* Hte [*argU proL* Camr]	Stratagene
DH5α	F^-φ 80d*lacZ*ΔM15 Δ(*lacZ*YA-*arg*F) U169 *rec*A1 *end*A1 *hsd*R17(r_k^- m_k^+) *pho*A *sup*E44 λ^- *thi*-1 *gyr*A96	Invitrogen
Mach1 T1R	F– Φ80*lacZ*ΔM15 Δ*lac*X74 *hsd*R(rK–, mK+) Δ*rec*A1398 *end*A1 *ton*A	Invitrogen
XL1-Blue	*recA*1 *end*A1 *gyr*A96 *thi*-1 *hsd*R17 *sup*E44 *rel*A1 *lac*	Stratagene

Plasmids

All αA- and αB-crystallin constructs were cloned using pET28b as vector.

3.1.7 Media and Antibiotics for the Cultivation of *E. coli*

LB_0	LB medium	20 g/l
	for plates: Agar Agar	20 g/l
Antibiotics (1000x stocks)	Ampicillin	200 µg/l (in ddH_2O)
	Chloramphenicol	35 µg/l (in ethanol)
	Kanamycin	50 µg/l (in ddH_2O)

All media were sterilized using an autoclave at 121°C for 20 min. Antibiotics stocks were passed through a sterile filter (0.22 µm) and stored at -20°C.

3.1.8 Buffers for Molecular Biological Methods

TAE (50x)	Tris/Acetate pH 8.0	2 M
	EDTA	50 mM
BJ buffer	Glycerol	50% (v/v)
	EDTA (pH 8.0)	10 mM
	Bromphenolblue	0.2% (w/v)
	Xylencyanol	0.2% (w/v)

3.1.9 Proteins, Standards and Kits for Protein Chemical Methods

Pyruvate kinase (PK)	Roche
Malate dehydrogenase (MDH), from pig heart	Roche

Lysozyme, from chicken egg white	Sigma
p53	Dr. Julia Rohrberg
Low-range molecular weight standard (LMW)	BioRad Laboratories
Protein standard for HPLC	GE Healthcare
α-Chymotrypsin	Sigma
Trypsin	Sigma
Roti Mark, prestained	Roth
ECL detection system	GE Healthcare

3.1.10 Antibodies

α-αB-crystallin	StressMarq
α-Hsc70	StressMarq
α-Hdj1	StressMarq
α-αB-crystallin, polyclonal	Pineda
α-αA-crystallin, polyclonal	Pineda
α-rabbit, monoclonal	Sigma

3.1.11 Chemicals for Protein Labeling, Modification and Cross-linking

4-Acetamido-4'-((iodoacetyl) amino)stilbene-2,2'-disulfonic acid, disodium salt (AIAS)	Invitrogen
5-(and-6)-Carboxyfluorescein (FAM)	Invitrogen
5-(and-6)-Carboxytetramethylrhodamine, succinimidyl ester (TAMRA)	Invitrogen
7-Diethylamino-3-(4'-maleimidylphenyl)-4-methylcoumarin (CPM)	Invitrogen
ATTO-488 maleimide	ATTO-TEC
ATTO-488 NHS ester	ATTO-TEC
ATTO-532 maleimide	ATTO-TEC
ATTO-550 maleimide	ATTO-TEC
ATTO-550 NHS ester	ATTO-TEC
ATTO-647 maleimide	ATTO-TEC
BS^3 (Bis[sulfosuccinimidyl] suberate)	Pierce
DTSSP (3,3´-Dithiobis[sulfosuccinimidylpropionate])	Pierce
EDC (1-Ethyl-3-[3-dimethylaminopropyl]carbodiimide hydrochloride)	Pierce

EZ-Link HPDP-Biotin	Pierce
Fluorescein-5-isothiocyanate (FITC)	Invitrogen
Glutaraldehyde	Sigma
Lucifer yellow iodoacetamide (LYI)	Invitrogen
Sulfo-NHS (N-hydroxysulfosuccinimide)	Pierce

3.1.12 Chromatography Materials and Columns

Resource-Q; Source 15 (6 mL)	GE Healthcare
Superdex 200 Prep Grade	GE Healthcare
Superdex 75 Prep Grade	GE Healthcare
HiPrep 26/10 Desalting column	GE Healthcare
HisTrap FF	GE Healthcare
Q Sepharose Fast Flow	GE Healthcare
SP Sepharose Fast Flow	GE Healthcare
TSK G4000PW HPLC gel filtration	Tosoh Bioscience
Hydroxylapatit column	BioRad Laboratories

3.1.13 Buffers for Protein Chemical Methods

General Buffers

Phosphate-buffered saline (PBS)	NaCl	137 mM
	KCl	2.7 mM
	$Na_2HPO_4 \cdot H_2O$	10 mM
	KH_2PO_4	2.0 mM
	pH 7.4	
HKM buffer	Hepes/KOH	25 mM
	KCl	150 mM
	$MgCl_2$	5 mM

Buffers for Protein Purification

TE buffer/TE lysis buffer	Tris/HCl, pH 9	50 mM
	EDTA	2 mM
TNE elution buffer	Tris/HCl, pH 9	50 mM
	NaCl	1 M
	EDTA	2 mM
TNE gel filtration buffer	Tris/HCl, pH 9	50 mM
	NaCl	150 mM
	EDTA	2 mM

Buffers and Solutions for SDS Polyacrylamide Gel Electrophoresis

Fairbanks A (Coomassie staining)	2-Propanol	25% (v/v)
	Acetic acid	10% (v/v)
	Coomassie Blue R	0.05% (w/v)
Fairbanks D (destaining solution)	Acetic acid	10% (v/v)
Lämmli sample buffer (5x)	Tris/HCl, pH 6.8	0.3 M
	SDS	10% (w/v)
	Glycerol	50% (v/v)
	2-Mercaptoethanol	5% (v/v)
	Bromophenol blue	0.05% (w/v)
SDS running buffer (10x)	Tris/HCl, pH 8	0.25 M
	Glycine	2 M
	SDS	1% (w/v)
Separation gel buffer (2x)	Tris/HCl, pH8.8	1.5 M
	SDS	0.8% (w/v)
Stacking gel buffer (4x)	Tris/HCl, pH 6.8	0.25 M
	SDS	0.4% (w/v)

Buffers and Solutions for Western Blotting

Transfer buffer	Tris/HCl, pH 7.5	50 mM
	Glycine	40 mM
	SDS	0.04% (w/v)
	Methanol	20% (v/v)
PBS-T	1x PBS	
	Tween	0.1% (w/v)

Buffers and Solutions for Electrophoretic Mobility Shift Assay

EMSA running buffer	Tris/HCl, pH 8	30 mM
	Boric acid	30 mM
	EDTA	5 mM
	TritonX-100	0.1% (v/v)
DNA binding buffer (2x)	Hepes/KOH, pH 8	80 mM
	Glycerol	15% (v/v)
	$MgCl_2$	20 mM
	TritonX-100	0.2% (v/v)
	BSA	2 mg ml^{-1}
	DTT	10 mM
	KCl	100 mM
Reaction mix	Cy5-p21 (0.5 pmol/µL)	4 µL
	DNA binding buffer (2x)	200 µL
	Unspecific DNA (100 pmol/µL)	0.8 µL

3.2 Software, Databases and Web-based Tools

Software

Adobe Illustrator CS2	Adobe Inc.
Adobe Photoshop CS2	Adobe Inc.
BioEdit	Ibis Biosciences
DCDT+	John Philo
EndNote Web	Thomson Reuters
ImageQuant	GE Healthcare
Microsoft Office 2001	Microsoft
MMass	Open Source
MoverZ	Genomic Solutions
Origin 8.0	OriginLab Corp.
Pymol	Schrödinger
SedFit	Peter Schuck
Sednterp	John Philo
Sedphat	Peter Schuck
SedView	Hayes, Stafford
UltraScan	Borries Demeler

Databases

PDB	www.rcsb.org/pdb
PDBe	www.ebi.ac.uk/pdbe
PubMed	www.ncbi.nlm.nih.gov/pubmed
ISI Knowledge	portal.isiknowledge.com
UniProt	www.uniprot.org

Web-based Tools

FindPept	http://web.expasy.org/findpept/
NCBI Blast	http://blast.ncbi.nlm.nih.gov/
PeptideCutter	http://web.expasy.org/peptide_cutter/
ProtParam	http://web.expasy.org/protparam/
ProtScale	http://web.expasy.org/protscale/

3.3 Molecular Biological Methods

All solutions used for molecular biological methods were sterile. All experiments were conducted at room temperature if not stated else. Polymerase chain reaction (PCR), DNA electrophoresis, restriction digestion, cultivation and transformation of *E. coli* were performed according to standard protocols as described elsewhere (Sambrook and Russell, 2001). The most frequently used molecular biological methods are briefly summarized in the following.

3.3.1 Cultivation and Storage of *E. coli*

E. coli was cultivated in an incubator at 37 °C either on LB plates or in LB liquid media. Strains were selected by addition of appropriate antibiotics to the media. Liquid cultures were inoculated 1:50 from fresh overnight cultures or by transferring single colonies from plates. Bacterial division was monitored by VIS spectroscopy at 600 nm.
For long-term storage, 2 mL of a freshly inoculated culture were centrifuged at 5000 rpm in a desk top centrifuge and the sediment was resuspended in 600 µL medium. 600 µL 50% glycerol were added to the bacterial suspension resulting in a 25% glycerol culture stock. The culture was frozen using liquid nitrogen and stored at -80°C.

3.3.2 Agarose Gel Electrophoresis

Agarose gel electrophoresis was used to determine the approximate size of DNA fragments and to purify PCR products or plasmid DNA by gel extraction. Gels were made of 1-2% agarose and TAE buffer. To estimate the size of the DNA fragments, samples were compared to a 1kb DNA standard (Peqlab). A constant voltage of 125 mV was applied to run the gels. DNA bands were stained using ethidium bromide or Stain G and detected by UV light.

3.3.3 Polymerase Chain Reaction

Polymerase chain reaction (PCR) was used for target DNA amplification and mutagenesis. PCRs were carried out using different polymerases. Primers were designed with the BioEdit software for specific gene amplification and ordered from MWG (Germany).
The following general cycling scheme was used for most PCRs:

Melting	94°C, 45 s (2 min before first cycle)
Annealing	58-64°C (depending on primers), 45 s
Amplification	Temperature according to manual of polymerase used, at least 2 min per 1000 bp (5 min after last cycle)
Cycles	35

3.3.4 Cloning of αB-Crystallin Variants

αB-crystallin variants were cloned by different strategies depending on the kind of the mutation. Deletion variants or single site mutants in proximity to the termini were amplified in a single step polymerase chain reaction (PCR). For most internal single site mutants, including the phosphorylation-mimicking Glu variants, fragments of the target genes were produced by a sequence of two PCR reactions. First, fragments up- and downstream of the mutation site were amplified individually using each of the "terminal" primers together with "internal" primers, which contained the exchanged codon and are reverse-complement to each other. Both fragments were fused by a second PCR using both PCR fragments as self-priming templates together with the "terminal" primers.

Amplified DNA was purified using the Wizard® SV Gel and PCR Clean-Up System (Promega) according to the manufacturer's instructions. Purified fragments were enzymatically digested using restriction enzymes. The restricted DNA fragments were purified as described above.

Vector DNA was amplified using *E. coli* Mach1, XL1 Blue or DH5α. The plasmid DNA was isolated from transformed *E. coli* cells with the Wizard® *Plus* Minipreps DNA Purification System (Promega) in accordance to the manufacturer's manual. Purified vector DNA was enzymatically digested as described above to match insert DNA restriction sites.

Insert DNA was ligated into the corresponding vector DNA using T4 DNA ligase. The reaction was carried out in QL buffer at room temperature for 12 min and immediately used for transformation of *E. coli* cells. Ligation constructs were isolated in accordance to the Wizard® *Plus* Minipreps DNA Purification System Handbook. Isolated DNA was stored at -20°C.

Several cysteine variants of αB-crystallin were cloned in a single step including mutagenesis and amplification of the whole template plasmid. For that purpose the QuikChange® II Site-Directed Mutagenesis Kit (Stratagene) was utilized according to the manufacturer's instruction manual.
All constructs were sent to either GATC or MWG (both Germany) for sequencing in forward direction using a T7 promoter primer.

3.4 Protein Chemical Methods

3.4.1 SDS Polyacrylamide Electrophoresis

SDS-PAGE was performed in accordance to the protocol of Laemmli (1970). Polyacrylamid separation gels were cast to final concentrations of 5% (w/v) acrylamide/bisacrylamide 19:1 (40% w/v) for stacking gels and 10-18% (w/v) acrylamide/bisacrylamide 19:1 (40% w/v) for separation gels. Polymerization of the solution was induced by adding ammonium persulfate (APS, 10% w/v in H_2O) and tetramethylethylendiamin (TEMED). Prior to loading, all samples were mixed with 5x Laemmli sample buffer and incubated at 95°C for 5 min. Electrophoresis was carried out at constant voltages (175 V) for 30-60 min. Gels were stained with Coomassie according to a modified protocol of Fairbanks et al. (1971).

3.4.2 Protein Purification

In general, all purification steps described were carried out at ~4°C. The final protein preparations were dialyzed against the desired buffers and stored at -80°C. The homogeneity was assessed by SDS-PAGE analysis combined with Coomassie staining. The identity and correct molecular mass of each sample was confirmed using MALDI-TOF mass spectrometry (MS).

Recombinant α-Crystallin

Wild-type αA- and αB-crystallin, as well as different variants, including cysteine, alanine and phosphomimicking glutamate mutants, were purified within the scope of this project. The established purification protocol at basic buffer conditions yielded high amounts of homogeneous protein and was suitable for all variants mentioned in this thesis. For gene expression, *E. coli* BL21 (DE3) was transformed with the respective plasmid. Expression

cultures in LB medium were inoculated 1:100 using an overnight culture of transformed *E. coli* BL21 (DE3). Protein expression was induced by 1 mM IPTG at OD_{600} = 0.6. After cell disruption, the cleared lysate was applied on a Q Sepharose column (GE) equilibrated with TE buffer. Elution was carried out with a linear NaCl gradient. Fractions containing the target protein were pooled, concentrated and loaded onto a Superdex 200-pg column (GE) run in TE, 100 mM NaCl. Fractions containing the target protein were applied to a Resource Q column (GE) in TE buffer and the protein was eluted with a linear NaCl gradient.

Bovine αL-Crystallin

Bovine αL-crystallin was purified from cow/calf lenses. Lenses were obtained from a local slaughterhouse. All preparative steps were undertaken at 4°C. The *sclera* was opened with a scalpel and the lenses carefully removed from the vitreous body. The ciliary muscle was removed and the lenses were transferred to 10 mL TE lysis buffer and 0.5 mL protease inhibitor Mix G (Sigma) were added. Then, the lens tissue was disrupted with a handheld homogenizer consisting of a glass cylinder and a plunger. The homogenate was centrifuged (10000 g, 20 min, 8°C) to remove cellular debris and undisrupted cells.

The cleared lysate was purified as described for recombinantly expressed α-crystallin. Due to the small starting volume and high content of the target protein a pre-packed 6 mL Resource Q column has been used for the first purification step. This was followed by a Superdex 200-pg and a Resource Q column. All buffers and chromatography parameters were identical to the procedure described for recombinant α-crystallin.

γD-Crystallin

γD-crystallin was purified using a similar protocol as for recombinant α-crystallin with a Superdex 75-pg column (GE) as second purification step.

Hsc70

Hsc70 was purified as described elsewhere (Pandya et al., 2009) using a Superdex 200 SEC column (GE) as additional last step.

Hdj1

For Hdj1 gene expression, *E. coli* BL21(DE3) was transformed with a Hdj1-pET21b plasmid, the cells were grown at 37°C and induced by 1 mM IPTG. Cleared lysate was applied on SP Sepharose column (GE) equilibrated with TE buffer (50 mM Tris, 2 mM

EDTA, pH 7.5). The pooled fractions were loaded onto a Superdex 200-pg column run in PBS.

3.4.3 Preparation of HeLa Cell Lysates

HeLa cells were grown at 37°C. The cells were harvested by centrifugation for 4 min applying 500 g at 4°C. The supernatant was removed and the cells were resuspended in cold hypotonic buffer (40 mM sodium phosphate, pH 7.4) in the presence of protease inhibitor Mix M (Serva). The HeLa cell suspension was incubated for 15 min on ice to allow for hypotonic swelling. To disrupt the cells, the suspension was passed several times through a sterile needle (Terumo Europe, Neolus with 6 mm diameter). The lysate was cleared by centrifugation (10 min at 12.000 g, 4°C) and the supernatant decanted into sterile tubes and 10x PBS stock was added to yield physiological salt concentrations. The lysate was ATP depleted by addition of hexokinase (10 U/mL) in the presence of 2 mM $MgSO_4$ for 30 min at 10°C. The cleared and ATP-depleted HeLa cell lysate was frozen in liquid nitrogen and stored at -80°C.

3.4.4 Modification of Proteins with Spectroscopic and Functional Probes

Proteins can be chemically modified to introduce a vast number of different probes or functional groups. Here, the incorporation was achieved using amine-reactive groups, e.g. NHS esters, isothiocyanates, or using thiol-reactive groups, e.g. maleimides, to yield site-specific modification. The primary purpose of chemical modification during this thesis was the introduction of fluorescent probes. All reactions were carried out according to published protocols of the manufacturers.

3.4.5 Western Blotting

The blotting of proteins from SDS-PAGE gels (see 3.4.1) onto PVDF membranes (BioRad) was carried out using a FastBlots system (Biometra). For the blotting the following components were stacked from bottom to top and placed between the plate electrodes: three layers of blotting paper (Whatman), the PVDF membrane, the gel and three layers of blotting paper (Whatman). Prior to blotting, the membrane was activated by rinsing with methanol. The activated membrane, the blotting paper and the gel were incubated for 5 min in western blot transfer buffer. The blotting was performed applying 72 mA per gel for 90 min. After blotting, the membrane was incubated in blocking buffer

for 30 min. The primary antibody was diluted in PBS-T with 1% (w/v) milk powder and incubated with the membrane at 4°C over night. The secondary antibody was applied after three washing steps with PBS-T (10 min at RT). The secondary antibody was diluted in PBS-T with 1% (w/v) milk powder and incubated with the membrane at RT for 1 h. After another three washing steps the blot was analyzed by chemiluminescent detection using ECL Western Blotting Detection Regents (GE Healthcare) and photographic film (Kodak), which was developed after exposure using an Optimax TR (MS-Laborgeräte).

3.4.6 Electrophoretic Mobility Shift Assay (EMSA)

Electrophoretic mobility shift assay (EMSA) was used to study the binding of p53 to DNA. A mixture of a fluorescently-labeled oligonucleotide and the DNA-binding target protein is incubated and afterwards separated by native gel electrophoresis. Unbound oligonucleotide moves fast through the gel matrix whereas the protein-DNA complex shows slower migration. Detection is achieved by the fluorescence of the labeled DNA probe.
Here, the p21 promotor, which is specifically bound by p53 (Szak et al., 2001), labeled with Cy5 was used as oligonucleotide. To ensure specific binding, unspecific DNA of the same length was added to the assay mixture. The protein samples were incubated in EMSA DNA binding buffer for 15 min. After addition of the EMSA reaction mix, the samples were loaded on a 4% polyacrylamid gel. Electrophoresis was carried out in EMSA running buffer for 3 h at 4°C applying 25 mA per gel. The fluorescence of the Cy5-labeled p21-DNA was detected in a Typhoon 9600 phosphoimager (Amersham).

3.5 Spectroscopy

3.5.1 Ultraviolet (UV)-Visible Spectroscopy

When absorption occurs, electrons are excited and are lifted from the electronic ground state to an excited state. The molecular elements, which are responsible for absorption, are called chromophores. Various functional groups in proteins absorb light in the UV range.
UV spectroscopy was used to determine protein concentrations. Calculation of the protein concentration from UV absorbance was carried out according to the Beer-Lambert law (Equation 1).

$$A = \varepsilon \cdot c \cdot d \leftrightarrow c = \frac{A}{\varepsilon \cdot d}$$

Equation 1 | Beer-Lambert law. A = Absorbance, ε = molar extinction coefficient (M^{-1} cm^{-1}), c = molar protein concentration (M), path length (cm)

Theoretical molar extinction coefficients were determined using the ProtParam tool (Wilkins et al., 1999). All UV spectra were recorded with a Cary 50 UV/Vis spectrophotometer (Varian) at 20 °C and baseline corrected for buffer absorbance.

3.5.2 Circular Dichroism (CD) Spectroscopy

Biopolymers, such as proteins or nucleic acids are chemically asymmetric structures and exhibit optical activity. The optical activity is a result of the difference of either the refractive index or the absorption of the two types of circularly polarized light. The latter phenomenon is called circular dichroism (CD). Beer-Lambert law applies to both right- and left-handed circularly polarized light and CD is defined as the difference in extinction coefficients for each:

$$\Delta A(\lambda) = A_L(\lambda) - A_R(\lambda) = [\varepsilon_L(\lambda) - \varepsilon_R(\lambda)]lc = \Delta\varepsilon lc$$

Equation 2 | A = absorption, λ = wavelength, ε = extinction coefficient, l = path length, c = concentration, subscripts denote the handedness of the light

CD spectra of proteins in the far UV region (260-170 nm) show distinctive signals due to the differential absorption of backbone amide groups in asymmetric secondary structures. α-helical structures exhibit a negative band at about 222 nm and a negative and positive couplet at about 208 and 190 nm. The CD for β-sheet structures has a negative band at about 215 nm and a positive band at about 198 nm. Therefore, far UV CD spectroscopy could be used for secondary structure analysis of proteins.

CD is measured as ellipticity, Θ, in degrees. The conversion of the measurement signal to mean residue ellipticity is carried out by:

$$\Theta_{MRW} = \frac{\Theta \cdot 100 \cdot M}{d \cdot c \cdot N_{aa}}$$

Equation 3 | Θ_{MRW} = mean residue ellipticity (deg cm^2 $dmol^{-1}$), Θ = ellipticity (deg), M = molecular mass (g/mol), d = path length (cm), c = concentration (M), N_{aa} = number of amino acid residues

For secondary structure analysis CD spectra were recorded at a final concentration of 0.1 mg/mL in a 1 mm quartz cuvette (Hellma) at 20°C. Parameters for acquirements were set to a wavelength range of 250-190 nm, 20 nm/s, 16 accumulations. Data were converted into mean residue ellipticity using Equation 3.

3.5.3 Fluorescence Spectroscopy

The absorption of photons goes along with the excitation of a molecule from its ground to a higher energy state. Following excitation, a molecule loses energy as heat by cascading through the vibronic levels of all excited singlet states (internal conversion). From the lowest vibrational level (S_1) the molecule returns to the ground (S_0) by either internal conversion, conversion to the triplet state (intersystem crossing) or emission of a photon (fluorescence).

The aromatic amino acid residues in proteins, tryptophan, tyrosine and phenylalanine, are intrinsic fluorophores. Tryptophan has the highest quantum yield and is able to quench tyrosine fluorescence by resonance energy transfer, its fluorescence is often dominant in proteins. Numerous extrinsic fluorescence probes with different binding characteristics are available for specific applications.

Fluorescence Resonance Energy Transfer (FRET)

A donor chromophore in its excited state can transfer energy by a non-radiative long-range dipole-dipole coupling mechanism (resonance energy transfer) to an acceptor chromophore in close proximity (typically <10 nm). When both molecules are fluorescent, the term fluorescence resonance energy transfer (FRET) is used, although the energy is not transferred by fluorescence. The requirements are on the one hand a transition dipole interaction between the two fluorophores and on the other hand an overlap of the emission spectrum of the donor with the absorption spectrum of the acceptor. The FRET efficiency (E) is strongly dependent on the distance (r) between donor and acceptor group (with an inverse 6^{th} power law). R_0 is the Förster distance of this pair of donor and acceptor at which the FRET efficiency is 50%:

$$E = \frac{1}{1 + (\frac{r}{R_0})^6}$$

Equation 4 | E = FRET efficiency, r = donor-acceptor-distance, R_0 = Förster distance

Quenching of Fluorescence

In solution fluorescence can be eliminated by wide number of diffusing molecules. In general this is referred to as fluorescence quenching and is induced by the conversion of a $S_1 \rightarrow T_1$ transition (ISC) to the triplet state. The triplets are completely quenched in solution. In order to transfer excited state energy, the fluorophore and the quencher have to be in contact. This is either possible by complex formation (static quenching) or by diffusion-controlled collision (dynamic or collisional quenching).

The accessibility of a fluorescence probe for quenching molecules, expressed in the quenching constant, provides useful structural data about the environment of the site of labeling. In this study, fluorescence quenching was used to determine the accessibility of different domains in αB-crystallin. For this purpose, cysteine variants were modified with lucifer yellow and the fluorescence quenched by sodium iodide. To gain information about, which parts of aB are involved in substrate binding, either in a direct manner as substrate binding site or indirectly by means of conformational changes, fluorescence quenching was carried out with labelled αB-crystallin in a complex with bound lysozyme.

The cysteine mutants A4C, S59C, S115C and A172C were labelled with lucifer yellow iodoacetamide (LYI) and the degree of labeling was determined as described in *3.4.5*. A total concentration of 250 µM lucifer yellow were incubated in PBS buffer containing 1.5 mM TCEP with and without lysozyme (molar ratio 1:2 lysozyme:LYI-αB-crystallin) at 25°C for 60 min. Fluorescence was monitored in a 1.5 mL stirred cuvette with a fluorescence spectrometer (SPEX FluoroMax 1, Jobin Yvon). LYI fluorescence was excited at 425 nm and detected at 530 nm using a signal integration time of 2 s. Quenching of lucifer yellow fluorescence was attained by stepwise addition of a 5 M sodium iodide quenching solution in PBS containing 100 mM sodium thiosulfate. The dynamic quenching constant, K_{SV}, was derived from linear fitting of Stern-Volmer plots (F_0/F vs. $[Q]$). Linear curve fits were obtained using Origin software using the Stern-Volmer equation.

$$\frac{F}{F_0} = 1 + K_{SV}[Q]$$

Equation 5 | Stern-Volmer equation. F_0 and F are the fluorescence intensities in the absence and presence of quencher, respectively. K_{SV} = quenching constant (M^{-1}), $[Q]$ = concentration of quencher (M)

Fluorescence of the intrinsic tryptophan probes was quenched by stepwise addition of acrylamide (5 M) in the presence of 20 µM protein. The fluorescence was monitored with

a Fluoromax 3 (Jobin Yvon). The experiments were carried out at 37°C in PBS. For analysis, the relative decrease in fluorescence (F_0/F) was plotted against the quencher concentration (Stern-Volmer plot).

ANS Fluorescence

The environment-sensitive fluorescent dye 1-anilinonaphthalene-8-sulfonic acid (ANS, Sigma-Aldrich) can be used to study protein folding or to assess overall hydrophobicity. These applications take advantage of the strong fluorescence enhancement exhibited by the dye when the exposure to water is lowered. Consequently, fluorescence of ANS increases substantially when proteins to which it is bound undergo transitions from unfolded to fully or partially folded states. Molten globule intermediates or partially unfolded regions are characterized by particularly high ANS fluorescence intensities due to the exposure of hydrophobic regions.

Here, ANS fluorescence was used to compare the overall surface hydrophobicity of αB-crystallin and various variants. To this end, 10 µM protein were mixed with 1 mM ANS in PBS. Fluorescence spectra were recorded from 400 to 520 nm with an excitation wavelength of 372 nm. All ANS spectra were recorded at 37°C using a FluoroMax 3 (Jobin-Yvon).

3.6 Quaternary Structure Analysis

3.6.1 Analytical Gel-filtration Chromatography

The basic principle of high-performance liquid chromatography (HPLC) is to force an analyte through a stationary phase by pumping a liquid (mobile phase) at high pressures. An applied sample is separated by physical or chemical interactions at high resolutions within a short running time.

Here, HPLC was used as analytical gel-filtration chromatography for quaternary structure analysis of proteins, primarily α-crystallin variants, substrate complexes and chemically modified proteins. As gel filtration column a TSK G 4000 PW (Tosoh Biosciences) was used. All experiments were carried out in PBS, unless stated differently, at a flow rate of 0.5 mL/min. Elution profiles of the samples were recorded using fluorescence and UV detection. The detector settings were adjusted in dependence of sample concentration and experimental needs.

3.6.2 Dynamic Light Scattering

Dynamic light scattering (DLS) measurements were performed with an ALV/CGS-8 apparatus equipped with an ALV/5000/6010 digital autocorrelator operated in the single cross-correlation mode. A Uniphase (power >35 mW) He-Ne laser operating at a wavelength of 632.8 nm was employed as a light source. Scattering was monitored using a pair of avalanche photon counting modules (Perkin Elmer SPCM-CD2969). A fraction of the incoming laser beam was monitored continuously by two quadrant photodiodes placed after a precision attenuator. The readings of the photodiodes were employed to normalize the total scattered intensities and to exclude artifacts stemming from long-term fluctuations or changes in the pointing stability of the laser beam. Data were analyzed using the inverse Laplace transformation algorithm CONTIN (Provencher, 1982).

3.6.3 Analytical Ultracentrifugation

Analytical ultracentrifugation (AUC) consists of the application of centrifugal force with the simultaneous real-time observation of the sedimentation of macromolecules in the centrifugal field. Since proteins are studied in solution, AUC allows their hydrodynamic and thermodynamic characterization in solution, without interaction with any matrix or surface. There are two basic types of ultracentrifugation experiments for the characterization of proteins: sedimentation velocity (SV) and sedimentation equilibrium (SE) methods, which are described in the following sections.

In SV experiments, application of a sufficiently large centrifugal force field leads to movement of molecules toward the bottom of the centrifuge cell. The sedimentation process is determined by three factors – the gravitational force, the buoyancy and the hydrodynamic friction. Since the gravitational force is proportional to the square of the rotor speed, adjusting the rotor speed allows the study of a wide range of particle sizes, ranging from kDa to GDa molecular weights. From the balance of these three forces, one can derive the Svedberg equation.

$$s = \frac{v}{\omega^2 r} = \frac{MD(1 - \bar{V}\rho)}{RT}$$

Equation 6 | Svedberg equation. s = sedimentation coefficient (s), v = observed radial velocity (m/s), ω = angular velocity of the rotor (m/s^2), $\omega^2 r$ = centrifugal field, M = molar mass (g/mol), $\bar{V}$ = partial specific volume (cm^3/g), ρ = density of the solvent (g/cm^3), D = diffusion coefficient (m^2/s), R = gas constant (8.314472 J/K mol), T = absolute temperature (K)

The sedimentation coefficient represents the sedimentation velocity v in relation to the centrifugal field $\omega^2 r$. The s-values are commonly reported in Svedberg (S) units, which correspond to 10^{-13} s.

When the centrifugal force is sufficiently small, the process of diffusion significantly opposes the process of sedimentation, and an equilibrium concentration distribution of macromolecules is obtained throughout the cell. For an ideal non-interacting single component system, the equilibrium distribution is an exponential function of the buoyant mass of the molecule, $M(1-\overline{V}\rho)$, as described by:

$$c(r) = c_0 \cdot e^{\frac{M(1-\overline{V}\rho)\omega^2(r^2-r_0^2)}{2RT}}$$

Equation 7 | $c(r)$ = sample concentration at radial position r, c_0 = sample concentration at reference radial distance r_0, $\overline{V}$ = partial specific volume, ω = angular velocity of the rotor, R = gas constant, T = absolute temperature

3.6.4 Electron Microscopy

All EM experiments mentioned in this thesis were performed in close collaboration with the group of Prof. Sevil Weinkauf (Technische Universität München, Garching). Most EM experiments and data analysis were conducted by Dr. Nathalie Braun from the Weinkauf lab. A detailed description of the EM methods is published elsewhere (Braun et al., 2011; Peschek et al., 2009).

3.6.5 Protein Cross-linking Combined with Mass Spectrometry

Cross-linking experiments were carried out using BS^3 (Pierce) as cross-linker. The reaction mixtures were separated into a monomer and two oligomer bands by SDS-PAGE and trypsin digested.Cross-linked peptides were fractionated, desalted and analyzed on LTQ Orbitrap Velos (Thermo Scientific) mass spectrometer. The data were processed using MaxQuant and in-house Xi software (Prof. Juri Rappsilber, Edinburgh, UK). For details see Braun et al. (2011).

3.7 Functional Analysis

3.7.1 Studying Subunit Exchange Kinetics

S153C mutants of WT αB-crystallin and αB-crystallin-3E were labeled with lucifer yellow iodoacetamide (LYI) and 4-acetamido-4'-((iodoacetyl)amino)stilbene-2,2'disulfonic acid (AIAS) (both from Molecular Probes) according to the manufacturer's protocol for 2 h at room temperature in PBS. Unbound label molecules were removed using a HiPrep™ 26/10 Desalting Column (GE Healthcare). The donor- and acceptor-labelled proteins (each 1 µM) were incubated separately in PBS at 37°C prior to measurement. Subunit exchange was initiated by mixing equal volumes of both labeled proteins and the change in donor fluorescence was monitored using a Fluoromax 3 (Jobin Yvon). Data analysis was carried out according to Bova et al. (1997).

3.7.2 Assays for the Study of Chaperone Activity

As mentioned in the introduction, α-crystallins and many other sHsps can efficiently suppress protein aggregation in an ATP-independent manner by binding non-native proteins (Horwitz, 1992; Jakob et al., 1993). There are several ways to study this holdase function and the interaction with substrate proteins. The most common *in vitro* assays involve subjecting substrate proteins to denaturation by heat or reduction of disulfide bonds, then either monitor (i) the prevention of the formation of light-scattering aggregates or (ii) how proteins are maintained in the soluble fraction as determined by centrifugation and SDS-PAGE (Basha et al., 2012). Within the scope of this thesis, several *in vitro* substrates were used as listed in the following including experimental details:

Lysozyme

The aggregation of 10 µM lysozyme (from chicken egg white, Sigma-Aldrich) was initiated by 1 mM tris(2-carboxyethyl)phosphine (TCEP, Sigma-Aldrich). All lysozyme assays were carried out at 37°C in PBS buffer. The aggregation process was followed at 400 nm by recording absorbance changes in a Varian Cary 50 UV/VIS spectrophotometer (Agilent) equipped with a temperature-adjustable cuvette holder. To determine the chaperone activity of α-crystallins, increasing concentrations of each α-crystallin species were added before reduction. The solubility of denatured lysozyme in the absence and presence of α-crystallin was determined by SDS-PAGE and Coomassie staining, analyzing the sediment and supernatant fraction after centrifugation at 10,000 g for 5 min in a table-

top centrifuge. The insoluble fraction was washed after the first centrifugation step by resuspending the pellet in PBS followed by a second centrifugation step.

Malat Dehydrogenase

The heat-induced aggregation of 2 µM MDH (mitochondrial MDH from pig heart, Roche) was carried out at 45°C in PBS or HKM buffer. The aggregation process was followed at 350 nm by recording absorbance changes in a Varian Cary 50 UV/VIS spectrophotometer (Agilent) equipped with a temperature-adjustable cuvette holder. To determine the chaperone activity, αB-crystallin variants were added before incubation at 45°C.

γD-Crystallin

Human γD-crystallin was denatured in PBS containing 5 M GdnCl. The aggregation was initiated by diluting denatured γD-crystallin 1:50 into PBS at 37°C with varying amounts of αB-crystallin yielding a final concentration of 2 µM γD. The aggregation process was followed at 350 nm by recording absorbance changes in a Varian Cary 50 UV/VIS spectrophotometer (Agilent) equipped with a temperature-adjustable cuvette holder.

p53

The heat-induced aggregation of 1 µM p53 was carried out at 42°C in PBS or HKM buffer. The aggregation process was followed at 350 nm by recording absorbance changes in a Varian Cary 50 UV/VIS spectrophotometer (Agilent) equipped with a temperature-adjustable cuvette holder. To determine the chaperone activity, αB-crystallin variants were added before incubation at 42°C.

HeLa Cell Lysate

To simulate the aggregation protecting function of αB-crystallin within the cell, HeLa cell lysate (see 3.4.3 for preparation) was heat-stressed at 45°C for 40 min in the presence of various amounts of αB-crystallin. The soluble and insoluble protein fraction was separated by centrifugation (10 min, 10,000 g, 4°C) followed by SDS-PAGE analysis. The insoluble fraction was washed after the first centrifugation step by resuspending the pellet in PBS followed by a second centrifugation step.

3.7.3 Limited Proteolysis

αB-crystallin (10 µM) was incubated with 1:25 (w:w) α-chymotrypsin (Sigma) in 100 mM Tris, 100 mM NaCl, 10 mM $CaCl_2$, pH 7.8 at 25°C for 30 min. Proteolysis reactions were terminated with 2 mM phenylmethylsulfonyl fluoride (Sigma) after various time points and

analyzed by SDS-PAGE on 15% acrylamide gels followed by Coomassie blue staining. The peptides were identified by LC-MS.

3.7.4 Substrate Refolding/Reactivation Experiments

MDH Refolding

2 µM MDH (in 25 mM Hepes, 50 mM KCl, 5 mM $MgCl_2$, pH 7.4) were incubated with and without 10 µM WT αB-crystallin and αB-crystallin-3E, respectively at 46°C for 45 min. MDH samples were cooled on ice and diluted 1:1 by adding the respective refolding mix containing combinations of Hsc70 (2 µM), Hdj1 (0.5 µM) and an ATP-regenerating system consisting of phosphoenol pyruvate (3 mM), pyruvate kinase (20 µg/mL) and ATP (2 mM), then shifted to 30°C. Samples were taken after different time points. 10 µL of each sample were mixed with 190 µL assay buffer (0.5 mM oxaloacetate, 0.2 mM NADH in HKM buffer). The MDH activity was measured at 340 nm for 15 min at 30°C in a Varian Cary 50 UV/VIS spectrophotometer (Agilent).

p53 Reactivation

3 µM p53 was incubated at 42°C for 30 min in the absence or presence of 15 µM WT αB-crystallin or αB-crystallin-3E in 25 mM Hepes, 150 mM KCl, 5 mM $MgCl_2$, pH 7.4. As positive control, p53 was kept at 4°C. Reactivation of p53 was performed using 2 µM Hsc70 and 0.5 µM Hdj1 in presence of an ATP regenerative system (3 mM PEP, 20 µg/mL PK, 2 mM ATP) in 25 mM Hepes, 150 mM KCl, 5 mM $MgCl_2$, 1 mM DTT, pH 7.4 for 270 min at 30°C and 30 min at 25°C. For determination of p53 DNA-binding activity an electrophoretic mobility shift assay (EMSA) with Cy5 labeled p21-DNA was performed as described before (3.4.6).

4 Results

4.1 Purification of α-Crystallins

Human αA- and αB-crystallin were recombinantly expressed in *E. coli* and purified to homogeneity. The purification protocol was developed and optimized during previous work on α-crystallins in the scope of my master's thesis (Peschek, 2007). All purification steps were carried out at basic pH in Tris/HCl buffer (for details see *Materials and Methods*). MALDI-TOF MS analysis confirmed the correct monomer masses, 19,909 Da for αA and 20,159 Da for αB (Figure 13A&B).

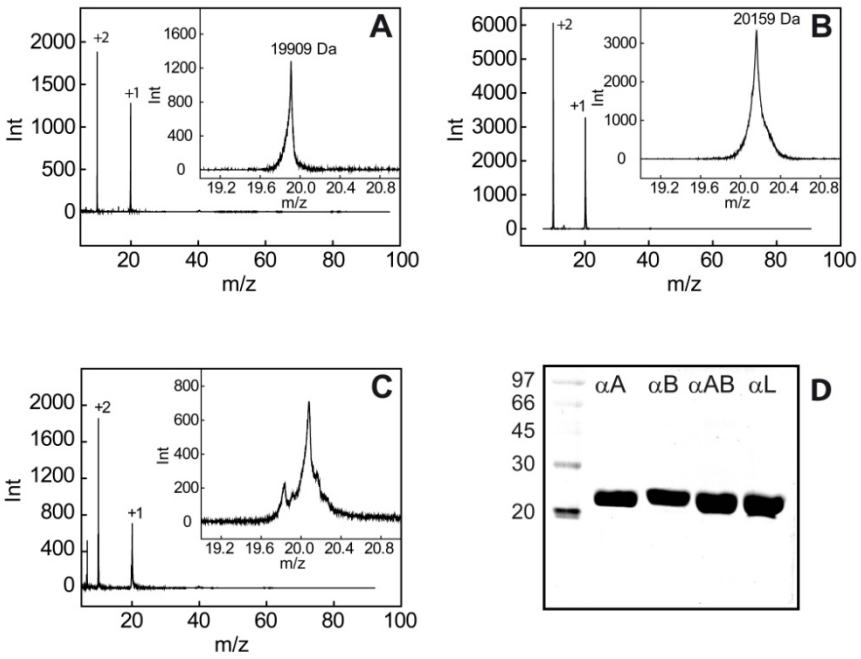

Figure 13 | Analysis of the mass and homogeneity of α-crystallin preparations. MALDI-TOF mass spectrometry analysis of human recombinant αA- (A) and αB-crystallin preparations (B) revealed the correct mass according to the primary structure of both isoforms. The mass spectrum of the authentic αL-crystallin preparation (C) shows the masses of bovine αA- and αB-crystallin with several posttranslational modifications. The insets depict a magnified view of the single-charged molecular ions. (D) SDS-PAGE analysis of the purified α-crystallin species confirmed the homogeneity of the preparations.
Figure adapted from Peschek et al. (2009).

In addition, authentic bovine α-crystallin, a mixture of the two occurring isoforms αA- and αB-crystallin (termed "αL-crystallin" to indicate native lens α-crystallin) was purified from cow lenses. MS analysis identified the presence of both isoforms and additional species

that correspond to posttranslationally modified protein (Figure 13C). The homogeneity of each purification was assessed by SDS-PAGE (Figure 13D).

All α-crystallin mutants that were produced in the scope of this thesis were purified based on the same protocol and tested for homogeneity as described above.

4.2 Basic Structural Characterization of α-Crystallins

4.2.1 Circular Dichroism Spectroscopy

The secondary and tertiary structure of recombinantly produced human αA- and αB-crystallin, a 1:1 mixture of proteins as well as αL-crystallin were assessed by circular dichroism (CD) spectroscopy (Figure 14). Far UV CD spectroscopy provides information about the content of secondary structure elements due to the differential absorption in the UV region (260-170 nm) of backbone amide groups in asymmetric secondary structures. The far UV CD spectra of all four α-crystallin preparations displayed a broad minimum at about 215 nm with an intensity of approximately -4000 deg cm^2 $dmol^{-1}$ and a maximum at 200 nm (Figure 14A). These are two major characteristics for proteins with mainly β-sheet structure.

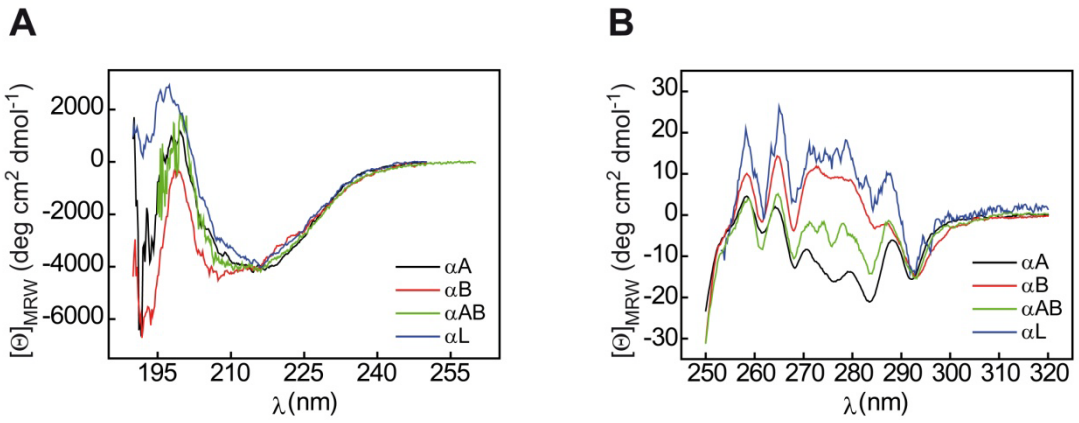

Figure 14 | CD analysis of α-crystallin species. (A) Far UV and (B) near UV CD spectra of human recombinant αA-crystallin (black line), αB-crystallin (red line), αAB-crystallin (the equimolar mixture of both isoforms; green line) and the authentic αL-crystallin from bovine lenses (blue line). Deconvolution of far UV CD spectra revealed about 60 % β sheet and 7% α-helix content. The near UV CD spectra provide information on the surrounding environment of the absorbing chromophores and serve as "fingerprints" of each protein. Both experiments are in good agreement with previously published data (Sun et al., 1997) assuring the correct folding state of all α-crystallin preparations.
Figure adapted from Peschek et al. (2009).

The recorded CD spectra in the near UV range differed between both isoforms (Figure 14B). Since the signal in this range (250-320 nm) mainly reflects the specific environment of the aromatic residues, which vary in the respective primary sequences, it is difficult to draw further conclusions. It should be noted that the mixture of both recombinant isoforms is different from αL-crystallin. However, due to the difference in the species of origin, a direct comparison cannot be made. The CD spectra in the far and near UV range corresponded to previously published data (Sun et al., 1997).

4.2.2 Hydrodynamic Properties of α-Crystallins

Most monodisperse oligomeric sHsps studied so far form assemblies consisting of 12 or 24 subunits (Haslbeck et al., 2005a). For α-crystallin and other metazoan sHsps, however, structural data in the literature suggest a polydisperse (i.e. heterogeneous) ensemble with a continuum of different oligomeric states (Aquilina et al., 2003; Haley et al., 2000). To address this issue and to study the hydrodynamic properties, the recombinant α-crystallin isoforms as well as authentic αL-crystallin were subjected to analytical size exclusion chromatography (SEC) and dynamic light scattering (DLS). Elution profiles of α-crystallins from an analytical SEC column are shown in Figure 15A. αB-crystallin eluted in a single narrow and symmetric peak with a full width at half maximum (FWHM) of 1.45 min. According to linear calibration, the elution time corresponded to a molecular mass of ~475 kDa consistent with a complex of 24 subunits (20.2 kDa monomeric mass). Similarly, αA-crystallin eluted in a single and symmetric peak with a slightly smaller apparent molecular mass of 440 kDa (19.9 kDa monomeric mass). Although the FWHM of αL-crystallin was very similar to that observed for αA- and αB-crystallin, the elution time was smaller, indicating that its hydrodynamic properties differ from that of recombinant αA- and αB-crystallin. Interestingly, αAB-crystallin exhibited similar elution times as the isolated recombinant proteins, showing that the assembly of both isoforms into αA-αB-hetero-oligomers by subunit exchange (Bova et al., 2000) per se is not responsible for the different hydrodynamic behavior of αL-crystallin. For comparison, Hsp26 from yeast and Hsp16.5 from *M. jannaschii*, which form 24-mers (Kim et al., 1998; White et al., 2006), were also subjected to SEC. Their FWHMs were very similar to those obtained for the different α-crystallin preparations (data not shown).

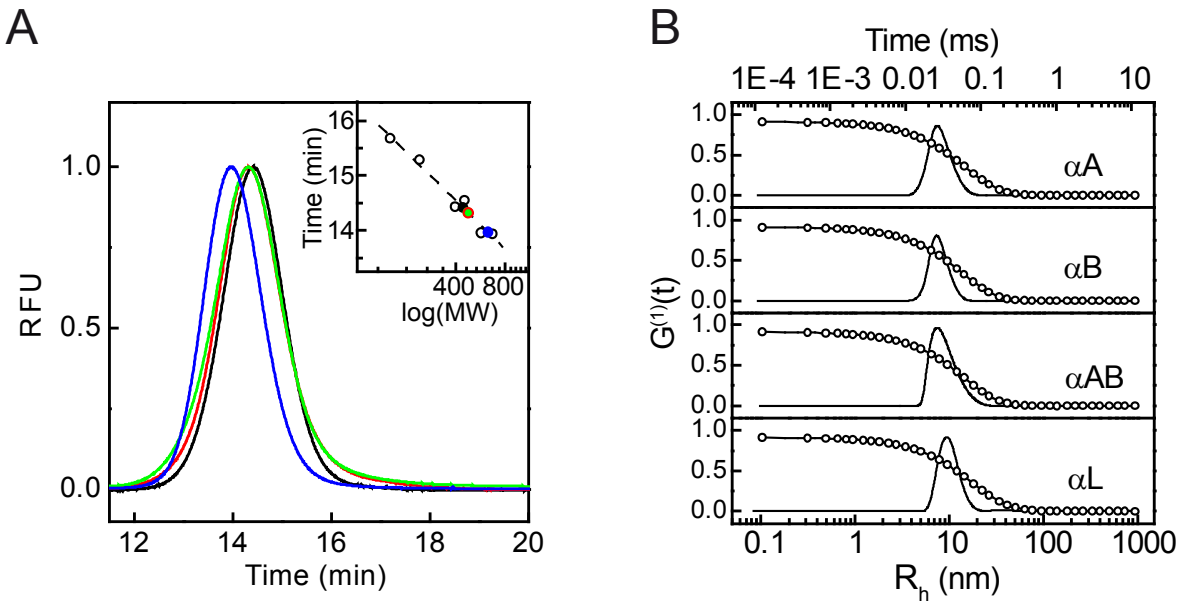

Figure 15 | Hydrodynamic analysis. (A) The SEC elution profiles of recombinant human αA- (black line), αB-crystallin (red line), an equimolar mixture of both isoforms (αAB-crystallin) (green line) and authentic bovine αL-crystallin (blue line) were obtained using a Tosoh TSK 4000 PW column. All species eluted from the SEC column within a single, narrow and symmetric peak with a width at half height in the range of 1.4 min. Inset: Linear calibration revealed a molecular mass of 441 kDa for αA-crystallin, approximately 475 kDa for αB-crystallin as well as for the mixture of both isoforms and 628 kDa for αL-crystallin. (B) DLS autocorrelation function (ACF) plots of αA-, αB-, αAB- and αL-crystallin and the corresponding mass-weighted particle size distributions. The hydrodynamic radii are 8.04 ± 0.23 nm for αA- (peak weight 99.88 %), 7.26 ± 0.18 nm for αB- (peak weight 99.80 %), 8.83 ± 0.29 nm for αAB- (peak weight 100%), and 10.19 ± 0.27 nm for αL-crystallin (peak weight 99.31 %).
Figure adapted from Peschek et al. (2009).

To further address the issue of solution quaternary structure, we subjected the four α-crystallin samples to DLS (Figure 15B). The respective mass-weighted particle size distributions indicated hydrodynamic radii of 8.04 ± 0.23 nm for αA-, 7.26 ± 0.18 nm for αB-, 8.83 ± 0.29 nm for αAB- and 10.19 ± 0.27 nm for αL-crystallin (Figure 15B), which is in good agreement with the relative hydrodynamic sizes from the SEC analyses.

4.3 Quaternary Structure Analysis

The advantage of analytical ultracentrifugation (AUC) as method is its potential to study biomacromolecules in solution without the need of any separation matrix like in analytical gel-filtration. In addition, the resolution of AUC in separating different species within a heterogeneous mixture is larger in comparison to DLS. Here, AUC was used to study the quaternary structure of the different α-crystallins. Furthermore, compiled data from AUC and EM was used to assess the degree of heterogeneity within different preparations.

4.3.1 Sedimentation Velocity Analytical Ultracentrifugation

In sedimentation velocity (SV) AUC experiments, the α-crystallin samples studied generated a single sedimentation boundary. Data analysis was carried out using the time derivative (dc/dt) method (Stafford, 1992). For αB-crystallin, dc/dt analysis revealed a narrow distribution of apparent sedimentation coefficients (s*) with the highest frequency at about 16.5 S (Figure 16B).

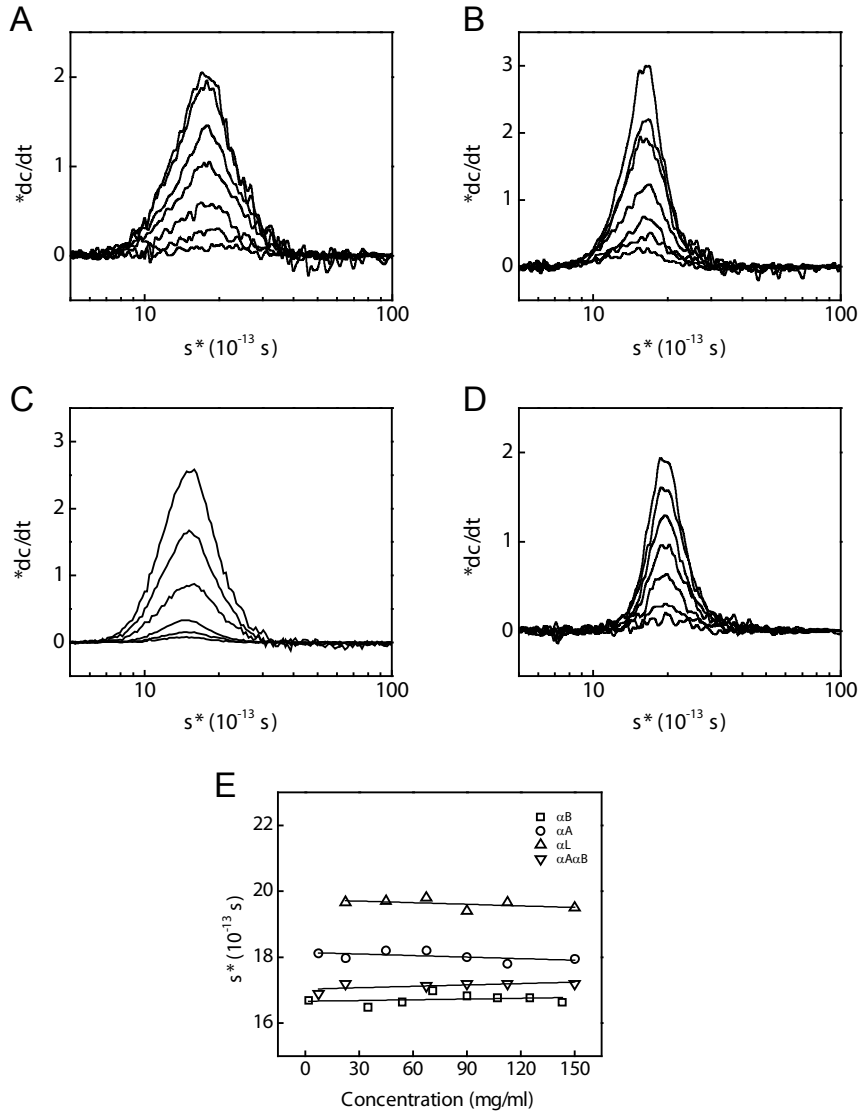

Figure 16 | SV-AUC analysis. Sedimentation velocity data of (A) human recombinant αA-, (B) αB-crystallin, (C) αAB-crystallin and (D) the authentic αL-crystallin from bovine lenses were analyzed using the dc/dt method. Within the tested concentration range (2-150 μM) no changes in the apparent sedimentation coefficient (s*) could be observed. αA- as well as αAB-crystallin exhibit a broader s* distribution than αB-crystallin. **(C)** Concentration-dependent analysis of the sedimentation coefficient (s) by SV AUC as a function of the concentration of αA-Crystallin (circles), αB-crystallin (squares), αAB-crystallin (reverse triangles) and αL-crystallin (triangles).
Figure adapted from Peschek et al. (2009).

αA-crystallin and αAB-crystallin, however, exhibited s*-values of 18 S and 17 S, respectively, with broader distributions (Figure 16A,C). This result indicates that αA has a higher degree of heterogeneity than αB. When both isoforms were mixed, the resulting hetero-oligomer exhibited hydrodynamic properties in between the isolated forms. The authentic αL-crystallin showed the largest s*-value of 20 S (Figure 16D). This finding is in agreement with the observed larger hydrodynamic size by SEC and DLS.
The s*-values of all four species were shown to be independent of concentration within the range of 2-150 µM (Figure 16E), which was also reported previously (Horwitz, 2009).

4.3.2 Sedimentation Equilibrium Analytical Ultracentrifugation

Since αB-crystallin was found to exhibit the highest degree of homogeneity, we performed sedimentation equilibrium (SE) AUC to analyze its quaternary structure more precisely. We determined a concentration-independent molecular mass of 482 ± 12 kDa in the range of 2.5 µM and 50 µM (0.05-1.25 mg mL^{-1}), which is in agreement with the theoretical mass of 484 kDa for a 24-mer (Figure 17).

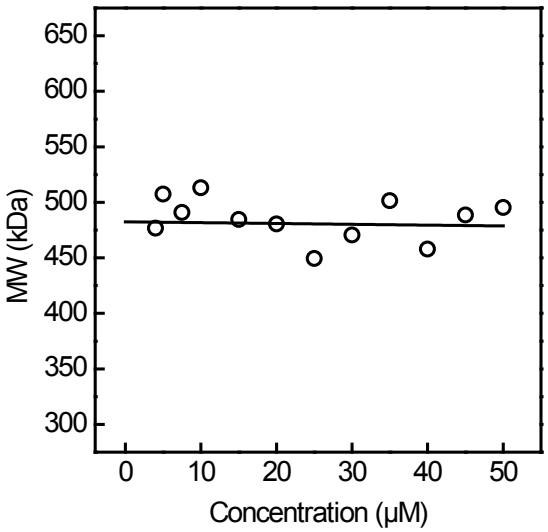

Figure 17 | SE-AUC analysis. Apparent molecular masses for αB-crystallin determined from SE AUC experiments as a function of the protein concentration. Data were fitted to a molecular mass of 482 ± 12 kDa.
Figure adapted from Peschek et al. (2009).

4.3.3 Dealing with Heterogeneity of α-Crystallins by a Combination of Methods

To further investigate the nature of the different assemblies, α-crystallin preparations were separated by analytical gel-filtration into an early, a medium and a late peak fraction

(Figure 18A-D, insets). Subsequently, the obtained fractions were analyzed separately by SV-AUC and TEM. In between fractionation and analysis, the samples were kept on ice and the time span was kept as short as possible. Interestingly, the αA-crystallin fractions vary in their sedimentation coefficients with an inverse correlation between elution time in SEC and s-values (Figure 18A, left panel). The s-value distributions of the early and late fraction were shifted by ~10 S. TEM revealed the presence of small (11.5 nm diameter) and large (13.5 nm) assemblies in the medium αA fraction (Figure 18A, right panel, top). In the fraction at early elution times, large oligomers (13.5 nm) and elongated assemblies resulting from oligomer-oligomer associations were detected (Figure 18A, right panel, bottom).

On the contrary, αB-crystallin exhibited much less variance between the three samples representing a higher degree of homogeneity. The medium and late fractions after SEC (Figure 18B, inset) yielded very similar s-distributions with the highest frequency at 16.7 S, indicating the absence of smaller oligomeric species (Figure 18B, left panel). TEM analysis confirmed this finding: predominantly globular oligomers (13.5 nm), similar to the large ones in αA-crystallin samples, were identified (Figure 18B, right panel, top). The early SEC fraction contained a population of interacting oligomers sedimenting with 18.5 S. TEM revealed the presence of large assemblies in this fraction, which appear to be a population of interacting oligomers (Figure 18B, right panel, bottom). However, the amount of "clustered" oligomers was lower than in the respective αA-crystallin samples.

αAB-crystallin fractions (Figure 18C) turned out to be similar to those of αA-crystallin: while the early fraction contained larger oligomers and oligomer clusters (Figure 18C, right panel, bottom), the medium fraction was characterized by the presence of both larger and smaller oligomers (Figure 18C, right panel, top). The smaller and larger species might be an intrinsic property of αA-crystallin. Though, it is also possible that the large species do not take part in the dynamic oligomer equilibrium.

The authentic αL-crystallin exhibited the highest degree of heterogeneity within our analyses (Figure 18D). In general, s-values were larger in comparison to the recombinant preparations (Figure 18D, left panel), which corresponds well to SEC and DLS data. TEM analysis of the medium fraction revealed the existence of populations of smaller and larger oligomers (Figure 18D, right panel, top). The early fraction produced a broad and asymmetric s-distribution ranging from 15-45 S (Figure 18D, left panel). In accordance, a significantly higher degree of oligomer-oligomer association as well as larger oligomer

clusters were observed by TEM (Figure 18D, right panel, bottom) when compared to the other recombinant α-crystallin samples.

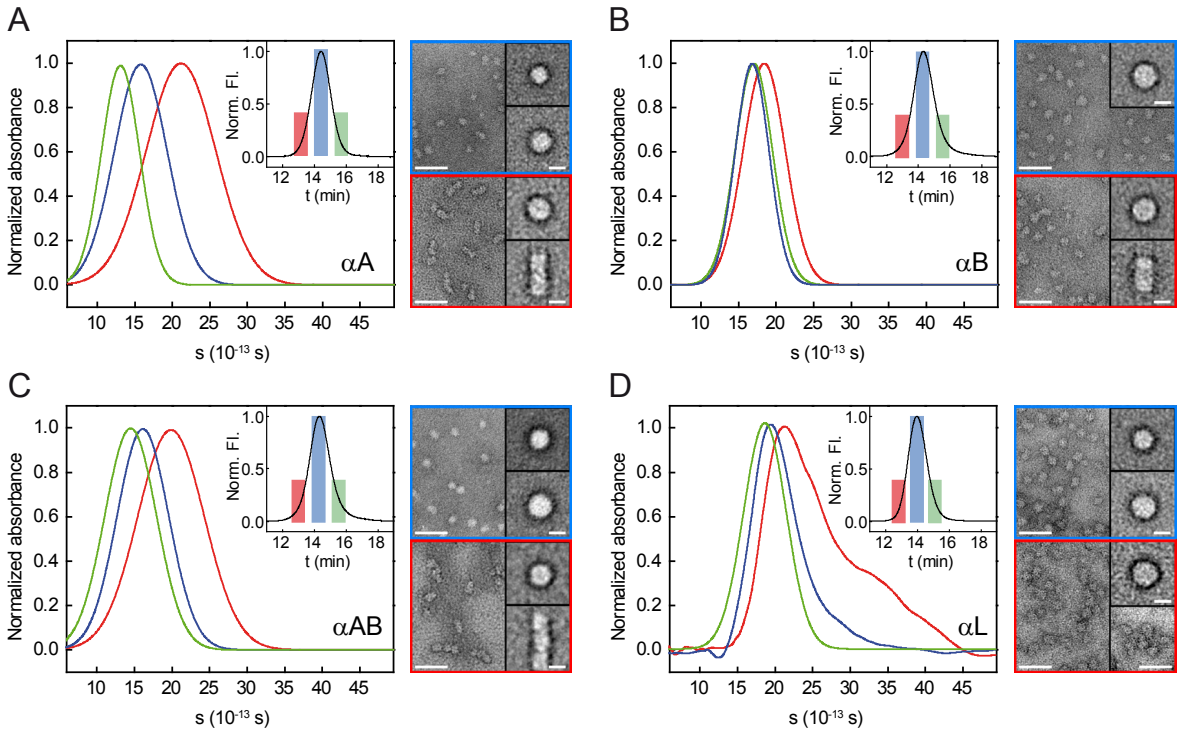

Figure 18 | Heterogeneity of α-crystallins. (A-D) Analysis of fractions obtained from SEC (see methods) by SV analytical ultracentrifugation (left panels) and transmission electron microscopy (right panels). s-distributions for the early (red), medium (blue) and late (green) fraction of the elution peaks (Insets) were determined using the dc/dt method. Representative electron micrographs of negatively stained (ammonium molybdate, 1.5% [w/vol], pH 5.5) α-crystallin samples obtained from the medium (blue frame) and the early SEC fraction (red frame) are depicted (scale bars: 50 nm). For each sample, average images (scale bars: 10 nm) are included for every population with more than 10% abundance. (A) αA-crystallin. (B) αB-crystallin. Note the much higher degree of homogeneity. (C) αAB-crystallin. (D) Authentic αL-crystallin.
Figure adapted from Peschek et al. (2009).

The combined SEC/AUC/TEM analyses demonstrated that αA- and αB-crystallin differ in their propensities to associate to heterogeneous populations. However, αA-crystallin also forms smaller oligomers and more large clusters consisting of individual oligomers. This heterogeneity also dominates in mixed complexes consisting of both αA- and αB-crystallin. The propensity of αA-crystallin oligomers to further associate to larger particles may result in a continuum of assemblies which could explain the previously suggested polydisperse character of α-crystallin which is composed of both αA- and αB-crystallin. Interestingly, authentic αL-crystallin seems to possess a much higher degree of heterogeneity including large oligomer clusters than the mixture of recombinant αA- and αB-crystallin. The formation of oligomer clusters might be influenced by the posttranslational modifications of the α-crystallins in the eye lens. Whether the observed

difference is important for its function in maintaining the transparency of the eye lens or whether it is merely an epiphenomenon of aging remains to be elucidated.

4.3.4 Electron Microscopy and 3D Reconstruction of αB-Crystallin

Due to the heterogeneity and dynamic subunit exchange, all attempts to crystallize full-length α-crystallins (or other metazoan sHsps) failed so far. Albeit the heterogeneity lowers the resolution, recent advances in single particle EM allow to image even irregular and heterogeneous protein samples. Hence, an EM-based structure analysis was undertaken in close collaboration with the group of Prof. Weinkauf. Due to the aforementioned results on heterogeneity and quaternary structure of the different α-crystallin preparations, we focused our efforts to reveal the three-dimensional structure using EM on αB-crystallin. For this purpose, 2565 single particle images (Figure 19A) were selected from electron micrographs of the negatively-stained samples and subjected to multivariate statistical analysis (MSA) and classification.

Eigenimages, i.e. images representing the most important differences in the data set, obtained after a first cycle of translational alignment already indicated the presence of 3-fold symmetry (Figure 19B). In addition, preliminary class averages (Figure 19C) showed the presence of projection images with 3-fold symmetry. In view of the established structural model at that time (Haley et al., 2000; Haley et al., 1998), which corresponded to an asymmetric 32-meric assembly (Figure 10), and the discussed polydispersity (Horwitz, 2009), this was a rather unexpected discovery.

Since SEC (Figure 15A) and SE-AUC (Figure 15B) analysis indicated 24-mers as the prevalent assembly form of αB-crystallin, the 3D reconstruction was based on the assumption of 24-meric oligomers. The compatible point group symmetries, i.e. C3, D3, tetrahedral and octahedral, were imposed for the calculation of the respective preliminary three-dimensional models by angular reconstitution. For each imposed symmetry the preliminary model was refined in iterative cycles as described elsewhere (Peschek et al., 2009). Only tetrahedral symmetry gave consistent results and led to a final three-dimensional model at approximately 20 Å resolution. Selected class averages and corresponding reprojections of the final three-dimensional model are shown in Figure 19D&E, respectively.

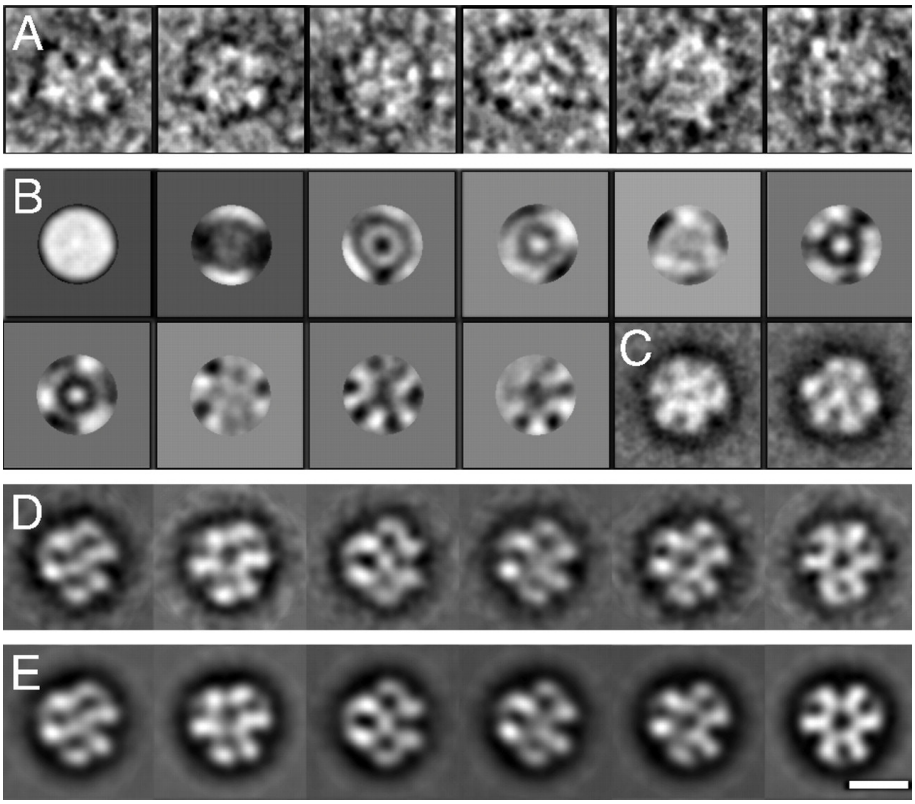

Figure 19 | Image analysis of negatively stained αB-crystallin oligomers. (A) Gallery of single αB-crystallin oligomers. (B) First 10 *eigenimages* (statistical difference images) obtained after translational alignment of the data set. (C) Two class averages with apparent 3-fold and mirror-symmetries resulting from the MSA of the translationally aligned data set. (D) Characteristic final class averages. (E) Two-dimensional reprojections of the three-dimensional model of αB-crystallin in the orientations found for the class averages shown in D. Scale bar: 10 nm.
Figure taken from Peschek et al. (2009). Data provided by Prof. Sevil Weinkauf and Dr. Nathalie Braun.

The three-dimensional reconstruction shows that human αB-crystallin oligomer is roughly spherical with a diameter of 13.5 nm (Figure 20A). The oligomer has a large central cavity of approximately 8.5 nm diameter, which is surrounded by a symmetrical protein shell with a mean thickness varying from 2.5 nm to 4 nm (Figure 20B). The protein shell shows openings at the positions of the 2- and 3-fold axes, with diameters of approximately 3.5 nm for the 2-fold axes and 3 nm and 2 nm for the two unequal 3-fold axes. The overall quaternary structure of recombinant human αB-crystallin resembles the structures of Hsp20.2 from *Archaeoglobus fulgidus* (Haslbeck et al., 2008) and Hsp16.5 from *Methanocaldococcus jannaschii* (Kim et al., 1998), which both form 24-meric complexes with octahedral symmetry. As shown in Figure 20C, the dimeric ACD of Hsp16.5 from *M. jannaschii* was tentatively positioned in the corresponding position of the αB-crystallin model.

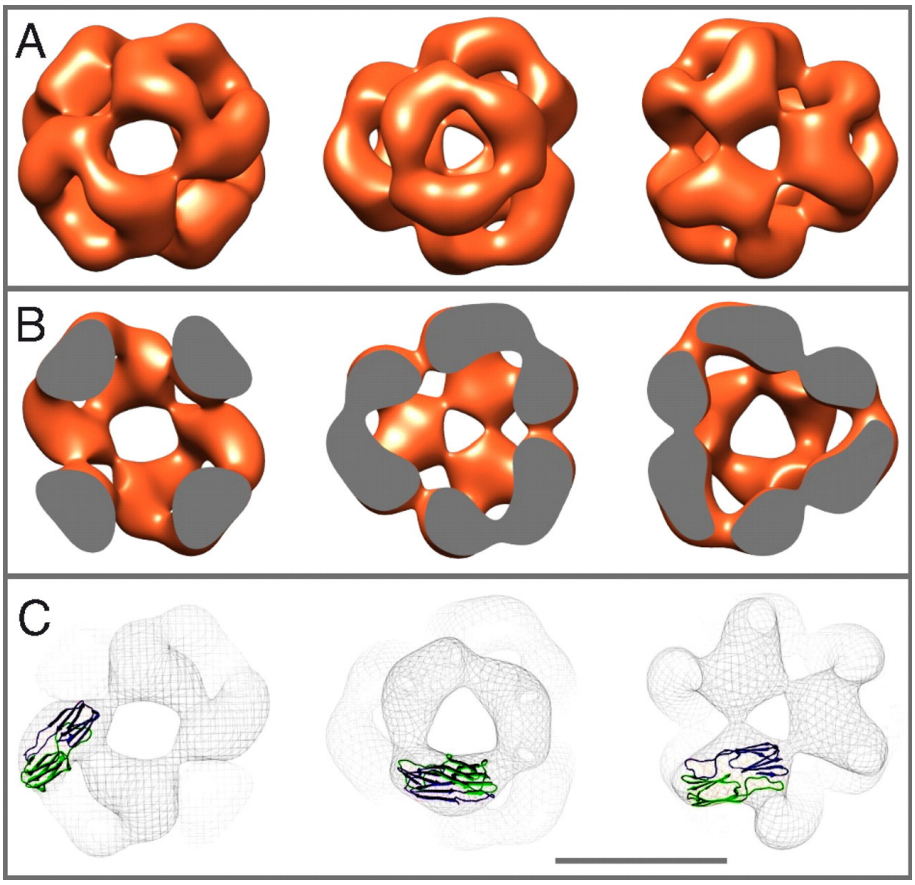

Figure 20 | 3D reconstruction of human recombinant αB-crystallin. (A) Surface representations of the three-dimensional model of human recombinant αB-crystallin. The density threshold applied for the surface representation has been chosen such that the corresponding molecular mass was in agreement with a 24-meric αB-crystallin. The molecules are viewed along the 2-fold axis (first row) and the two unequal 3-fold axes (second and third row). (B) Density cross sections through the three-dimensional model of αB-crystallin. (C) Superposition of the ribbon representation of the dimeric α-crystallin domain of Hsp16.5 from *M. jannaschii* (Kim et al., 1998) with the meshed surface representations of the three dimensional model of αB-crystallin. Scale bar: 10 nm.
Figure taken from Peschek et al. (2009). Data provided by Prof. Sevil Weinkauf and Dr. Nathalie Braun.

4.4 A Hybrid Approach: Combining Structural Methods to Decipher the Molecular Architecture of αB-Crystallin

Given its oligomeric plasticity and dynamics, the structural analysis of αB-crystallin is very challenging. In recent years, an increasing number of high-resolution structures of the isolated ACD were solved by X-ray crystallography or NMR (Clark et al., 2011; Jehle et al., 2010; Laganowsky et al., 2010). However, the full-length protein is too large for solution NMR and all attempts to crystallize it failed so far. Thus, the most promising approach is the integration of multiple structural methods, which cover the whole resolution range, and supporting biochemical techniques to so-called "hybrid approaches". The above-mentioned combination of SEC, AUC and TEM to study the quaternary

structure and heterogeneity of different α-crystallins was a successful example of integrating several methods. Thus, we pursued efforts to yield a structural model with higher resolution and to understand the dynamic oligomer equilibrium in more detail. To this end, data from cryo-EM, NMR spectroscopy, structural modeling and biochemical methods were combined. Of course, such a broad range of methods demanded the collaboration of multiple groups, which led to the collaboration between the groups of Prof. Buchner (biochemistry), Prof. Weinkauf (EM), Prof. Zacharias (modeling; all three Technische Universität München) and Juri Rappsilber (crosslinking/MS; University of Edinburgh). In the context of my thesis, I contributed to this work performing all biochemical and crosslinking experiments. To summarize the whole project, all experimental aspects are described in the following section.

4.4.1 Cryo-EM Model and Pseudo-Atomic Structure of the αB-Crystallin 24-mer

Encouraged by the knowledge how to deal with heterogeneity and the results from negative-stain EM, we continued the structural elucidation of αB-crystallin using cryo-EM. In order to improve the resolution of about 20 Å obtained by negative stain EM, a very stringent selection of particles into the final data set was applied (see Braun et al. (2011) for a detailed description of image processing and data separation). About one third (27,057 particle images) of the collected particles, which we assigned to 24-mers, was sorted into 280 classes and used to calculate 3D reconstructions (see Braun et al. (2011) for a detailed description of 3D reconstruction). Eventually, we obtained a 3D model of the 24-meric αB-crystallin assembly at a resolution of 9.4 Å (Braun et al., 2011). The depicted model (Figure 21A) shows a hollow, spherical complex with a diameter of ~13.5 nm and tetrahedral symmetry. In this and other respects, the model is similar to the one obtained using negative-stain EM. The interior is accessible through openings at the twofold symmetry axes and one threefold symmetry axis (termed 3_o; "open" threefold symmetry axis). The area around 3_0 shows three mass-rich dome-shaped structures. At the other threefold axes, the most striking difference to the previous model is the mass accumulation at the other threefold symmetry axis (termed 3_c; "open" threefold symmetry axis).

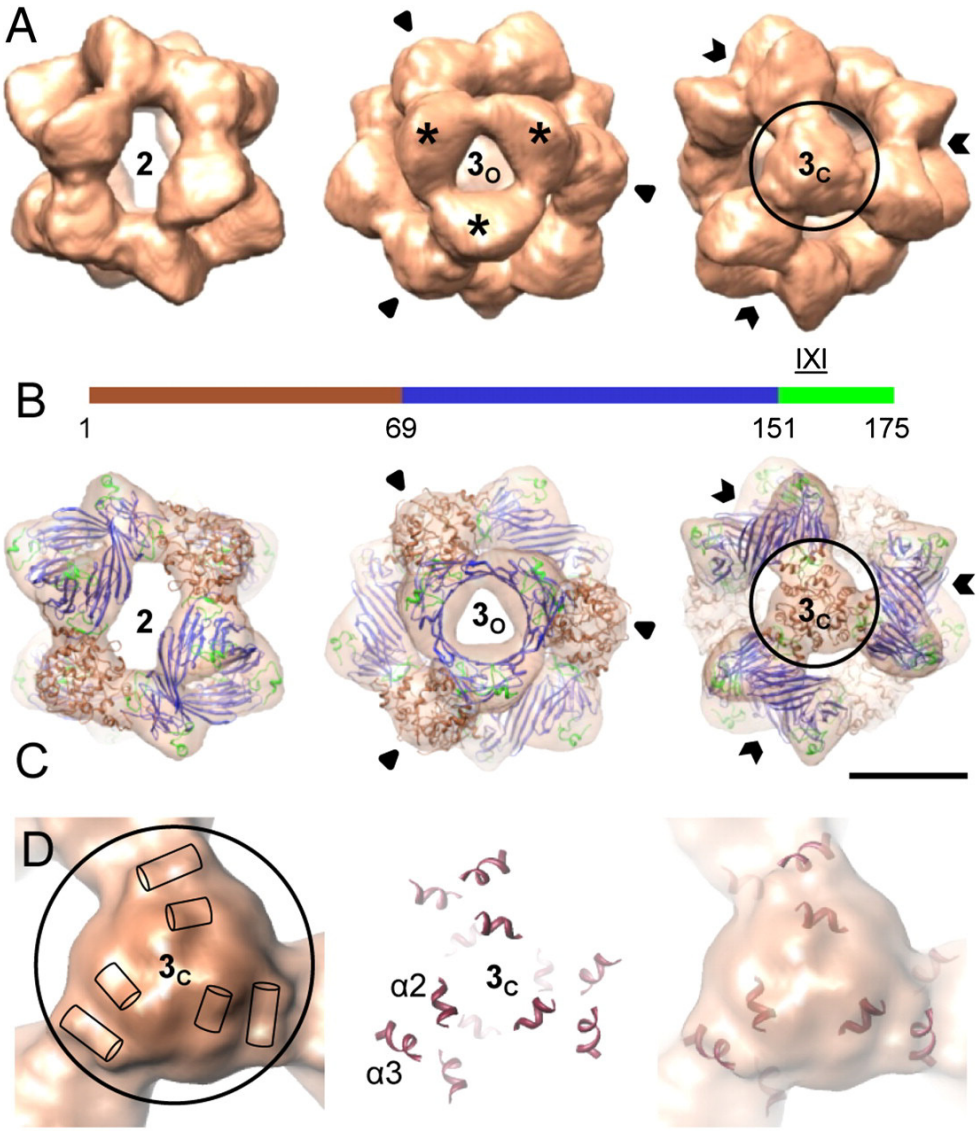

Figure 21 | 3D model of the αB-crystallin 24-mer. (A) Surface representations of the cryo-EM density map of the αB-crystallin 24-mer viewed along a two- (left) and the different threefold symmetry axes, one intercepting the area harboring a "window" (3_o, open arrows) (middle) and the other a mass accumulation (3_c, closed arrows) (right). Mass-rich "domes" surrounding 3_o are highlighted by stars. The isosurface threshold was set to enclose a molecular mass of 485 kDa. (B) Domain organization of human αB-crystallin: NTD (residues 1-68) (brown), ACD (residues 69-150) (blue), CTD (residues 151-175) (green). The position of the conserved IXI motif is indicated. (C) Views of the oligomer with the docked hybrid model of αB-crystallin 24-mer (ribbon representation) superimposed. Ribbon color coding is the same as in (B). Scale bar, 5 nm. (D) Close-up view of the encircled area in C around the 3_c axis (left). The positions of the rod-like structures are illustrated by cylinders. Helices α2 and α3 in the pseudoatomic model (center) and in superimposition with the trasparent density map.
Figure taken from Braun et al. (2011). Data provided by Prof. Sevil Weinkauf and Dr. Nathalie Braun.

Based on the improved resolution, we created a pseudoatomic model of the αB-crystallin 24-mer (Figure 21B) using a hybrid approach of multiple structural methods. To this end, the NMR structure (PDB 2KLR) of human αB-crystallin ACD (residues 69-150) was used (Jehle et al., 2010). Models of both terminal domains were generated by computational structure prediction methods (Figure 22A) The EM envelope and reported interactions

from NMR (Jehle et al., 2010) were the only constraints applied during the docking process (see Braun et al. (2011) for details).

According to the proposed model, the monomeric subunits are present in two distinct conformers (Figure 22B&C): a monomer with a linear arrangement of the terminal domains ("extended monomer"; M_e) and a monomer with an angle of 55° between ACD and NTD ("bent monomer"; M_b).

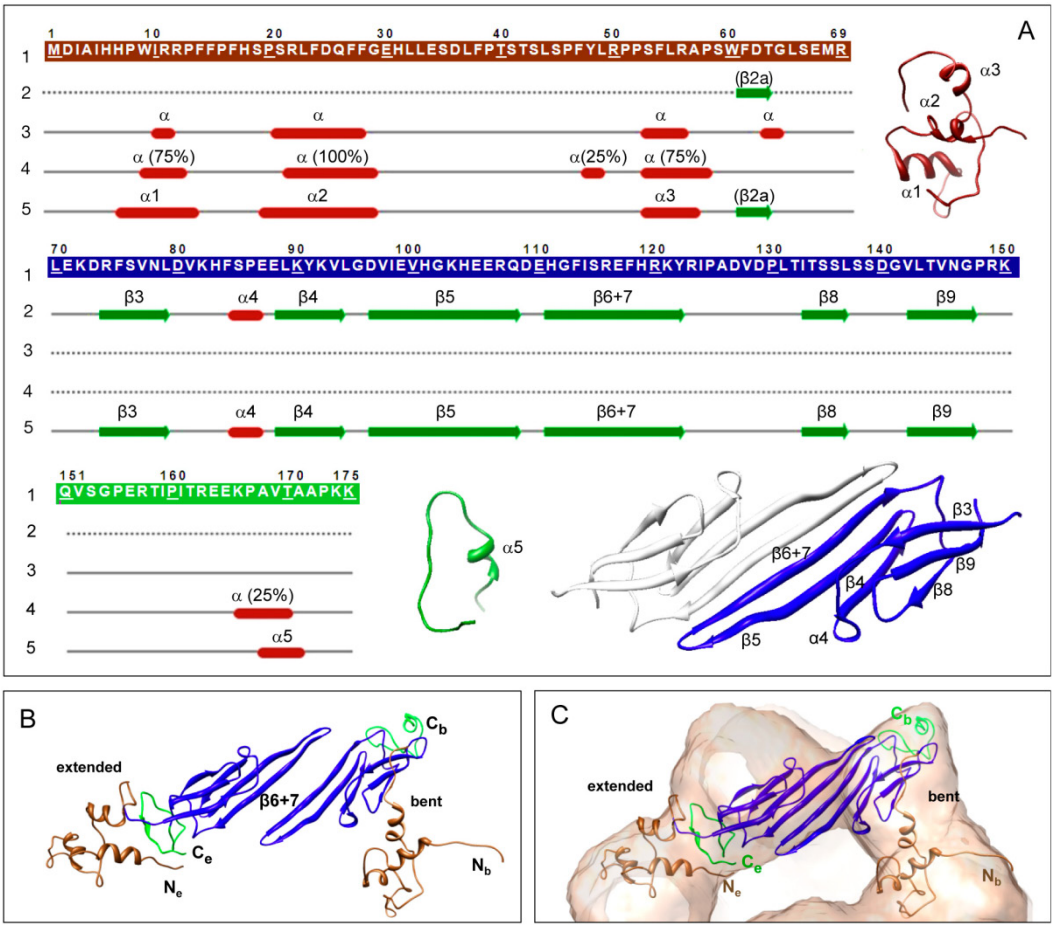

Figure 22 | Secondary structure prediction and structural modeling. (A) First line: Primary sequence of human αB-crystallin (Swiss-Prot ID P02511) consisting of N- (brown), α-crystallin- (blue) and C-terminal (green) domains. Second line: Secondary structure elements observed in the NMR structure of the ACD (PDB 2KLR). Third and fourh lines: Secondary structure elements predicted by the servers I-Tasser and Phyre, respectively. The percentages in the brackets relate to the frequency of prediction by different Phyre programs. α and β denote α-helices and β-strands, respectively. Fifth line: Secondary structure elements included in the pseudoatomic model of human αB-crystallin. 3D models for the N- (brown) and C-terminal (green) domains predicted by I-Tasser and the NMR structure of the dimeric ACD are shown in the color coding of the primary sequence. (B) Ribbon representation of the two monomer types and (C) their localization within the density map.
Figure taken from Braun et al. (2011). Data provided by Prof. Sevil Weinkauf and Dr. Nathalie Braun.

The model also contains two types of dimers with different intersubunit contacts. The dimerization in type I dimers (DI) is mediated by the interaction of the β6+7 strand in antiparallel orientation (Figure 23A). This is the typical dimerization pattern as reported in

the published NMR and X-ray structures of isolated ACDs (see *2.2.2 The α-Crystallin Domain Dimer*). In the type II dimer (DII), the dimer interaction site is formed by antiparallel β4 strands and additional contributions of different domains (Figure 23B). A substantial contribution to the interaction surface is further made by binding of the IXI motifs of both conformers to the hydrophobic groove formed by β4 and β8 as shown by NMR previously (Jehle et al., 2010). The recurring unit within our model is a hexamer comprising both types of monomers, which shapes the EM density around 3_o (Figure 23C).

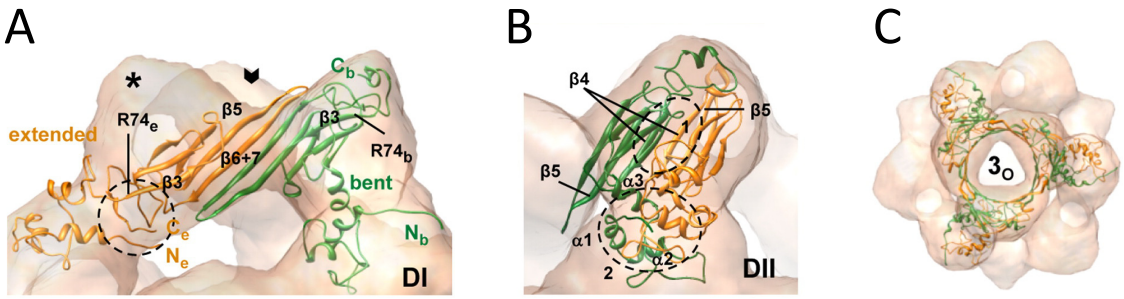

Figure 23 | Dimer conformations and hexameric substructure. (A) Spatial arrangement of extended and bent monomers in type I dimer (DI). A 3-fold axis and one "dome" are indicated by an open arrow and a star, respectively. The encircled area harbors N and C termini of M_e. (B) Spatial arrangement of extended and bent monomers in type II dimer (DII). (C) αB-crystallin hexamer substructure viewed along a 3_o axis. Conformationally different monomers extended and bent are shown in orange and green, respectively.
Figure adapted from Braun et al. (2011). Data provided by Prof. Sevil Weinkauf and Dr. Nathalie Braun.

The NTD (residues 1-69) accounts for 40% of the length of the αB-crystallin primary sequence, but there is only very sparse structural data available for this region. Consequently, a substantial portion of the oligomer has to represent the NTDs. We fitted them into the only "free" space of the EM map, the density at 3_c. Secondary structure prediction revealed the presence of three α-helical segments within the NTD (Figure 22A). Rod-like structures on the surface of the EM map were tentatively assigned to two of these segments (Figure 21D). Supporting evidence for the correct positioning of the NTDs within the EM map stems from cross-linking experiments described in the next section.

4.4.2 Probing Structural Parameters Using Biochemical and Biophysical Methods

The pseudo-atomic model of the αB-crystallin 24-mer was based on both, restraints from experimental data and molecular modeling. Regarding the terminal regions, especially the NTD, data from structural methods are sparse. Therefore, we used additional biochemical and biophysical methods to accompany EM and modeling. Thus, we could corroborate our model in several aspects as outlined in the following.

Fluorescence Quenching

The position within the density map implies a certain surface accessibility of the different regions. In this regard, a striking feature of the 24-mer model is the location of the M_b C terminus (R163-K175) at the tip of the dome-shaped structures around 3_o (Figure 23A). If the proposed model is correct, this region should be fully solvent-exposed. To determine the accessibility of distinct sites, the presence of site-specific probes and a suitable read-out are required. To this end, I introduced the fluorescent dye lucifer yellow site-specifically via thiol-modification in cysteine variants, of αB-crystallin. Cysteines were introduced by mutagenesis at three sites: close to the N terminus (A4C), in the center of the ACD (S115C) and close to the C terminus (A172C). It could be shown that neither the secondary nor the quaternary structure is affected in the cysteine variants using far UV CD spectroscopy and SEC (data not shown).

The accessibility of the attached probe was determined by fluorescence quenching. Lucifer yellow fluorescence was quenched upon stepwise addition of the quencher iodide (Figure 24, left column). Fluorescence data were analyzed on the basis of the Stern-Volmer equation (Equation 5). The resulting Stern-Volmer plots including linear fits are depicted in Figure 24 (right column).

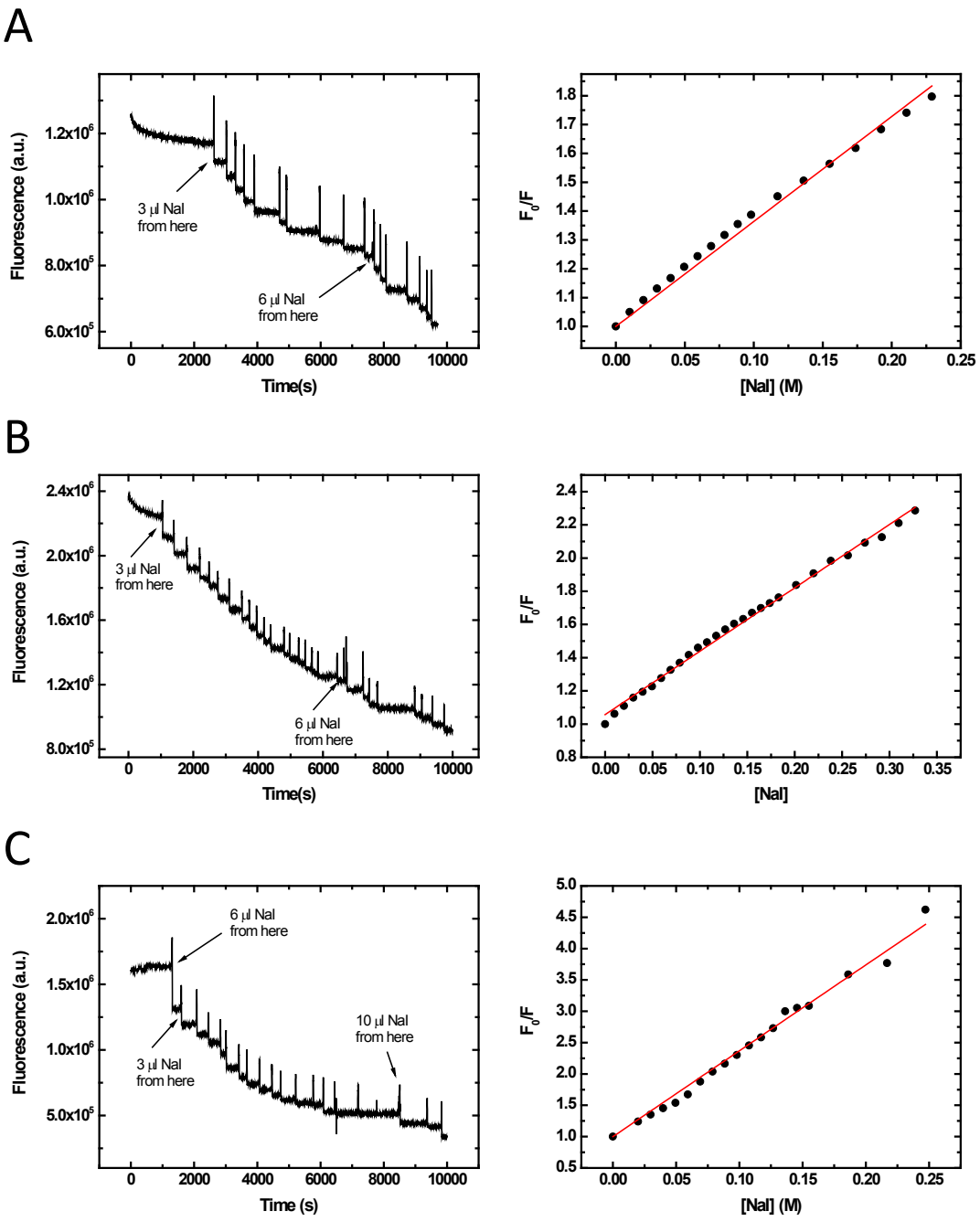

Figure 24 | Quenching of lucifer yellow fluorescence. Fluorescence of lucifer yellow of the cysteine mutants (A) A4C, (B) S115C and (C) A172C was quenched by stepwise addition of a 5 M sodium iodide solution (left panels). The added volumina are indicated in the graphs. The respective Stern-Volmer plots were generated by plotting F_0/F against quencher concentration (right panels). The linear fits are depicted in red.

The determined quenching constants, K_{SV}, are compared in Figure 25. Since values for K_{SV} are given in units of L mol^{-1}, the reciprocal values are the quencher concentration at which 50% of the intensity is quenched ($F_0/F = 2$). According to this, A172C displays the highest quencher accessibility ($K_{SV} = 13.7$ L mol^{-1}). A4C and S115C show much lower accessibility exhibiting quenching constants of 3.6 and 4.3 L mol^{-1}, respectively. Taken

together, the results of site-specific quenching of fluorescence are in agreement with the pseudo-atomic 24-mer model and suggest a contribution of the rather polar and hydrophilic CTD to the overall solubility of the oligomer.

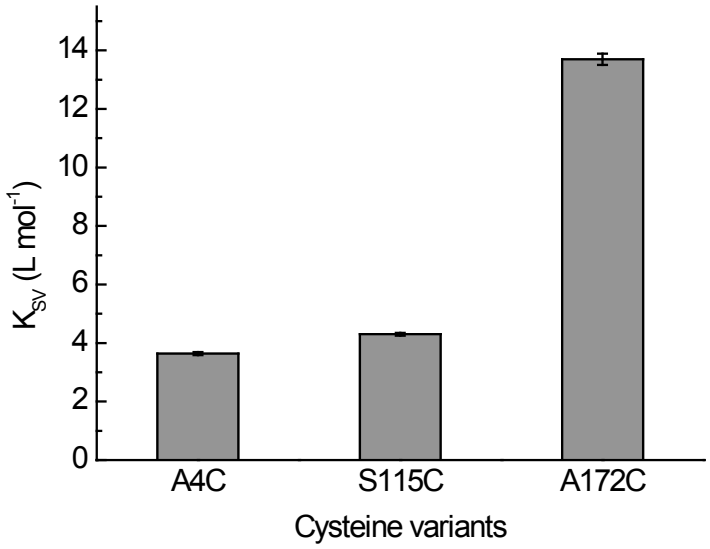

Figure 25 | Fluorescence quenching reveals different surface accessibility of specific sites. The Stern-Volmer constants (K_{SV}) for quenching of lucifer yellow attached at positions 4, 115 and 172 of αB-crystallin indicate the highest surface exposition for the C terminus (K_{SV} = 13.7 L mol^{-1}) in comparison to the N terminus (K_{SV} = 3.6 L mol^{-1}) and a position within the ACD (K_{SV} = 4.2 L mol^{-1}).

Cross-Linking Combined with Mass Spectrometry

Cross-linking in combination with mass spectrometry and bioinformatics is a versatile technology to map interactions in multi-protein complexes and thus a useful tool in integrated structural biology (Rappsilber, 2011). Here, the method was used to validate inter- and intramolecular contacts within the αB-crystallin oligomer.

First, the feasibility of cross-linking was tested using the cleavable, amine-reactive cross-linker 3,3´-dithiobis(sulfosuccinimidylpropionate) (DTSSP). SDS-PAGE analysis showed similar cross-linking patterns ranging from monomer and dimer bands to very large multi-subunit cross-links. The result was independent of the reaction time and could be reversed by TCEP-induced cleavage of the linker (Figure 26).

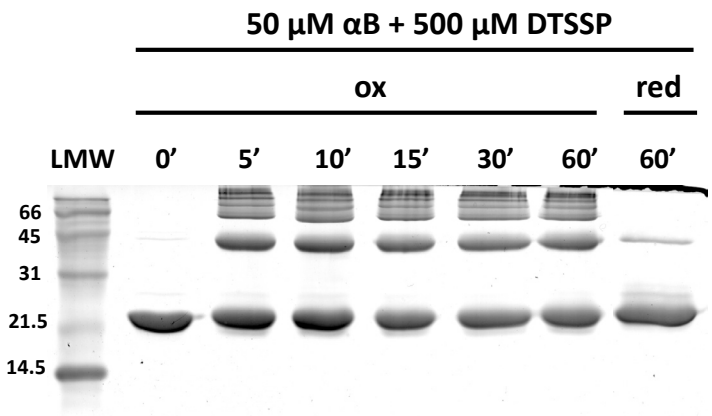

Figure 26 | SDS-PAGE of cross-linking with DTSSP. 50 µM αB-crystallin were cross-linked by a 10-fold molar excess of DTSSP. The reaction was quenched by addition of Tris at different times and analyzed by SDS-PAGE under non-reducing (ox) conditions. Under reducing conditions (red), the cross-linker was almost completely cleaved.

For the combined cross-linking/MS analysis, bis(sulfosuccinimidyl)suberate (BS^3), the non-cleavable analog of DTSSP was used. It should be noted that BS^3 mainly targets primary amines but also possesses reactivity towards hydroxyl groups of serine and threonine residues. The cross-linking reaction, as judged from SDS-PAGE, worked equally well (Figure 27). Monomer, dimer and high molecular weight (HMW) fraction bands were excised and separately prepared for MS analysis. Thus, intramolecular cross-links can be identified from the monomer band. The dimer band ensures the presence of (presumably preferred) intermolecular cross-links while cross-linking of multiple subunits can be excluded. The HMW fraction exhibits a relatively high amount of cross-linked peptides and most of intermolecular contact sides were derived from the HMW data set.

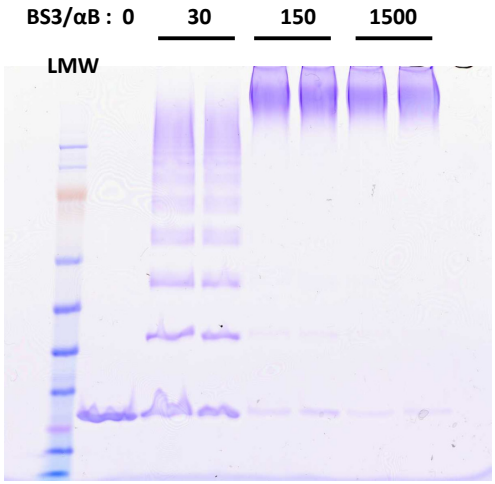

Figure 27 | SDS-PAGE of cross-linking with BS^3. αB-crystallin (9.2 µg) was cross-linked using BS^3 with a protein-to-cross-linker molar ratio of 1:30, 1:150 and 1:1500 at room temperature. Bands corresponding to monomer, dimer to pentamer and high-molecular-mass cross-linking products were pooled for MS analysis.

According to our model, the hexameric substructures are associated via N-terminal interactions at the 3_c area. MS revealed intermolecular linkage of N-terminal methionines (Met1) (Figure 28). The distance in our model is 9.9 Å, which is below spacer length of the linker (11.4 Å) plus length of the methionine side chain. This result supports the structure prediction and positioning of the NTDs in the model.

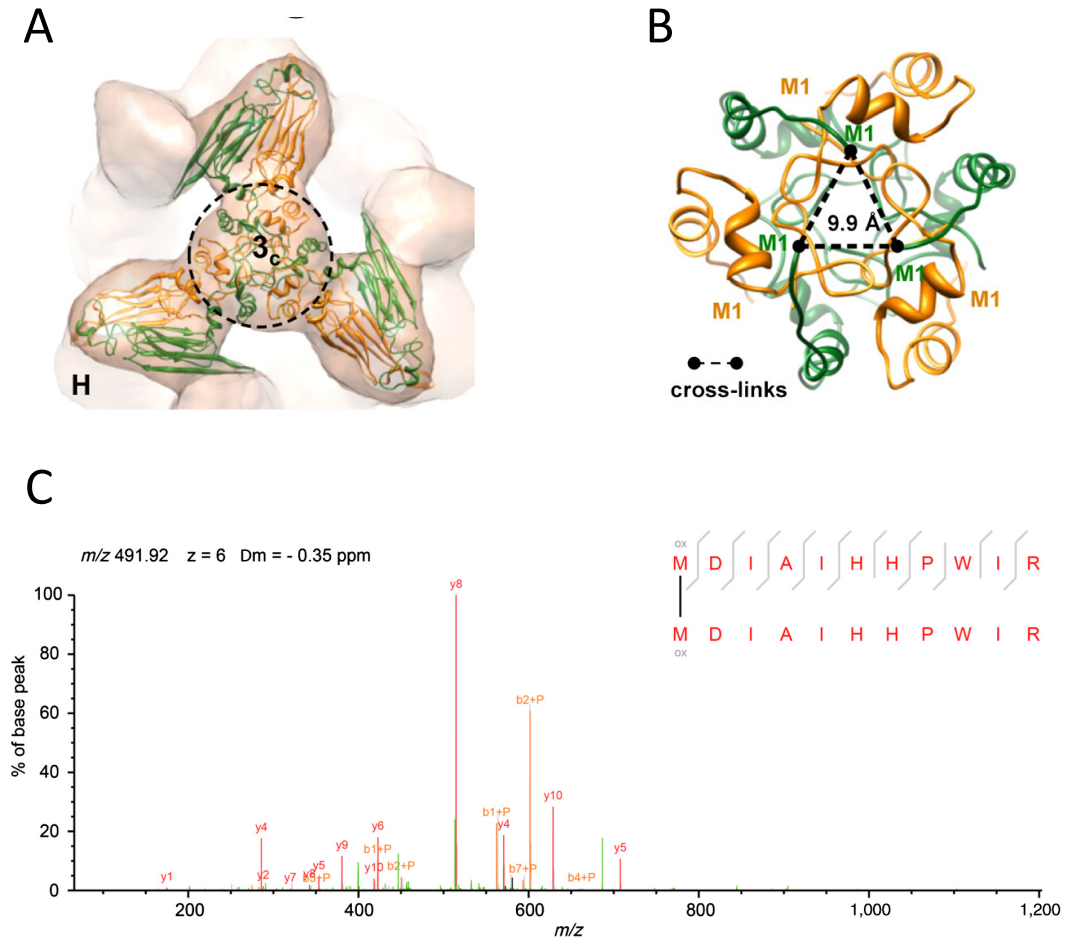

Figure 28 | Proximity of NTDs revealed by cross-linking combined with MS. (A) Hexamer assembly site at the area 3_c. The encircled area indicates the area enlarged in B. (B) Intermolecular cross-links between the N termini of bent monomers at the same area. (C) MS fragmentation spectrum of a cross-linked peptide that includes a link between two αB-crystallin N -termini, M1 and M1.
Figure taken from Braun et al. (2011). EM data provided by Prof. Sevil Weinkauf and Dr. Nathalie Braun, MS data provided by Prof. Juri Rappsilber.

We could identify numerous additional interaction sites, which were all below the total length of the linker arm and lysine side chain (27.4 Å). The sites are illustrated in an interaction map (Figure 29). Unfortunately, the NTD entirely lacks Lys residues. Thus, the N-terminal Met1 is the only primary amine within the NTD. In addition, in many cases cross-links had both intra- and intermolecular counterparts within the pseudo-atomic model

below the upper limit of about 27 Å. Nevertheless, some of the interaction sites could be unambiguously assigned to either of both options and not a single cross-link had a potential correspondent within the model. The only aspects, which cannot be taken into account, are the heterogeneity of the αB-crystallin ensemble and the plasticity of dynamic regions. Especially the NTD is dynamic and might adopt alternative conformations in different assemblies. Obviously, further structural investigations are needed to fully understand the role of the NTD of αB-crystallin in oligomerization and thus in the molecular chaperone function.

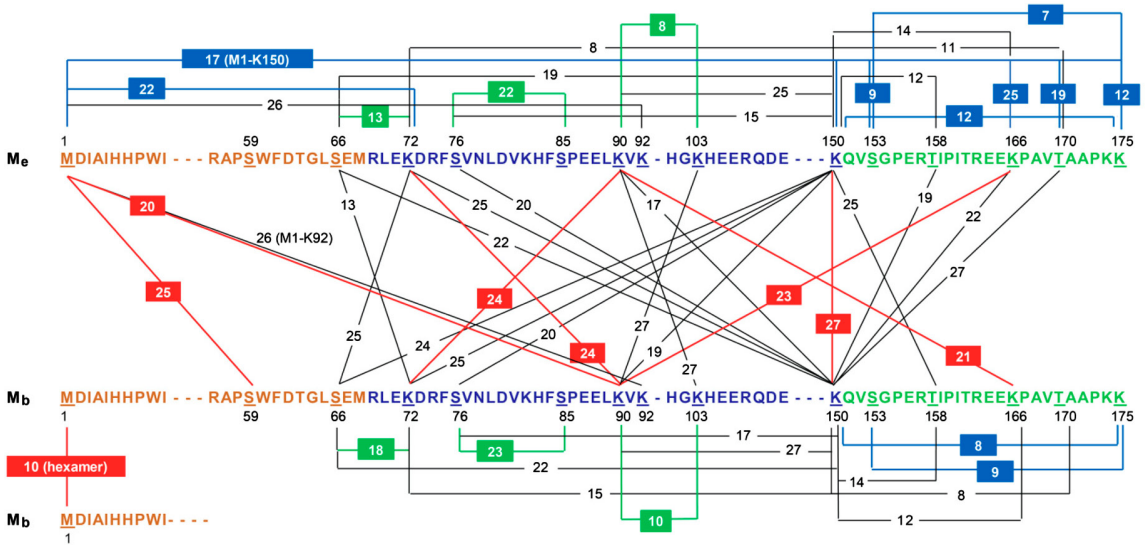

Figure 29 | Map of cross-linking interaction sites. The map illustrates all identified linkage sites within and between αB-crystallin conformers (M_e and M_b). Cross-linked residues are connected by solid lines including the distances derived from the pseudoatomic model of the αB-crystallin 24-mer. Cross-links that are unambiguously assigned to an intra- or intermolecular residue pair in the pseudoatomic model are shown in blue and red, respectively. Green lines indicate intramolecular cross-links within the ACD.
Figure taken from Braun et al. (2011). Data provided by Prof. Sevil Weinkauf and Prof. Juri Rappsilber.

4.4.3 Studying αB-Crystallin Heterogeneity and the Dynamic Oligomer Equilibrium

The dynamic oligomer equilibrium of αB-crystallin causes a heterogeneous ensemble of multiple different oligomeric assemblies. This heterogeneity has prevented structural elucidation at high resolution and even methods that offer intermediate to low resolution are strongly impaired. A sophisticated image processing procedure with stringent data separation was required to yield the 24-mer model at 9.4 Å resolution. However, only one third of the complete data set is represented by this model. Thus, the question arises which assembly forms the remaining two thirds adopt. The presence of subunit exchange implies a dynamic oligomer equilibrium of interconverting oligomeric species. Therefore, distinct intermolecular contacts within oligomers have to disintegrate and reassociate in the course

of this process. The oligomer dynamics further require the presence of exchanging subunits. Using our hybrid approach we tackled these open questions.

The 3D reconstruction process revealed varying levels of mass at the 3_c areas. Models without imposed symmetry yielded variances in the hexamer assembly sites (Figure 30). This result suggests preferential detachment at these sites and the presence of hexamers as intermediate assemblies. However, a distinct population of hexameric species could not be detected by SEC or AUC (Figure 15 and Figure 16).

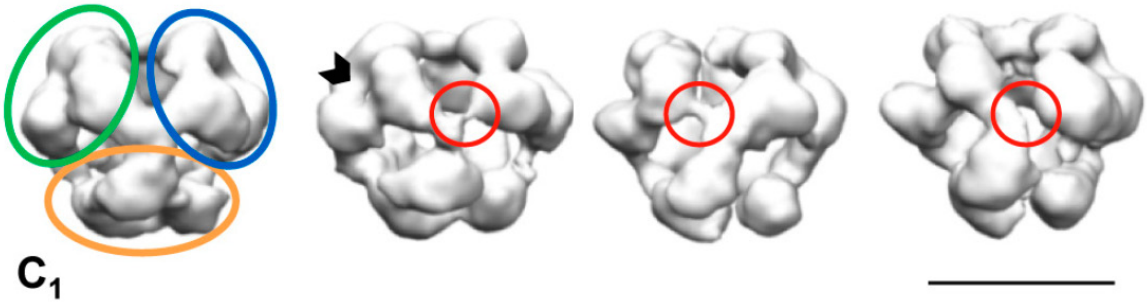

Figure 30 | Heterogeneity within the EM data. Randomly reconstructed 3D models without imposing symmetry. Hexameric "building blocks" are highlighted by large circles. Areas of large structural variations are marked by small, red circles. Scale bar: 10 nm. Figure adapted from Braun et al. (2011).
Data provided by Prof. Sevil Weinkauf and Dr. Nathalie Braun.

To test the hypothesis that the various intermolecular interaction sites contribute to different extents to oligomerization determining the oligomer equilibrium, SV-AUC analysis in the presence of destabilizing concentrations of guanidinium chloride (GdnCl) was performed. As expected, αB-crystallin oligomers were shifted to smaller size with increasing amounts of the denaturant. Interestingly, the dissociation proceeded via several steps and showed the existence of stable, small intermediate species (Figure 31). Low concentrations of GdnCl already have an effect on oligomeric size. At 0.25 M GdnCl the s-value distribution gets narrower and is shifted to smaller sizes. With higher denaturant concentrations additional peaks appear. At 1 M GdnCl, the s-value distribution showed four rather narrow peaks, which we assigned to dimers, hexamers, 12-mers and 18-mers of αB-crystallin, while only monomeric αB-crystallin was present above 1.25 M GdnCl. It should be noted that the assignment is most accurate for small species. Monomeric and dimeric αB-crystallin can be identified unambiguously 6-mers and 12-mers still with some certainty, but all peaks assigned to higher assembly forms represent very likely a mixture of multiple oligomeric species. Nevertheless, these results indicate different stabilities for the distinct oligomerization sites. These species are presumably also present at low

abundance under native conditions suggesting exchanging units larger than monomers. However, isolated hexamers appear to be a rather rare species and were only detected at one condition with low abundance. Still, they can function as important building block in constructing defined oligomer assemblies. The same is true, and probably even more surprising, in the case of dimers. Despite the ACD functioning as a stable dimerization domain, none of the experimental conditions yielded isolated dimers. This observation indicates the importance of the terminal domains in αB-crystallin oligomerization.

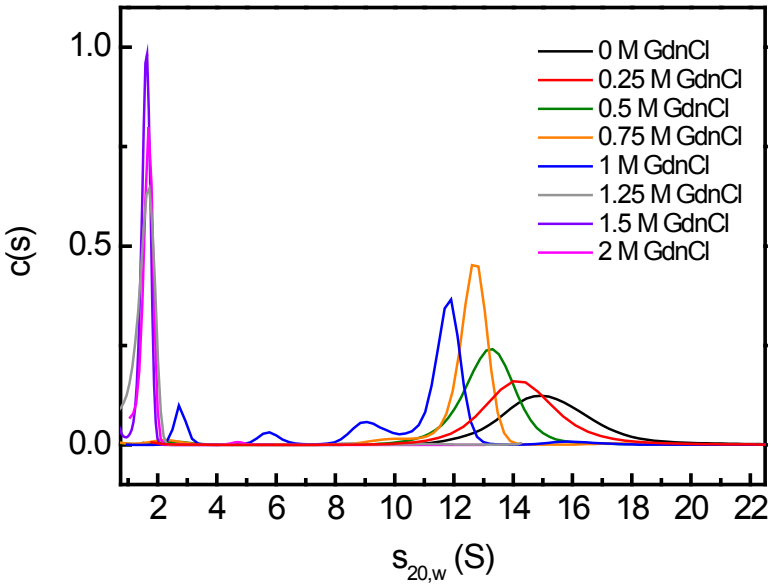

Figure 31 | Monitoring GdnCl-induced dissociation by SV-AUC. The c(s) distributions were determined for SV experiments in the presence of varying GdnCl concentrations. All calculated distributions were corrected for viscosity and density of the respective denaturant concentration. The color code is given in the legend.

To separate the single particle data set further, we constructed models from hexameric units as building blocks (n × 6-mers). These hypothetical models were used as references to separate the data in three subsets: particles (1) smaller (2) larger or (3) comparable in size with the 24-mer. We could identify 12-mers in subset (1) and 36- and 48-mers in subset (2). Due to an additional density in the 18-mer reconstruction, which we assigned to a dimer, we expanded the number of models first to multiples of hexamers plus dimers bridging two 3c areas and finally also 24-mers lacking dimers and monomers. Using all these models as initial references enabled us to assign 80% of the entire cryo-EM data set to distinct oligomeric species and to obtain the respective 3D reconstructions (Figure 32).

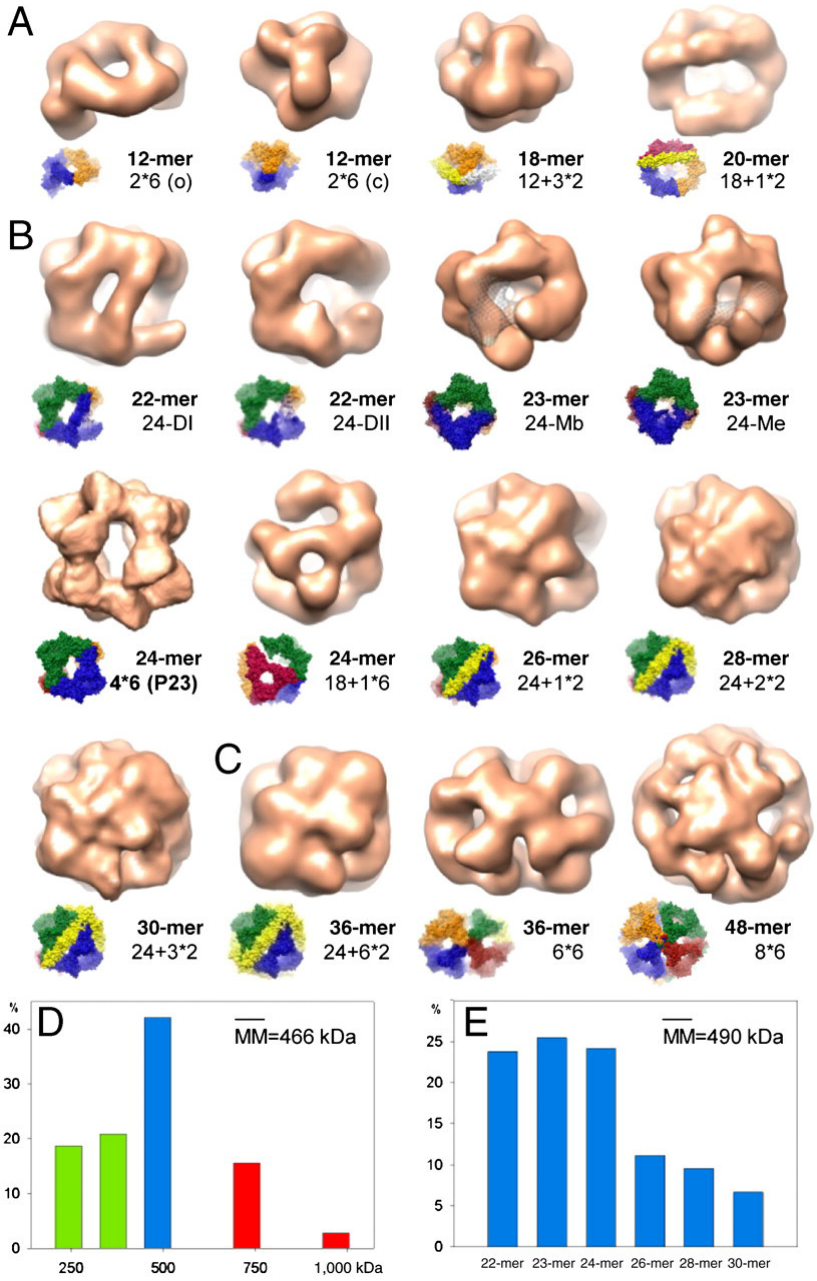

Figure 32 | Different 3D reconstructions of αB-crystallin oligomers and their distribution. Oligomers found in the "small" data set (A), in the "24-mer" data set (B) and in the "large" data set (C). The missing volume of the monomer in the 23-mers in (B) is highlighted in mesh representation. Scale bar: 10 nm. (D) Distribution of the oligomer masses to data sets "small", "24mer" and "large". Particles with molecular masses corresponding to 12-, 18- and 20-mers are included in green bars, to the 24mer in the blue bar, to 36- and 48mers in red bars. (E) Distribution of oligomers within the supposed 24-mer population (blue bar in D).
Figure taken from Braun et al. (2011). Data provided by Prof. Sevil Weinkauf and Dr. Nathalie Braun.

Our results revealed that most species contain even numbers of subunits, which is in agreement with MS studies (Aquilina et al., 2003; Benesch et al., 2008). Interestingly, the molecular architecture, which we found in the 24-mer, is also present in the other αB-crystallin oligomers. The oligomer distribution using the initial three subsets also

indicates 24-mers as the dominant species (Figure 32D) However, our detailed analysis showed that additional assemblies close to the 24-mer (e.g. 22-, 23- and 26-mers) are also represented by this fraction (Figure 32E).

4.5 The Molecular Chaperone Activity of α-Crystallins

In 1992, Joseph Horwitz showed that α-crystallin can function as molecular chaperone. He subjected various enzymes and β-crystallin to heat stress and observed an aggregation-suppressing effect in the presence of αL-crystallin (Horwitz, 1992). Since then, the chaperone function of α-crystallins was investigated in numerous studies. Today, it is the general perception that α-crystallins, and sHsps in general, possess an ATP-independent holdase activity. Nevertheless, it is still not known how non-native substrate proteins are recognized (Basha et al., 2012).

4.5.1 Binding of the Model Substrate Lysozyme

To study the chaperone activity of α-crystallins, lysozyme from chicken egg white was used as model substrate. Although lysozyme is not a potential physiological substrate, it is suited as a model substrate for *in vitro* experiments. Lysozyme is a small protein of 14.3 kDa mass and has eight cysteine residues, which are all involved in disulfide bridges, rendering lysozyme a very stable protein. However, reduction of its four disulfide bonds destabilizes the protein dramatically resulting in its aggregation (Goldberg et al., 1991). Thus, the induction of aggregation can be triggered precisely upon addition of reducing agents like DTT or TCEP. Since α-crystallins do not form S-S bonds, they are not affected by reducing agents. Reduced lysozyme aggregates at temperatures above 30°C allowing to study substrate binding by α-crystallins at physiological temperature. In the scope of this thesis, lysozyme was not only used as a model substrate in light-scattering assays but also to establish further methods for studying the interaction of α-crystallins with substrates.

The functional properties of the different α-crystallins were compared in lysozyme aggregation assays. In the presence of equimolar concentrations (referred to monomer concentration throuout this thesis) of either recombinant α-crystallin species, the aggregation signal was reduced by approximately half, and when a 2-fold molar excess over lysozyme was used, the signal was entirely suppressed (Figure 33A&B). Analysis of the supernatant and pellet fractions of the samples by SDS-PAGE confirmed this picture

(Figure 33E). Also, αAB-crystallin (Figure 33C&E) and authentic αL-crystallin (Figure 33D&E) suppressed lysozyme aggregation in a concentration-dependent manner with efficacies similar to those observed for the isolated recombinant isoforms.

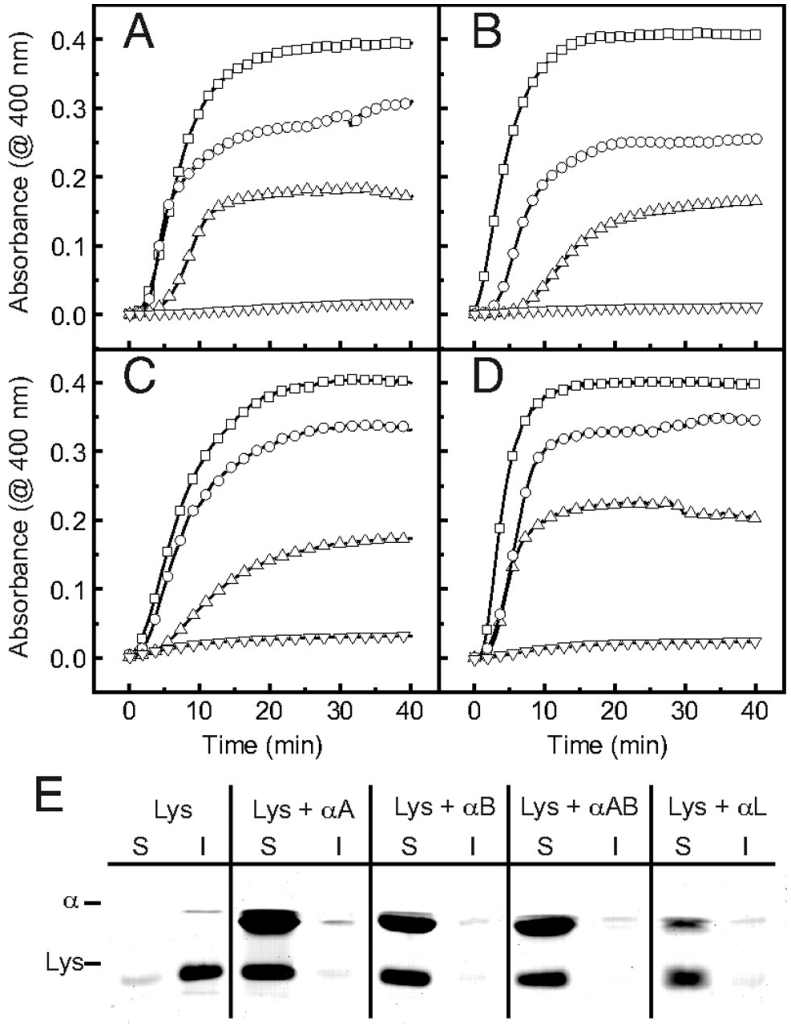

Figure 33 | Suppression of lysozyme aggregation by α-crystallins. The chaperone function of α-crystallin was assessed at 37°C by its ability to suppress the aggregation of 10 µM lysozyme. Lysozyme aggregation was monitored at 400 nm in a UV/VIS spectrophotometer in the absence (squares) and presence of 5 µM (circles), 10 µM (triangles) and 20 µM (reverse triangle) α-crystallin. (A) αA-crystallin, (B) αB-crystallin, (C) αAB-crystallin (equimolar mixture of recombinant αA- and αB-crystallin) and (D) authentic αL-crystallin. (E) The solubility of denatured lysozyme (Lys) in the absence and presence of a 2-fold molar excess of respective α-crystallin (α) was analyzed by comparing the soluble supernatant fraction (S) and the insoluble sediment fraction (I) using SDS-PAGE.
Figure taken from Peschek et al. (2009).

As the ability to suppress lysozyme aggregation was comparable for all forms, all further efforts were focused on studying the chaperone function of αB-crystallin. Due to its ubiquitous expression and its link to several human diseases, it is also of more general interest than αA-crystallin, which only plays a role in the eye lens. Certainly, the accumulated knowledge on the molecular architecture of αB-crystallin including the

aforementioned pseudoatomic model renders it an interesting model to study the chaperone function of metazoan sHsps and the underlying structure-function relationship (see *4.6 The Structure-Function Relationship of αB-Crystallin*).

αB-crystallin was shown to completely suppresses the formation of light-scattering aggregates of lysozyme when present before induction of aggregation by reduction. When lysozyme was first reduced and αB added at different times during the aggregation process, an immediate arrest in the signal increase was observed (Figure 34). Thus, αB-crystallin does not only sequester monomeric non-native lysozyme but also inhibits the growth of preformed lysozyme aggregates. This result indicates that upregulation of αB-crystallin expression as a cellular response to stress may also be beneficial when protein aggregation has already commenced.

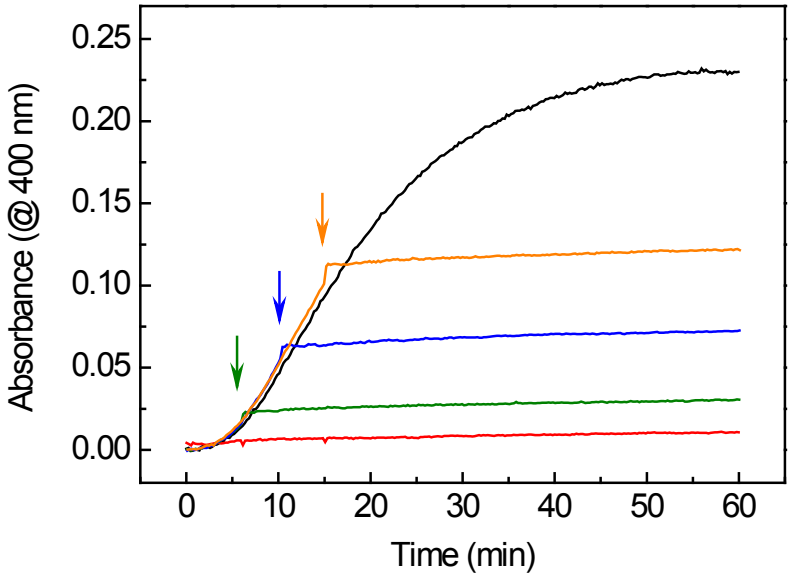

Figure 34 | Interrupted lysozyme aggregation assay. The TCEP reduction-induced aggregation of 5 µM lysozyme was monitored by absorbance at 400 nm (black). 20 µM αB-crystallin suppressed the light-scattering signal completely if present prior to addition of TCEP. The formation of further light-scattering aggregates was immediately inhibited by addition of 20 µM αB 5 min (green), 10 min (blue) and 15 min (orange) after induction of aggregation. The addition of αB is indicated by arrows using the same color code.

4.5.2 Formation of αB-Crystallin-Substrate Complexes

Binding of non-native proteins leads to the formation of stable αB-substrate complexes. No aggregation of reduced lysozyme was detected in the presence of αB-crystallin monitoring light-scattering over several weeks (not shown). That demonstrates the stability of αB-lysozyme complexes.

The conventional light-scattering assay is a rather simple and practical method to study aggregation suppression but it does not allow to monitor binding or complex formation. Therefore, I used DLS to follow the change in hydrodynamic radius (R_h) over time after addition of TCEP. In the presence of a 20-fold excess of αB-crystallin over lysozyme, R_h-values shifted from 7.5 nm to 9.25 nm (Figure 35). The R_h increased directly after addition of TCEP and reached a stable plateau after ~20 min. Shifting the ratio of both proteins to a 15-fold or 10-fold excess of αB-crystallin yielded final R_h-values of 15.5 nm or 19 nm, respectively. This massive increase in the hydrodynamic radius indicates the formation of complexes that consist of more than a single αB-crystallin oligomer. It should be noted that in light-scattering chaperone assays a two-fold excess of αB-crystallin was sufficient to suppress the signal increase completely.

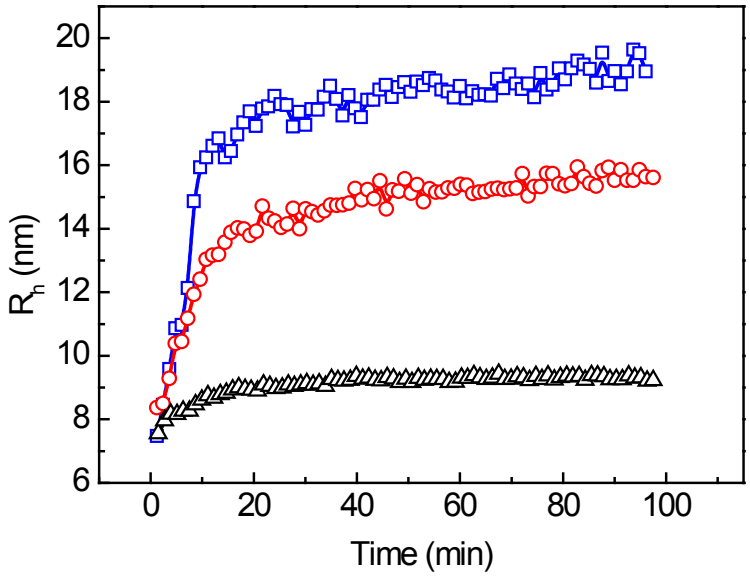

Figure 35 | Monitoring complex formation by DLS. An excess of αB-crystallin (25 µM) was mixed with lysozyme in molar ratios of 20:1 (black triangles), 15:1 (red circles) and 10:1 (blue squares). After addition of TCEP, the hydrodynamic radius (R_h) was monitored using DLS. The increasing R_h-values indicate the formation of αB-lysozyme-complexes. Depending on the molar ratio, the radius of the final complexes ranges from 9.5 to 19 nm.

SV-AUC experiments were carried out to determine the hydrodynamic properties of different ratios of αB-crystallin to lysozyme. The various concentration-radius distribution plots are depicted in Figure 36. Native lysozyme is not completely sedimented at 42,000 rpm, whereas samples with 4:1 and 2:1 ratios of αB-crystallin to lysozyme contain very large complexes, which do not show a sedimentation plateau.

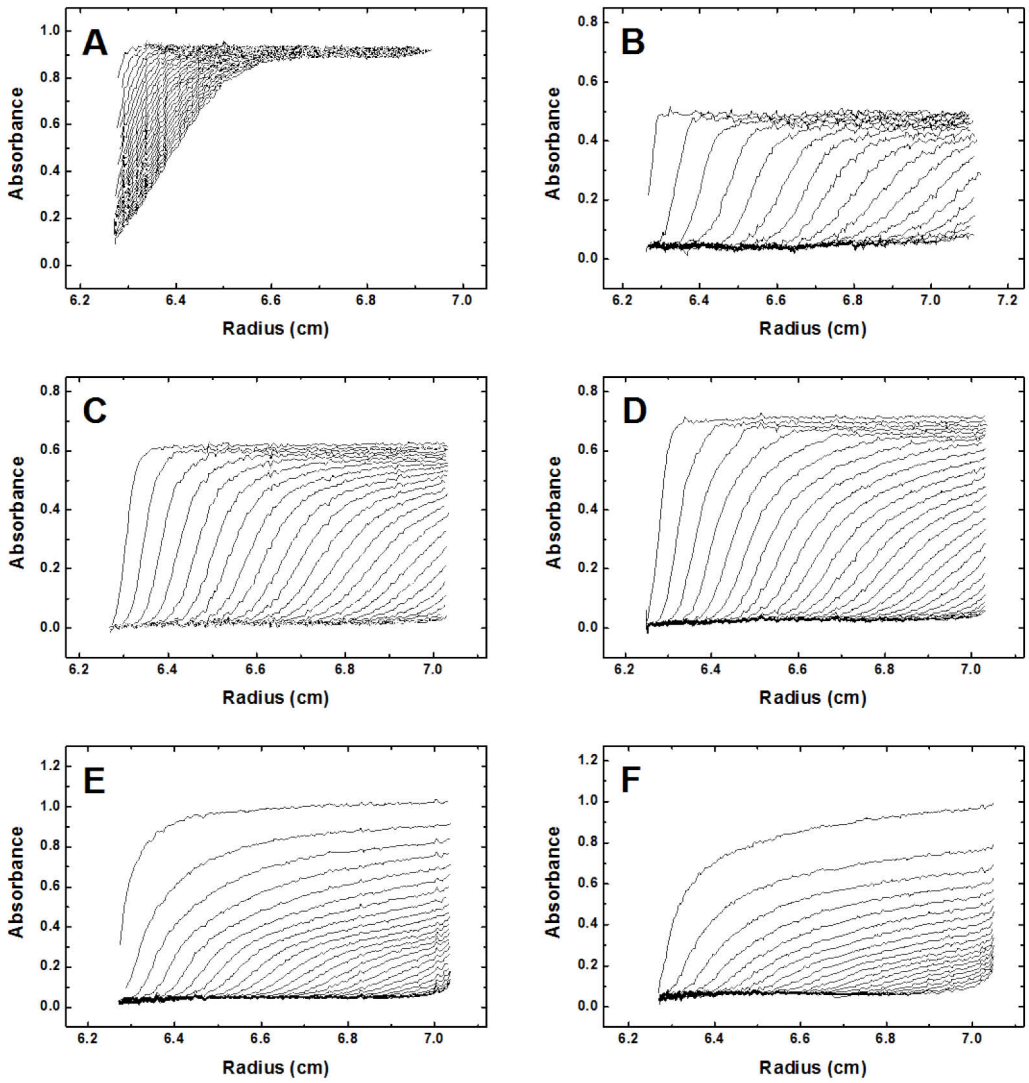

Figure 36 | Sedimentation velocity experiments of αB-crystallin-lysozyme complexes. The radial concentration distributions were recorded at 20 °C. Sedimentation was carried out at 42000 rpm in PBS buffer with 1.5 mM TCEP. (A) lysozyme (without TCEP); (B) αB-crystallin; (C): αB:lysozyme = 16:1; (D) αB:lysozyme = 8:1; (E) αB:lysozyme = 4:1; (F) αB:lysozyme = 2:1.

The apparent sedimentation coefficients show, similar to the DLS results, a strong increase in s-value depending on the amount of lysozyme present (Table 2). However, the apparent s-values increase in a disproportional way in comparison to the expected values for stochastic binding of denaturing lysozyme. Again, aggregation assays did not show any change in absorbance signal within the studied range.

Table 2 | Hydrodynamic properties of αB-crystallin and its complexes with lysozyme as determined by SV-AUC experiments.

Sample	Sed. coefficient (S)	Average mass by SV-AUC experiments (kDa)	Theoretical mass by molar ratio (kDa)
Lysozyme	1.71	16.4	14.3
αB-Crystallin	16.7	490	484
αB:Lys = 16:1	18.0	627	505
αB:Lys = 8:1	20.8	773	527
αB:Lys = 4:1	56.9	2585	570
αB:Lys = 2:1	89.5	5147	656

To prove the aforementioned hypothesis, the morphology of individual αB-lysozyme complexes was studied in dependence on the ratio of both proteins using negative staining and EM (Figure 37). Up to a ratio of about 20:1 excess of αB-crystallin single oligomers bound reduced, non-native lysozyme indicated by an increase in particle size. When higher relative amounts of lysozyme were used, αB-crystallin oligomers began to form large agglomerates, which is in very good agreement with the results from the DLS and SV-AUC analysis. While a 20:1 ratio (αB:lysozyme) showed only a small increase in hydrodynamic radius, R_h values doubled in the case of a 15:1 ratio and almost tripled for 10:1 (Figure 35). A similar picture emerged from sedimentation analysis of αB-lysozyme complexes (Table 2). Thus, EM provided evidence for the hypothesized two binding modes, which are reflected by an initial formation of single-oligomer substrate complexes followed by large multi-oligomer clusters.

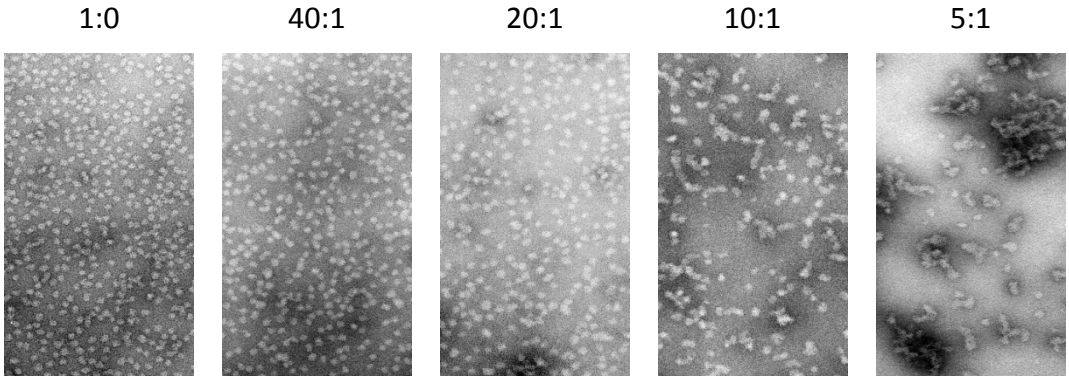

Figure 37 | Morphology of substrate complexes. αB-crystallin was mixed with increasing amounts of lysozyme and incubated under reducing conditions (0.5 mM TCEP) at 37°C for 1 h. The samples were then analyzed by EM after negative-staining with ammonium molybdate. The ratio of αB:lysozyme is given above the respective EM images.

4.5.3 Probing Substrate Binding by Limited Proteolysis

Limited proteolysis is a powerful tool for probing the higher order structure of proteins, as it provides information on the surface accessibility of target residues (Hubbard, 1998). If peptide bonds are readily cleaved in the absence of a substrate, yet exhibit restricted cleavage in the presence of substrate, it implies that these amino acids are involved in the interaction with the client protein. This effect may be a direct result as part of a substrate-binding site interaction or indirect conformational changes upon binding, which diminish the accessibility for the protease. Basically, limited proteolysis can provide a picture of the regions affected by substrate interaction.

SDS-PAGE-based analysis revealed different cleavage patterns in dependence of the binding state (Figure 38). As shown above, in the presence of a reducing agent, lysozyme is aggregation-prone and bound by αB-crystallin. αB-crystallin is cleaved very slowly under these conditions. Under non-reducing conditions a second, slightly smaller band emerges in the course of time. Based on these results, substrate binding protects αB-crystallin from cleavage by α-chymotrypsin.

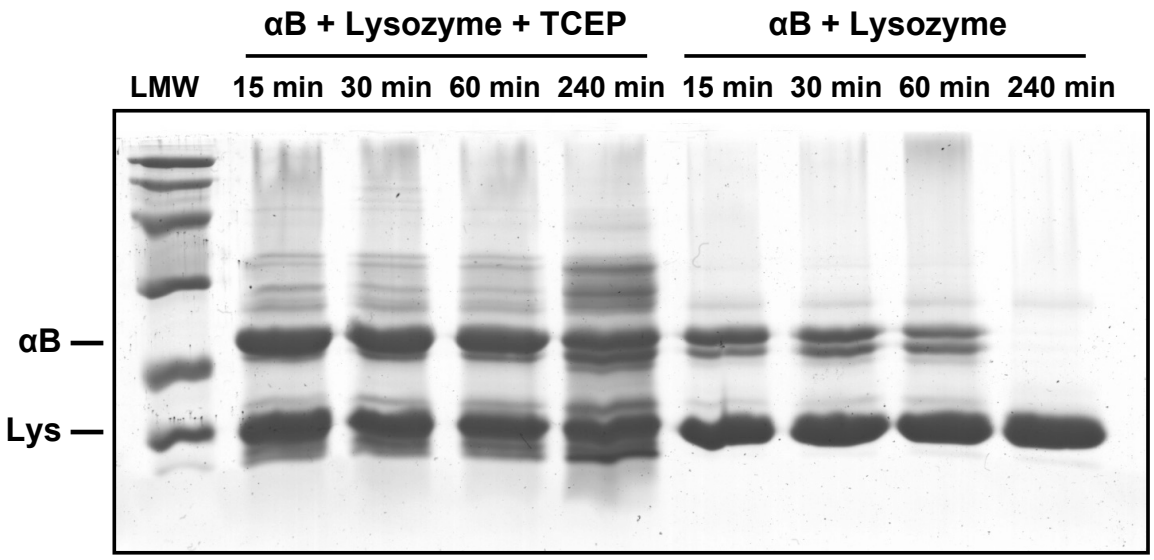

Figure 38 | Limited proteolysis of αB-lysozyme complexes. The binding of reduced lysozyme to αB-crystallin was probed by limited proteolysis using chymotrypsin as protease. αB-crystallin and lysozyme were mixed in a 1:3 ratio (w:w) in the absence (right lains) and in the presence of 1.5 mM TCEP. Digestion of the substrate complexes was initiated by addition of 1:15 (w:w) ratio of α-chymotrypsin to αB-crystallin and 10 mM $CaCl_2$ and cleavage was carried out at 10°C. SDS-PAGE analysis revealed a protection of αB from proteolytical cleavage upon lysozyme binding.

LC-ESI-MS identified the major proteolytic product as residues 10-175. In addition, a peptide with a monoisotopic mass of 1119.5 Da corresponding to the peptide αB(1-9) was

found in the non-complexed sample. In the presence of TCEP, the peptide is only detectable after digestion over night. In contrast, the corresponding mass peak is already present after 15 min when lysozyme is not bound.

In summary, αB-crystallin is protected against proteolysis by α-chymotrypsin upon substrate binding. MS analysis showed that the cleavage site at the C-terminal peptide bond of Trp9 is protected against protease cleavage upon substrate binding indicating an involvement of the NTD in substrate binding. However, due to the biased distribution of cleavage sites, which are predominantly present within the NTD and lack completely in the CTD (Figure 39), the role of the C-terminal extension cannot be probed by proteolysis using chymotrypsin.

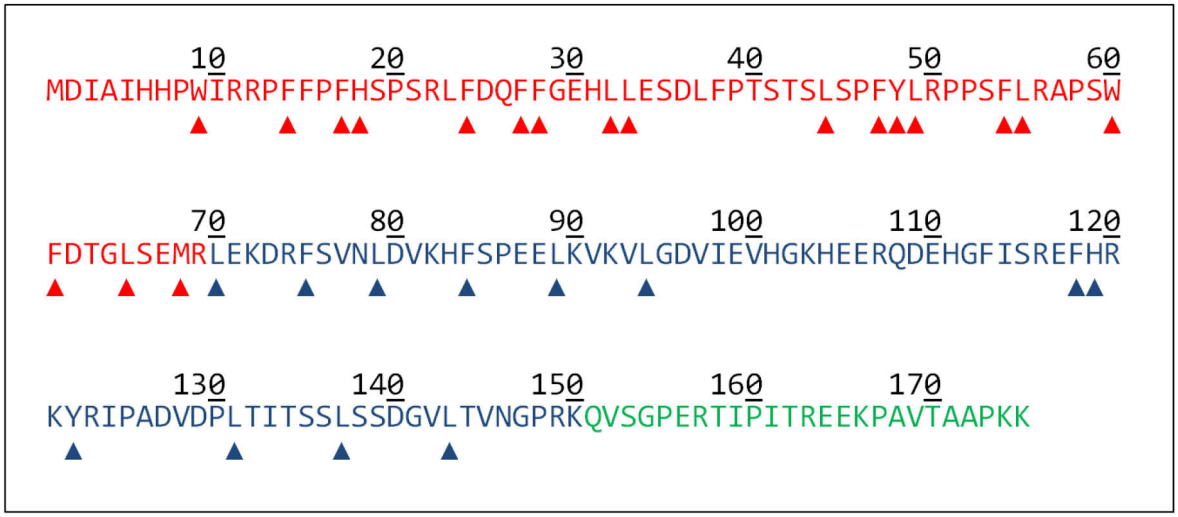

Figure 39 | Predicted chymotryptic cleavage sites within αB-crystallin. The theoretical chymotryptic cleavage sites were predicted using the web-based ExPASy PeptideCutter tool (http://web.expasy.org/peptide_cutter/) with the sophisticated algorithm for chymotrypsin set to a lowest probability limit of 25% (Keil, 1987). The 31 sites are marked by a triangle pointing to the residue, after which cleavage occurs. The NTD is depicted in red letters, ACD in blue and CTD in green.

4.5.4 Monitoring Substrate Binding by FRET

In the previous section, I have discussed some of the advantages and drawbacks of different methods in monitoring substrate binding and complex formation. In order to study the kinetics of αB-crystallin-substrate interactions, including early events in the course of binding, a FRET-based *in vitro* assay was developed that allows monitoring this process.

The initial goal was to attach a pair of fluorescent labels suited for FRET to both αB-crystallin and a substrate protein. The donor dye has to be used for the labeling of αB to prevent a decrease of donor fluorescence due to aggregation, which might occur in the

case of a donor-labeled substrate protein. Ideally, the donor fluorescence should only decrease due to energy transfer to the acceptor-labeled substrate. The principle of such a FRET-based assay is illustrated in Figure 40.

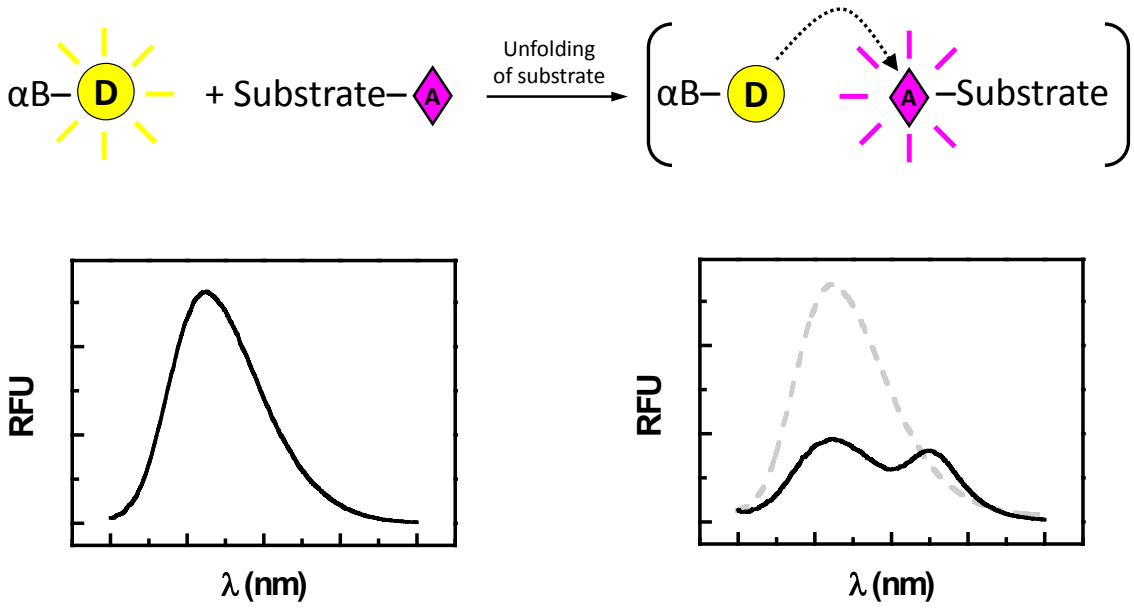

Figure 40 | FRET-based *in vitro* assay to study substrate binding. The cartoon illustrates the principle of the FRET-based substrate binding assay. Donor-labeled αB is mixed with acceptor-labeled substrate. Under non-stress conditions, no FRET signal can be observed. The formation of αB-substrate complexes is induced by a shift to conditions that promote substrate unfolding. Binding results in a decrease in donor fluorescence and a concomitant increase in acceptor fluorescence.

Development of a FRET-Based Binding Assay

I selected thiol-reactive lucifer yellow iodoacetamide (LYI) as the donor dye and the amine-reactive 5(6)-carboxytetramethylrhodamine succinimidyl ester (TAMRA) as acceptor dye. LYI was site-specifically coupled to αB-S59C (αB-LYI) and lysozyme was unspecifically labeled with TAMRA (lysozyme-TAMRA). First, I tested the functionality using a light-scattering aggregation assay. The result was very similar to aggregation assays with unlabeled proteins indicating the general suitability. A twofold excess of αB-LYI was sufficient to suppress the TCEP-induced aggregation of lysozyme-TAMRA (Figure 41).

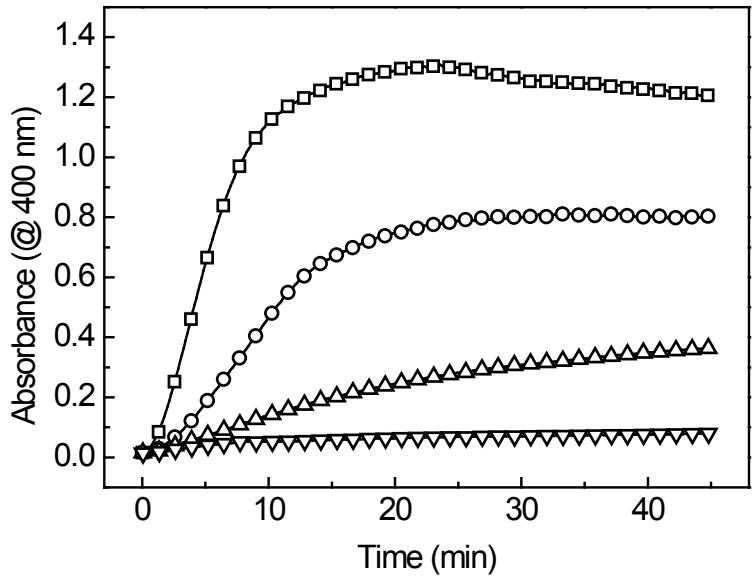

Figure 41 | Aggregation assay with labeled proteins. The chaperone function of αB-LYI was assessed at 37°C by its ability to suppress the aggregation of 10 µM lysozyme-TAMRA. Lysozyme aggregation was monitored at 400 nm in a UV/VIS spectrophotometer in the absence (squares) and presence of 5 µM (circles), 10 µM (triangles) and 20 µM (reverse triangle) αB-LYI.

In the next step, three titration experiments were performed. Under reducing conditions, unlabeled lysozyme was added in stepwise manner to αB-LYI (Figure 42A). The binding of lysozyme caused a slight decrease in LYI fluorescence, which is most probably due to a change in the environment of the fluorophore. The effect should be considered, but it is not large enough to disturb FRET measurements. A similar experiment carried out at non-reducing conditions using lysozyme-TAMRA revealed a minor influence on the donor fluorescence (Figure 42B). Not until an excess of substrate, a minor decrease of the donor signal was observed, while the acceptor signal showed a small increase. Upon addition of TCEP, a large change due to FRET was observed indicating binding of reduced non-native lysozyme. Finally, titrating lysozyme-TAMRA to αB-LYI yielded a series of emission spectra with a decreasing donor and increasing acceptor signal all intersecting in an isosbestic point (Figure 42C).

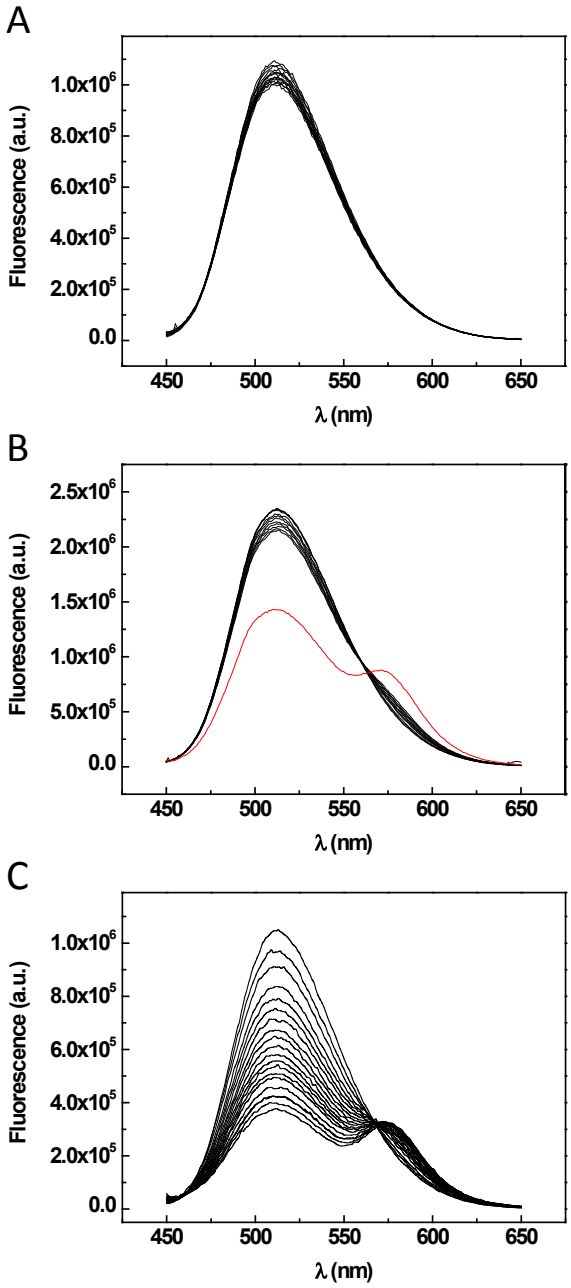

Figure 42 | Emission spectra of substrate titration experiments. (A) Fluorescence emission spectra of αB-LYI were recorded after titration with unlabeled lysozyme under redusing conditions (1 mM TCEP). (B) Under non-reducing conditions, emission spectra of αB-LYI were recorded after stepwise addition of lysozyme-TAMRA. After the last titration step, TCEP was added to a final concentration of 1 mM. The emission spectrum under reducing conditions (red) showed a strong change due to FRET. (C) Substrate titration experiment using αB-LYI and lysozyme-TAMRA in the presence of 1 mM TCEP.

FRET is often described as a method to determine intermolecular distances, which is reflected by the term "molecular ruler". This might be possible (in theory) for simple systems consisting of two interacting proteins but is inapplicable for the described system. On the one hand, I could show that binding of unlabeled lysozyme influences the fluorescence independent of FRET, on the other hand, there is no mathematical solution to

deal with multiple donors and/or multiple acceptors in a quantitative way to allow calculating transfer efficiencies. Nevertheless, the titration experiments show that the described FRET assay can be used in a qualitative way or to monitor changes upon binding kinetically.

FRET Binding Kinetics

To monitor the substrate binding kinetics, 10 µM αB-LYI were mixed with 2.5 µM lysozyme-TAMRA and the decrease in LYI fluorescence was monitored after addition of 1 mM TCEP at 511 nm (Figure 43).

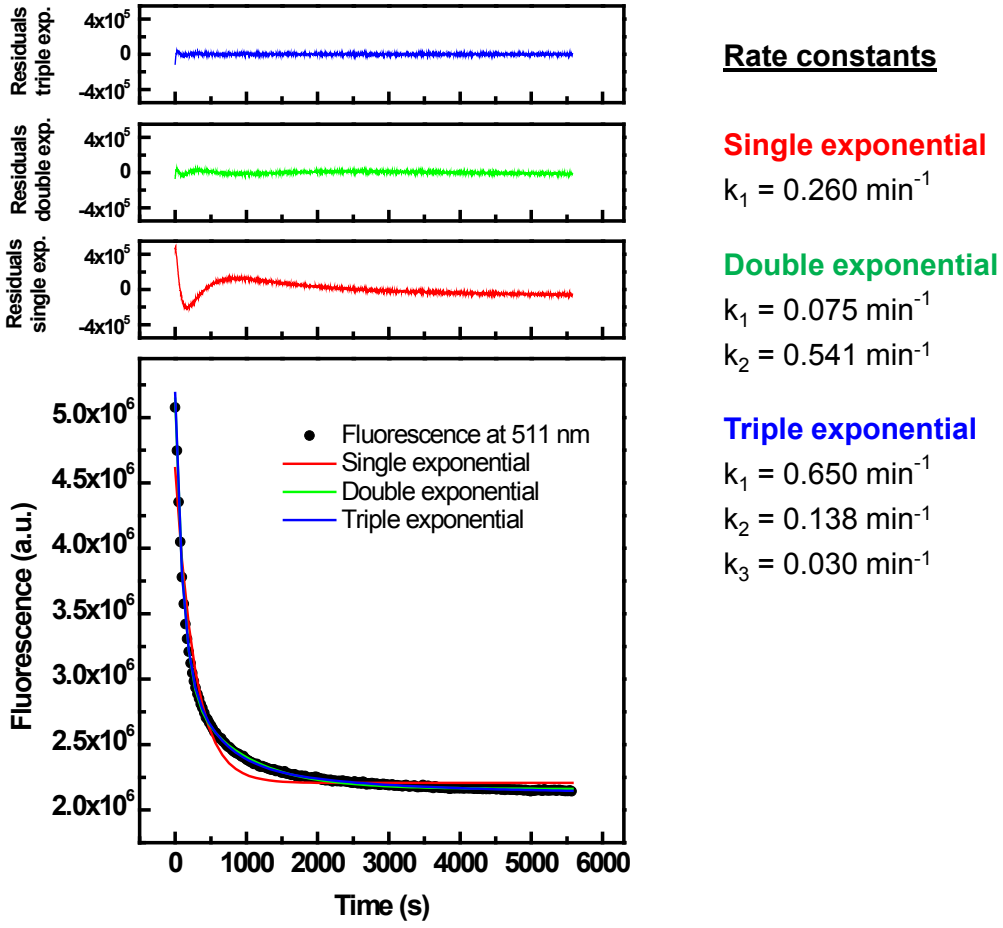

Figure 43 | Monitoring lysozyme binding kinetics by FRET. Binding of 10 µM αB-LYI to 2.5 µM lysozyme-TAMRA was monitored by the decrease in fluorescence at 511 nm in the presence of 1 mM TCEP at 37°C (black circles). Data was fitted using single (red), double (green) and triple (blue) exponential functions. The residuals plots show that only a triple exponential fitting function describes the experimental data sufficiently.

Analysis revealed the existence of multiple processes since neither a single exponential nor a double exponential equation was sufficient to describe the FRET data. This result is not surprising because reduction and unfolding of lysozyme have to take place prior to

binding. Therefore, shortly after addition of TCEP, only a minor fraction of lysozyme is reduced and non-native, and thus in its binding-competent state.

Even though the complexity of the FRET binding kinetics complicates a quantitative analysis, the data can be used for a comparison with the aggregate formation as determined by light-scattering assays. It is obvious that the characteristics of both graphs are very different. During the lag phase of the aggregation curve, about 3/4 of the FRET signal change had already occurred.

Taken together, the presented FRET assay allows monitoring substrate binding, even if the kinetics is composed of multiple processes. Binding of reduced lysozyme to αB-crystallin is much faster than the formation of light-scattering aggregates in the absence of the chaperone. This result indicates a binding of early unfolding intermediates, which was also suggested by previous studies. In order to maintain substrates during stress in a refolding-competent state, immediate or early binding during the unfolding process may be essential.

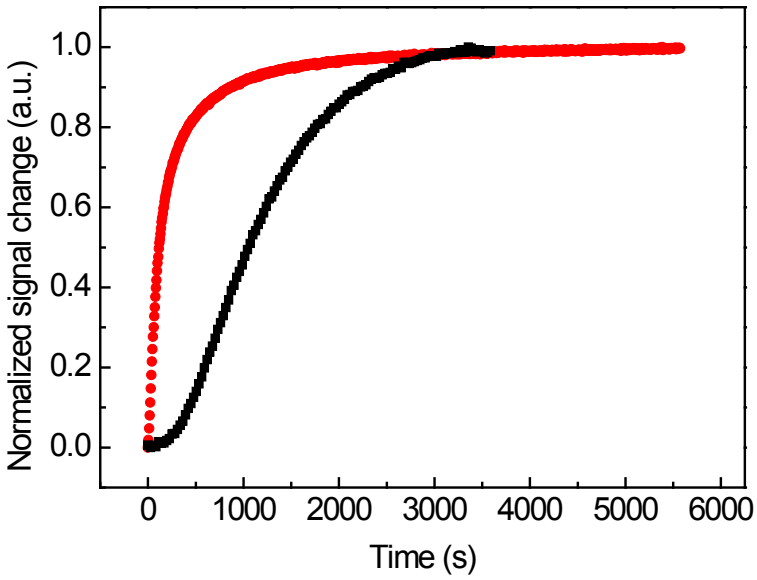

Figure 44 | Comparison of FRET binding kinetic with aggregation kinetic. The light-scattering signal of lysozyme aggregation from **Figure 34** (black squares) and the inversed FRET binding kinetics (red circles) are depicted. Both signals were normalized (0 to 1). The formation of light-scattering aggregates was slower than the FRET-induced changes of fluorescence indicating the binding of early unfolding intermediates.

Monitoring Substrate Release

In general, sHsp-substrate complexes are considered not to be dead-end products within the cell. For several sHsp members, previous studies could show substrate refolding in assistance of ATP-dependent chaperone systems (Ehrnsperger et al., 1997; Goloubinoff et al., 1999; Lee et al., 1997; Mogk et al., 2003). In the case of αB-crystallin, a similar

function is very likely but could not be shown so far. It should be noted that such interplay with other chaperones does not play a role in the eye lens due to the lack of protein turn-over.

All previous studies that suggested refolding by ATP-dependent chaperone systems made use of enzymes as model substrates monitoring reactivation by their specific activity (see *4.7.2 Refolding of Malat Dehydrogenase*). Here, the FRET assay was used to follow substrate release directly. Lysozyme turned out to be an appropriate model substrate to study binding. However, the use of reducing conditions, which are needed to initiate binding, impeded the release by the Hsp70 chaperone system (human Hsc70, human Hdj1 and ATP) completely (Figure 45). This might be explained by immediate rebinding during reducing conditions. The chaperones should not be affected by the presence of reducing agent.

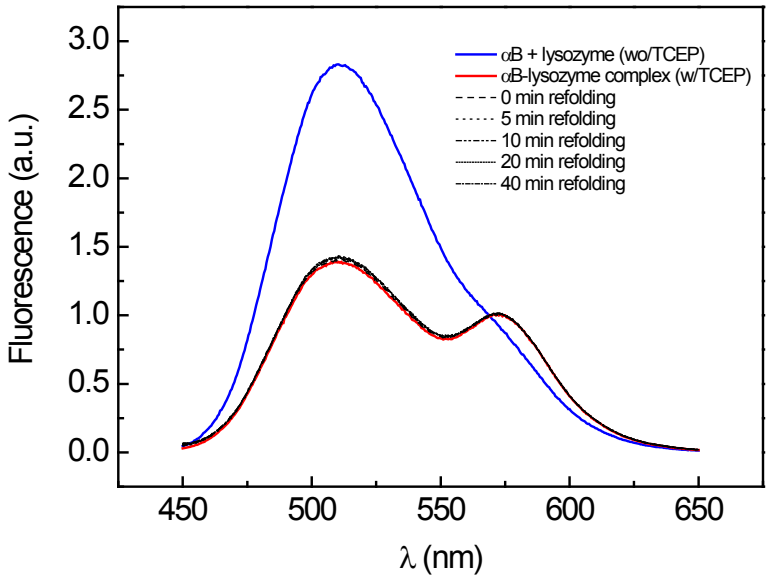

Figure 45 | Testing lysozyme release from αB-crystallin by the Hsp70 chaperone system. Fluorescence emission spectra of 2.5 µM αB-LYI and 0.5 µM lysozyme-TAMRA were recorded under non-reducing conditions (blue) and under reducing conditions after addition of 1 mM TCEP (red). The decrease of donor fluorescence and the concomitant increase of acceptor fluorescence indicate the formation of αB-lysozyme complexes. The FRET signal was monitored at the indicated time points after the addition 0.5 µM Hsc70, 0.1 µM Hdj1 and 2 mM ATP. No reversal of the FRET signal could be observed.

To inhibit reassociation of αB and lysozyme, the addition of oxidized glutathione (GSSG) was tested. Certainly, a productive refolding of fully reduced lysozyme to the native state is by no means possible due to the stochastic re-oxidation of eight cysteine residues, which would need to form four correct disulfide bonds. Since a 5-fold molar excess of GSSG over TCEP was sufficient to inhibit aggregation as followed by light scattering, this

amount was added after complex formation to enable substrate release. The single experimental steps are depicted in Figure 46.

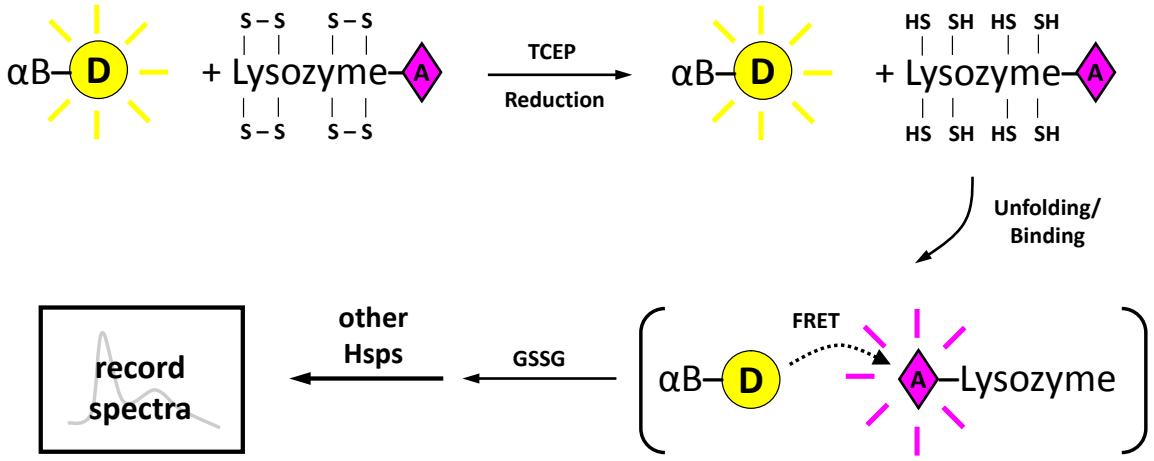

Figure 46 | Schematic overview of the steps to monitor substrate release using FRET.

To test the spontaneous release of αB-crystallin-bound lysozyme, fluorescence emission spectra were recorded after addition of GSSG (Figure 47A). These experiments revealed a partial reversion of the FRET signal indicating a partial release of lysozyme after a return to non-reducing conditions. About 1/3 of the signal decrease, which was caused by binding, was reversed after 120 min (Figure 48). Due to the aforementioned complex FRET system, which is composed of multiple fluorophores with distances below the Förster radius, it is not possible to determine the amount of released lysozyme by the change in fluorescence intensity.

In the next steps, the effect of the Hsp70 chaperone system in promoting substrate release was studied. In the presence of Hsc70 and ATP, the substrate release was more efficient as judged from the reversion of the donor fluorescence in the emission spectra (Figure 47B). About 2/3 of the initial donor fluorescence intensity was reached within 140 min (Figure 48). When Hdj1 was added together with Hsc70 and ATP, the donor fluorescence regained up to 75% of the starting signal (Figure 47C). Although the relative reversion of the donor fluorescence yielded similar final values for Hsc70/ATP and Hsc70/Hdj1/ATP, the FRET release kinetics were accelerated by the presence of Hdj1. Within the first 10 min after addition of the release mix, the maximum reversion of the FRET signal was reached, whereas ~2 h were needed to complete this process in the absence of Hdj1 (Figure 48).

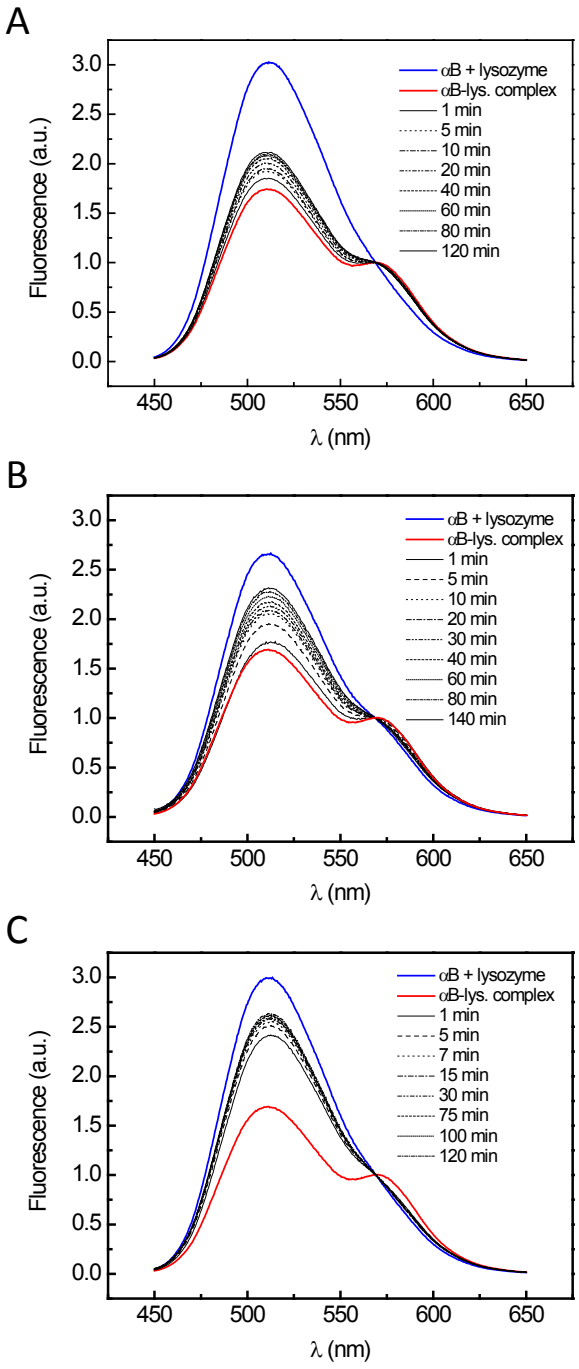

Figure 47 | Monitoring lysozyme release by FRET. Fluorescence emission spectra of 2.5 µM αB-LYI and 0.5 µM lysozyme-TAMRA were recorded under non-reducing conditions (blue) and under reducing conditions after addition of 1 mM TCEP (red). The decrease of donor fluorescence and the concomitant increase of acceptor fluorescence indicate the formation of αB-lysozyme complexes. The reversion of the FRET signal was monitored at the indicated time points. The release of lysozyme was initiated by the addition of (A) 5 mM GSSG, (B) 5 mM GSSG, 0.5 µM Hsc70 and 2 mM ATP or (C) 5 mM GSSG, 0.5 µM Hsc70, 0.1 µM Hdj1 and 2 mM ATP.

Taken together, the lysozyme FRET assay provides a tool to not only monitor binding, but also the release, which is mediated by additional factors. The redox state has to be reverted from reducing conditions to non-reducing conditions, which was attained by a 5-fold molar

excess of GSSG over TCEP resulting in a GSH/GSSG redox system. The presented results show the suitability of the FRET assay to monitor substrate binding and release, but more efforts are needed to understand the release process in more detail and to pin down the individual contributions of the components of the Hsp70 system.

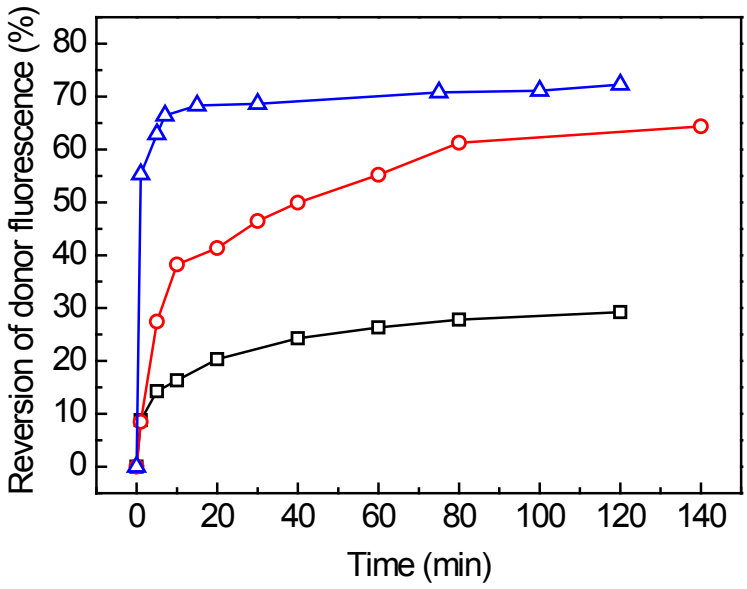

Figure 48 | Comparison of lysozyme release kinetics. Relative changes of the donor fluorescence intensity after initiation of the release are plotted against time. 0.5 µM lysozyme-TAMRA were bound to 2.5 µM αB-LYI in the presence of 1 mM TCEP, lysozyme release was initiated by the addition of 5 mM GSSG (black, squares), 5 mM GSSG, 0.5 µM Hsc70 and 2 mM ATP (red, circles) or 5 mM GSSG, 0.5 µM Hsc70, 0.1 µM Hdj1 and 2 mM ATP (blue, triangles). The depicted data is taken from the fluorescence emission spectra at 512 nm (Figure 47).

4.6 The Structure-Function Relationship of αB-Crystallin

The formation of large oligomers is a key characteristic of many sHsps. We have seen that αB-crystallin, like many other metazoan sHsps, assembles into oligomers with a variable number of subunits. Within this dynamic oligomer equilibrium, αB can adopt numerous different oligomeric states, which are all based on a common molecular architecture. To elucidate the structure-function relationship of αB-crystallin, I tried to answer the following questions: How is the complex oligomerization, which is the most striking structural feature of αB-crystallin, linked to its chaperone function as a holdase towards non-native proteins? How is this function regulated on structural level?

The idea that smaller oligomeric forms bind substrate is appealing and has been discussed in literature (Basha et al., 2012). Based on a recent MS study, a model of sHsp activation by reorganization into larger oligomers was suggested (Eyles and Gierasch, 2010; Stengel

et al., 2010). In general, an oligomerization-dependent shift from a storage form to the active state would imply an important role of subunit exchange for substrate binding. In addition, environmental conditions and posttranslational modifications are potential elicitors for sHsp activation. Phosphorylation was shown to alter the oligomeric state of several sHsps and certainly plays an important, yet not understood role in controlling their activity (Basha et al., 2012; Ecroyd et al., 2007; Hayes et al., 2009).

In vivo studies showed that αB-crystallin is phosphorylated at distinct serine residues in response to stress (Figure 49A). Phosphorylation of αB-crystallin is known to reduce its oligomer size and alter its chaperone function (Ahmad et al., 2008; Aquilina et al., 2004; Ecroyd et al., 2007; Ito et al., 2001). This finding indicates a key role of modulating the dynamic oligomer equilibrium of αB-crystallin in control of its chaperone function. Thus, we used phosphorylation-mimicking as tool to understand the correlation between quaternary structure and chaperone function.

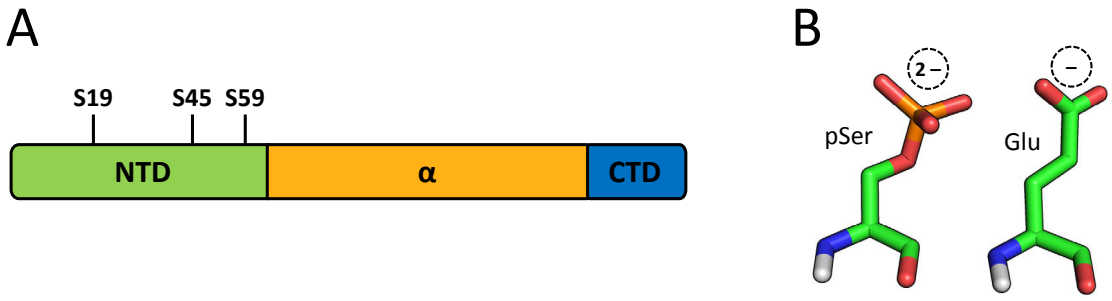

Figure 49 | Phosphorylation sites and mimicking by glutamates. (A) The domain structure of αB-crystallin is depicted with the three major phosphorylation sites S19, S45 and S59 and their relative position in the NTD. (B) Stick representations of phospho-serine (pSer) and phospho-mimicking glutamate (Glu) demonstrate the similarity of both residues.

Due to their negative charge and similar side chain length, glutamates are a well-accepted substitution to mimic phospho-serines (Figure 49B). All seven possible phosphorylation-mimicking glutamate variants at the three major phosphorylation sites Ser19, Ser45 and Ser59 were recombinantly expressed in *E. coli* and the proteins were purified to homogeneity. Far-UV CD spectroscopy confirmed that all Glu variants were properly folded (Figure 50). All spectra displayed a similar curve progression with a minimum at ~215 nm. The introduction of phosphomimicking glutamates caused an overall increased negative ellipticity relative to WT αB-crystallin.

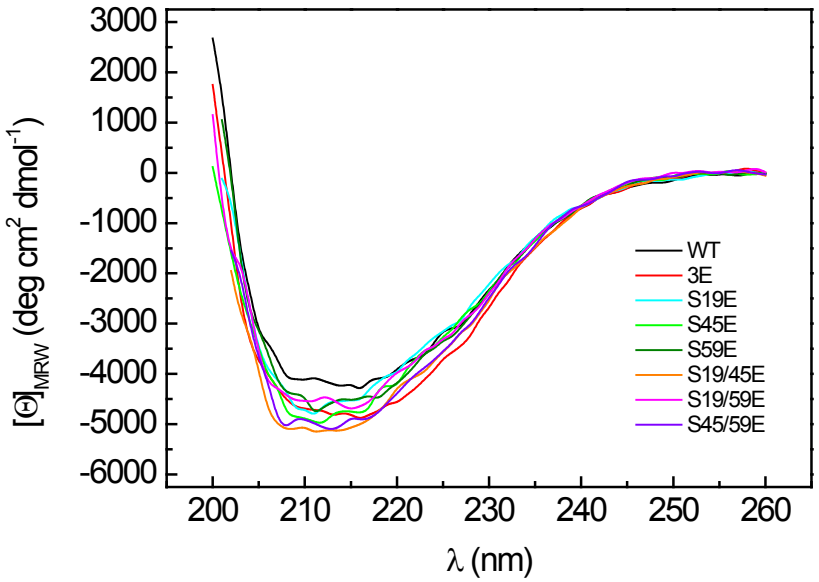

Figure 50 | Effects of mimicking phosphorylation on the secondary structure studied by far UV CD spectroscopy. Far UV CD spectra of WT αB-crystallin and phospho-mimicking mutants were recorded at 37°C in PBS. The protein concentration was adjusted to 10 µM using UV absorbance immediately before the CD measurements.

4.6.1 Effects of Mimicking Phosphorylation on the Oligomer Equilibrium

In order to study the effects of phosphorylation on quaternary structure, we performed size-exclusion chromatography (SEC), analytical ultracentrifugation (AUC) and electron microscopy (EM) with the different Glu variants and compared these results to wild-type αB-crystallin. Despite its limited resolution, SEC revealed an influence of phospho-mimicking on the quaternary structure of αB-crystallin: the shift to later elution times indicated a reduction in the mean oligomer size for phospho-mimicking mutants (Figure 51). However, different influences of the individual sites could not be assessed by this method. In fact, the elution profiles of all 1E and 2E variants were similar, with only 3E displaying an additional reduction of its oligomeric size.

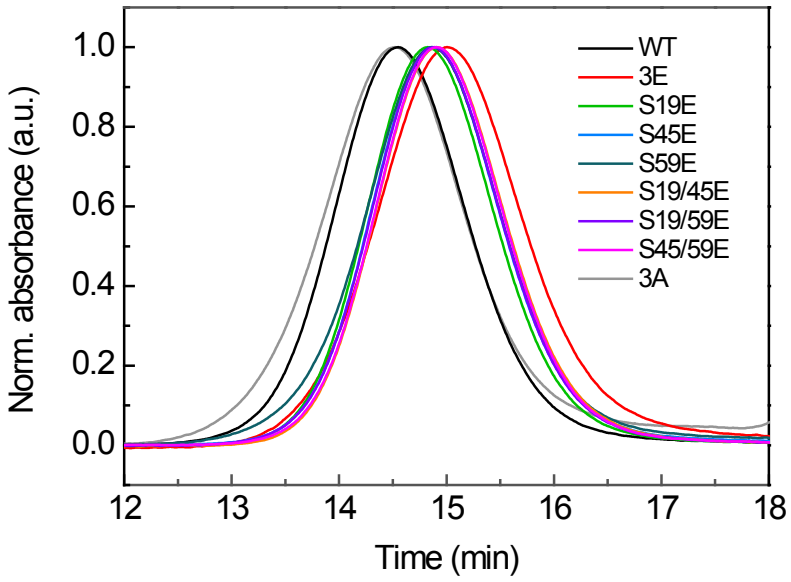

Figure 51 | Effects of mimicking phosphorylation on the quaternary structure studied by analytical gel filtration. SEC elution profiles of WT αB-crystallin, all combinations of Glu mutants at the phosphorylation sites Ser19, Ser45 and Ser59 and αB-crystallin-3A. The color code is given in the legend. Data were collected using a Tosoh TSK 4000 PW column equilibrated in PBS.

To analyze the quaternary structure in more detail, we performed sedimentation velocity (SV) AUC. The resulting size distributions showed that the introduction of phospho-mimicking glutamates led to smaller sedimentation coefficients (Figure 52). For WT αB-crystallin, dc/dt analysis (Stafford, 1992) using the DCDT+ software (Philo, 2006) resulted in a symmetrical distribution (g(s*)) with a corrected weight average sedimentation coefficient ($<s_{20,w}>$) of 16.1 S. Interestingly, all Glu variants resulted in size distributions smaller than observed for WT αB-crystallin. The 1E and 2E variants showed symmetric distributions consisting of single peaks with sizes reduced by ~3 S and ~4 S, respectively. αB-crystallin-3E displayed an asymmetrical distribution with a weight average $s_{20,w}$-value of 12.2 S (Figure 52).

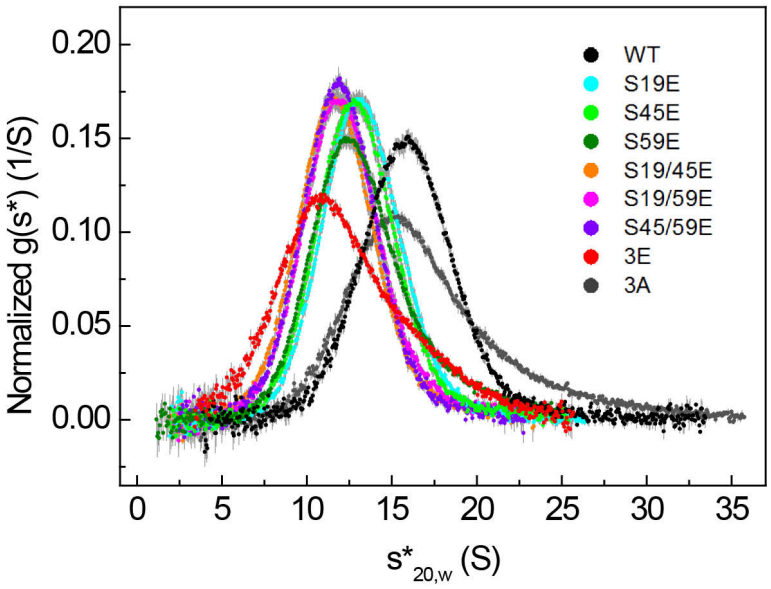

Figure 52 | Effects of mimicking phosphorylation on the quaternary structure studied by SV-AUC. Size distributions of WT αB-crystallin, all combinations of Glu mutants at the phosphorylation sites Ser19, Ser45 and Ser59 and αB-crystallin-3A. The concentration of all samples was adjusted to 30 µM. All sedimentation experiments were carried out using 30,000 rpm at 20°C in PBS. The s-value distributions (g(s*)) were calculated using the DCDT+ software and normalized to yield an area under the curve of one. The color code is given in the legend.

The size distribution of αB-crystallin was shown to be independent of the concentration within a concentration range of 2-150 µM (Figure 16). In an additional SV-AUC experiment, WT αB-crystallin and αB-crystallin-3E were analyzed in the low concentration range of 1-10 µM. As expected, WT αB-crystallin did not show any dissociation (Figure 53A). αB-crystallin-3E exhibited a slight reduction of the g(s*) distribution, but remained also predominantly oligomeric. These results revealed an concentration-independent oligomerization although the 24-mer (and related species) was destabilized upon introduction of phosphorylation-mimicking Glu residues.

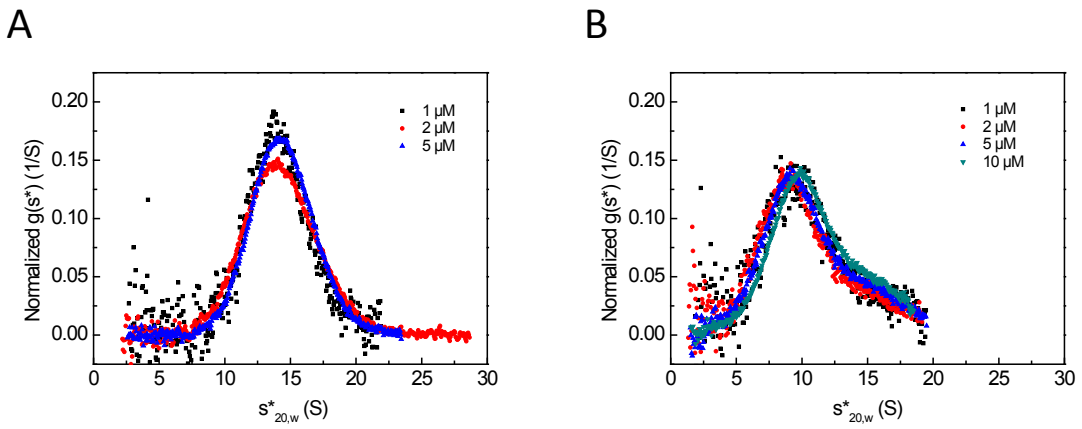

Figure 53 | Oligomer size of wild type αB-crystallin and αB-crystallin-3E at low concentrations. (A) The size distribution of WT αB-crystallin does not change within the tested concentration range. Even at the lowest concentration of 1 µM, no increase in dissociation was observed. (B) αB-crystallin-3E shows a slight size reduction at low protein concentrations but remains predominantly oligomeric. All sedimentation experiments were carried out using 30,000 rpm at 20°C in PBS. The s-value distributions (g(s*)) were calculated using the DCDT+ software and normalized to yield an area under the curve of 1. The symbol and color code of the analyzed protein concentrations is given in the legend.

Due to the asymmetrical shape of the distribution of αB-crystallin-3E we further analyzed the data by c(s) analysis using the Sedfit software (Schuck, 2000) (Figure 54). The calculated distributions for WT αB-crystallin and αB-crystallin-3E were comparable to the g(s*) analysis results but in case of αB-crystallin-3E the separation into two populations consisting of small and wild-type-like oligomers was even more pronounced. The calculated molecular masses according to the frictional coefficient of the best fit were ~500 and ~250 kDa, which corresponds to average oligomer sizes of 24 and 12 subunits, respectively. In the case of αB-crystallin-3E, an additional small peak of 3 S was present indicating low amounts of dimeric or small suboligomeric species (Figure 54).

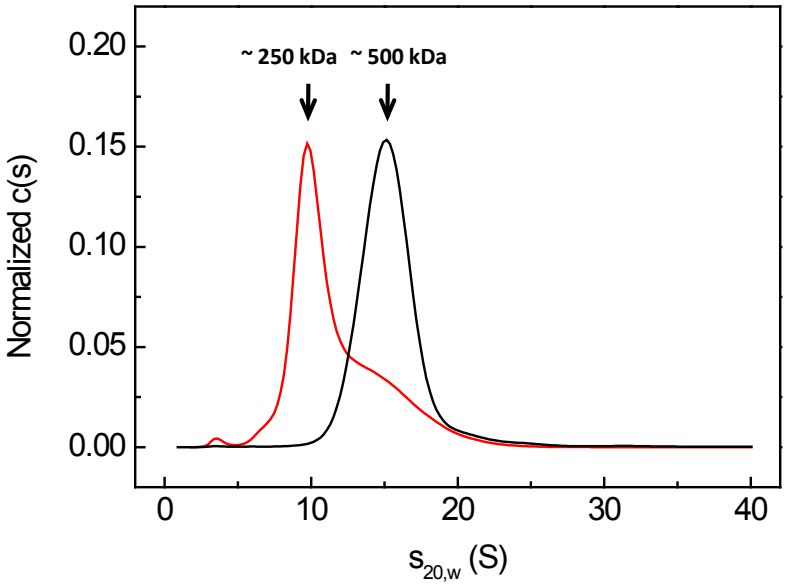

Figure 54 | c(s) analysis of WT αB-crystallin and αB-crystallin-3E. The s-value distributions (c(s)) of WT αB-crystallin (black) and αB-crystallin-3E (red) were calculated using the Sedfit software. The masses indicated by the arrow were calculated using the frictional coefficients of the best fit. All sedimentation experiments were carried out using 30,000 rpm at 20°C in PBS.

In SV experiments, the sedimentation coefficient of oligomeric proteins is determined by their molecular mass as well as their assembly kinetics. To exclude the influence of the latter, we performed an additional sedimentation equilibrium (SE) experiment comparing WT αB-crystallin and αB-crystallin-3E. The obtained radial concentration distributions revealed that both proteins indeed differ in their average molecular masses. A simplified fit for a single ideal component (Equation 7) resulted in a calculated mass of 490 kDa for WT αB-crystallin and 330 kDa for αB-crystallin-3E (Figure 55).

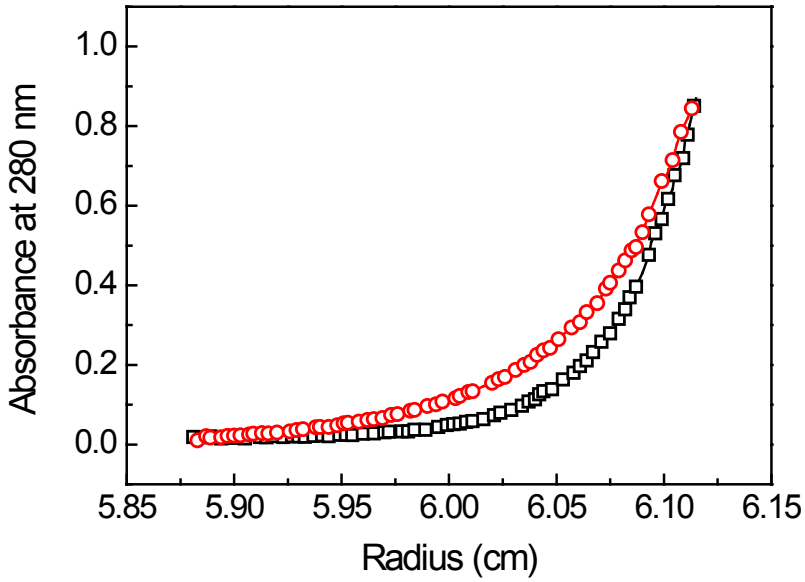

Figure 55 | Sedimentation equilibrium analysis of WT αB-crystallin and αB-crystallin-3E. SE-AUC was used to compare the average size of WT αB-crystallin (black) and αB-crystallin-3E (red) under equilibrium conditions. The concentration distributions were fitted using a single exponential function to yield average molecular masses of 490 kDa for WT αB-crystallin and 330 kDa for αB-crystallin-3E. The depicted concentration-radius plots were obtained using 12,000 rpm at 20°C in PBS.

To investigate the changes in oligomer size in more detail, wild type αB-crystallin and the 3E mutant were subjected to NS-EM. The method allows determining size distributions based on the diameters of single molecules. As shown in Figure 56A, WT αB-crystallin showed a relatively homogeneous preparation of ammonium molybdate-stained particles composed of oligomers with diameters ranging from about 12 nm to 14 nm (Figure 56C). The images of the 3E mutant were dominated by smaller particles and a rather heterogeneous composition (Figure 56B). In comparison to WT αB-crystallin, the respective size distribution of αB-crystallin-3E was shifted towards smaller oligomers with diameters ranging from about 10 nm to 13.5 nm (Figure 56C).

The data set was separated into four size-related subpopulations by projection matching iterations using the oligomer models of αB-crystallin from the previous cryo-EM work (Braun et al., 2011). Approximately 80% of the 3E particles were assigned to the two smallest oligomer populations corresponding to 2-6-mers and 12-20-mers, respectively (Figure 56D) indicating a clear shift towards smaller oligomers when compared to WT αB-crystallin. The assignment of 40% to 2-6-mer subpopulation is especially striking because oligomers of the smallest subpopulation were hardly present in WT αB-crystallin preparations.

In summary, mimicking phosphorylation reduced the mean particle diameter and introduced a higher degree of heterogeneity. The SEC and AUC analyses indicated, in line with previous reports (Ahmad et al., 2008; Ito et al., 2001), a reduction of the average molecular mass of phospho-mimetic mutants of αB-crystallin. EM provided useful additional information about the associated structural changes with regard to single species within the ensemble of oligomers.

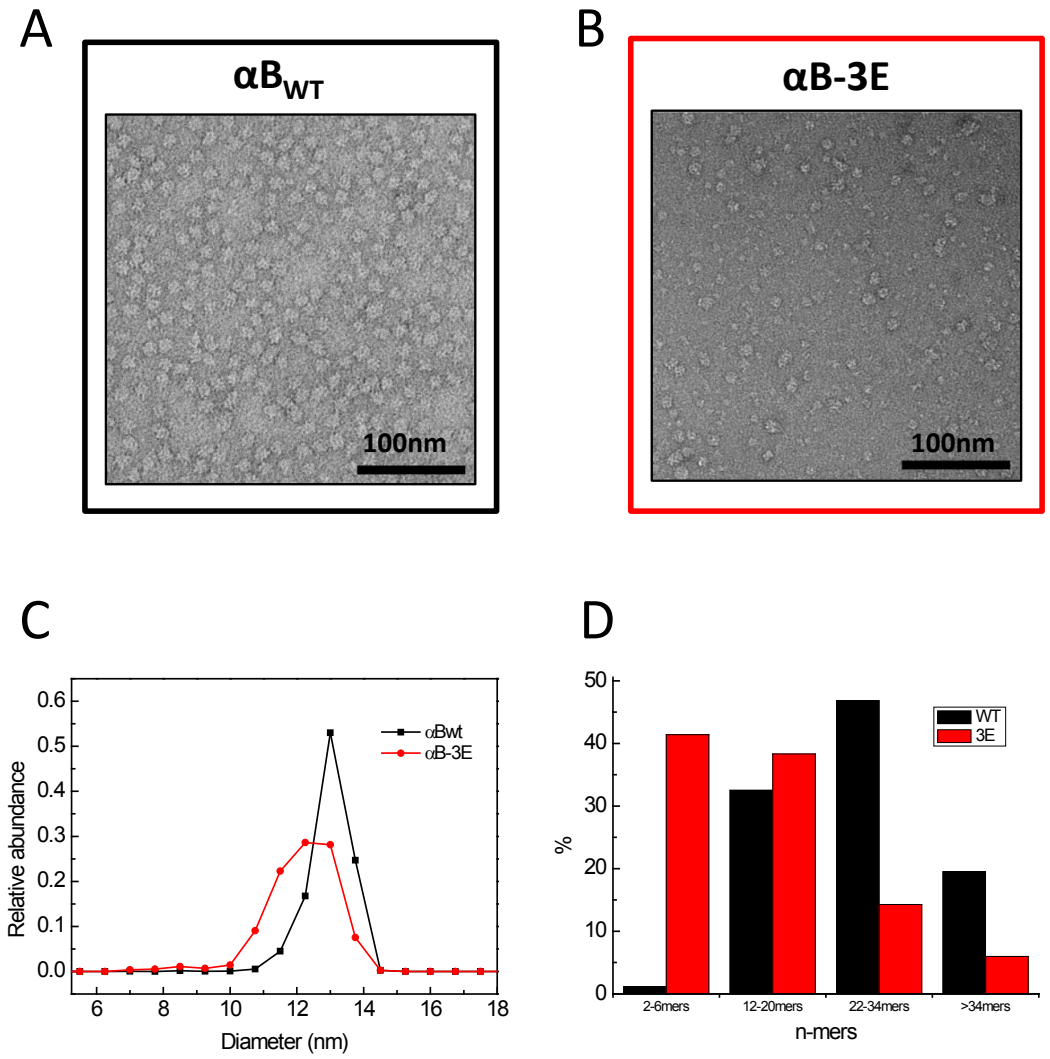

Figure 56 | Negative stain EM analysis of WT αB-crystallin and αB-crystallin-3E. The oligomer equilibrium of WT αB-crystallin (black) and αB-crystallin-3E (red) were stained using ammonium molybdate and analyzed by EM. (A) The EM image of WT αB-crystallin shows a relatively homogeneous particle composition. (B) The 3E mutant is dominated by smaller particles showing a much higher degree of heterogeneity. (C) This observation is illustrated by the respective size distribution plots. Mimicking phosphorylation reduces the mean particle diameter and leads to a broader distribution. (D) The data set was separated into four size-related subpopulations (2-6-mers, 12-20-mers, 22-34-mers and >34-mers) by projection matching iterations using the oligomer models of αB crystallin from the previous cryo-EM work (Braun et al, 2011). The results indicate a clear shift towards smaller oligomers upon mimicking of phosphorylation. Approximately 80% of the 3E particles were assigned to the two smallest oligomer populations corresponding to 2-6-mers and 12-20-mers, respectively.

4.6.2 Proximal Negative Charges Cause Partial Dissociation by Increased Subunit Exchange Rates

All multimeric sHsps are known to form dynamic assemblies, which constantly exchange subunits in a temperature-dependent manner. By attaching suited pairs of fluorescent labels, the apparent subunit exchange (SX) rates can be determined using fluorescence resonance energy transfer (FRET) as described previously (Bova et al., 1997). To exclude the risk that the labeling with fluorescent probes affects WT αB-crystallin and αB-crystallin-3E to different extents, subunit exchange was studied using reversal of FRET as used in a previous study (Ahmad et al., 2008). To this end, WT αB-crystallin-S59C was labeled with the FRET label pair 4-acetamido-4'-((iodoacetyl)amino)stilbene-2,2'disulfonic acid (AIAS) and lucifer yellow iodacetamide (LYI). The labeled αB-crystallin oligomers were mixed in equimolar ratio and incubated at 30°C over night to yield a saturated energy transfer by SX. Upon addition of a 25-fold molar excess of unlabeled WT and 3E αB-crystallin to this FRET hetero-oligomers, an increase in the ratio of the fluorescence intensity at 415 nm to that at 520 nm was observed with time (Figure 57), indicating a reversal of FRET due to the SX process.

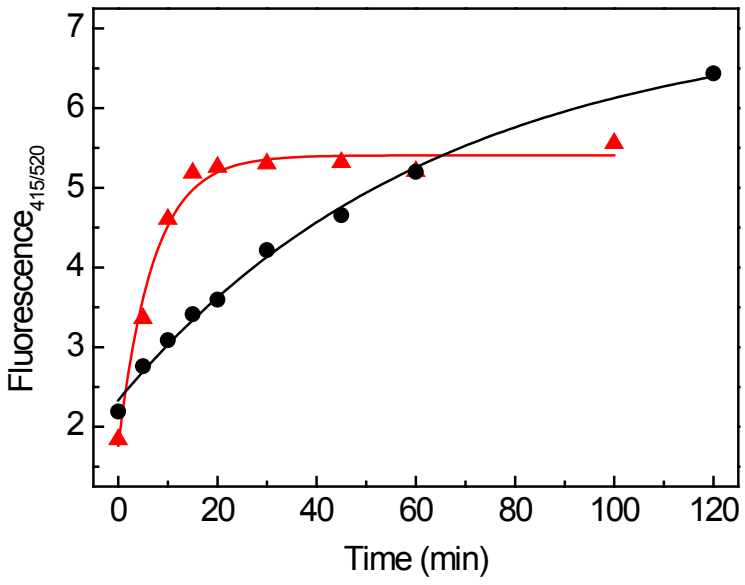

Figure 57 | Subunit exchange kinetics of WT αB-crystallin and αB-crystallin-3E. AIAS- and LYI-labeled αB-crystallin oligomers were mixed in equimolar ratio and incubated at 30°C over night to yield a saturated energy transfer by SX. Upon addition of a 25-fold molar excess of unlabeled WT (black circles) and 3E αB-crystallin (red triangles) to this FRET hetero-oligomers, an increase in the ratio of the fluorescence intensity at 415 nm to that at 520 nm was observed with time. Using a previously published exponential model the data was fitted (lines). The obtained rate constant was 0.020 (±0.001) min^{-1} in the case of WT αB-crystallin and 0.142 (±0.017) min^{-1} in the case of αB-crystallin-3E.

Using a previously published exponential model, the obtained rate constant was 0.020 (±0.001) min^{-1} in the case of WT αB-crystallin and 0.142 (±0.017) min^{-1} in the case of αB-crystallin-3E. Thus, this result showed that the rate of SX is larger in the case of 3E compared to that of the wild type. The correlation between increased dissociation rates and reduced mean oligomer size aggrees well with a previous report that linked oligomer equilibrium with quaternary dynamics (Baldwin et al., 2011b).

In a previously published pseudo-atomic model of a 24-meric αB-crystallin assembly, it was shown that the phosphorylation sites Ser19, 45 and 59 are all in close proximity within "dome-shaped" structural elements harboring the N termini (Braun et al., 2011). Therefore, we hypothesized that the introduction of negative charges, either by phosphorylation or mimicking glutamates, leads to destabilization of the oligomers. To confirm the importance of charged residues, alanines were introduced at the same positions. In fact, αB-crystallin-3A exhibited an oligomeric size similar to WT αB-crystallin as confirmed by SEC and SV-AUC (Figure 60 & Figure 61). However, the atomic structure of the N-terminal region was solely based on structure prediction and modeling. Thus, we introduced cysteine residues at the respective sites to perform disulfide crosslinking. SDS-PAGE of all three Cys mutants showed a dimer band under non-reducing conditions, which is not present under reducing conditions (Figure 58). The observed spontaneous formation of disulfide bonds confirms a close proximity of the phosphorylation sites.

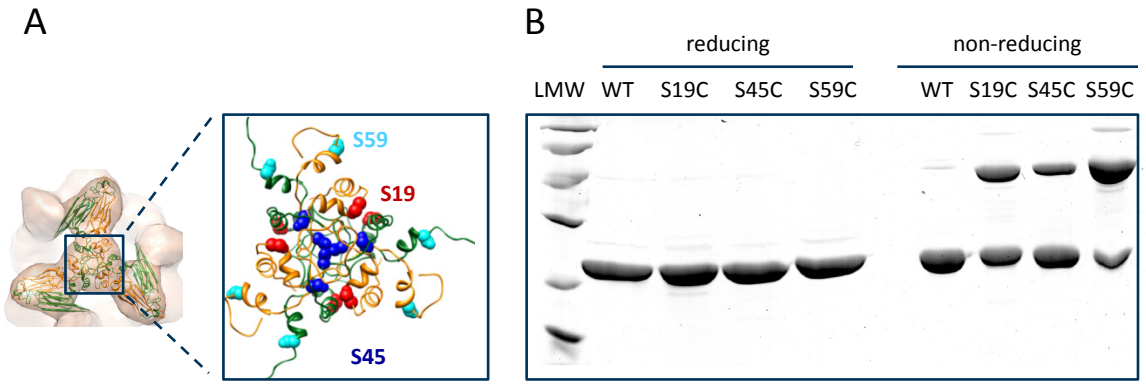

Figure 58 | Proximity of the major phosphorylation sites within the αB-crystallin oligomer. (A) Location of the three phosphorylation sites in the pseudoatomic 24-mer model of αB-crystallin. (B) Cysteine cross-linking of Ser-to-Cys mutants of αB-crystallin at the phospho-sites. While only the monomer bands were detected under reducing conditions, all three Cys mutants showed an additional dimer band without reducing agent indicating the close proximity of the phosphorylation sites.

4.6.3 Modulating the Quaternary Structure of αB-Crystallin by Hetero-oligomer Formation

The formation of hetero-oligomers by subunit exchange was shown for closely related sHsps, like for instance HspB2 and HspB3 (den Engelsman et al., 2009) or for the two α-crystallin isoforms with each other or with Hsp27 (Bova et al., 2000). The physiological relevance of this process is still unclear. In the previous section, it was shown that WT αB-crystallin and αB-crystallin-3E can exchange subunits and that the exchange rate is increased in the presence of phosphorylation-mimicking mutations.

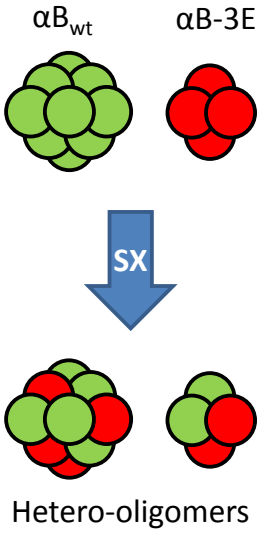

Figure 59 | Principle of hetero-oligomer formation. αB-crystallin WT and 3E were incubated together for sufficient time to allow statistical mixing of the oligomers by subunit exchange (SX).

To study the structure of these heterocomplexes, WT αB-crystallin and αB-crystallin-3E were mixed at different ratios and subsequently incubated over night at 30°C to ensure statistical mixing of the different subunits (Figure 59) by subunit exchange.

The influence of hetero-oligomer formation on the quaternary structure was analyzed by SEC. The elution profiles showed that the hydrodynamic size was reduced depending on the WT-to-3E-ratio: The more 3E was incorporated into the oligomers, the smaller their mean size was (Figure 60).

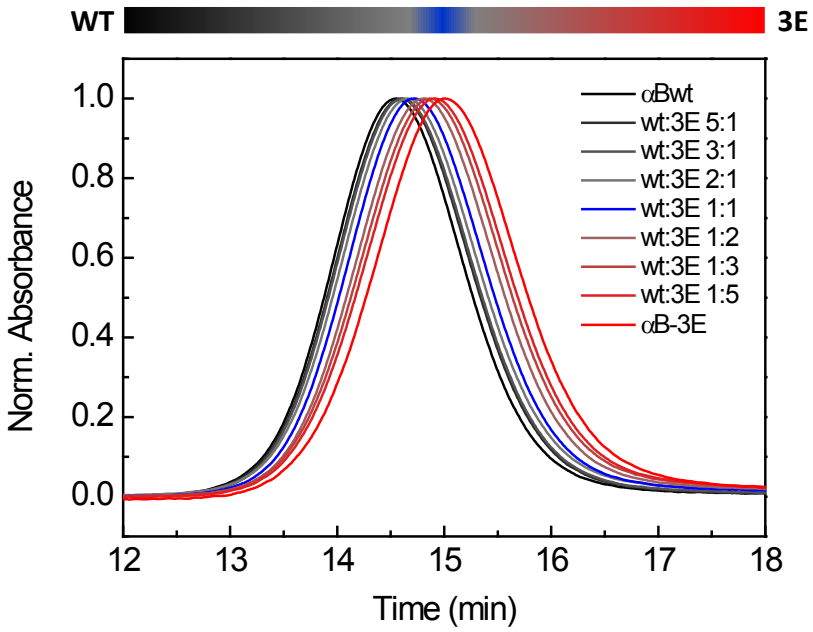

Figure 60 | Quaternary structure of WT αB-crystallin-αB-crystallin-3E-hetero-oligomers studied by SEC. WT αB-crystallin and αB-crystallin-3E were mixed at different ratios and subsequently incubated over night at 30°C to ensure statistical mixing of the two different subunits by subunit exchange. WT αB-crystallin (black) eluted at the earliest time and αB-crystallin-3E (red) at the latest. The different ratios of both proteins exhibited intermediate elution times depending on the ratio of both proteins. The tested ratios are given in the legend. The color bar above the graph illustrates the mixing ratios. The total protein concentration of each sample was 25 µM. Data was collected using a Tosoh TSK 4000 PW column equilibrated in PBS.

Next, the same hetero-oligomer samples were further subjected to SV-AUC. The g(s*) size distributions, which were calculated using the DCDT+ software, confirmed the results from SEC analysis (Figure 61). The weight-average sedimentation coefficient correlates well with the fraction of 3E (Figure 61, inset). In addition, a broadening of the size distributions was observed indicating an increased heterogeneity depending on the amount of incorporated 3E.

Taken together, both methods revealed a direct correlation between the mean oligomer size and the ratio between WT αB-crystallin and αB-crystallin-3E. These results indicate that the formation of hetero-oligomers of phosphorylated and non-phosphorylated subunits represents an additional level to modulate the oligomer equilibrium besides the existence of multiple phosphorylation sites.

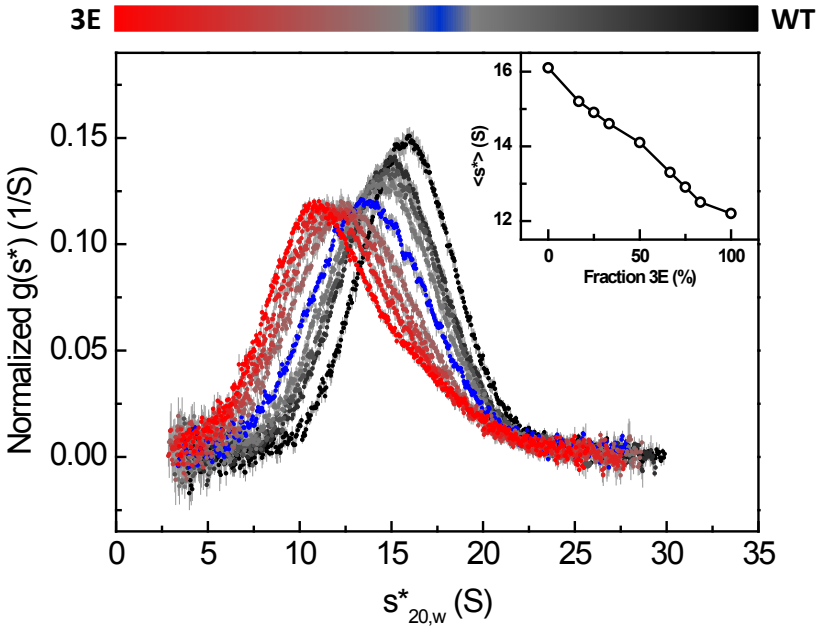

Figure 61 | Quaternary structure of WT αB-crystallin-αB-crystallin-3E-hetero-oligomers studied by SV-AUC. WT αB-crystallin and αB-crystallin-3E were mixed at different ratios and subsequently incubated over night at 30°C to ensure statistical mixing of the two different subunits by subunit exchange. WT αB-crystallin (black) eluted at the earliest time and αB-crystallin-3E (red) at the latest. The different ratios of both proteins exhibited intermediate elution times depending on the ratio of both proteins. The tested ratios are given in the legend. The color bar above the graph illustrates the mixing ratios. The total protein concentration of each sample was 25 µM. All sedimentation experiments were carried out using 30,000 rpm at 20°C in PBS. The s-value distributions (g(s*)) were calculated using the DCDT+ software and normalized to yield an area under the curve of one.

4.6.4 Effects of Mimicking Phosphorylation on Chaperone Function

Most previous studies using phosphorylation-mimicking αB-crystallin mutants reported a more efficient aggregation suppression of various model substrates *in vitro* (Ahmad et al., 2008; Ecroyd et al., 2007; Koteiche and McHaourab, 2003). Here, the effect of phosphorylation-mimicking mutations on the chaperone function was analyzed using two presumably physiological clients: the eye lens protein γD-crystallin (γD) and the transcription factor p53.

The aggregation of γD after dilution of the fully denatured protein (5 M GdnCl) into physiological buffer was partially inhibited by a 5-fold molar excess of WT αB-crystallin (Figure 62). αB-crystallin-3E was more potent in aggregation suppression. The observed immediate sharp increase in light scattering, which was still present using an excess of αB-crystallin, is in accordance to other studies (Acosta-Sampson and King, 2010).

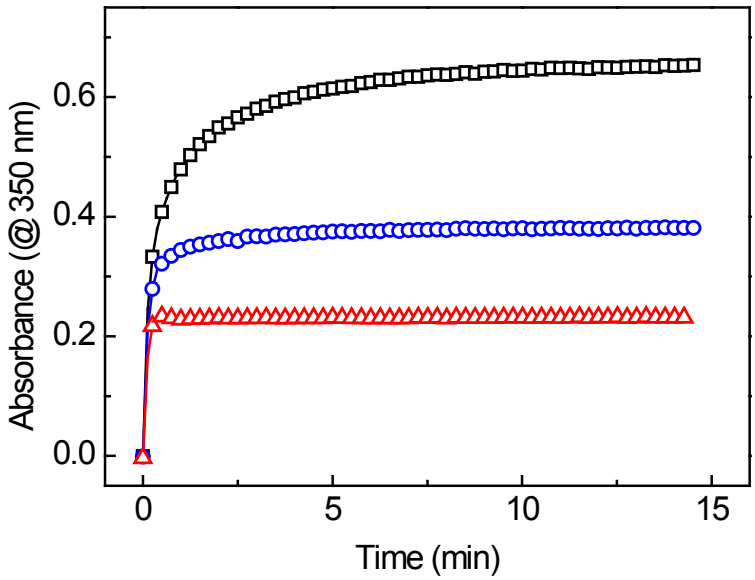

Figure 62 | Aggregation of γD-crystallin. The aggregation of γD was initiated by diluting fully denatured protein (in 5 M GdnCl) 1:100 into PBS at 37°C. The final γD concentration was 1 µM. The aggregation of 1 µM γD only (black squares) and in the presence of 5 µM WT αB-crystallin (blue circles) or 5 µM αB-crystallin-3E (red triangles) was monitored by absorbance at 350 nm.

The transcription factor p53, which is known to be aggregation-prone at elevated temperatures *in vitro* (Bullock and Fersht, 2001), is described as a client for different chaperones, in particular Hsp90 (King et al., 2001). αB-crystallin has also been shown to be associated with p53 *in vivo*. The expression of αB-crystallin is transactivated by p53 (Evans et al., 2010; Watanabe et al., 2009). In addition, a direct interaction of both proteins has been shown by pull-down experiments (Watanabe et al., 2009). Furthermore, lens epithelial cells of αB-crystallin knock-out mice showed hyperproliferation due to impaired p53 checkpoint function (Bai et al., 2003).

The aggregation of p53 was induced by heat shock at 42°C, which causes the formation of light-scattering aggregates after a lag phase of about 5 min (Figure 63). Interestingly, suppression of p53 aggregation showed a strong dependency on the presence of phospho-mimicking substitutions for all substrates tested. While WT αB-crystallin could not prevent the thermal aggregation of p53 at all, αB-crystallin-3E efficiently suppressed the formation of light scattering aggregates at sub-stoichiometric concentrations (Figure 63A). The pronounced difference in chaperone function allowed studying the influence of phosphorylation in more detail by comparing all different mimicking Glu variants. The suppression of light scattering was correlated with the increasing number of introduced Glu residues (Figure 63A). The individual contributions of the three studied phosphorylation

sites on p53 aggregation suppression were essentially indistinguishable. Like WT, αB-crystallin-3A did not suppress p53 aggregation (Figure 63A). Hetero-oligomers of WT αB-crystallin and αB-crystallin-3E, which were produced as described in *4.6.3*, exhibited intermediate activities depending on the ratio between both subunits (Figure 63B). Again, a correlation between the fraction of phospho-mimicking αB-crystallin and holdase activity was observed. These results link the oligomer size of αB-crystallin directly to its chaperone activity.

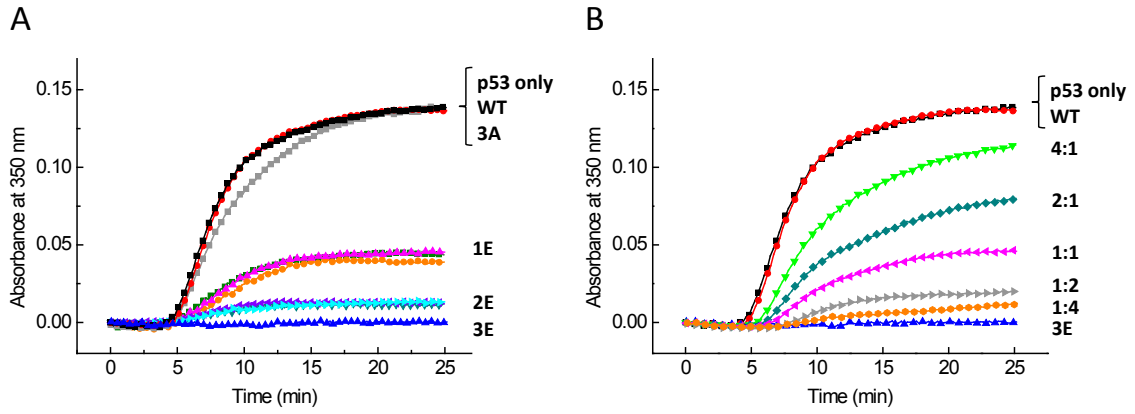

Figure 63 | p53 aggregation assays. The aggregation of 1 µM p53 (black squares) was induced by heat shock at 42°C and monitored by absorbance at 350 nm in PBS. (A) The chaperone activity of wild type αB-crystallin, all phospho-mimicking mutants and αB-crystallin-3A was assessed in the presence of 0.5 µM of the respective αB variant. Strikingly, 0.5 µM WT αB-crystallin (red circles) did not affect the light-scattering signal at all whereas 0.5 µM αB-crystallin-3E suppressed the formation of light-scattering aggregates completely. 1E and 2E mutants (see graph labels) showed intermediate activity depending on the amount of introduced Glu residues. αB-crystallin-3A showed no chaperone activity. (B) Hetero-oligomers of WT αB-crystallin and αB-crystallin-3E exhibited intermediate activities depending on the ratio between both subunits.

Based on these results, it is reasonable to assume that the presence of small oligomeric species, which depends on the phosphorylation-induced dissociation, is essential to bind unfolding intermediates of p53. To further test this hypothesis, p53 was labeled with the fluorescent dye FITC and analyzed by SV-AUC using a fluorescence detection system (Figure 64). The calculated s-value of p53-FITC in the presence of a 10-fold excess of αB-crystallin-3E shifted after incubation at 42°C for 45 min from 4.9 S to 11 S. According to the c(s) distributions, the complexes ranged in size between αB-crystallin-3E and WT with the maximum of the distribution being only 1 S larger compared to αB-crystallin-3E. This implies a preferential binding of smaller oligomeric species to p53 and explains why only phosphorylated αB is able to efficiently suppress the thermal aggregation of p53.

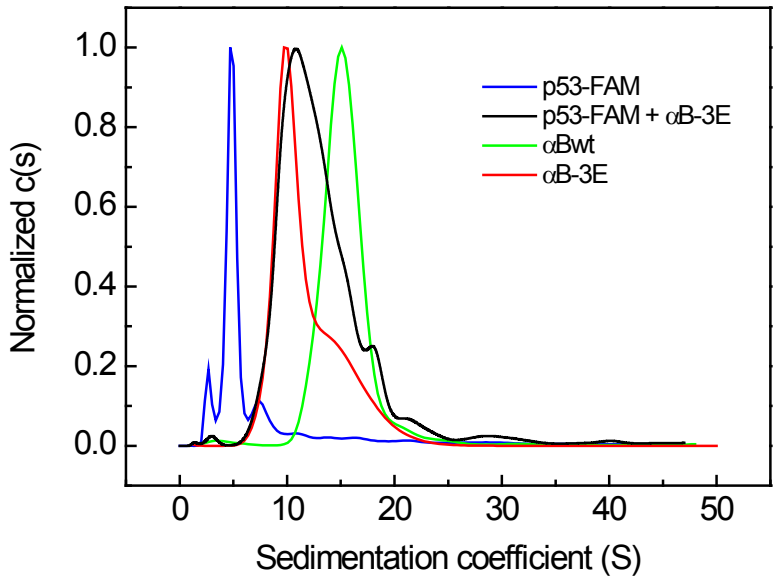

Figure 64 | Analysis of p53 binding to αB-crystallin by fluorescence SV-AUC. Normalized c(s) distributions of fluorescein-labeled p53 alone (black) and in complex with αB-crystallin-3E (red). The depicted size-distribution shows that the complexes range in size between αB-crystallin-3E (blue) and WT αB-crystallin (green). This implies a preferential binding of smaller oligomeric species to p53 and explains why phosphorylation-mimicking is needed to efficiently suppress the thermal aggregation of p53. Sedimentation was carried out at 42,000 rpm and 20°C in PBS.

4.6.5 Partial Dissociation Induced by Phosphorylation Alters the Surface Properties

The aforementioned experiments showed that mimicking phosphorylation of αB-crystallin results in a reduction of the mean oligomer size and a concomitant increase in substrate binding capacity. Therefore, it can be assumed that the phosphorylation-induced partial dissociation increases the accessibility of interaction surfaces. A combination of biochemical methods was applied to probe the surface properties and accessibility of αB-crystallin. The fluorescence of the environment-sensitive dye ANS increased with the amount of introduced phospho-mimicking Glu residues indicating a gain in surface hydrophobicity (Figure 65). However, this method only allows monitoring overall differences in surface hydrophobicity, but does not provide any structural information about the involved sites.

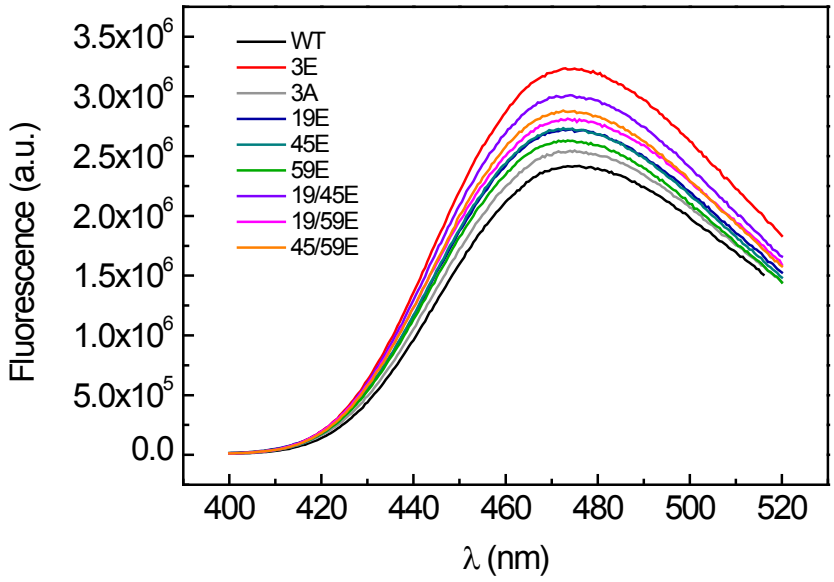

Figure 65 | Probing surface hydrophobicity by ANS fluorescence. ANS fluorescence was used to compare the overall surface hydrophobicity of αB-crystallin and various variants (see legend for color coding). To this end, 10 µM protein were mixed with 1 mM ANS in PBS. The fluorescence of the environment-sensitive dye ANS increased with the amount of introduced phospho-mimicking Glu residues indicating a gain in overall surface hydrophobicity. Fluorescence spectra were recorded from 400 nm to 520 nm with an excitation wavelength of 372 nm. All ANS spectra were recorded at 37°C.

Fluorescence quenching by acrylamide was performed to assess the accessibility of the intrinsic tryptophan probes Trp9 and Trp60, which are the only tryptophan residues in the αB primary sequence and are both located within the NTD. Fluorescence of the intrinsic Trp probes of WT αB-crystallin and αB-crystallin-3E was quenched by step-wise addition of the quencher acrylamide. Plotting the relative decrease in fluorescence (F_0/F) against the quencher concentration (Stern-Volmer plot) indicated more efficient quenching for the phospho-mimicking mutant (Figure 66). The upward curvature of the Stern-Volmer plots indicates simultaneous static and dynamic quenching, which is why the quenching constants could not be determined by linear fits (as described in *4.4.2* for quenching of lucifer yellow fluorescence). Nevertheless, qualitative assessment of the plots revealed a larger quenching effect for αB-crystallin-3E hinting to an increased accessibility at the respective sites towards the quenching agent upon phosphorylation.

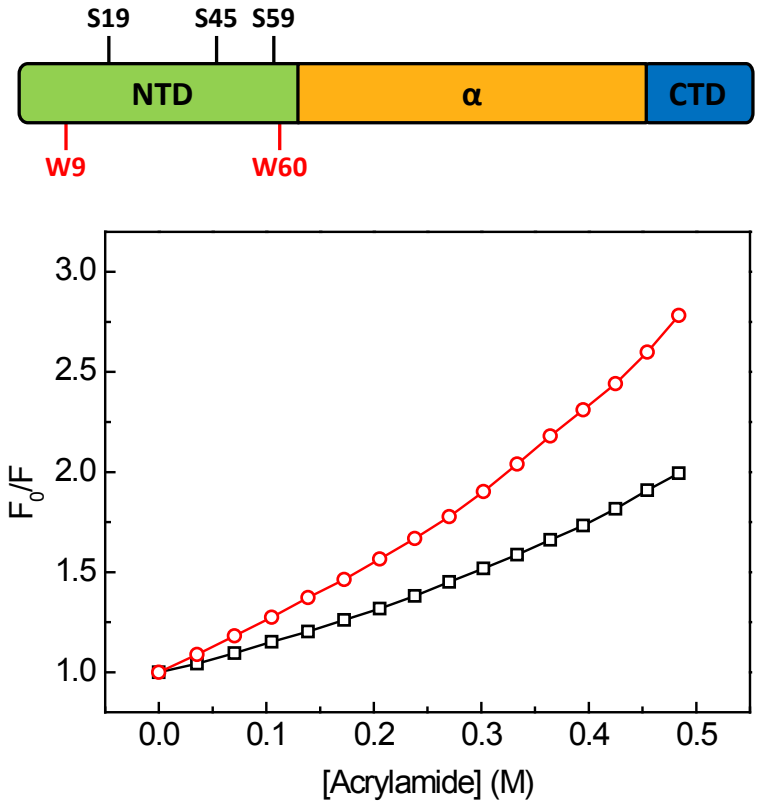

Figure 66 | Quenching of tryptophan fluorescence. The relative position of Trp9 and Trp60 within the NTD is depicted in the scheme above the graph. The experiments were carried out at 37°C in PBS. Fluorescence of the intrinsic Trp probes of 20 µM WT αB-crystallin (black squares) and 20 µM αB-crystallin-3E was quenched by the step-wise addition of acrylamide. Plotting the relative decrease in fluorescence (F_0/F) against the quencher concentration (Stern-Volmer plot) indicated higher accessibility, i.e. more quenching, for the phospho-mimicking mutant.

Limited proteolysis experiments can be used to probe conformational features of proteins (Hubbard, 1998). α-chymotrypsin was used as a protease because several predicted cleavage sites are located within the N-terminal region (Figure 39), which is the primary candidate for an involvement in substrate interactions. Analysis of the experiments by SDS-PAGE revealed a faster proteolytic cleavage of αB-crystallin-3E compared to WT αB-crystallin (Figure 67). After 45 min αB-crystallin-3E was almost completely degraded while the wild type αB band was still present. In addition, the cleavage patterns of both proteins differed. The major peptide products of proteolytical cleavage were identified using LC-MS. This approach revealed the bonds following W9, F47 and M68 as the three major proteolysis sites. The band corresponding to αB-crystallin(10-175) occurs in both proteins indicating a similar accessibility of the most N-terminal cleavage site W9 for WT and 3E. However, the αB-crystallin(48-175) band was detected after shorter incubation times in the case of the phospho-mimicking mutant. The difference was even more pronounced for αB-crystallin(69-175), which could not be detected for WT αB-crystallin in

the course of the experiment. Limited proteolysis revealed that phosphorylation induces structural changes within the NTD indicating an important function of this domain in controlling the oligomer size by phosphorylation.

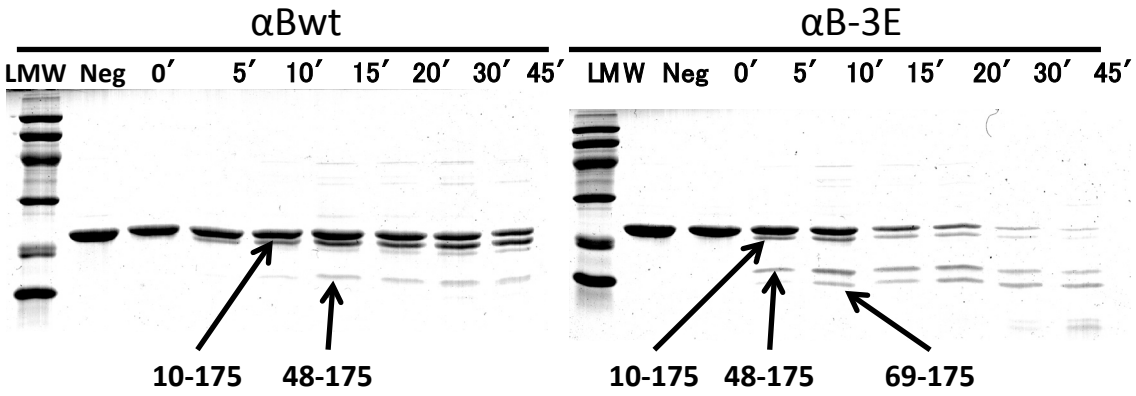

Figure 67 | Assessing conformational properties of WT αB-crystallin and αB-crystallin-3E by limited proteolysis. αB-crystallin (10 µM) was incubated with 1:25 (w:w) α-chymotrypsin in 100 mM Tris, 100 mM NaCl, 10 mM $CaCl_2$, pH 7.8 at 25°C for 30 min. Proteolysis reactions were terminated with 2 mM phenylmethylsulfonyl fluoride (PMSF) after various time points and analyzed by SDS-PAGE. The cleavage products were identified using LC-MS. The respective bands are indicated by an arrow and labeled with the identified peptide. Samples without chymotrypsin (Neg) were included as control.

Taken together, the results of ANS binding, tryptophan fluorescence quenching and limited proteolysis support the idea that partial dissociation caused by phosphorylation increases the surface accessibility of sites within the N-terminal region thereby enhancing the overall hydrophobicity compared to the non-phosphorylated storage form of αB-crystallin.

4.7 The Role of αB-Crystallin in the Cellular Proteostasis Network

Numerous diseases were shown to be linked to αB-crystallin. The "disease mutant" R120G was shown to cause cataract and desmin-related myopathy (Vicart et al., 1998) indicating a chaperone function in the eye lens and muscle cells. Although more specific interactions with cytoskeletal components, as well as proteins involved in cell cycle control have been described, the identification of *in vivo* substrates needs further attention (Basha et al., 2012). Interplay of αB-crystallin with other components of the cellular proteostasis control can be assumed from other sHsps but more definite experimental evidence is needed.

4.7.1 Thermal Aggregation of HeLa Cell Lysate Proteins

Lysates of HeLa cells were prepared by hypotonic swelling. Western blotting showed that HeLa lysates did not contain detectable amounts of αB-crystallin, whereas Hsc70 and Hdj1 could be detected (Figure 68). No cross-reactivities of the monoclonal antibodies with yeast proteins were detected.

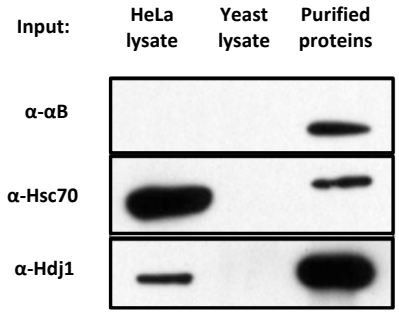

Figure 68 | Detection of αB-crystallin and other Hsps in HeLa lysate by western blotting. Yeast lysate as well as the recombinantly produced and purified proteins were used as control.

Non-stressed HeLa lysate was divided into a soluble and an insoluble fraction by centrifugation and subsequently analyzed by SDS-PAGE (Figure 69). As expected, the whole protein content was found in the soluble fraction, because the lysate was cleared by centrifugation during preparation. After incubation at 45°C for 40 min, a large portion of lysate proteins was found in the insoluble fraction.

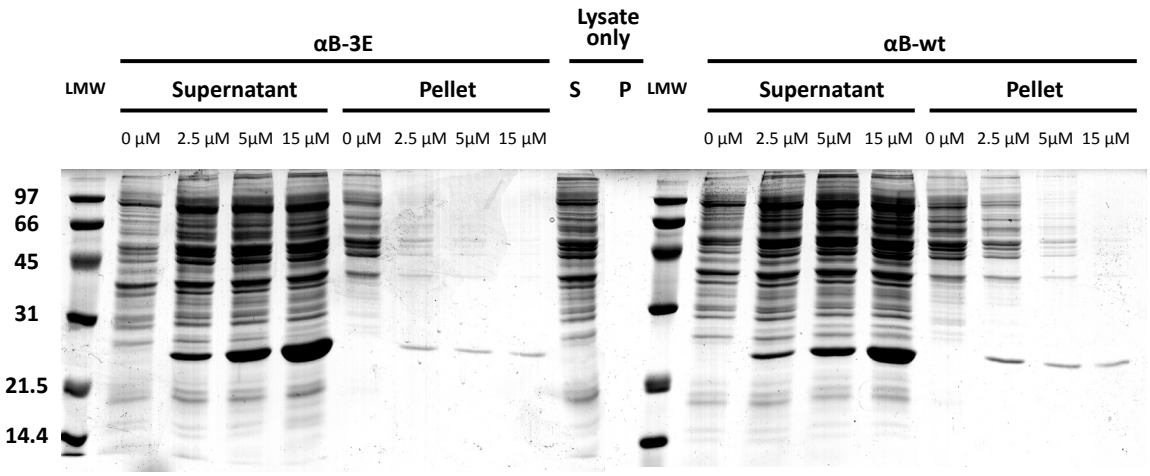

Figure 69 | Thermal aggregation of HeLa cell lysate. HeLa cell lysate (final absorbance $A_{280} \approx 2$) was heat-stressed at 45°C for 40 min in the presence of various amounts of WT αB-crystallin (right gel) and αB-crystallin-3E (left gel). The soluble (supernatant; S) and the insoluble (pellet; P) protein fractions were separated by centrifugation (10 min, 10,000 g, 4°C) followed by SDS-PAGE analysis. Both αB variants suppressed the aggregation of numerous lysate proteins with αB-crystallin-3E showing higher chaperone activity.

To study the holdase function of αB-crystallin in the presence of the complete proteome, HeLa lysate samples were supplemented with different amounts of WT αB-crystallin and αB-crystallin-3E prior to heat shock. The presence of αB-crystallin shifts the heat-aggregated proteins in a concentration-dependent way to the soluble fraction. In the presence of 15 µM WT αB-crystallin, only few faint bands were visible in the insoluble fraction. In the case of αB-crystallin-3E, 5 µM were already sufficient to yield a comparable effect and aggregation was fully suppressed by 15 µM (Figure 69). To analyze the heat-sensitive fraction of the proteome, the pellet fraction was subjected to ESI-MS after tryptic digestion. A set of more than 300 proteins was identified, for which at least two unique peptides were found (for the full list see 6 *Appendix*). Among these proteins were numerous metabolic enzymes with housekeeping functions, e.g. enolase or glyceraldehydes-3-phosphate dehydrogenase (GAPDH), which are both enzymes in glycolysis. It should be noted that the high levels of such housekeeping enzymes probably facilitated their identification by MS analysis. Furthermore, glycolytic enzymes are often overexpressed in cancer cells, called the Warburg effect (Koppenol et al., 2011; Warburg, 1956). However, many heat shock proteins were also among the identified hits, which can be explained by their affinity towards non-native proteins. Finally, also potential *in vivo* substrates of αB-crystallin, like actin and tubulin (Mounier and Arrigo, 2002; Wettstein et al., 2012), were found in the insoluble fraction after heat shock. All these proteins do not necessarily represent important *in vivo* substrates, but this approach showed that all these proteins can be protected from heat-induced aggregation within a complex protein environment by the chaperone function of αB-crystallin.

Taken together, the thermal aggregation of HeLa cell lysate revealed that αB-crystallin is able to efficiently suppress the aggregation of all heat-labile lysate proteins indicating a rather promiscuous binding to unfolding polypeptides. This result suggests a rather general function of αB-crystallin in protecting the proteome from stress-induced aggregation.

4.7.2 Refolding of Malat Dehydrogenase

The work presented in this thesis shows that αB-crystallin is able to capture rather promiscuously unfolding proteins to prevent their aggregation *in vitro*. This property was studied in many different ways since its first description by Horwitz in 1992, but the cellular fate of αB-substrate complexes remained largely unknown. Previous studies showed for several sHsps that they keep bound substrates in a refolding competent state. The subsequent refolding is mediated *in vitro* by ATP-dependent chaperones including the

Hsp70 system (Ehrnsperger et al., 1997; Lee et al., 1997) and also the Hsp100 chaperones (Haslbeck et al., 2005b; Mogk et al., 2003). For α-crystallins, such an interaction with other chaperones in substrate refolding has not been reported yet.

To test the refolding of substrates that are bound to αB-crystallin, the temperature-induced aggregation of the model substrate malate dehydrogenase (MDH) was used. MDH aggregation assays revealed binding by αB-crystallin and confirmed the stimulating effect of phospho-mimicking on its holdase activity (Figure 70). However, the beneficial effect of αB-crystallin-3E was rather subtle compared to equivalent concentrations of WT αB-crystallin.

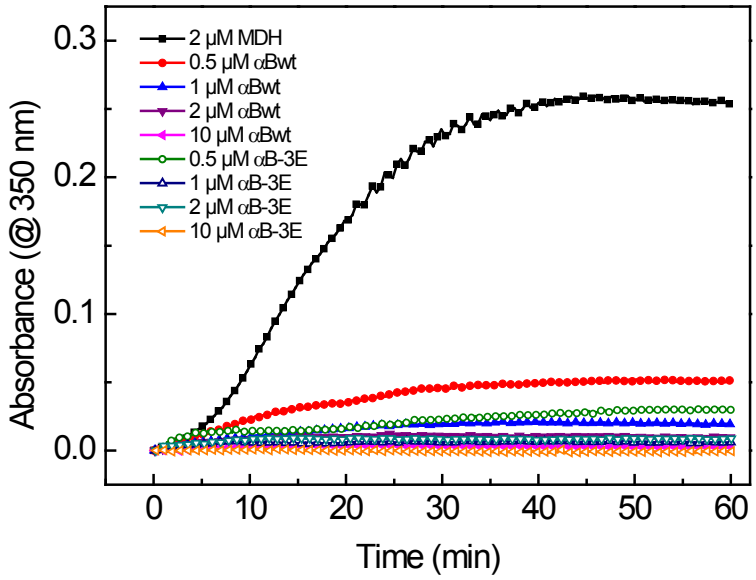

Figure 70 | Thermal aggregation of MDH. The aggregation of 2 µM MDH (black squares) was induced by heat shock at 46°C and monitored by absorbance at 350 nm in HKM buffer. The chaperone activity of WT αB-crystallin and αB-crystallin-3E was assessed in the presence of 0.5-10 µM of the respective αB variant see legend for color and symbol coding).

The enzyme MDH was heat-denatured either without αB-crystallin or in the presence of a 5-fold excess WT αB-crystallin or 3E. The inactive MDH was subsequently reactivated in the presence of combinations of human Hsc70 and Hdj1 (Hsp40) and an ATP-regenerating system. Reactivation was followed over 5 h using a colorimetric enzyme assay. The presence of αB-crystallin is essential to yield any refolding activity. Interestingly, a more than 3-fold higher final regeneration of MDH was observed when bound to 3E compared to WT αB-crystallin (Figure 71) even though a 5-fold excess of each αB-crystallin variant was used, which was in both cases sufficient to suppress MDH aggregation completely (Figure 70). As expected the substrate release and refolding strictly depended on the

presence of ATP. In addition, efficient refolding was only possible in the presence of Hsc70 and Hdj1 implying an essential cooperation of both chaperones in the release and refolding of substrates bound to αB-crystallin.

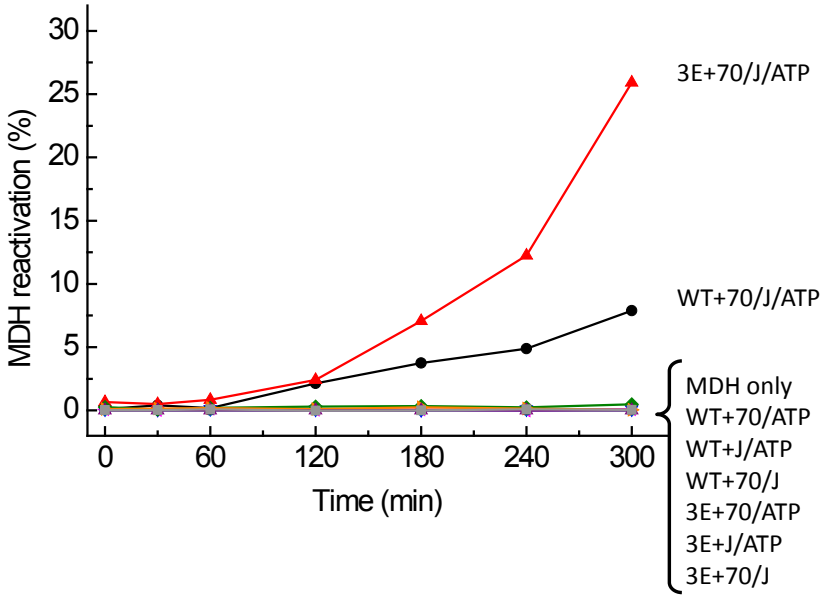

Figure 71 | Refolding of heat-denatured MDH. 2 µM MDH were heat-denatured for 45 min at 46°C either without αB-crystallin or in the presence of 10 µM WT αB-crystallin or 10 µM 3E. The inactive MDH was subsequently reactivated in the presence of a mixture of human Hsc70 ("70") and the Hsp40 co-chaperone Hdj1 ("J") and an ATP-regenerating system. Reactivation was followed over time using a colorimetric enzyme assay. Refolding yields are based on the activity of a native control which was equally treated.

The MDH refolding experiments indicate that the function of phosphorylation is not limited to modulating the substrate binding property but also affects the subsequent refolding by the Hsp70 system.

4.7.3 Reactivation of the Transcription Factor p53

As shown, thermal aggregation of the transcription factor p53 was efficiently suppressed by binding preferentially to small oligomeric species of αB-crystallin-3E (Figure 63). Since MDH could be efficiently refolded by Hsc70 and Hdj1 after binding to αB-crystallin-3E, we wondered if p53 can be reactivated by the same chaperone system. As the native state of p53 is correlated to its DNA binding ability, an electrophoretic mobility shift assay (EMSA) was performed to probe refolding of heat-denatured p53 by binding to its specific response element. 3 µM p53 were incubated at 42°C for 30 min in the absence or presence of 15 µM WT αB-crystallin or αB-crystallin-3E. As a positive control, native p53 was kept at 4°C. Reactivation of p53 was performed using 2 µM Hsc70

and 0.5 µM Hdj1 in the presence of an ATP regenerative system. An ATP-dependent partial refolding of p53 by Hsc70 and Hdj1 could be observed when the thermal inactivation was performed in the presence of αB-crystallin-3E (Figure 72). As expected, WT αB-crystallin alone did not allow p53 reactivation. Similar to the results with MDH, neither Hsc70 nor Hdj1 alone were sufficient to result in DNA binding-competent, refolded p53.

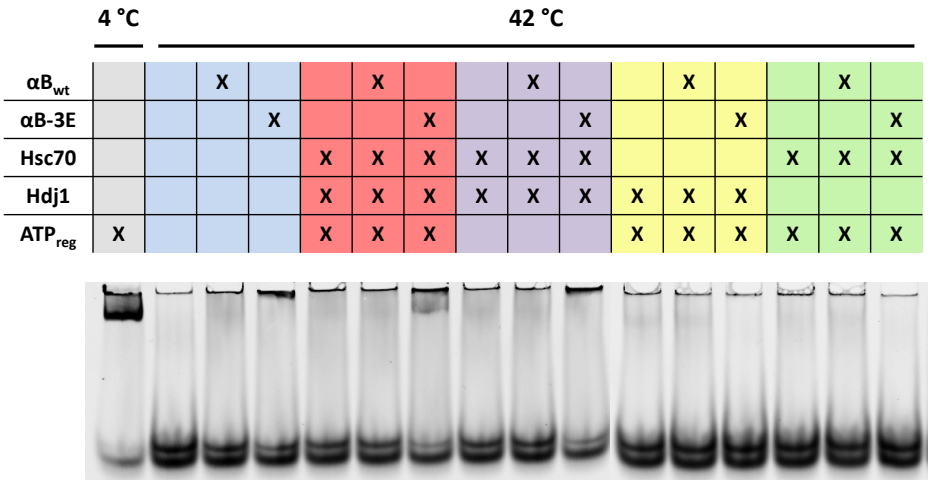

Figure 72 | Reactivation of heat-denatured p53. Human recombinant p53 was heat-denatured in HKM buffer at 42°C for 30 min either without or in the presence of 15 µM WT αB-crystallin or 15 µM 3E (as control native p53 was kept at 4°C, grey). Human Hsc70, Hdj1, an ATP regenerating system, WT αB-crystallin or αB-crystallin-3E were used in different combinations to rescue p53. To measure DNA-binding ability of reactivated p53 an electrophoretic mobility shift assay (EMSA) with a specific Cy5-labeled p21 gene promoter-derived sequence was performed. The presence of αB-crystallin-3E, Hsc70, Hdj1 and ATP is essential to yield reactivated p53 (red). Neither Hsc70 (yellow) nor Hdj1 (green) alone were sufficient. No reactivation was observed without ATP (violet).

The p53 reactivation experiments showed that αB-crystallin can keep even complex substrate proteins in a refolding-competent state during stress conditions. The transcription factor p53 is a tetrameric protein with highly flexible regions, which renders the refolding after heat-inactivation presumably complicated. Nevertheless, a system comprised of Hsc70 and Hdj1 allowed partial refolding. The example of p53 implies a crucial role of phosphorylation in the regulation of αB-crystallin function within the cellular proteostasis network.

5 Discussion

Small heat shock proteins constitute a diverse and widespread family of molecular chaperones. They are virtually ubiquitous proteins, which are present in all kingdoms of life. In fact, only very few parasitic bacteria are known that do not contain at least one sHsp representative in their genome. sHsps were first identified in *Drosophila melanogaster* as heat-inducible proteins of small monomer mass (Tissieres et al., 1974). The expression of many sHsps is upregulated as part of the cellular stress response, but they also function constitutively in many cell types and organisms (Basha, 2012). Most sHsps are able to act as ATP-independent molecular chaperones by preventing the irreversible aggregation of non-native proteins, which is achieved by their efficient holdase activity. Strikingly, in comparison to the other major Hsp families, sHsps are less studied – probably therefore also less understood. This perception can be found throughout literature (Basha et al., 2012; Haslbeck et al., 2005a), which is noteworthy regarding their ubiquitousness. Supposedly, this can be explained by their structural diversity and rather general function. Among the most prominent members of the sHsp family are the α-crystallins.

Within the scope of this thesis, the structure and function of α-crystallins were investigated *in vitro*. This work was essentially focused on the question how the dynamic α-crystallin oligomers accomplish their function as molecular chaperones. To tackle this question, various biochemical and biophysical methods were applied.

5.1 The Dynamic Architecture of α-Crystallins

Most proteins are characterized by an inherently highly dynamic behavior, which is reflected by interconverting conformers. These structural changes can span all levels of protein organization ranging from local fluctuations to large domain movements or even different oligomeric assemblies. The switching of proteins between different conformations is considered an essential trait to fulfill their biological functions.

The α-crystallins assemble into large oligomers with a variable number of subunits. The different oligomeric assemblies are interconverted by a temperature-dependent dynamic exchange of subunits. To understand the chaperone function of α-crystallins, a detailed investigation of its striking structural organization was an important goal of this work.

However, the aforementioned properties have impeded high-resolution structural studies. In recent years, several structures of isolated α-crystallin domains (ACD) were solved by X-ray crystallography or NMR (Bagneris et al., 2009; Jehle et al., 2009; Laganowsky et al., 2010), but not a single full-length structure of α-crystallin (or any other oligomeric metazoan sHsp) is available. Although the eponymous ACD is the defining structural element of the sHsp family, oligomerization is dependent on the N- and C-terminal segments because isolated ACDs only form stable dimers (Bagneris et al., 2009). During the presented work, numerous attempts to crystallize full-length αB-crystallin were undertaken and failed. Also partial cross-linking using combinations of introduced cysteines did not allow for successful crystallization. In this regard, the name "crystallin" is rather ironic. Thus, multiple structural methods covering the whole resolution range and supporting biochemical techniques were integrated in so-called "hybrid approaches".

Our initial approach combined SEC, AUC, and NS-EM analysis to study the structure of recombinant αA- and αB-crystallin as well as authentic α-crystallin from bovine lenses. Interestingly, the s-values from AUC analysis of all four species were shown to be independent of concentration within the range of 2-150 µM, which was also reported previously (Horwitz, 2009). This property allows comparing the results of structural methods, which are used at different concentrations of αB-crystallin.
According to the combined results from AUC and NS-EM, human recombinant αB-crystallin formed distinct complexes consisting of 24 subunits. αA-crystallin forms also smaller oligomers and large clusters consisting of individual oligomers. This heterogeneity also dominated in mixed complexes consisting of both αA- and αB-crystallin. Interestingly, authentic αL-crystallin seemed to possess, as compared to the mixture of recombinant αA- and αB-crystallin, a larger degree of heterogeneity including large oligomer clusters giving rise to the assumption that the formation of oligomer clusters might be influenced by posttranslational modifications of the α-crystallins in the eye lens. Whether these modifications are important for maintaining the transparency of the eye lens or are merely the result of aging remains to be elucidated. It is noteworthy that the deletion of αB-crystallin has no lens phenotype while the deletion of αA-crystallin leads to severe cataract, i.e. the formation of large aggregates of eye lens proteins, as shown by gene deletion studies in mice (Brady et al., 1997; Brady et al., 2001). Thus, it is tempting to speculate that the two α-crystallins differ not only in their structural but also in their functional properties in lenticular cells with αA-crystallin being the more active chaperone

towards lens proteins such as the β- and γ-crystallins. However, *in vitro* aggregation assays did not reveal increased chaperone activity of αA-crystallin. Furthermore, the additional heterogeneity introduced by αA-crystallin might be essential to abolish higher order structures of α-crystallins under the extremely high protein concentrations (~450 mg/ml) in the eye lens. However, the exact reasons for the presence of two different isoforms in the eye lens and the essential role of αA-crystallin evidenced by knock-out mice remain elusive. It is not clear whether differences in the physicochemical properties of αA and αB or in the regulation of their expression are the cause. Another aspect to consider is that α-crystallins have to be permanently active in the eye lens for several decades due to the lack of protein turn-over. In the case of α-crystallin, binding sites permanently available on the surface of the oligomer may interact with each other leading to the formation of larger assemblies.

Due to the highest homogeneity among the analyzed α-crystallins, all further efforts were focused on αB-crystallin. By negative stain electron microscopy and image processing, we were able to reconstruct a three-dimensional model of the αB-crystallin assembly at 20 Å resolution. In line with the oligomer architectures observed for other sHsps, the αB-crystallin oligomer model obtained from NS-EM and image processing was a hollow, sphere-like assembly. Admittedly, the homogeneity of αB-crystallin was overestimated at that point of the project. Nevertheless, this structure represented a significant advance in understanding the structural biology of αB-crystallin. An earlier cryo-EM study suggested an asymmetric and roughly spherical model of 32-meric αB-crystallin (Haley et al., 1998) (Figure 73). The asymmetric model has been supposed to reflect the polydispersity of αB-crystallin. The 32-meric model was not challenged for several years although studies using tandem MS proposed the oligomer size to range from 24 to 32 subunits with 28-mers being the most frequent assembly form (Aquilina et al., 2003). Our model presented a new concept of αB-crystallin structure as we proposed an assembly with tetrahedral symmetry. In recent years, further integrated structural biology approaches have been applied to study its molecular architecture. Consecutively, two models using solid-state NMR accompanied by small-angle X-ray scattering (SAXS) (Jehle et al., 2010) and SAXS/EM (Jehle et al., 2011) were proposed, which were both based on our tetrahedral 24-mer model (Figure 73).

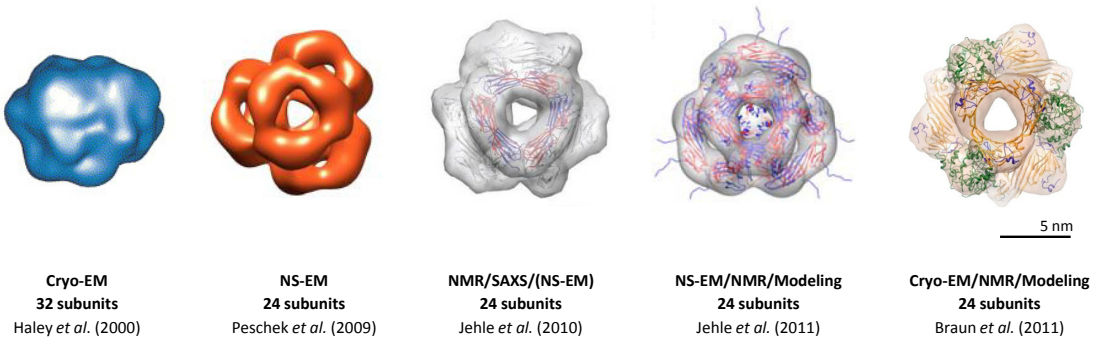

Figure 73 | Evolution of proposed αB-crystallin oligomer structures. Selected 3D reconstructions for αB-crystallin are depicted according to their publication date from left to right. The main methods, number of subunits within the reconstruction and references are given below the respective 3D model.

Subsequently, we reconstructed a 3D model of 24-meric αB-crystallin using cryo-EM at a resolution of 9.4 Å. The major improvement in resolution cannot be explained only by the use of vitrified instead of negatively-stained preparations for EM but elaborated methods of single particle analysis performed in the group of Prof. Sevil Weinkauf (Technische Universität München) were essential to deal with the inherent heterogeneity. Combining the EM model with NMR data and molecular modeling, a pseudoatomic model of 24-meric αB was constructed. Biochemical methods including cross-linking/MS and site-specific quenching of fluorescence could validate essential features of the calculated model, such as the association of hexameric substructures through interactions of the N-terminal regions, which cluster at the area around the closed 3-fold symmetry axis. In our model, the N termini do not point towards the interior of the oligomer as proposed in a previous study (Jehle et al., 2011) (Figure 73). The location of the NTD within the oligomer is a crucial aspect because of a lack of high-resolution structural data of this domain, which is a key regulator of αB-crystallin oligomerization and function. The physical contacts between NTDs of different subunits were evidenced by cross-linking of the N termini (Met1). Unfortunately, the complete lack of lysine residues within the NTD reduced the number of supporting cross-links. Clearly, our model only suggests one static structure for the NTD, which is rather improbable to be true in solution due to its high degree of flexibility. In the crystal structure of MjHsp16.5, the NTDs are not resolved (Kim et al., 1998) indicating that even in the context of a monodisperse sHsp assembly the N-terminal region does not necessarily adopt one defined conformation. Model-based mutagenesis within the NTD of αB-crystallin might be carried out to underpin the proposed structure. The predicted α-helices, which were assigned to rod-like densities, could be probed by the introduction of

proline or glycine residues, which have poor helix-forming propensities. In this regard, it would also be interesting to test whether perturbation of the predicted α-helices affects the oligomerization.

The 24-meric model represents a large fraction of the αB EM data set, but it is only one assembly form out of many possibilities within the oligomer equilibrium. The varying number of subunits impedes structural elucidation. Sophisticated single particle analysis allowed separation of the heterogeneous data set and the 3D reconstruction of additional well-defined assemblies with larger or smaller number of subunits. Based on a common molecular architecture, only few structural variations are necessary to cause heterogeneity. In the presence of destabilizing concentrations of the denaturant GdnCl, intermediate substructures were enriched indicating different intermolecular contacts, which all contribute to the oligomer formation. A recent study suggested, on the basis of MS experiments performed under a range of conditions, a simple mathematical model for oligomerization of αB-crystallin with just two oligomer-independent interactions between constituent monomers (Baldwin et al., 2011b). However, a structure-based thermodynamic and kinetic description that explains all aspects of the dynamic oligomer equilibrium including the roles of the NTD and CTD is still lacking. How mutants can destabilize intersubunit contacts leading to increased dissociation is exemplified by phosphor-mimicking mutants, which are discussed in one of the following sections.

5.2 The Chaperone Function of α-Crystallins

Small heat-shock proteins function as molecular chaperones (Horwitz, 1992; Jakob et al., 1993), yet their role within the cellular proteostasis is rather poorly understood compared to other major chaperone families. They seem to bind promiscuously to miscellaneous client proteins in an ATP-independent manner. sHsps are thus widely considered as ubiquitous buffering system towards deleterious protein aggregation in the cell, which is illustrated by the term “molecular sponges” (Eyles and Gierasch, 2010). Phylogenetic studies proposed that sHsps diverged early in evolution implying a very basic and rather general role in cellular proteostasis.

Monitoring the reduction-induced aggregation of the model substrate lysozyme allowed assessing the chaperone function of α-crystallins. αA-, αB- and αL-crystallin all suppressed aggregation to a similar extent. Therefore, all further efforts were focused on the ubiquitous isoform αB. The substrate complexes between reduced lysozyme and αB

proved to be rather stable. This property facilitated the study of the morphology of these complexes by different methods.

Although it is not known to what extent the *in vitro* aggregation of model substrates is suited to mimic physiological conditions, the DLS and SV-AUC experiments suggest two different kinds of substrate complex formation. When present in large excess, one αB-crystallin oligomer binds multiple substrate molecules. With increasing concentrations of aggregating substrate, several αB-crystallin molecules are recruited into MDa-sized substrate complex. These methods do not reveal the sequence of these processes. Aggregation and binding by the chaperone are competing processes. The huge complexes, which form at a two-fold molar excess (with regard to the monomer concentration) of αB-crystallin, might be the result of aggregate formation. These forming protein aggregates are then bound by the concerted action of several αB-crystallin oligomers. Although the degree of substrate unfolding required for recognition by αB-crystallin is still being investigated, there is evidence that early unfolding states are recognized (Cheng et al., 2008; McHaourab et al., 2009), which would contradict the binding of microaggregates. Another possibility is that non-native substrate molecules bind one by one to α-crystallin complexes, which leads to the accumulation of hydrophobic residues. With increasing amounts of bound substrate, multiple αB oligomers bind simultaneously to unfolded proteins to sequester aggregation-prone hydrophobic patches within large clusters (Figure 74). A similar model has been previously proposed for yeast Hsp26 (Haslbeck et al., 2005b) and murine Hsp25 (Ehrnsperger et al., 1999).

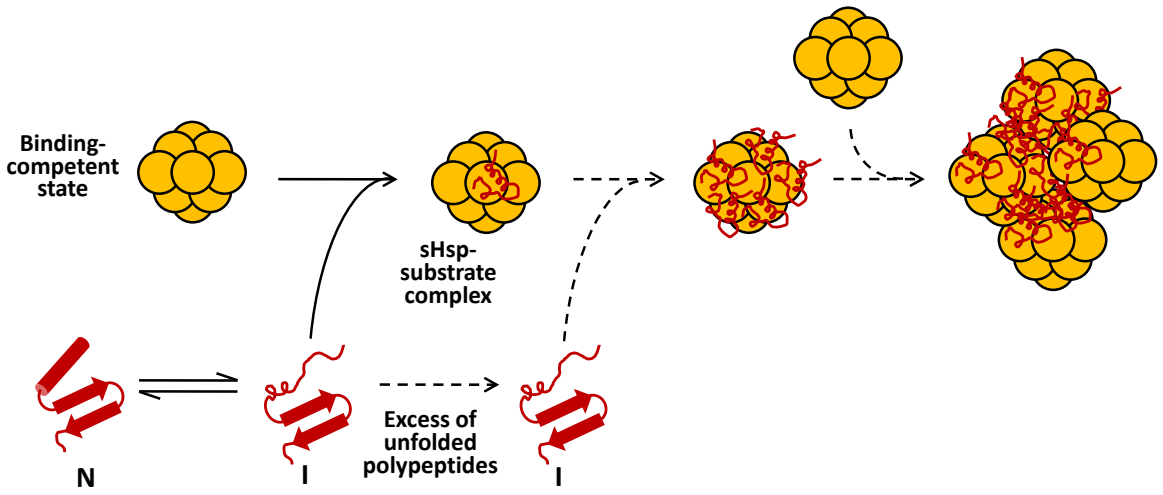

Figure 74 | Model of stepwise substrate binding.

The most commonly used methods to assess chaperone function of sHsps are aggregation assays in which the formation of light-scattering aggregates is monitored by absorbance in a UV spectrophotometer. This method is a very convenient and simple functional assay but the process of sHsp-substrate complex formation cannot be followed directly. In this regard, DLS was an advantage since it records the changes in hydrodynamic radius. However, the sensitivity of this method is limited and it does not provide any selectivity. The increase of the average R_h-value of the ensemble does not necessarily correlate with binding. Small aggregates might also cause an increase of the mean hydrodynamic radius. Therefore, a FRET-based assay was established. Using FRET, also early events during the binding process can be followed. Another advantage is the possibility to follow substrate release during refolding by ATP-dependent chaperone systems. The Hsp70 system comprised of human Hsc70 and Hdj1 mediated partial reversal of the FRET signal indicating the potential of this assay to monitor also substrate release. Due to the dependence on a redox system, lysozyme is limited as a model substrate. A major future goal is the transfer of this FRET-based assay to other substrates. The mechanism of substrate release is still poorly understood and a method that enables direct monitoring of this process might turn out to be a useful tool.

5.3 Regulating Structure and Chaperone Function of αB-Crystallin by Phosphorylation

Different mechanisms have been suggested to regulate the holdase function of sHsps. Besides protein expression, structural changes induced by different stimuli, such as temperature, pH or post-translational modifications are described. αB-crystallin is regulated within the cell in a similar way: Upon stress, its expression is increased (Ito et al., 1996; Klemenz et al., 1991) and three distinct Ser residues are phosphorylated (Ito et al., 1997).

We applied the concept of mimicking the phosphorylated state of αB-crystallin with Glu mutants and studied the influence of phosphorylation on structure and function in detail providing new mechanistic insights on how such a regulation might be achieved. Previous studies have shown by means of chromatographic methods and mass spectrometry that the introduction of phospho-mimicking residues leads to smaller αB-crystallin oligomers (Aquilina et al., 2004; Ito et al., 2001) and to increased SX rates (Ahmad et al., 2008). We confirmed both findings using different biophysical and structural methods. SEC and SV-

AUC revealed a direct correlation between oligomer size reduction and the number of introduced phospho-mimicking glutamates. Interestingly, αB-crystallin-3E exhibited a broad S-value distribution with two maxima. The smaller peak corresponded to 12-mers according to c(s) analysis. NS-EM images confirmed the increase in smaller assemblies and the increased heterogeneity. Especially suboligomeric species (2-6-mer class), which are hardly detectable for wild-type αB-crystallin, represented a major species of αB-crystallin-3E. Hetero-oligomers, which were formed via SX after mixing of WT and 3E, also showed changes in oligomer equilibria depending on the ratio of both subunits. Increased incorporation of αB-crystallin-3E into the mixed oligomers caused reduction of the average oligomer size. In the scope of a previously published pseudoatomic model of a 24-meric WT αB-crystallin assembly, we hypothesized already that the phosphorylation sites are proximal within dome-like structures comprised of N-terminal regions (Braun et al., 2011), which could be confirmed using cysteine cross-linking. It is tempting to speculate that the close proximity of the introduced charges destabilizes the oligomers resulting in accelerated dissociation rates and thus an increased amount of smaller assembly forms.

Regarding the chaperone function, most previous studies described increased binding of non-native proteins by mimicking phosphorylation (Ahmad et al., 2008; Ecroyd et al., 2007; Koteiche and McHaourab, 2003) but also contrary results were published (Ito et al., 2001). Our data for the model substrate MDH and two potentially physiological clients, γD-crystallin and p53 indicated more efficient aggregation suppression after αB-crystallin phosphorylation. The suppression of heat-induced aggregation of the transcription factor p53 had a strong correlation with the presence of phospho-mimicking glutamates. The interaction of αB-crystallin and p53 has been shown by pull-down experiments in human cell lines (Watanabe et al., 2009). In the cell, both proteins are also linked through the transactivation of αB-crystallin expression by p53 (Evans et al., 2010; Watanabe et al., 2009). Furthermore, cells of αB-crystallin knockout mice show hyperproliferation due to impaired p53 checkpoint function in these cells (Bai et al., 2003). Despite these reports, the interaction between αB-crystallin and p53 is not a generally established concept. However, a recent study linked p53-related cancer to aggregation and the heat shock response. An aggregation-prone mutant of p53 had a dominant-negative effect on wild-type p53 function due to coaggregation inducing the upregulation of several Hsps (Xu et al., 2011).

The relevance of phosphorylation of αB-crystallin in the eye-lens also remains elusive. Our data indicated improved aggregation suppression of αB-crystallin-3E towards lens proteins

of the β/γ-crystallin family. This role in the maintenance of eye lens transparency has been already postulated in the first report on αB-crystallin chaperone function (Horwitz, 1992). However, Wang et al. have found that phosphorylated and unphosphorylated αB-crystallin purified from rat lenses possess similar chaperone activity (Wang et al., 1995). The role of phosphorylation in the eye lens might be different, because authentic αL-crystallin exhibits larger oligomer sizes in comparison to recombinantly produced protein. In addition, the observed increase in polydispersity upon phosphorylation might be important for lens transparency by inhibiting crystallization or phase separation of αB-crystallin under the high concentrations present in lenticular cells.

With regard to the impacts of the individual phosphorylation sites, we could not observe major differences between the three studied residues. Nonetheless, the existence of three sites might enable a more variable regulation *in vivo* by distinct serines being phosphorylated in response to diverse stress conditions. It was shown that different kinases and their pathways are involved in the phosphorylation of αB-crystallin resulting in different modification patterns depending on the kind of stress (Hoover et al., 2000; Kato et al., 1998). It is rather unlikely that the majority of oligomers within the cell is fully phosphorylated at all three sites simultaneously. However, our results for the different 1E and 2E mutants show that the binding activity is increased progressively by the amount of introduced phospho-mimicking residues. The observed effects of mimicking Glu residues on structure and function of αB-crystallin might be even stronger with phosphoserines, as described for Hsp27 (Hayes et al., 2009), suggesting a considerable activation upon partial phosphorylation. The activity of phosphatases, which are not known for αB-crystallin so far, would allow returning to the less active storage form by dephosphorylation. Together with the results on WT/3E hetero-oligomers, our data imply a potential regulation mechanism for αB-crystallin: By means of partial or differential phosphorylation and SX the binding affinity of αB-crystallin towards unfolded proteins may be adjusted precisely according to the demand of the cell.

5.4 The Structure-Function Relationship

Mimicking of phosphorylation had two major effects on αB-crystallin: a shift of the oligomer equilibrium towards smaller species and a concomitant increase in chaperone function. However, the αB-crystallin was activated to a different extent depending on the substrate studied. This observation implies a direct correlation between both properties. To

study the structure-function relationship of αB-crystallin, p53 turned out to be a very useful substrate because it is only prevented from heat-induced aggregation by phospho-mimicking mutants of αB. Hence, small oligomers were identified as the p53-binding species by fluorescence AUC indicating that these small oligomers are the more active assembly forms. Consequently, phosphorylation results in higher chaperone activity of the ensemble. This leads to the following key question: Which feature of small oligomers causes their preferential binding of non-native substrates? There are mainly two possible reasons: (1) Substrate interaction sites, which are buried in the 24-mer, become accessible upon activation. Such a mechanism would imply that the interaction sites do exist in the storage form but are covered by neighboring subunits. Upon removal of subunits the interacting patches are exposed. (2) Detachment of the NTDs leads to their destabilization, which results in a partial unfolding of N-terminal regions. The predicted α-helices might be a potential conformational switch. In this model, the reorganized flexible NTDs are involved in substrate binding. An activation mechanism, which combines aspects of both models, is also possible.

Based on several biochemical methods, we showed that an increased surface hydrophobicity and an altered accessibility to certain regions facilitate the binding of unfolding intermediates. ANS fluorescence indicated an increase of overall surface hydrophobicity upon mimicking of phosphorylation. This result is in contrast to a previous study (Ito et al., 1997). However, an increase of accessible hydrophobic patches is intuitively more likely to correspond to the more active αB-crystallin-3E. It should be noted that most of the hydrophobic residues are located within the NTD (Figure 75). Quenching of fluorescence revealed an increased accessibility of the intrinsic probes Trp9 and Trp60. Since the tryptophans are located within the NTD, none of the suggested activation mechanisms can be ruled out.

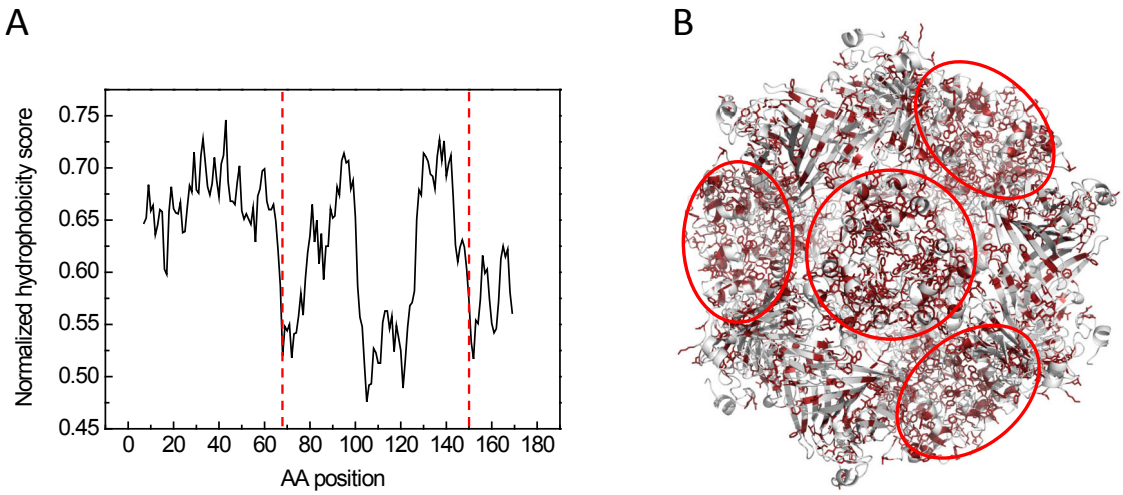

Figure 75 | Hydrophobicity of αB-crystallin. (A) Hydrophobicity plot of the αB-crystallin sequence. The hydrophobicity score was calculated on the basis of a hydrophobicity scale by Eisenberg et al. (1984) using the web-based application ProtScale (Wilkins et al., 1999). Domain barriers are indicated by interrupted red lines. (B) The presence of hydrophobic residues Trp, Phe, Tyr, Leu, Ile and Met within the αB 24-mer model is depicted in red. The areas around the 3_c axis are encircled.

Limited proteolysis combined with LC-MS revealed two sites within the NTD, F47 and M68, which are more accessible in αB-crystallin-3E compared to wild-type αB-crystallin. This result hints to an increased flexibility of the "C-terminal regions" within the NTD. A recent study has proposed a model in which energy-independent chaperones use order-to-disorder transitions to control substrate binding and release (Reichmann et al., 2012). The redox-regulated Hsp33, which functions as holdase during oxidative stress, is activated by partial unfolding. For αB-crystallin, such a mechanism could be achieved by phosphorylation-induced partial unfolding of the NTD. However, the major limitation is the indisputable identification of the substrate binding site. Clearly, the NTD functions as a phosphorylation-controlled switch for the oligomerization and chaperone function of αB-crystallin. Whether this domain is also the major site of substrate interaction, remains to be elucidated. Limited proteolysis experiments revealed reduced cleavage within the NTD upon binding of lysozyme but more evidence is needed. Sophisticated cross-linking applications or H/D exchange experiments combined with MS might help to overcome this problem.

5.5 The Role of αB-Crystallin within the Cellular Proteostasis

The role of αB-crystallin, and sHsps in general, within the cellular proteostasis network is not fully understood. The currently proposed function is not limited to the prevention of aggregation by their holdase activity. Instead, sHsps are supposed to maintain substrates in a refolding-competent state for subsequent refolding by ATP-dependent chaperones. The interplay of sHsps with the Hsp70 chaperone system in substrate refolding was first shown for Hsp25 (Ehrnsperger et al., 1997) and Hsp18.1 from pea (Lee et al., 1997). Chaperones from the Hsp100 family (Mogk et al., 2003) and chaperonins (Veinger et al., 1998) were also shown to assist in this process. Refolding of αB-crystallin-bound substrates by the Hsp70 chaperone system has not been reported so far. However, a very recent study showed that αB-crystallin stimulates depolymerization of α-synuclein amyloid by human Hsp70, Hsp110 and Hsp40 (Duennwald et al., 2012).

Our refolding experiments with MDH showed that, despite complete aggregation suppression, wild-type αB-crystallin yielded less efficient Hsp70-assisted refolding than αB-crystallin-3E indicating a positive influence of phosphorylation on the interplay with the Hsp70 system in client refolding. A minimal human Hsp70 system comprised of Hsc70 and Hdj1 mediated the ATP-dependent release and refolding of substrates bound to αB-crystallin. Neither Hsc70 nor Hdj1 alone were sufficient to accomplish this task. Though, other or additional components of the human Hsp70 system might further improve the interplay with αB-crystallin and also other sHsps. A simplified model of αB-crystallin activation and function within the cellular proteostasis network is illustrated in Figure 76.

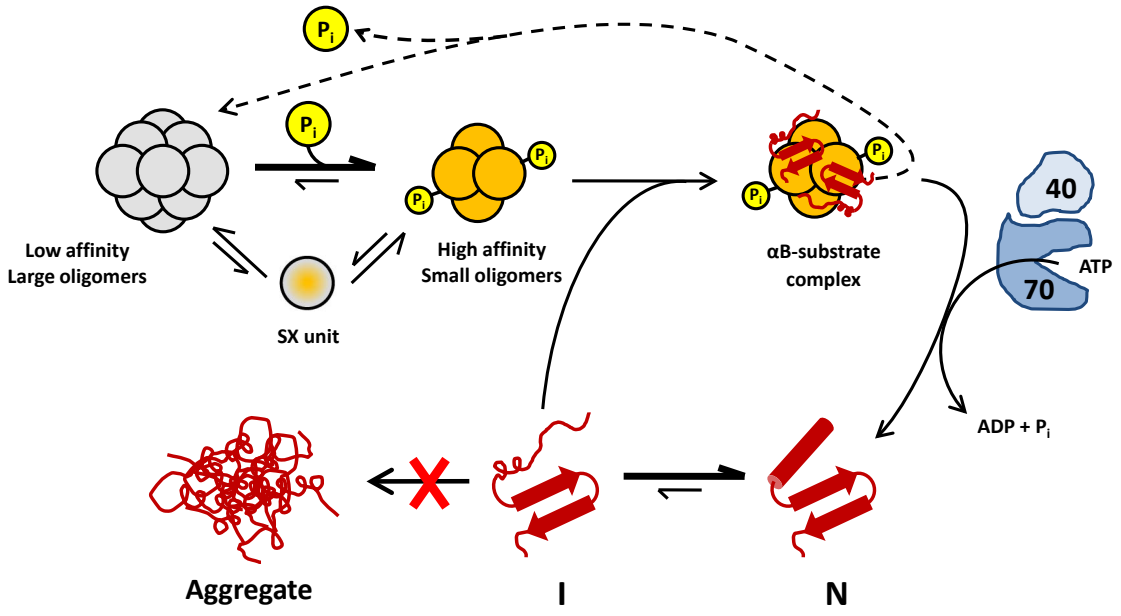

Figure 76 | Model of αB-crystallin activation and function within the proteostasis network. The chaperone function of αB-crystallin is correlated to its oligomer size. The 24-mer and related large assemblies represent the storage form, which is characterized by low affinity to unfolding proteins. Small oligomeric forms represent the active state. Both species are present in the dynamic oligomer equilibrium and can be interconverted by subunit exchange. Upon phosphorylation, the equilibrium is shifted towards smaller oligomers by partial dissociation. The active species bind unfolding intermediates to form stable αB-substrate complexes. The subsequent release and refolding of the bound substrate molecules is mediated by the Hsp70 system in ATP-dependent manner.

With regard to the chaperone function, most studies have been performed using model substrates. The identification of *in vivo* substrates is still a largely unexplored area of research. Two studies in bacteria and yeast have revealed rather promiscuous binding to a diverse set of substrates (Basha et al., 2004; Haslbeck et al., 2004a). For αB-crystallin, a similar picture emerged from the work presented in this thesis. Thermal aggregation of HeLa cell lysate revealed that αB-crystallin efficiently suppressed the aggregation of most heat-labile lysate proteins indicating a rather promiscuous binding to unfolding polypeptides. This result suggests that αB-crystallin functions as a "generalist" in protecting the proteome from stress-induced aggregation. Although MS analysis identified a large number of proteins that are shifted to the soluble fraction upon addition of αB, not all of these proteins have to interact directly with the chaperone. Aggregating proteins can also sequester meta-stable proteins to the insoluble fraction by coaggregation (Olzscha et al., 2011). Pull-down experiments might be useful to select proteins that interact directly with αB-crystallin. In preliminary experiments, thiol-specific biotinylation of αB-crystallin-S153C was shown to enable affinity pull-downs using streptavidin without interfering with the oligomeric size and chaperone function (data not shown). This

approach might allow identifying proteins that interact with αB-crystallin or preformed αB-substrate complexes in the future.

Besides the binding of partially folded client proteins and the interplay with the Hsp70 chaperone system in client remodeling, further known or putative interaction partners of αB-crystallin exist within the cell. Interestingly, the stress protection towards F-actin and other cytoskeleton components (Launay et al., 2006) as well as the anti-apoptotic effect in different cell types is reported to depend on the phosphorylation status of αB-crystallin (Launay et al., 2010). The partial dissociation of oligomers upon phosphorylation accompanied by changes of the surface might switch on the interaction with such clients specifically. To this end, it remains unclear whether phosphoserines themselves are involved in these interactions or whether they serve merely as activity switches to enable the access to surfaces that are buried in the non-phosphorylated αB-crystallin oligomers. For the interaction with unfolded proteins, the latter seems reasonable since the negative charges should interfere with the hydrophobic interactions involved in its chaperone function. However, mapping of the client interaction sites of αB-crystallin at high resolution is still missing and marks an important future goal.

6 Appendix

Table 3 | Heat-labile proteins from HeLa cell lysate identified by ESI-MS. The list contains all human proteins with more than two identified unique peptides. The hits are sorted according to their overall sequence coverage.

Description	Coverage (%)	Σ# Unique peptides
tubulin, beta polypeptide	65.99	5
glyceraldehyde-3-phosphate dehydrogenase	58.21	11
aldo-keto reductase family 1, member C2	55.42	9
enolase 1	53.46	16
aldo-keto reductase family 1, member C3	53.25	8
tubulin, alpha, ubiquitous	51.22	4
tubulin, beta, 2	51.01	3
cell division cycle 2 protein isoform 2	49.58	7
ribosomal protein SA	49.49	10
annexin 5	48.44	10
glutathione transferase	47.14	6
phosphoglycerate kinase 1	46.28	12
beta actin	45.60	11
chloride intracellular channel 1	43.15	6
triosephosphate isomerase 1	41.37	7
pyridoxal kinase	40.38	7
peptidylprolyl isomerase A isoform 2	40.00	2
pyruvate kinase 3 isoform 1	39.92	13
transketolase	38.84	13
eukaryotic translation initiation factor 4A, isoform 1	38.67	9
annexin I	38.44	9
carbonyl reductase 1	36.82	6
NAD(P)H menadione oxidoreductase 1, dioxin-inducible isoform b	36.67	7
guanine nucleotide binding protein (G protein), beta polypeptide 2-like 1	36.59	7
heat shock 90kDa protein 1, beta	35.77	8
peroxiredoxin 6	34.38	8
glutathione S-transferase M3	34.22	7
proliferating cell nuclear antigen	34.10	5
protein phosphatase 2, catalytic subunit, alpha isoform	33.66	7
lactate dehydrogenase B	31.74	6
ribosomal protein P0	31.55	6
transaldolase 1	31.45	10
PREDICTED: similar to Dihydrofolate reductase isoform 1	31.02	4
tubulin alpha 6	30.73	2
annexin A2 isoform 2	30.68	8
annexin IV	30.22	7
tyrosine 3/tryptophan 5 -monooxygenase activation protein, theta polypeptide	30.20	6
transgelin 2	30.15	4
keratin 1	30.12	14
secretory leukocyte peptidase inhibitor precursor	29.55	3
peroxiredoxin 1	29.15	4
keratin 10	28.94	13
keratin 9	28.89	8
prolactin-induced protein	28.77	3
adenylate kinase 1	28.35	4

tumor protein, translationally-controlled 1	27.91	3
chaperonin containing TCP1, subunit 2	27.85	9
heat shock 27kDa protein 1	27.80	4
pyrophosphatase 1	26.99	5
alanyl-tRNA synthetase	26.96	16
NADP-dependent leukotriene B4 12-hydroxydehydrogenase	26.14	5
argininosuccinate synthetase	25.73	7
adenine phosphoribosyltransferase isoform a	25.56	3
nucleophosmin 1 isoform 2	25.28	4
ubiquitin-activating enzyme E1	25.14	16
5-aminoimidazole-4-carboxamide ribonucleotide formyltransferase/IMP cyclohydrolase	25.00	8
eukaryotic translation elongation factor 2	24.94	12
heat shock 70kDa protein 8 isoform 2	24.14	5
ribosomal protein S3	23.87	4
fatty acid synthase	23.86	37
eukaryotic translation initiation factor 3, subunit 2 beta, 36kDa	23.38	6
5'-nucleotidase, cytosolic III isoform 2	23.23	5
ribosomal protein L9	22.92	3
integrin beta 4 binding protein isoform a	22.86	3
glutathione S-transferase M1 isoform 2	22.65	3
protein phosphatase 1, catalytic subunit, beta isoform 1	22.63	5
proteasome 26S non-ATPase subunit 7	22.22	5
esterase D/formylglutathione hydrolase	21.99	3
heat shock protein 90kDa alpha (cytosolic), class A member 1 isoform 2	21.86	6
chaperonin containing TCP1, subunit 4 (delta)	21.71	6
ribosomal protein S5	21.57	3
eukaryotic translation elongation factor 1 gamma	21.05	5
SUMO-1 activating enzyme subunit 1	20.52	5
PREDICTED: similar to 60S ribosomal protein L6 (TAX-responsive enhancer element binding protein 107) (TAXREB107) (Neoplasm-related protein C140) isoform 4	20.48	3
ATP citrate lyase isoform 1	20.44	15
phosphomannomutase 2	20.33	4
phosphoglucomutase 1	20.28	8
APEX nuclease	20.13	5
PREDICTED: similar to Phosphoglycerate mutase 1 (Phosphoglycerate mutase isozyme B) (PGAM-B)	20.00	2
lactate dehydrogenase A	19.88	4
serine (or cysteine) proteinase inhibitor, clade B (ovalbumin), member 5	19.73	5
threonyl-tRNA synthetase	19.64	9
UDP-galactose-4-epimerase	19.54	5
PREDICTED: similar to Importin alpha-2 subunit (Karyopherin alpha-2 subunit) (SRP1-alpha) (RAG cohort protein 1) isoform 3	19.43	3
proteasome 26S ATPase subunit 4 isoform 2	19.38	4
ribosomal protein S8	19.23	3
3'(2'), 5'-bisphosphate nucleotidase 1	19.16	3
PREDICTED: similar to 60S ribosomal protein L7 isoform 2	18.92	3
phosphoglycerate dehydrogenase	18.57	6
chaperonin containing TCP1, subunit 7 isoform a	18.23	6
phosphoserine aminotransferase isoform 1	18.11	5
ribosomal protein S7	18.04	2
cytidylate kinase	17.98	3
tubulin, beta 6	17.94	3
dihydropyrimidinase-like 2	17.83	6
T-complex protein 1 isoform a	17.63	5
ras-related nuclear protein	17.59	3
eukaryotic translation elongation factor 1 alpha 1	17.53	4

FK506-binding protein 4	17.21	5
chaperonin containing TCP1, subunit 8 (theta)	17.15	6
isocitrate dehydrogenase 1 (NADP+), soluble	16.91	5
eukaryotic translation initiation factor 2, subunit 1 alpha, 35kDa	16.83	4
proteasome beta 3 subunit	16.59	2
ribosomal protein S2	16.38	4
myosin, heavy polypeptide 9, non-muscle	16.38	23
proteasome 26S non-ATPase subunit 1	16.37	8
glucose phosphate isomerase	16.31	6
lysozyme precursor	16.22	2
GDP dissociation inhibitor 2	16.18	4
proteasome alpha 7 subunit	16.13	3
RAB1A, member RAS oncogene family	16.10	2
aldo-keto reductase family 1, member A1	16.00	3
cyclin-dependent kinase 2 isoform 2	15.53	2
isopentenyl-diphosphate delta isomerase	15.49	3
26S proteasome-associated pad1 homolog	15.48	2
proliferation-associated 2G4, 38kDa	15.48	5
methionine adenosyltransferase II, beta isoform 2	15.48	3
phosphofructokinase, platelet	15.43	7
serine/threonine kinase receptor associated protein	15.43	4
hypothetical protein LOC28989	15.25	2
glyoxylate reductase/hydroxypyruvate reductase	15.24	3
glyoxalase I	15.22	2
aldo-keto reductase family 1, member B1	15.19	3
phosphomevalonate kinase	15.10	2
chaperonin containing TCP1, subunit 3 isoform b	15.07	5
DNA directed RNA polymerase II polypeptide E	14.76	2
eukaryotic translation elongation factor 1 beta 2	14.67	2
vacuolar protein sorting 35	14.45	8
thioredoxin reductase 1	14.43	3
BUB3 budding uninhibited by benzimidazoles 3 isoform b	14.42	3
fumarate hydratase precursor	14.31	4
leukotriene A4 hydrolase	14.24	5
heat shock 70kDa protein 1-like	14.20	2
ribosomal protein L5	14.14	3
ribosomal protein L17	14.13	2
proteasome 26S ATPase subunit 3	14.12	4
proteasome beta 1 subunit	14.11	2
biliverdin reductase B (flavin reductase (NADPH))	14.08	2
hypothetical protein LOC84267	14.00	2
programmed cell death 6 interacting protein	13.94	8
heat shock 70kDa protein 4 isoform a	13.81	6
proteasome activator subunit 3 isoform 1	13.78	3
eukaryotic translation initiation factor 3, subunit 12	13.76	2
brain creatine kinase	13.65	3
annexin A3	13.62	4
CSE1 chromosome segregation 1-like protein	13.59	9
nascent-polypeptide-associated complex alpha polypeptide	13.49	2
acyl-CoA thioesterase 7 isoform hBACHd	13.07	3
sepiapterin reductase (7,8-dihydrobiopterin:NADP+ oxidoreductase)	13.03	2
NAD(P)H dehydrogenase, quinone 2	12.99	3
poly(rC) binding protein 1	12.92	3

exportin 1	12.89	9
proteasome alpha 5 subunit	12.86	2
N-acetylneuraminic acid phosphate synthase	12.81	3
aldo-keto reductase family 7, member A2	12.81	3
protein-L-isoaspartate (D-aspartate) O-methyltransferase	12.78	2
Rho GDP dissociation inhibitor (GDI) alpha	12.75	2
heat shock 105kD	12.70	7
ubiquitin-activating enzyme E1C isoform 3	12.67	2
ATP-binding cassette, sub-family E, member 1	12.52	5
proteasome 26S non-ATPase subunit 12 isoform 1	12.50	3
translin-associated factor X	12.41	2
clathrin heavy chain 1	12.36	13
methylenetetrahydrofolate dehydrogenase 1	12.30	8
vacuolar H+ ATPase E1 isoform c	12.24	2
proteasome 26S ATPase subunit 2	12.01	4
nucleolin	11.97	5
UDP-glucose dehydrogenase	11.74	3
isoleucine-tRNA synthetase	11.57	11
capping protein (actin filament) muscle Z-line, alpha 2	11.54	2
IQ motif containing GTPase activating protein 1	11.47	14
epiplakin 1	11.45	7
MYG1 protein	11.44	3
ARP1 actin-related protein 1 homolog A, centractin alpha	11.44	3
ribosomal protein S3a	11.36	2
cytosolic leucyl-tRNA synthetase	11.14	9
chromosome 12 open reading frame 5	11.11	2
phosphoribosyl pyrophosphate synthetase 2 isoform 2	11.01	2
PREDICTED: similar to ribosomal protein L13 isoform 2	10.94	2
mitogen-activated protein kinase 1	10.83	2
eukaryotic translation initiation factor 3, subunit 6 48kDa	10.79	3
mitogen-activated protein kinase kinase 2	10.75	3
ribosomal protein L3 isoform b	10.73	2
proteasome alpha 2 subunit	10.68	2
keratin 2a	10.64	4
dynein, cytoplasmic, heavy polypeptide 1	10.57	36
glutamyl-prolyl tRNA synthetase	10.52	10
protein arginine methyltransferase 5 isoform b	10.48	3
SUMO-1 activating enzyme subunit 2	10.47	3
calpain, small subunit 1	10.45	2
adenosine kinase isoform a	10.43	2
apolipoprotein A-I binding protein precursor	10.42	2
tyrosyl-tRNA synthetase	10.42	3
nicotinamide N-methyltransferase	10.23	2
glutamate-cysteine ligase regulatory protein	10.22	2
glucosamine-6-phosphate deaminase 1	10.03	2
PREDICTED: similar to Annexin A8 (Annexin VIII) (Vascular anticoagulant-beta) (VAC-beta)	9.92	2
deoxythymidylate kinase (thymidylate kinase)	9.91	2
methyltransferase-like protein 1 isoform a	9.78	2
tissue specific transplantation antigen P35B	9.66	2
translin	9.65	2
ribosomal protein L8	9.34	2
PREDICTED: similar to ATP-dependent DNA helicase II, 70 kDa subunit (Lupus Ku autoantigen protein p70) (Ku70) (70 kDa subunit of Ku antigen) (Thyroid-lupus autoantigen) (TLAA) (CTC box binding factor 75 kDa subunit) (CTCBF) (CTC75) isoform 4	9.30	2

sorbitol dehydrogenase	9.24	2
alpha isoform of regulatory subunit A, protein phosphatase 2	9.17	3
seryl-tRNA synthetase	9.14	2
arginyl aminopeptidase (aminopeptidase B)	9.08	3
coatomer protein complex, subunit gamma 1	9.04	5
calpain 2, large subunit	8.86	3
nuclear distribution gene C homolog (A. nidulans)	8.76	2
adenylyl cyclase-associated protein	8.63	2
glutamate-cysteine ligase, catalytic subunit	8.48	3
tRNA exportin	8.42	6
ribosomal protein S4, X-linked X isoform	8.37	2
glucose-6-phosphate dehydrogenase	8.35	2
heat shock 70kDa protein 5 (glucose-regulated protein, 78kDa)	8.26	2
ribonucleoside-diphosphate reductase M1 chain	8.21	4
heat shock 70kDa protein 1B	8.11	2
chaperonin containing TCP1, subunit 5 (epsilon)	7.95	3
pirin	7.93	2
spermine synthase	7.92	2
cytosolic malate dehydrogenase	7.78	2
biliverdin reductase A	7.77	2
hypothetical protein LOC134147	7.76	2
valyl-tRNA synthetase	7.75	7
arginyl-tRNA synthetase	7.73	3
DEAD/H (Asp-Glu-Ala-Asp/His) box polypeptide 3	7.70	3
phosphogluconate dehydrogenase	7.66	2
inositol(myo)-1(or 4)-monophosphatase 2	7.64	2
eukaryotic translation initiation factor 3 subunit 6 interacting protein	7.62	3
heterogeneous nuclear ribonucleoprotein H1	7.57	2
albumin precursor	7.55	3
WD repeat-containing protein 1 isoform 1	7.43	3
Ubiquitin isopeptidase T	7.43	3
proteasome 26S ATPase subunit 5	7.39	2
proteasome 26S non-ATPase subunit 2	7.27	3
phosphoribosylformylglycinamidine synthase	7.10	6
karyopherin beta 1	7.08	4
eukaryotic translation initiation factor 4 gamma, 1 isoform 4	7.06	7
B5 receptor	6.95	2
talin 1	6.85	10
cytosolic malic enzyme 1	6.82	2
ATPase, H+ transporting, lysosomal 70kD, V1 subunit A, isoform 1	6.81	3
guanine monophosphate synthetase	6.64	3
glycogen phosphorylase, liver	6.61	4
GTP-binding protein PTD004 isoform 1	6.57	2
RAN binding protein 5	6.55	4
hypothetical protein LOC23170	6.52	2
fascin 1	6.49	2
phosphoribosylglycinamide formyltransferase, phosphoribosylglycinamide synthetase, phosphoribosylaminoimidazole synthetase isoform 1	6.44	4
minichromosome maintenance protein 3	6.44	3
structural maintenance of chromosomes 2-like 1	6.35	6
platelet-activating factor acetylhydrolase, isoform Ib, alpha subunit (45kD)	6.34	2
actin related protein 2/3 complex subunit 2	6.33	2
annexin VI isoform 2	6.30	3
protein kinase, DNA-activated, catalytic polypeptide	6.23	19

heat shock 70kDa protein 4-like	6.20	2
proteasome 26S ATPase subunit 1	6.14	2
NOL1/NOP2/Sun domain family 2 protein	6.13	3
bifunctional phosphopantetheine adenylyl transferase/dephospho CoA kinase	5.85	3
glycyl-tRNA synthetase	5.84	2
CTP synthase	5.75	2
protein disulfide isomerase-associated 3 precursor	5.74	2
proteasome 26S non-ATPase subunit 3	5.62	2
thyroid hormone receptor interactor 13	5.56	2
dipeptidyl peptidase III	5.56	2
annexin A11	5.54	2
dynein, cytoplasmic, intermediate polypeptide 2	5.49	2
dynamin 1-like protein isoform 3	5.44	2
acetyl-Coenzyme A acetyltransferase 2	5.29	2
carbamoyl-phosphate synthetase 1, mitochondrial	5.07	5
filamin 1 (actin-binding protein-280)	4.80	9
carbamoylphosphate synthetase 2/aspartate transcarbamylase/dihydroorotase	4.76	7
GCN1 general control of amino-acid synthesis 1-like 1	4.72	8
nardilysin (N-arginine dibasic convertase)	4.68	4
karyopherin alpha 1	4.65	2
coatomer protein complex, subunit beta	4.51	3
PREDICTED: similar to eukaryotic translation initiation factor 3, subunit 8, 110kDa isoform 12	4.46	2
aminopeptidase puromycin sensitive	4.34	3
ribosomal protein S6 kinase, 90kDa, polypeptide 3	4.32	2
alpha glucosidase II alpha subunit isoform 2	4.13	3
aldehyde dehydrogenase 9A1	4.05	2
lysyl-tRNA synthetase	4.02	2
eukaryotic translation initiation factor 5B	4.02	3
coatomer protein complex, subunit beta 2 (beta prime)	3.97	2
adaptor-related protein complex 2, beta 1 subunit isoform b	3.84	2
glucosamine-fructose-6-phosphate aminotransferase	3.82	2
DEAD (Asp-Glu-Ala-Asp) box polypeptide 46	3.78	3
tumor rejection antigen (gp96) 1	3.74	2
oxygen regulated protein precursor	3.70	2
transportin 3	3.68	2
exportin 7	3.68	2
coatomer protein complex, subunit alpha	3.59	3
filamin B, beta (actin binding protein 278)	3.57	6
ATP-binding cassette, sub-family F, member 1 isoform b	3.47	2
heterogeneous nuclear ribonucleoprotein U isoform b	3.35	2
tripartite motif-containing 28 protein	3.35	2
dynactin 1 isoform 2	3.32	3
hypothetical protein LOC55236	3.14	3
eukaryotic translation initiation factor 3, subunit 10 theta, 150/170kDa	3.11	4
importin 7	3.08	2
mutS homolog 6	2.94	3
major vault protein	2.91	2
DEAH (Asp-Glu-Ala-His) box polypeptide 9	2.76	3
acetyl-Coenzyme A carboxylase alpha isoform 4	2.73	4
chromatin-specific transcription elongation factor large subunit	2.48	2
splicing factor 3b, subunit 3	2.47	2
ubiquitin specific protease 7 (herpes virus-associated)	2.45	2
beta-tubulin cofactor D isoform 1	2.27	2

exportin 5	2.24	2
SMC4 structural maintenance of chromosomes 4-like 1 isoform a	2.02	2
ubiquitin specific protease 9, X-linked isoform 4	1.41	3
retinoblastoma-associated factor 600	0.96	4

7 Abbreviations

3A	αB-crystallin-3A (S19/45/59A)
3E	αB-crystallin-3E (S19/45/59E)
ACD	α-Crystallin domain
AUC	Analytical ultracentrifugation
CTD	C-terminal domain
DLS	Dynamic light scattering
EM	Electron microscopy
FRET	Fluorescence resonance energy transfer
GdnCl	Guanidinium chloride
Hsp	Heat shock protein
LYI	Lucifer yellow iodoacetamide
M_b	Bent monomer (within the model of the αB-crystallin 24-mer)
MDH	Malate dehydrogenase
M_e	Extended monomer (within the model of the αB-crystallin 24-mer)
NMR	Nuclear magnetic resonance
NTD	N-terminal domain
R_h	Hydrodynamic radius
RT	Room temperature
SE	Sedimentation equilibrium
SEC	Size exclusion chromatography
sHsps	Small heat shock proteins
sHsp	Small heat shock protein
SV	Sedimentation velocity
SX	Subunit exchange
TAMRA	5(6)-Carboxytetramethylrhodamine succinimidyl ester
TEM	Transmission electron microscopy
αA	αA-crystallin
αB	αB-crystallin
αL	αL-crystallin (bovine α-crystallin purified from cow lenses)
γD	γD-crystallin

8 References

Ahmad, M.F., Raman, B., Ramakrishna, T., and Rao Ch, M. (2008). Effect of phosphorylation on alpha B-crystallin: differences in stability, subunit exchange and chaperone activity of homo and mixed oligomers of alpha B-crystallin and its phosphorylation-mimicking mutant. J Mol Biol *375*, 1040-1051.

Ahrman, E., Lambert, W., Aquilina, J.A., Robinson, C.V., and Emanuelsson, C.S. (2007). Chemical cross-linking of the chloroplast localized small heat-shock protein, Hsp21, and the model substrate citrate synthase. Protein Sci *16*, 1464-1478.

Andley, U.P., Song, Z., Wawrousek, E.F., Brady, J.P., Bassnett, S., and Fleming, T.P. (2001). Lens epithelial cells derived from alphaB-crystallin knockout mice demonstrate hyperproliferation and genomic instability. FASEB J *15*, 221-229.

Anfinsen, C.B. (1973). Principles that govern the folding of protein chains. Science *181*, 223-230.

Anfinsen, C.B., Haber, E., Sela, M., and White, F.H., Jr. (1961). The kinetics of formation of native ribonuclease during oxidation of the reduced polypeptide chain. Proc Natl Acad Sci U S A *47*, 1309-1314.

Aquilina, J.A., Benesch, J.L., Bateman, O.A., Slingsby, C., and Robinson, C.V. (2003). Polydispersity of a mammalian chaperone: mass spectrometry reveals the population of oligomers in alphaB-crystallin. Proc Natl Acad Sci U S A *100*, 10611-10616.

Aquilina, J.A., Benesch, J.L., Ding, L.L., Yaron, O., Horwitz, J., and Robinson, C.V. (2004). Phosphorylation of alphaB-crystallin alters chaperone function through loss of dimeric substructure. J Biol Chem *279*, 28675-28680.

Aquilina, J.A., Benesch, J.L., Ding, L.L., Yaron, O., Horwitz, J., and Robinson, C.V. (2005). Subunit exchange of polydisperse proteins: mass spectrometry reveals consequences of alphaA-crystallin truncation. J Biol Chem *280*, 14485-14491.

Bagneris, C., Bateman, O.A., Naylor, C.E., Cronin, N., Boelens, W.C., Keep, N.H., and Slingsby, C. (2009). Crystal structures of alpha-crystallin domain dimers of alphaB-crystallin and Hsp20. J Mol Biol *392*, 1242-1252.

Bai, F., Xi, J.H., Wawrousek, E.F., Fleming, T.P., and Andley, U.P. (2003). Hyperproliferation and p53 status of lens epithelial cells derived from alphaB-crystallin knockout mice. J Biol Chem *278*, 36876-36886.

Balch, W.E., Morimoto, R.I., Dillin, A., and Kelly, J.W. (2008). Adapting proteostasis for disease intervention. Science *319*, 916-919.

Baldwin, A.J., Lioe, H., Hilton, G.R., Baker, L.A., Rubinstein, J.L., Kay, L.E., and Benesch, J.L. (2011a). The polydispersity of αB-crystallin is rationalized by an interconverting polyhedral architecture. Structure *19*, 1855-1863.

Baldwin, A.J., Lioe, H., Robinson, C.V., Kay, L.E., and Benesch, J.L. (2011b). αB-crystallin polydispersity is a consequence of unbiased quaternary dynamics. J Mol Biol *413*, 297-309.

Basha, E., Friedrich, K.L., and Vierling, E. (2006). The N-terminal arm of small heat shock proteins is important for both chaperone activity and substrate specificity. J Biol Chem *281*, 39943-39952.

Basha, E., Lee, G.J., Breci, L.A., Hausrath, A.C., Buan, N.R., Giese, K.C., and Vierling, E. (2004). The identity of proteins associated with a small heat shock protein during heat stress in vivo indicates that these chaperones protect a wide range of cellular functions. J Biol Chem *279*, 7566-7575.

Basha, E., O'Neill, H., and Vierling, E. (2012). Small heat shock proteins and alpha-crystallins: dynamic proteins with flexible functions. Trends Biochem Sci *37*, 106-117.

Bence, N.F., Sampat, R.M., and Kopito, R.R. (2001). Impairment of the ubiquitin-proteasome system by protein aggregation. Science *292*, 1552-1555.

Benesch, J.L., Ayoub, M., Robinson, C.V., and Aquilina, J.A. (2008). Small heat shock protein activity is regulated by variable oligomeric substructure. J Biol Chem *283*, 28513-28517.

Berzelius, J.J. (1830). Lärobok i Kemien, Vol 2 (Stockholm: Norstedt & Söner).

Biswas, A., and Das, K.P. (2004). Role of ATP on the interaction of alpha-crystallin with its substrates and its implications for the molecular chaperone function. J Biol Chem *279*, 42648-42657.

Bloemendal, H., de Jong, W., Jaenicke, R., Lubsen, N.H., Slingsby, C., and Tardieu, A. (2004). Ageing and vision: structure, stability and function of lens crystallins. Prog Biophys Mol Biol *86*, 407-485.

Bova, M.P., Ding, L.L., Horwitz, J., and Fung, B.K. (1997). Subunit exchange of alphaA-crystallin. J Biol Chem *272*, 29511-29517.

Bova, M.P., McHaourab, H.S., Han, Y., and Fung, B.K. (2000). Subunit exchange of small heat shock proteins. Analysis of oligomer formation of alphaA-crystallin and Hsp27 by fluorescence resonance energy transfer and site-directed truncations. J Biol Chem *275*, 1035-1042.

Boyle, D.L., Takemoto, L., Brady, J.P., and Wawrousek, E.F. (2003). Morphological characterization of the AlphaA- and AlphaB-crystallin double knockout mouse lens. BMC Ophthalmology *3*, 3.

Brady, J.P., Garland, D., Duglas-Tabor, Y., Robison, W.G., Jr., Groome, A., and Wawrousek, E.F. (1997). Targeted disruption of the mouse alpha A-crystallin gene induces cataract and cytoplasmic inclusion bodies containing the small heat shock protein alpha B-crystallin. Proc Natl Acad Sci U S A *94*, 884-889.

Brady, J.P., Garland, D.L., Green, D.E., Tamm, E.R., Giblin, F.J., and Wawrousek, E.F. (2001). AlphaB-crystallin in lens development and muscle integrity: a gene knockout approach. Invest Ophthalmol Vis Sci *42*, 2924-2934.

Braun, N., Zacharias, M., Peschek, J., Kastenmüller, A., Zou, J., Hanzlik, M., Haslbeck, M., Rappsilber, J., Buchner, J., and Weinkauf, S. (2011). Multiple molecular architectures of the eye lens chaperone αB-crystallin elucidated by a triple hybrid approach. Proc Natl Acad Sci U S A *108*, 20491-20496.

Buchberger, A., Schroder, H., Hesterkamp, T., Schonfeld, H.J., and Bukau, B. (1996). Substrate shuttling between the DnaK and GroEL systems indicates a chaperone network promoting protein folding. J Mol Biol *261*, 328-333.

Buchner, J. (1996). Supervising the fold: functional principles of molecular chaperones. FASEB J *10*, 10-19.

Buchner, J., Ehrnsperger, M., Gaestel, M., and Walke, S. (1998). Purification and characterization of small heat shock proteins. Methods Enzymol *290*, 339-349.

Bukach, O.V., Seit-Nebi, A.S., Marston, S.B., and Gusev, N.B. (2004). Some properties of human small heat shock protein Hsp20 (HspB6). Eur J Biochem *271*, 291-302.

Bullock, A.N., and Fersht, A.R. (2001). Rescuing the function of mutant p53. Nat Rev Cancer *1*, 68-76.

Carra, S., Seguin, S.J., Lambert, H., and Landry, J. (2008). HspB8 chaperone activity toward poly(Q)-containing proteins depends on its association with Bag3, a stimulator of macroautophagy. J Biol Chem *283*, 1437-1444.

Cashikar, A.G., Duennwald, M., and Lindquist, S.L. (2005). A chaperone pathway in protein disaggregation. Hsp26 alters the nature of protein aggregates to facilitate reactivation by Hsp104. J Biol Chem *280*, 23869-23875.

Caspers, G.J., Leunissen, J.A., and de Jong, W.W. (1995). The expanding small heat-shock protein family, and structure predictions of the conserved "alpha-crystallin domain". J Mol Evol *40*, 238-248.

Chabas, D., Baranzini, S.E., Mitchell, D., Bernard, C.C., Rittling, S.R., Denhardt, D.T., Sobel, R.A., Lock, C., Karpuj, M., Pedotti, R.*, et al.* (2001). The influence of the proinflammatory cytokine, osteopontin, on autoimmune demyelinating disease. Science *294*, 1731-1735.

Chai, Y., Shao, J., Miller, V.M., Williams, A., and Paulson, H.L. (2002). Live-cell imaging reveals divergent intracellular dynamics of polyglutamine disease proteins and supports a sequestration model of pathogenesis. Proc Natl Acad Sci U S A *99*, 9310-9315.

Chen, J., Feige, M.J., Franzmann, T.M., Bepperling, A., and Buchner, J. (2010). Regions outside the alpha-crystallin domain of the small heat shock protein Hsp26 are required for its dimerization. J Mol Biol *398*, 122-131.

Cheng, G., Basha, E., Wysocki, V.H., and Vierling, E. (2008). Insights into small heat shock protein and substrate structure during chaperone action derived from hydrogen/deuterium exchange and mass spectrometry. J Biol Chem *283*, 26634-26642.

Clark, A.R., Lubsen, N.H., and Slingsby, C. (2012). sHSP in the eye lens: Crystallin mutations, cataract and proteostasis. Int J Biochem Cell Biol.

Clark, A.R., Naylor, C.E., Bagneris, C., Keep, N.H., and Slingsby, C. (2011). Crystal structure of R120G disease mutant of human alphaB-crystallin domain dimer shows closure of a groove. J Mol Biol *408*, 118-134.

de Jong, W.W., Caspers, G.J., and Leunissen, J.A. (1998). Genealogy of the alpha-crystallin--small heat-shock protein superfamily. Int J Biol Macromol *22*, 151-162.

den Engelsman, J., Boros, S., Dankers, P.Y., Kamps, B., Vree Egberts, W.T., Bode, C.S., Lane, L.A., Aquilina, J.A., Benesch, J.L., Robinson, C.V.*, et al.* (2009). The small heat-shock proteins HSPB2 and HSPB3 form well-defined heterooligomers in a unique 3 to 1 subunit ratio. J Mol Biol *393*, 1022-1032.

Dinner, A.R., Sali, A., Smith, L.J., Dobson, C.M., and Karplus, M. (2000). Understanding protein folding via free-energy surfaces from theory and experiment. Trends Biochem Sci *25*, 331-339.

Dobson, C.M. (2003). Protein folding and misfolding. Nature *426*, 884-890.

Dobson, C.M., and Karplus, M. (1999). The fundamentals of protein folding: bringing together theory and experiment. Curr Opin Struct Biol *9*, 92-101.

Dougan, D.A., Mogk, A., Zeth, K., Turgay, K., and Bukau, B. (2002). AAA+ proteins and substrate recognition, it all depends on their partner in crime. FEBS Lett *529*, 6-10.

Duennwald, M.L., Echeverria, A., and Shorter, J. (2012). Small heat shock proteins potentiate amyloid dissolution by protein disaggregases from yeast and humans. PLoS Biol *10*, e1001346.

Dyson, H.J. (2011). Expanding the proteome: disordered and alternatively folded proteins. Q Rev Biophys *44*, 467-518.

Ecroyd, H., Meehan, S., Horwitz, J., Aquilina, J.A., Benesch, J.L., Robinson, C.V., Macphee, C.E., and Carver, J.A. (2007). Mimicking phosphorylation of alphaB-crystallin affects its chaperone activity. Biochem J *401*, 129-141.

Ehrnsperger, M., Graber, S., Gaestel, M., and Buchner, J. (1997). Binding of non-native protein to Hsp25 during heat shock creates a reservoir of folding intermediates for reactivation. EMBO J *16*, 221-229.

Ehrnsperger, M., Lilie, H., Gaestel, M., and Buchner, J. (1999). The dynamics of Hsp25 quaternary structure. Structure and function of different oligomeric species. J Biol Chem *274*, 14867-14874.

Eisenberg, D., Schwarz, E., Komaromy, M., and Wall, R. (1984). Analysis of membrane and surface protein sequences with the hydrophobic moment plot. J Mol Biol *179*, 125-142.

Ellis, J. (1987). Proteins as molecular chaperones. Nature *328*, 378-379.

Ellis, R.J. (2001). Macromolecular crowding: obvious but underappreciated. Trends Biochem Sci *26*, 597-604.

Ellis, R.J., and Minton, A.P. (2006). Protein aggregation in crowded environments. Biol Chem *387*, 485-497.

Ellis, R.J., van der Vies, S.M., and Hemmingsen, S.M. (1989). The molecular chaperone concept. Biochem Soc Symp *55*, 145-153.

Evans, J.R., Bosman, J.D., Brown-Endres, L., Yehiely, F., and Cryns, V.L. (2010). Induction of the small heat shock protein alphaB-crystallin by genotoxic stress is mediated by p53 and p73. Breast Cancer Res Treat *122*, 159-168.

Eyles, S.J., and Gierasch, L.M. (2010). Nature's molecular sponges: small heat shock proteins grow into their chaperone roles. Proc Natl Acad Sci U S A *107*, 2727-2728.

Fairbanks, G., Steck, T.L., and Wallach, D.F. (1971). Electrophoretic analysis of the major polypeptides of the human erythrocyte membrane. Biochemistry *10*, 2606-2617.

Fersht, A.R., and Daggett, V. (2002). Protein folding and unfolding at atomic resolution. Cell *108*, 573-582.

Franzmann, T.M., Menhorn, P., Walter, S., and Buchner, J. (2008). Activation of the chaperone Hsp26 is controlled by the rearrangement of its thermosensor domain. Mol Cell *29*, 207-216.

Franzmann, T.M., Wuhr, M., Richter, K., Walter, S., and Buchner, J. (2005). The activation mechanism of Hsp26 does not require dissociation of the oligomer. J Mol Biol *350*, 1083-1093.

Frydman, J. (2001). Folding of newly translated proteins in vivo: the role of molecular chaperones. Annu Rev Biochem *70*, 603-647.

Frydman, J., Nimmesgern, E., Ohtsuka, K., and Hartl, F.U. (1994). Folding of nascent polypeptide chains in a high molecular mass assembly with molecular chaperones. Nature *370*, 111-117.

Georgopoulos, C., and Welch, W.J. (1993). Role of the major heat shock proteins as molecular chaperones. Annu Rev Cell Biol *9*, 601-634.

Ghosh, J.G., Houck, S.A., Doneanu, C.E., and Clark, J.I. (2006). The beta4-beta8 groove is an ATP-interactive site in the alpha crystallin core domain of the small heat shock protein, human alphaB crystallin. J Mol Biol *364*, 364-375.

Ghosh, J.G., Shenoy, A.K., Jr., and Clark, J.I. (2007). Interactions between important regulatory proteins and human alphaB crystallin. Biochemistry *46*, 6308-6317.

Goldberg, A.L. (2003). Protein degradation and protection against misfolded or damaged proteins. Nature *426*, 895-899.

Goldberg, M.E., Rudolph, R., and Jaenicke, R. (1991). A kinetic study of the competition between renaturation and aggregation during the refolding of denatured-reduced egg white lysozyme. Biochemistry *30*, 2790-2797.

Goloubinoff, P., Mogk, A., Zvi, A.P., Tomoyasu, T., and Bukau, B. (1999). Sequential mechanism of solubilization and refolding of stable protein aggregates by a bichaperone network. Proc Natl Acad Sci U S A *96*, 13732-13737.

Groenen, P.J., Merck, K.B., de Jong, W.W., and Bloemendal, H. (1994). Structure and modifications of the junior chaperone alpha-crystallin. From lens transparency to molecular pathology. Eur J Biochem *225*, 1-19.

Haley, D.A., Bova, M.P., Huang, Q.L., McHaourab, H.S., and Stewart, P.L. (2000). Small heat-shock protein structures reveal a continuum from symmetric to variable assemblies. J Mol Biol *298*, 261-272.

Haley, D.A., Horwitz, J., and Stewart, P.L. (1998). The small heat-shock protein, alphaB-crystallin, has a variable quaternary structure. J Mol Biol *277*, 27-35.

Hartl, F.U., Bracher, A., and Hayer-Hartl, M. (2011). Molecular chaperones in protein folding and proteostasis. Nature *475*, 324-332.

Hartl, F.U., and Hayer-Hartl, M. (2002). Molecular chaperones in the cytosol: from nascent chain to folded protein. Science *295*, 1852-1858.

Hartl, F.U., and Hayer-Hartl, M. (2009). Converging concepts of protein folding in vitro and in vivo. Nat Struct Mol Biol *16*, 574-581.

Haslbeck, M., Braun, N., Stromer, T., Richter, B., Model, N., Weinkauf, S., and Buchner, J. (2004a). Hsp42 is the general small heat shock protein in the cytosol of Saccharomyces cerevisiae. EMBO J *23*, 638-649.

Haslbeck, M., Franzmann, T., Weinfurtner, D., and Buchner, J. (2005a). Some like it hot: the structure and function of small heat-shock proteins. Nat Struct Mol Biol *12*, 842-846.

Haslbeck, M., Ignatiou, A., Saibil, H., Helmich, S., Frenzl, E., Stromer, T., and Buchner, J. (2004b). A domain in the N-terminal part of Hsp26 is essential for chaperone function and oligomerization. J Mol Biol *343*, 445-455.

Haslbeck, M., Kastenmuller, A., Buchner, J., Weinkauf, S., and Braun, N. (2008). Structural dynamics of archaeal small heat shock proteins. J Mol Biol *378*, 362-374.

Haslbeck, M., Miess, A., Stromer, T., Walter, S., and Buchner, J. (2005b). Disassembling protein aggregates in the yeast cytosol. The cooperation of Hsp26 with Ssa1 and Hsp104. J Biol Chem *280*, 23861-23868.

Haslbeck, M., Walke, S., Stromer, T., Ehrnsperger, M., White, H.E., Chen, S., Saibil, H.R., and Buchner, J. (1999). Hsp26: a temperature-regulated chaperone. EMBO J *18*, 6744-6751.

Hayes, D., Napoli, V., Mazurkie, A., Stafford, W.F., and Graceffa, P. (2009). Phosphorylation dependence of hsp27 multimeric size and molecular chaperone function. J Biol Chem *284*, 18801-18807.

Hilton, G.R., Lioe, H., Stengel, F., Baldwin, A.J., and Benesch, J.L. (2012). Small Heat-Shock Proteins: Paramedics of the Cell. Top Curr Chem.

Hoffmann, J.H., Linke, K., Graf, P.C., Lilie, H., and Jakob, U. (2004). Identification of a redox-regulated chaperone network. EMBO J *23*, 160-168.

Holmberg, C.I., Staniszewski, K.E., Mensah, K.N., Matouschek, A., and Morimoto, R.I. (2004). Inefficient degradation of truncated polyglutamine proteins by the proteasome. EMBO J *23*, 4307-4318.

Hoover, H.E., Thuerauf, D.J., Martindale, J.J., and Glembotski, C.C. (2000). alpha B-crystallin gene induction and phosphorylation by MKK6-activated p38. A potential role for alpha B-crystallin as a target of the p38 branch of the cardiac stress response. J Biol Chem *275*, 23825-23833.

Horwitz, J. (1992). Alpha-crystallin can function as a molecular chaperone. Proc Natl Acad Sci U S A *89*, 10449-10453.

Horwitz, J. (2003). Alpha-crystallin. Exp Eye Res *76*, 145-153.

Horwitz, J. (2009). Alpha crystallin: the quest for a homogeneous quaternary structure. Exp Eye Res *88*, 190-194.

Horwitz, J., Bova, M.P., Ding, L.L., Haley, D.A., and Stewart, P.L. (1999). Lens alpha-crystallin: function and structure. Eye (Lond) *13 (Pt 3b)*, 403-408.

Hubbard, S.J. (1998). The structural aspects of limited proteolysis of native proteins. Biochim Biophys Acta *1382*, 191-206.

Ito, H., Hasegawa, K., Inaguma, Y., Kozawa, O., and Kato, K. (1996). Enhancement of stress-induced synthesis of hsp27 and alpha B crystallin by modulators of the arachidonic acid cascade. J Cell Physiol *166*, 332-339.

Ito, H., Kamei, K., Iwamoto, I., Inaguma, Y., Nohara, D., and Kato, K. (2001). Phosphorylation-induced change of the oligomerization state of alpha B-crystallin. J Biol Chem *276*, 5346-5352.

Ito, H., Okamoto, K., Nakayama, H., Isobe, T., and Kato, K. (1997). Phosphorylation of alphaB-crystallin in response to various types of stress. J Biol Chem *272*, 29934-29941.

Iwaki, T., Iwaki, A., Tateishi, J., Sakaki, Y., and Goldman, J.E. (1993). Alpha B-crystallin and 27-kd heat shock protein are regulated by stress conditions in the central nervous system and accumulate in Rosenthal fibers. Am J Pathol *143*, 487-495.

Iwaki, T., Kume-Iwaki, A., and Goldman, J.E. (1990). Cellular distribution of alpha B-crystallin in non-lenticular tissues. J Histochem Cytochem *38*, 31-39.

Iwaki, T., Kume-Iwaki, A., Liem, R.K., and Goldman, J.E. (1989). Alpha B-crystallin is expressed in non-lenticular tissues and accumulates in Alexander's disease brain. Cell *57*, 71-78.

Jaenicke, R. (1987). Folding and association of proteins. Prog Biophys Mol Biol *49*, 117-237.

Jahn, T.R., and Radford, S.E. (2005). The Yin and Yang of protein folding. FEBS J *272*, 5962-5970.

Jakob, U., Gaestel, M., Engel, K., and Buchner, J. (1993). Small heat shock proteins are molecular chaperones. J Biol Chem *268*, 1517-1520.

Jakob, U., Muse, W., Eser, M., and Bardwell, J.C. (1999). Chaperone activity with a redox switch. Cell *96*, 341-352.

Jaya, N., Garcia, V., and Vierling, E. (2009). Substrate binding site flexibility of the small heat shock protein molecular chaperones. Proc Natl Acad Sci U S A *106*, 15604-15609.

Jehle, S., Rajagopal, P., Bardiaux, B., Markovic, S., Kuhne, R., Stout, J.R., Higman, V.A., Klevit, R.E., van Rossum, B.J., and Oschkinat, H. (2010). Solid-state NMR and SAXS studies provide a structural basis for the activation of alphaB-crystallin oligomers. Nat Struct Mol Biol *17*, 1037-1042.

Jehle, S., van Rossum, B., Stout, J.R., Noguchi, S.M., Falber, K., Rehbein, K., Oschkinat, H., Klevit, R.E., and Rajagopal, P. (2009). alphaB-crystallin: a hybrid solid-state/solution-state NMR investigation reveals structural aspects of the heterogeneous oligomer. J Mol Biol *385*, 1481-1497.

Jehle, S., Vollmar, B.S., Bardiaux, B., Dove, K.K., Rajagopal, P., Gonen, T., Oschkinat, H., and Klevit, R.E. (2011). N-terminal domain of alphaB-crystallin provides a conformational switch for multimerization and structural heterogeneity. Proc Natl Acad Sci U S A *108*, 6409-6414.

Johnston, J.A., Ward, C.L., and Kopito, R.R. (1998). Aggresomes: a cellular response to misfolded proteins. J Cell Biol *143*, 1883-1898.

Kaganovich, D., Kopito, R., and Frydman, J. (2008). Misfolded proteins partition between two distinct quality control compartments. Nature *454*, 1088-1095.

Kappe, G., Boelens, W.C., and de Jong, W.W. (2010). Why proteins without an alpha-crystallin domain should not be included in the human small heat shock protein family HSPB. Cell Stress Chaperones *15*, 457-461.

Kappe, G., Franck, E., Verschuure, P., Boelens, W.C., Leunissen, J.A., and de Jong, W.W. (2003). The human genome encodes 10 alpha-crystallin-related small heat shock proteins: HspB1-10. Cell Stress Chaperones *8*, 53-61.

Kato, K., Ito, H., Kamei, K., Inaguma, Y., Iwamoto, I., and Saga, S. (1998). Phosphorylation of alphaB-crystallin in mitotic cells and identification of enzymatic activities responsible for phosphorylation. J Biol Chem *273*, 28346-28354.

Keil, B. (1987). Proteolysis Data Bank: specificity of alpha-chymotrypsin from computation of protein cleavages. Protein Seq Data Anal *1*, 13-20.

Kiefhaber, T., Rudolph, R., Kohler, H.H., and Buchner, J. (1991). Protein aggregation in vitro and in vivo: a quantitative model of the kinetic competition between folding and aggregation. Biotechnology (N Y) *9*, 825-829.

Kim, K.K., Kim, R., and Kim, S.H. (1998). Crystal structure of a small heat-shock protein. Nature *394*, 595-599.

King, F.W., Wawrzynow, A., Hohfeld, J., and Zylicz, M. (2001). Co-chaperones Bag-1, Hop and Hsp40 regulate Hsc70 and Hsp90 interactions with wild-type or mutant p53. EMBO J *20*, 6297-6305.

Kirkin, V., McEwan, D.G., Novak, I., and Dikic, I. (2009). A role for ubiquitin in selective autophagy. Mol Cell *34*, 259-269.

Kitagawa, M., Matsumura, Y., and Tsuchido, T. (2000). Small heat shock proteins, IbpA and IbpB, are involved in resistances to heat and superoxide stresses in Escherichia coli. FEMS Microbiol Lett *184*, 165-171.

Klemenz, R., Frohli, E., Steiger, R.H., Schafer, R., and Aoyama, A. (1991). Alpha B-crystallin is a small heat shock protein. Proc Natl Acad Sci U S A *88*, 3652-3656.

Kopito, R.R. (2000). Aggresomes, inclusion bodies and protein aggregation. Trends Cell Biol *10*, 524-530.

Koppenol, W.H., Bounds, P.L., and Dang, C.V. (2011). Otto Warburg's contributions to current concepts of cancer metabolism. Nat Rev Cancer *11*, 325-337.

Koretz, J.F., Doss, E.W., and LaButti, J.N. (1998). Environmental factors influencing the chaperone-like activity of alpha-crystallin. Int J Biol Macromol *22*, 283-294.

Koteiche, H.A., and McHaourab, H.S. (2003). Mechanism of chaperone function in small heat-shock proteins. Phosphorylation-induced activation of two-mode binding in alphaB-crystallin. J Biol Chem *278*, 10361-10367.

Kriehuber, T., Rattei, T., Weinmaier, T., Bepperling, A., Haslbeck, M., and Buchner, J. (2010). Independent evolution of the core domain and its flanking sequences in small heat shock proteins. FASEB J *24*, 3633-3642.

Laemmli, U.K. (1970). Cleavage of structural proteins during the assembly of the head of bacteriophage T4. Nature *227*, 680-685.

Laganowsky, A., Benesch, J.L., Landau, M., Ding, L., Sawaya, M.R., Cascio, D., Huang, Q., Robinson, C.V., Horwitz, J., and Eisenberg, D. (2010). Crystal structures of truncated alphaA and alphaB crystallins reveal structural mechanisms of polydispersity important for eye lens function. Protein Sci *19*, 1031-1043.

Langer, T., Lu, C., Echols, H., Flanagan, J., Hayer, M.K., and Hartl, F.U. (1992). Successive action of DnaK, DnaJ and GroEL along the pathway of chaperone-mediated protein folding. Nature *356*, 683-689.

Launay, N., Goudeau, B., Kato, K., Vicart, P., and Lilienbaum, A. (2006). Cell signaling pathways to alphaB-crystallin following stresses of the cytoskeleton. Exp Cell Res *312*, 3570-3584.

Launay, N., Tarze, A., Vicart, P., and Lilienbaum, A. (2010). Serine 59 phosphorylation of {alpha}B-crystallin down-regulates its anti-apoptotic function by binding and sequestering Bcl-2 in breast cancer cells. J Biol Chem *285*, 37324-37332.

Lee, G.J., Roseman, A.M., Saibil, H.R., and Vierling, E. (1997). A small heat shock protein stably binds heat-denatured model substrates and can maintain a substrate in a folding-competent state. EMBO J *16*, 659-671.

Lee, S., Prochaska, D.J., Fang, F., and Barnum, S.R. (1998). A 16.6-kilodalton protein in the Cyanobacterium synechocystis sp. PCC 6803 plays a role in the heat shock response. Curr Microbiol *37*, 403-407.

Leroux, M.R., Melki, R., Gordon, B., Batelier, G., and Candido, E.P. (1997). Structure-function studies on small heat shock protein oligomeric assembly and interaction with unfolded polypeptides. J Biol Chem *272*, 24646-24656.

Lin, D.I., Barbash, O., Kumar, K.G., Weber, J.D., Harper, J.W., Klein-Szanto, A.J., Rustgi, A., Fuchs, S.Y., and Diehl, J.A. (2006). Phosphorylation-dependent ubiquitination of cyclin D1 by the SCF(FBX4-alphaB crystallin) complex. Mol Cell *24*, 355-366.

Lindner, A.B., Madden, R., Demarez, A., Stewart, E.J., and Taddei, F. (2008). Asymmetric segregation of protein aggregates is associated with cellular aging and rejuvenation. Proc Natl Acad Sci U S A *105*, 3076-3081.

MacCoss, M.J., McDonald, W.H., Saraf, A., Sadygov, R., Clark, J.M., Tasto, J.J., Gould, K.L., Wolters, D., Washburn, M., Weiss, A*., et al.* (2002). Shotgun identification of protein modifications from protein complexes and lens tissue. Proc Natl Acad Sci U S A *99*, 7900-7905.

Masilamoni, J.G., Jesudason, E.P., Baben, B., Jebaraj, C.E., Dhandayuthapani, S., and Jayakumar, R. (2006). Molecular chaperone alpha-crystallin prevents detrimental effects of neuroinflammation. Biochim Biophys Acta *1762*, 284-293.

Masilamoni, J.G., Jesudason, E.P., Bharathi, S.N., and Jayakumar, R. (2005). The protective effect of alpha-crystallin against acute inflammation in mice. Biochim Biophys Acta *1740*, 411-420.

Matuszewska, M., Kuczynska-Wisnik, D., Laskowska, E., and Liberek, K. (2005). The small heat shock protein IbpA of Escherichia coli cooperates with IbpB in stabilization of thermally aggregated proteins in a disaggregation competent state. J Biol Chem *280*, 12292-12298.

McHaourab, H.S., Dodson, E.K., and Koteiche, H.A. (2002). Mechanism of chaperone function in small heat shock proteins. Two-mode binding of the excited states of T4 lysozyme mutants by alphaA-crystallin. J Biol Chem *277*, 40557-40566.

McHaourab, H.S., Godar, J.A., and Stewart, P.L. (2009). Structure and mechanism of protein stability sensors: chaperone activity of small heat shock proteins. Biochemistry *48*, 3828-3837.

Mendoza, J.A., Correa, M.D., and Zardeneta, G. (2012). GTP binds to alpha-crystallin and causes a significant conformational change. Int J Biol Macromol *50*, 895-898.

Mogk, A., Schlieker, C., Friedrich, K.L., Schonfeld, H.J., Vierling, E., and Bukau, B. (2003). Refolding of substrates bound to small Hsps relies on a disaggregation reaction mediated most efficiently by ClpB/DnaK. J Biol Chem *278*, 31033-31042.

Mogk, A., Tomoyasu, T., Goloubinoff, P., Rudiger, S., Roder, D., Langen, H., and Bukau, B. (1999). Identification of thermolabile Escherichia coli proteins: prevention and reversion of aggregation by DnaK and ClpB. EMBO J *18*, 6934-6949.

Mounier, N., and Arrigo, A.P. (2002). Actin cytoskeleton and small heat shock proteins: how do they interact? Cell Stress Chaperones *7*, 167-176.

Mörner, C.T. (1894). Untersuchung der Proteinsubstanzen in den lichtbrechenden Medien des Auges. I. Zeitschrift für physiologische Chemie *18*, 61-106.

Narberhaus, F. (2002). Alpha-crystallin-type heat shock proteins: socializing minichaperones in the context of a multichaperone network. Microbiol Mol Biol Rev *66*, 64-93; table of contents.

Nucifora, F.C., Jr., Sasaki, M., Peters, M.F., Huang, H., Cooper, J.K., Yamada, M., Takahashi, H., Tsuji, S., Troncoso, J., Dawson, V.L.*, et al.* (2001). Interference by huntingtin and atrophin-1 with cbp-mediated transcription leading to cellular toxicity. Science *291*, 2423-2428.

Olzscha, H., Schermann, S.M., Woerner, A.C., Pinkert, S., Hecht, M.H., Tartaglia, G.G., Vendruscolo, M., Hayer-Hartl, M., Hartl, F.U., and Vabulas, R.M. (2011). Amyloid-like aggregates sequester numerous metastable proteins with essential cellular functions. Cell *144*, 67-78.

Ousman, S.S., Tomooka, B.H., van Noort, J.M., Wawrousek, E.F., O'Connor, K.C., Hafler, D.A., Sobel, R.A., Robinson, W.H., and Steinman, L. (2007). Protective and therapeutic role for alphaB-crystallin in autoimmune demyelination. Nature *448*, 474-479.

Painter, A.J., Jaya, N., Basha, E., Vierling, E., Robinson, C.V., and Benesch, J.L. (2008). Real-time monitoring of protein complexes reveals their quaternary organization and dynamics. Chem Biol *15*, 246-253.

Pandey, P., Farber, R., Nakazawa, A., Kumar, S., Bharti, A., Nalin, C., Weichselbaum, R., Kufe, D., and Kharbanda, S. (2000). Hsp27 functions as a negative regulator of cytochrome c-dependent activation of procaspase-3. Oncogene *19*, 1975-1981.

Pandya, M.J., Bendz, H., Manzenrieder, F., Noessner, E., Kessler, H., Buchner, J., and Issels, R.D. (2009). Interaction of human heat shock protein 70 with tumor-associated peptides. Biol Chem *390*, 305-312.

Parsell, D.A., Kowal, A.S., Singer, M.A., and Lindquist, S. (1994). Protein disaggregation mediated by heat-shock protein Hsp104. Nature *372*, 475-478.

Pasta, S.Y., Raman, B., Ramakrishna, T., and Rao Ch, M. (2004). The IXI/V motif in the C-terminal extension of alpha-crystallins: alternative interactions and oligomeric assemblies. Mol Vis *10*, 655-662.

Peschek, J. (2007). Structure and Function of α-Crystallin (München: Technische Universität München).

Peschek, J., Braun, N., Franzmann, T.M., Georgalis, Y., Haslbeck, M., Weinkauf, S., and Buchner, J. (2009). The eye lens chaperone alpha-crystallin forms defined globular assemblies. Proc Natl Acad Sci U S A *106*, 13272-13277.

Philo, J.S. (2006). Improved methods for fitting sedimentation coefficient distributions derived by time-derivative techniques. Anal Biochem *354*, 238-246.

Powers, E.T., Morimoto, R.I., Dillin, A., Kelly, J.W., and Balch, W.E. (2009). Biological and chemical approaches to diseases of proteostasis deficiency. Annu Rev Biochem *78*, 959-991.

Provencher, S. (1982). CONTIN - A GENERAL-PURPOSE CONSTRAINED REGULARIZATION PROGRAM FOR INVERTING NOISY LINEAR ALGEBRAIC AND INTEGRAL-EQUATIONS. Computer Physics Communications *27*, 229-242.

Rajasekaran, N.S., Connell, P., Christians, E.S., Yan, L.J., Taylor, R.P., Orosz, A., Zhang, X.Q., Stevenson, T.J., Peshock, R.M., Leopold, J.A., *et al.* (2007). Human alpha B-crystallin mutation causes oxido-reductive stress and protein aggregation cardiomyopathy in mice. Cell *130*, 427-439.

Rappsilber, J. (2011). The beginning of a beautiful friendship: cross-linking/mass spectrometry and modelling of proteins and multi-protein complexes. J Struct Biol *173*, 530-540.

Reichmann, D., Xu, Y., Cremers, C.M., Ilbert, M., Mittelman, R., Fitzgerald, M.C., and Jakob, U. (2012). Order out of disorder: working cycle of an intrinsically unfolded chaperone. Cell *148*, 947-957.

Renkawek, K., de Jong, W.W., Merck, K.B., Frenken, C.W., van Workum, F.P., and Bosman, G.J. (1992). alpha B-crystallin is present in reactive glia in Creutzfeldt-Jakob disease. Acta Neuropathol *83*, 324-327.

Renkawek, K., Voorter, C.E., Bosman, G.J., van Workum, F.P., and de Jong, W.W. (1994). Expression of alpha B-crystallin in Alzheimer's disease. Acta Neuropathol *87*, 155-160.

Richmond, C.S., Glasner, J.D., Mau, R., Jin, H., and Blattner, F.R. (1999). Genome-wide expression profiling in Escherichia coli K-12. Nucleic Acids Res *27*, 3821-3835.

Richter, K., Haslbeck, M., and Buchner, J. (2010). The heat shock response: life on the verge of death. Mol Cell *40*, 253-266.

Rubinsztein, D.C. (2006). The roles of intracellular protein-degradation pathways in neurodegeneration. Nature *443*, 780-786.

Sambrook, J., and Russell, D.W. (2001). Molecular cloning: A laboratory manual (Cold Spring Harbor Laboratory Press).

Santhoshkumar, P., and Sharma, K.K. (2001). Phe71 is essential for chaperone-like function in alpha A-crystallin. J Biol Chem *276*, 47094-47099.

Schuck, P. (2000). Size-distribution analysis of macromolecules by sedimentation velocity ultracentrifugation and lamm equation modeling. Biophys J *78*, 1606-1619.

Seal, R.L., Gordon, S.M., Lush, M.J., Wright, M.W., and Bruford, E.A. (2011). genenames.org: the HGNC resources in 2011. Nucleic Acids Res *39*, D514-519.

Sharma, K.K., Kumar, R.S., Kumar, G.S., and Quinn, P.T. (2000). Synthesis and characterization of a peptide identified as a functional element in alphaA-crystallin. J Biol Chem *275*, 3767-3771.

Shashidharamurthy, R., Koteiche, H.A., Dong, J., and McHaourab, H.S. (2005). Mechanism of chaperone function in small heat shock proteins: dissociation of the HSP27 oligomer is required for recognition and binding of destabilized T4 lysozyme. J Biol Chem *280*, 5281-5289.

Smulders, R.H., and de Jong, W.W. (1997). The hydrophobic probe 4,4'-bis(1-anilino-8-naphthalene sulfonic acid) is specifically photoincorporated into the N-terminal domain of alpha B-crystallin. FEBS Lett *409*, 101-104.

Specht, S., Miller, S.B., Mogk, A., and Bukau, B. (2011). Hsp42 is required for sequestration of protein aggregates into deposition sites in Saccharomyces cerevisiae. J Cell Biol *195*, 617-629.

Stafford, W.F., 3rd (1992). Boundary analysis in sedimentation transport experiments: a procedure for obtaining sedimentation coefficient distributions using the time derivative of the concentration profile. Anal Biochem *203*, 295-301.

Stegh, A.H., Kesari, S., Mahoney, J.E., Jenq, H.T., Forloney, K.L., Protopopov, A., Louis, D.N., Chin, L., and DePinho, R.A. (2008). Bcl2L12-mediated inhibition of effector caspase-3 and caspase-7 via distinct mechanisms in glioblastoma. Proc Natl Acad Sci U S A *105*, 10703-10708.

Stengel, F., Baldwin, A.J., Painter, A.J., Jaya, N., Basha, E., Kay, L.E., Vierling, E., Robinson, C.V., and Benesch, J.L. (2010). Quaternary dynamics and plasticity underlie small heat shock protein chaperone function. Proc Natl Acad Sci U S A *107*, 2007-2012.

Sun, T.X., Das, B.K., and Liang, J.J. (1997). Conformational and functional differences between recombinant human lens alphaA- and alphaB-crystallin. J Biol Chem *272*, 6220-6225.

Szak, S.T., Mays, D., and Pietenpol, J.A. (2001). Kinetics of p53 binding to promoter sites in vivo. Mol Cell Biol *21*, 3375-3386.

Taylor, J.P., Tanaka, F., Robitschek, J., Sandoval, C.M., Taye, A., Markovic-Plese, S., and Fischbeck, K.H. (2003). Aggresomes protect cells by enhancing the degradation of toxic polyglutamine-containing protein. Hum Mol Genet *12*, 749-757.

Thomas, J.G., and Baneyx, F. (1998). Roles of the Escherichia coli small heat shock proteins IbpA and IbpB in thermal stress management: comparison with ClpA, ClpB, and HtpG In vivo. J Bacteriol *180*, 5165-5172.

Tissieres, A., Mitchell, H.K., and Tracy, U.M. (1974). Protein synthesis in salivary glands of Drosophila melanogaster: relation to chromosome puffs. J Mol Biol *84*, 389-398.

Tyedmers, J., Mogk, A., and Bukau, B. (2010). Cellular strategies for controlling protein aggregation. Nat Rev Mol Cell Biol *11*, 777-788.

Udgaonkar, J.B. (2008). Multiple routes and structural heterogeneity in protein folding. Annu Rev Biophys *37*, 489-510.

van de Klundert, F.A., Smulders, R.H., Gijsen, M.L., Lindner, R.A., Jaenicke, R., Carver, J.A., and de Jong, W.W. (1998). The mammalian small heat-shock protein Hsp20 forms dimers and is a poor chaperone. Eur J Biochem *258*, 1014-1021.

Van Montfort, R., Slingsby, C., and Vierling, E. (2001). Structure and function of the small heat shock protein/alpha-crystallin family of molecular chaperones. Adv Protein Chem *59*, 105-156.

van Montfort, R.L., Basha, E., Friedrich, K.L., Slingsby, C., and Vierling, E. (2001). Crystal structure and assembly of a eukaryotic small heat shock protein. Nat Struct Biol *8*, 1025-1030.

Veinger, L., Diamant, S., Buchner, J., and Goloubinoff, P. (1998). The small heat-shock protein IbpB from Escherichia coli stabilizes stress-denatured proteins for subsequent refolding by a multichaperone network. J Biol Chem *273*, 11032-11037.

Venkatraman, P., Wetzel, R., Tanaka, M., Nukina, N., and Goldberg, A.L. (2004). Eukaryotic proteasomes cannot digest polyglutamine sequences and release them during degradation of polyglutamine-containing proteins. Mol Cell *14*, 95-104.

Ventura, S., and Villaverde, A. (2006). Protein quality in bacterial inclusion bodies. Trends Biotechnol *24*, 179-185.

Verhoef, L.G., Lindsten, K., Masucci, M.G., and Dantuma, N.P. (2002). Aggregate formation inhibits proteasomal degradation of polyglutamine proteins. Hum Mol Genet *11*, 2689-2700.

Vicart, P., Caron, A., Guicheney, P., Li, Z., Prévost, M.C., Faure, A., Chateau, D., Chapon, F., Tomé, F., Dupret, J.M.*, et al.* (1998). A missense mutation in the alphaB-crystallin chaperone gene causes a desmin-related myopathy. Nat Genet *20*, 92-95.

Vos, M.J., Zijlstra, M.P., Carra, S., Sibon, O.C., and Kampinga, H.H. (2011). Small heat shock proteins, protein degradation and protein aggregation diseases. Autophagy *7*, 101-103.

Walter, S., and Buchner, J. (2002). Molecular chaperones--cellular machines for protein folding. Angew Chem Int Ed Engl *41*, 1098-1113.

Wandinger, S.K., Richter, K., and Buchner, J. (2008). The Hsp90 chaperone machinery. J Biol Chem *283*, 18473-18477.

Wang, K., Ma, W., and Spector, A. (1995). Phosphorylation of alpha-crystallin in rat lenses is stimulated by H2O2 but phosphorylation has no effect on chaperone activity. Exp Eye Res *61*, 115-124.

Warburg, O. (1956). On the origin of cancer cells. Science *123*, 309-314.

Watanabe, G., Kato, S., Nakata, H., Ishida, T., Ohuchi, N., and Ishioka, C. (2009). alphaB-crystallin: a novel p53-target gene required for p53-dependent apoptosis. Cancer Sci *100*, 2368-2375.

Welker, S., Rudolph, B., Frenzel, E., Hagn, F., Liebisch, G., Schmitz, G., Scheuring, J., Kerth, A., Blume, A., Weinkauf, S.*, et al.* (2010). Hsp12 is an intrinsically unstructured stress protein that folds upon membrane association and modulates membrane function. Mol Cell *39*, 507-520.

Wettstein, G., Bellaye, P.S., Micheau, O., and Bonniaud, P. (2012). Small heat shock proteins and the cytoskeleton: An essential interplay for cell integrity? Int J Biochem Cell Biol.

White, H.E., Orlova, E.V., Chen, S., Wang, L., Ignatiou, A., Gowen, B., Stromer, T., Franzmann, T.M., Haslbeck, M., Buchner, J.*, et al.* (2006). Multiple distinct assemblies reveal conformational flexibility in the small heat shock protein Hsp26. Structure *14*, 1197-1204.

Wigley, W.C., Fabunmi, R.P., Lee, M.G., Marino, C.R., Muallem, S., DeMartino, G.N., and Thomas, P.J. (1999). Dynamic association of proteasomal machinery with the centrosome. J Cell Biol *145*, 481-490.

Wilkins, M.R., Gasteiger, E., Bairoch, A., Sanchez, J.C., Williams, K.L., Appel, R.D., and Hochstrasser, D.F. (1999). Protein identification and analysis tools in the ExPASy server. Methods Mol Biol *112*, 531-552.

Winkler, J., Seybert, A., Konig, L., Pruggnaller, S., Haselmann, U., Sourjik, V., Weiss, M., Frangakis, A.S., Mogk, A., and Bukau, B. (2010). Quantitative and spatio-temporal features of protein aggregation in Escherichia coli and consequences on protein quality control and cellular ageing. EMBO J *29*, 910-923.

Xiao, X., and Benjamin, I.J. (1999). Stress-response proteins in cardiovascular disease. Am J Hum Genet *64*, 685-690.

Xu, J., Reumers, J., Couceiro, J.R., De Smet, F., Gallardo, R., Rudyak, S., Cornelis, A., Rozenski, J., Zwolinska, A., Marine, J.C.*, et al.* (2011). Gain of function of mutant p53 by coaggregation with multiple tumor suppressors. Nat Chem Biol *7*, 285-295.

Young, J.C., Agashe, V.R., Siegers, K., and Hartl, F.U. (2004). Pathways of chaperone-mediated protein folding in the cytosol. Nat Rev Mol Cell Biol *5*, 781-791.

Zimmerman, S.B., and Trach, S.O. (1991). Estimation of macromolecule concentrations and excluded volume effects for the cytoplasm of Escherichia coli. J Mol Biol *222*, 599-620.

9 Publications

Peschek J, Braun N, Franzmann TM, Georgalis Y, Haslbeck M, Weinkauf S & Buchner J (2009) The eye lens chaperone α-crystallin forms defined globular assemblies. *Proc Natl Acad Sci USA* 106:13272-13277

Braun N, Zacharias M, **Peschek J**, Kastenmüller A, Zou J, Hanzlik M, Haslbeck M, Rappsilber J, Buchner J & Weinkauf S (2011) Multiple molecular architectures of the eye lens chaperone αB-crystallin elucidated by a triple hybrid approach. *Proc Natl Acad Sci USA* 108:20491-20496

10 Danksagung

Ich möchte mich bei den Menschen bedanken, die mich während meiner Promotion begleitet, gefördert und inspiriert haben. Diese Unterstützung bedeutet mir sehr viel. Es sind viele Menschen, die auf unterschiedliche Weise zu dieser Arbeit beigetragen haben, und ich bitte jene um Veständnis, die ich hier nicht namentlich erwähnen kann.

Ich möchte mich zunächst sehr herzlich bei meinem Doktorvater Johannes Buchner für die Betreuung meiner Doktorarbeit, sowie den stets produktiven Austausch, der diese Arbeit ermöglicht und gestaltet hat, bedanken. Weiterhin möchte ich ihm für den großen wissenschaftlichen und kreativen Freiraum bei der Umsetzung meines Dissertationsprojektes danken. Dies hat mir ermöglicht, eigene Fragestellungen zu formulieren, und macht es mir schwer, mich von „meinem“ Projekt zu trennen.

Ich möchte mich bei Prof. Sevil Weinkauf und Dr. Nathalie Braun für die sehr interessante und produktive Zusammenarbeit bei der Struktraufklärung durch Elektronenmikroskopie und bei vielen weiteren Aspekten dieses Projekts bedanken.

Ich danke allen Doktoranden und Mitarbeitern des Lehrstuhls Biotechnologie, die mir während meiner Doktorarbeit geholfen haben und der Grund dafür sind, dass ich diesen Lebensabschnitt wissenschaftlich und auch persönlich als eine schöne und prägende Zeit in Erinnerung behalten werde. Bei Frau Hilber, der Sekretärin des Lehrstuhls, möchte ich mich für die hilfreichen Ratschläge in Belangen der Bürokratie, Verwaltung und Lebensführung bedanken. Besonderer Dank gebührt weiterhin Titus Franzmann, Alexander Bepperling, Katrin Back, Julia Rohrberg, Thomas Kriehuber, Sonja Schmid, Franziska Tippel und allen Praktikanten für die Unterstützung im Labor und die Hilfe bei verschiedenen Experimenten.

Ich danke der Studienstiftung des deutschen Volkes für die großzügige finanzielle und ideelle Förderung meiner Dissertation.

Schließlich danke ich meiner Familie und meinen Freunden, ohne die sehr vieles nicht möglich wäre. Mein tiefer Dank gilt meiner Mutter, der ich diese Arbeit widmen möchte. Děkuji.